ABSTRACT

Title of Dissertation:	TWO-PHASE FLOW REGIMES AND HEAT TRANSFER IN A MANIFOLDED-MICROGAP
	David Charles Deisenroth Doctor of Philosophy, 2018
Dissertation directed by:	Professor Michael Ohadi Professor Avram Bar-Cohen (co-advisor) Mechanical Engineering

Embedded cooling—an emerging thermal management paradigm for electronic devices—has motivated further research in compact, high heat flux, cooling solutions. Reliance on phase-change cooling and the associated two-phase flow of dielectric refrigerants allows small fluid flow rates to absorb large heat loads. Previous research has shown that dividing chip-scale microchannels into parallel arrays of channels with novel manifold designs can produce very high chip-scale heat transfer coefficients with low pressure drops. In such manifolded microchannel coolers, the coolant typically flows at relatively high velocities through U-shaped microgap channels, producing centripetal acceleration forces on the fluid that can be several orders of magnitude larger than gravity. Furthermore, the manifolded microchannels consist of high aspect ratio rectangular channels, short length to hydraulic diameter ratios ($L/D_h < 100$), and step-like inlet restrictions. The existing literature provides only limited information on each of

these effects, and nearly no information on the combined effects, on fluid flow and heat transfer performance.

This study provides fundamental insights into the impact of such channel features and coupled fluid forces on two-phase flow regimes and their associated transport rates. Moreover, because the flows in manifolded microchannel chip coolers are very small and optically inaccessible, a custom visualization test section was developed. The visualization test section was supported by a custom two-phase flow loop, which incorporated three power supplies, two chillers, and two dozen thermofluid sensors with live data monitoring. The fluid flow and wall heat transfer in the visualization test section was simultaneously imaged with a high-speed optical camera and a high-speed thermal camera. The results were reported with maps of the flow regime, wall temperature, wall temperature fluctuation, superheat, heat flux, and heat transfer coefficients under varying heat fluxes and mass fluxes for three manifold designs. Variations in flow phenomena and thermal performance among manifold designs and between R245fa and FC-72 were established. The post-annular flow regime of annular-rivulet was associated with a precipitous decline in wall heat transfer coefficients. The current experimental campaign is the first in the open literature to study the thermal and hydrodynamic characteristics of manifolded-microgap channels in such detail.

TWO-PHASE FLOW REGIMES AND HEAT TRANSFER IN A MANIFOLDED-MICROGAP

by

David Charles Deisenroth

Dissertation submitted to the Faculty of the Graduate School of the
University of Maryland, College Park, in partial fulfillment
of the requirements for the degree of
Doctor of Philosophy
2018

Advisory Committee:
Professor Michael Ohadi, Chair
Professor Avram Bar-Cohen (co-advisor)
Professor Siddhartha Das
Professor Marino diMarzo
Professor Bao Yang
Professor Alireza Khaligh

Acknowledgements

Thank you to Dr. Ohadi for his continued guidance and support throughout the course of this PhD project. Thank you to Dr. Shooshtari and Dr. Mandel for their technical feedback and insights. A special thank you to our beloved friend and colleague, Dr. Serguei Dessiatoun, who helped me to develop as an experimentalist and innovator. And also a big thank you to Dr. Bar-Cohen for his tireless technical guidance and big-picture insights. Many thanks to Kerri Poppler James for excellent academic advising and support with department resources. Thank you to all my other friends and colleagues at the TherPES and S^2TS labs who helped make my time at UMD productive and enjoyable.

Financial support from the National Science Foundation Graduate Research Fellowship Program under Grant No. DGE 1322106 made this work possible. Partial support of this work by The 3M Company through donation of Fluorinert™ fluids is gratefully acknowledged. FLIR Systems, Inc. is also gratefully acknowledged for donation of ResearchIR software for infrared image capture and processing.

Table of Contents

List of Tables

List of Figures

Chapter 1: Introduction to High Flux Electronics Cooling

1.1 Thermal Limitations of Electronic Devices

Heat generation is intrinsic to electronic devices and is primarily due to Joule heating. Without adequate cooling, semiconductor devices will approach an upper temperature limit at which a device will cease to function. At elevated temperatures, approaching this upper limit, semiconductor devices typically exhibit decreased functionality and efficiency. For example, light emitting diodes exhibit a rapid decline in luminous efficacy—light power per electric power—as temperature increases. In power diodes, high temperatures cause reverse saturation current to increase, decreasing functionality and generating more heat and temperature rise. Power diodes also become more susceptible to avalanche breakdown (loss of functionality) and subject to reverse bias with increasing temperature. Transistors suffer from decreased functionality at high temperatures, including increased leakage current and erroneous switching due to signal noise. From these examples, it can be observed that temperature is a critical concern for basic functionality and efficiency of electronics [1, 2].

Elevated temperatures also cause mechanical reliability issues in electronics [1]. Firstly, metallic wire traces have a coefficient of thermal expansion (CTE) about an order of magnitude greater than ceramics. This CTE mismatch between conductors and substrate materials—including traces on chip and on metal-ceramic substrates, as well as between chips and laminated printed wiring boards,—causes stresses that are exacerbated by large temperature changes, increasing fatigue failures, and reducing

longevity. Similarly, cyclical expansion due to large temperature changes can cause fatigue cracking in the wire bonds, solder balls, and die attach that connect/interconnect active devices to their packages. Elevated temperatures also accelerate the formation of brittle intermetallic compounds in wire bonds, solder balls, and die attach, further increasing susceptibility to cracking and loss of electrical connection. Furthermore, elevated temperatures decrease the current density threshold for electromigration, creating conditions for possible loss of electrical connection by this failure mode. And so, it can be observed that temperature control is a critical concern for both functionality and reliability as electronics become increasingly power dense.

Temperature control is becoming an increasingly relevant problem as chip heat fluxes increase due to increasing leakage currents as transistor size and spacing decrease in traditional silicon devices. As the lower size limit for on-chip features is approached, chip stacking and heterogeneous integration become increasingly attractive options for further increases in processing power and innovation of device capabilities; these burgeoning packaging approaches increase the heat density within electronics packages, requiring improved cooling approaches.

New wide bandgap semiconductor technologies, such as epitaxial GaN on diamond for high electron mobility transistors (HEMTs) can exhibit extraordinary performance compared with more traditional silicon devices. For power devices, SiC can handle much higher voltages than traditional silicon power devices, and because of the improved performance are becoming increasingly common. But, these rapidly

evolving wide bandgap devices also produce much greater heat fluxes than traditional silicon devices, and therefore need low-resistance thermal management solutions.

As device and package heat fluxes have continued to increase, some devices have become "thermally limited," in which the electrical capabilities cannot be fully realized because the thermal management system is insufficient to maintain operational junction temperatures. Oftentimes, the thermal management system performance is limited because the allowable size, weight, power, and cost (SWAP-C) of the cooling system competes with the overall SWAP-C of the electronics package. Therefore, there is a significant need for thermal management solutions that can dissipate high heat fluxes with manageable junction temperatures, while also minimizing the SWAP-C of the cooling system.

In traditional electronic packaging, thermal management has often been treated as an afterthought. Although materials, layers, and interconnects differ by application and manufacturer, many modern high heat flux packages have a detrimental similarity—several thermally resistive layers between the heat source (the junctions on the active surface of the die) and the heat sink. Figure 1.1 illustrates a traditional thermal management approach, in which the heat sink is located "remotely," from the heat source.

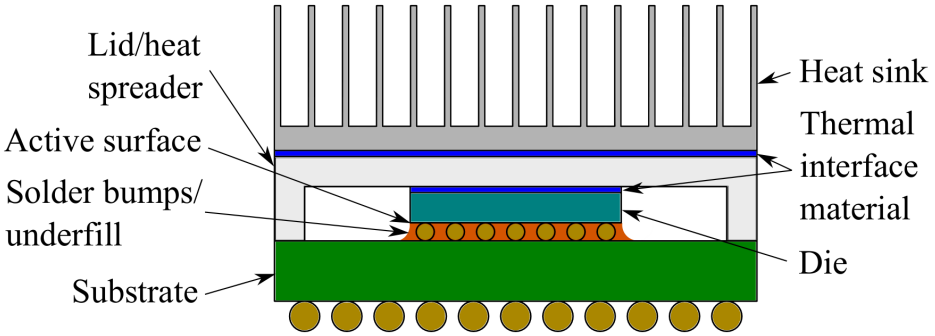

Figure 1.1: Example package illustrating traditional "remote" cooling

In this example, the primary sources of heat are the semiconductor junctions on the active surface of the die. The governing equation for heat transfer from the junctions to the ambient is shown in Equation (1), in which T_j is the junction temperature, T_{amb} is the ambient temperature to which heat is rejected, q is the heat dissipation from the die into the heat sinking layers, and R_{tot} is the total thermal resistance between the junctions and the ambient. It can be seen that for a given chip heat flux and ambient temperature, the junction temperatures rise with increasing thermal resistance.

$$T_j - T_{amb} = qR_{tot} \tag{1}$$

The thermal resistances comprising the total thermal resistance from the junction to the ambient are additive, as shown in Equation (2). The heat spreads through the near-junction materials (R_{NJ}) laterally within the semiconductor die, and then vertically through the thickness of the die (R_{die}). From the die, the heat must flow through a thermal interface material (R_{TIM1}) into the heat spreader (R_s), and into a second layer of thermal interface material (R_{TIM2}). From there, heat flows into the heat sink fins (R_{HS}) and then finally into a convecting cooling fluid (R_{conv}).

$$R_{tot} = R_{NJ} + R_{die} + R_{TIM1} + R_s + R_{TIM2} + R_{HS} + R_{conv} \quad (2)$$

The dominant thermal resistance is often the TIMs. The TIM layers are beneficial because they reduce the thermal resistance from a solid-solid contact resistance that would exist in the absence of a TIM by filling surface roughness features that would otherwise be filled with air [3]. These compliant TIMs also accommodate differential thermal expansion and contraction between CTE mismatched materials. TIMs are commonly composed of a polymer paste filled with conductive material. With this common approach, the thermal resistance of the TIM(s), is often the dominant thermal resistance, because with a thermal conductivity on the order of 1 W/m-K or less, so that even thin layers of TIM generate a large thermal resistance [4]. Metallic solder alloys can replace polymer TIMs in some instances, providing an order of magnitude, or greater, improvement in thermal conductivity, but are subject to the reliability problems discussed previously, and are much more expensive to develop and implement [3]. And so, for further development of high heat flux electronics, it is beneficial to remove the detrimental thermal resistances—particularly TIMs—from the package and cooling system.

1.2 **Embedded Cooling**

The thermal resistance between the junction and the cooling fluid can potentially be decreased by an order of magnitude by removing thermal resistances found in traditional electronics packaging [5]. Depending on the device and manufacturer, thermal resistances can include solders, thermal interface materials, and heat spreaders. “Embedded cooling” [6] is a thermal management approach that

removes these detrimental thermal resistances and puts the cooling fluid directly in contact with the die.

One embedded cooling approach is to put the cooling fluid in direct contact with the backside of an active die. Boteler [7] fabricated a manifold-microchannel cooler from silicon and bonded it to a SiC power device. The cooling fluid was single phase water and the thermal resistivity of the system was improved by an order of magnitude compared with conventional thermal packaging of a comparable device. The peak heat flux was 650 W/cm^2, allowing the power device to potentially handle an order of magnitude more power per package area. Ditri et al. [8] fabricated a palladium manifold to distribute fluidic jets across the backside of a GaN on SiC high power RF amplifier. The working fluid was a single 40% propylene glycol, 60% water mixture. The power added efficiency of the device was increased by 2.5 to 3.5 times as a direct result of the factor-of-three decrease in thermal resistance between the junction and the coolant, when compared with a more traditional remote cooling approach.

An embedded cooling approach with, perhaps, the greatest potential for desirable cooling system SWAP-C is an “intrachip” approach that embeds microchannels directly into the backside of the die. This approach was first documented by Tuckerman and Pease [9] in 1981. The cooling fluid was water, and a heat flux of 790 W/cm^2 was dissipated from the silicon chip with only a 71°C temperature rise, marking a substantial improvement compared to contemporary packages. Kermani et al. [10] demonstrated that a similar approach with manifolded-microchannels, showing that highly efficient junction temperatures could be

maintained for concentrated solar cells with low pumping power. Altman et al. [11] used a sophisticated fabrication process to form microchannels within diamond for manifold-microchannel cooling of a GaN on diamond HEMT monolithic microwave integrated circuits (MMIC) device. The transistors dissipated in excess of 30 kW/cm^2, with a chip base heat flux of more than 1 kW/cm^2. The peak transistor temperatures were nearly 100°C less than a comparable GaN on diamond device with remote cooling, and nearly 400°C less than a GaN on SiC device with remote cooling.

The benefits of embedded cooling can also be realized for cooling 3D stacked chip devices, which are likely to become increasingly prevalent in efforts to increase processor performance as the on-chip feature size is approached in silicon processor chips. Schultz et al. [12] demonstrated an "interchip" approach to cooling large, 20 mm by 20 mm, chips compatible with 3D stacking. Because the cooling fluid is put directly in contact with the active area of the dies, the cooling fluid—R1234ze—was dielectric. The fluid was fed through a hole in the center of the dies, from which it radially expanded to the outlet at the perimeter of the dies. The cooling system utilized the latent heat of vaporization of the fluid in order to reach heat fluxes of 350 W/cm^2 on high flux areas of the processor die, with temperature rise less than 30°C above the fluid inlet temperature.

From these examples, it can be seen that embedded cooling represents a paradigm shift in how electronics are cooled [13-15]. Reducing the thermal resistance between the active device and the cooling fluid allows for improvements in power capacity, efficiency, and processing capability in electronics devices—all of which enable improved functionality and further innovation.

1.3 Motivation for Pumped Two-Phase Cooling

The premise of embedded cooling is to reduce the thermal resistance between the junction and cooling fluid by removing the conductive thermal resistances found in traditional remote electronics cooling. To maximize the benefit of embedded cooling, the thermal resistance between the heat transfer surface and the cooling fluid must also be reduced. The efficacy of heat transfer to fluids is best expressed as heat transfer coefficient (HTC), shown in Equation (3), in which q'' is the wall heat flux, T_w is the wall temperature, and T_f is the fluid reference temperature. Conceptually, HTC is the area-specific inverse of thermal resistance, so high HTC's are desirable, indicating maximum heat transfer per surface area per temperature rise.

$$HTC = \frac{q''}{T_w - T_f} \tag{3}$$

The HTC's produced by different fluids under varying conditions span five orders of magnitude [16]. Factors affecting the HTC's produced include fluid density, thermal conductivity, specific heat, latent heat of vaporization, flow rate, surface roughness, hydraulic diameter, and more. Although there are many factors at play, an order of magnitude estimate of expected fluid-wall HTC's under typical conditions applicable to electronics coolers are as follows: air natural convection ~10 W/m^{2}K, air forced convection ~100 W/m^{2}K, liquid forced convection ~1,000 W/m^{2}K, pool boiling ~10,000 W/m^{2}K, and flow boiling ~10,000+ W/m^{2}K [16]. The need for increasing HTC's for electronics cooling is evidenced by how the time evolution of electronics cooling approaches has generally followed the trend of increasing order

HTC's—starting with natural convection in the earliest devices, moving to forced air cooling, then to liquid cooling in high performance desktop computers and servers.

Similarly to single-phase natural convection, heat rejection by phase change can be driven by forces occurring within the fluid. Single-phase natural convection is driven by temperature-induced buoyancy, while phase change passive coolers incorporate fluid forces generated by vapor buoyancy, capillarity, and differential bubble expansion. Modern portable computers and other SWAP-C limited, orientation independent, devices increasingly use "heat pipes." The flow in heat pipes is typically driven by a capillary wick, which transports liquid from the condenser back to the evaporator. A burgeoning area of study that is not limited by relatively the weak capillary forces driving standard heat pipes, while still utilizing passive (pumped by internal fluid forces) phase change cooling is in "pulsating heat pipes." In pulsating heat pipes, the flow is driven by differential bubble expansion and contraction in the evaporator and condenser sections [17]. Water is often the working fluid for these two types of heat pipes. A recent study used micropillar wicks for passive, capillary-pumped evaporation of water, achieving a peak chip-scale heat flux of 45 W/cm^2 at 19°C superheat before becoming limited by the efficacy of capillary pumping [18]. These passive systems may produce HTC's comparable to pool boiling, on the order of 10,000 W/m^2K, which are suitable for many modern applications. But, as packages become more power dense due to stacked chip architectures, heterogeneous integration, and increasing utilization of wide band gap semiconductor devices, the need for even higher chip-scale HTC's is growing.

Increased HTC's often come at the cost of increased pumping power in single-phase flows, with the exception of buoyancy-driven flows—the lowest HTC option. The fact that heat can conduct into a fluid without active pumping, and the fact that pipe flow can occur with adiabatic channel walls, indicate that heat transfer and momentum transfer are not mutually necessary. But, there is a strong relationship between the single-phase velocity boundary layer and the thermal boundary layer in forced convection, as explained by Reynold's Analogy [16]. Therefore, it is expected that for a given heat exchanger, heat transfer can be increased at the cost of increased pressure drop required to drive the flow. The principle of Reynold's Analogy is also relevant to pumped mass transfer [19] and pumped phase-change heat transfer [20]. The engineering challenge, then, is to design heat exchangers with the best trade-off between pumping power (pressure drop times volume flow rate) and heat transfer coefficient. Pumped two-phase cooling is advantageous because two-phase pumped cooling can remove more heat per pumping power than single-phase pumped cooling when configured correctly, although much research remains to be done in predictive modeling of heat transfer and pressure drop in diabatic two-phase flows [21-23].

In summary, electronics coolers have progressed from passive air cooling to forced air cooling, and forced liquid cooling to passive two-phase cooling. Therefore, the need for actively pumped two-phase cooling is likely to continue to increase, which is further evidenced by the growing number of studies on the topic [24-26].

1.4 **Remote Pumped Two-Phase Coolers**

Several recent, notable studies on high heat flux pumped two-phase chip coolers are shown in Table 1.1. Each of these remote chip coolers are constructed of

copper, meaning that these coolers are not embedded approaches, but could be used to eliminate the thermal resistance of polymer TIMs and heat spreaders by directly soldering the cooler to the backside of a die. It can be seen that each cooling approach utilizes area enhancement to maximize the heat transfer area exposed to diabatic two-phase flow. Each approach also uses manifolding in order to reduce the pressure drop while producing high heat transfer. The remote chip-scale coolers produced heat fluxes ranging from 200 W/cm^2 to 1230 W/cm^2 with temperature rises above the fluid reference temperature ranging from 22°C to about 56°C, pressure drops ranging from 6 kPa to 60 kPa, demonstrating the efficacy of localized pumped two-phase cooling. The differences in the studies include how surface area and other surface enhancements were achieved, as well as the type of manifolding, and the cooling fluid.

The approached used by Rau et al. [27] and Joshi and Dede [28] incorporated macroscale and microscale surface enhancements. The macroscale features were pin-fins, and a microporous coating was added, forming a multiscale surface enhancement. Both studies used similar manifolds, in which an array of 25 orifices produced jet impingement on the multiscale enhanced surface. Better performance was produced in the second study which used R245fa in contrast to HFE-7100 [28]. In the second study, pressure drop and temperature rise were also reduced while increasing peak heat flux.

The approach reported by Kalani and Kandlikar [29] used a tapered manifold, which increased the cross-sectional flow area moving downstream with a non-contacting manifold above the microchannels. This approach may increase vapor

venting, and was reported to reduce the pressure drop while fundamentally altering the flow regimes occurring within the channels. A peak heat flux of 506 W/cm^2 was reported with a wall temperature of about 130°C with water as the working fluid.

Manifold-microchannels (MMC), the area enhancement geometry of interest in this dissertation for high heat flux two-phase cooling, were used by Baummer et al. [30] to achieve a base heat flux of 300 W/cm^2 with HFE-7100 as the working fluid. A later generation of the design achieved 1230 W/cm^2 with the low-pressure refrigerant R245fa as the working fluid [31]. And so, it can be observed that MMC's can achieve very high heat fluxes with low superheats and low pressure drops in remote, chip-scale coolers.

Table 1.1: High heat flux chip-scale two-phase cooling approaches—remote

Ref.	Cooling Approach	Fluid	Sub-cooling (°C)	Peak heat flux (W/cm^2)	Saturation temperature (°C)	Peak super-heat (°C)	Superheat reference temperatures	Flow rate	Pressure drop (kPa)
[27]	Array of impinging jets on copper pin-fins coated with microporous surface enhancement	HFE-7100	10	206	61 [1]	35	$T_{heater} - T_{sat}$	30 mL/s	10.9
[28]	Array of impinging jets on copper pin-fins coated with microporous surface enhancement	R245fa	5	218	45	22	$T_{heater} - T_{in}$	10 g/s	6.4
[30]	Manifold microchannels in copper	HFE-7100	-	300	60	50	$T_{surface} - T_{sat}$	4.2 mL/s	-
[29]	Parallel microchannels in copper with non-contacting, tapered manifold expanding in streamwise direction	Water	10	506	100 [1]	26.2	$T_{wall} - T_{sat}$	393 kg/m^2s	-
[31]	Manifold microchannels in copper	R245fa	8.5	1230	36	56	$T_{wall} - T_{sat,av}$	1400 kg/m^2s	60

[1] At atmospheric pressure

1.5 Embedded Pumped Two-Phase Coolers

As discussed previously, embedded cooling reduces junction temperatures by removing interfacial thermal resistances, and this effect is particularly pronounced at very high heat fluxes. One of the focuses of the DARPA ICECool program was to increase the maturity of embedded two-phase cooling for chip-scale heat fluxes exceeding 1 W/cm^2 [32]. The majority of the notable studies on two-phase embedded cooling summarized in Table 1.2 are related to the ICECool program.

There are three general approaches in the studies shown in Table 1.2. Each of the coolers are embedded in the backside of the semiconductor die and incorporate surface area enhancement. The first general approach is use of a pin-fin microgap, the second is use of manifolded microchannels, and the third involves a porous copper surface enhancement on diamond fins. Within each approach, the manifolding differs, and the working fluid also differs.

Schultz et al. [12] used pin-fin microgap cooling, compatible with chip stacking, with a central fluid inlet allowing the R1234ze refrigerant to expand radially outward as phase change occurred. Heaters were used to mimic processor heat production, and the peak processor heat fluxes reached 350 W/cm^2 with a junction temperature rise of only 36°C [33]. Outside of the processor areas, a "background" heat flux of about 20 W/cm^2 was dissipated. The second pin-fin microgap cooler used hydrofoil-shaped pin-fins with R245fa as the cooling fluid and a single inlet and outlet on either end of the chip. A peak heat flux of 326 W/cm^2 was produced with 145°C of superheat and outlet quality of 13%. The third pin-fin microgap study used water as the working fluid with outlet pressure below atmospheric, reducing the

saturation temperature [34]. A peak heat flux of 444 W/cm^2 with 60°C superheat was achieved with subcooling of more than 50°C and outlet quality of 7%.

The first manifolded microchannel study used just one inlet and two outlets, forming channels with length on the order of 1 cm [21]. A peak heat flux of 255 W/cm^2 was achieved at 27°C of superheat and 74% outlet quality with R236fa as the working fluid. A more aggressive manifolding approach was used by Drummond et al. [35], in which a "hierarchical" manifold was constructed from stacked silicon wafers to form nine fluid inlets. The shorter flow length generated by the manifold-microchannel design dissipated 910 W/cm^2 with 162 kPa pressure drop and 28% outlet quality with HFE-7100 as the working fluid. Bae et al. [36] used an additively manufactured titanium manifold with 10 inlets bonded to a SiC chip to dissipate 1 kW/cm^2 with 200 kPa pressure drop and 85% outlet quality with R245fa as the working fluid. A previous generation of the design produced the highest heat flux two-phase embedded manifold-microchannel chip cooler in a Si chip, which was reported by Mandel et al. [37]. The system dissipated 1100 W/cm^2 with 87 kPa of pressure drop and 50% outlet quality with R245fa as the working fluid. From these studies, it can be observed that manifolded microchannels show excellent utility in dissipating high heat fluxes from electronic devices with low temperature rise and low pressure drop, while using dielectric cooling fluids. The MMC coolers achieved, by a large margin, the highest outlet quality (mass faction of vapor) of any of the studies reported here, with that of Bae et al. [36] exceeding 85%.

The highest heat flux study shown in Table 1.2 used water as the working fluid with a membrane based manifold to deliver water to the diamond fins that were

coated with porous copper [38]. A peak heat flux of 1342 W/cm^2 was reported with a pressure drop of 42 kPa while venting the water vapor to the ambient.

The coefficient of performance (COP) for each of the two-phase embedded coolers is also estimated in Table 1.2. In this context, the COP is the heat removed from the chip divided by the pumping power required to drive the flow, and is taken at the peak heat flux. The COP generated by the manifold microchannel coolers with refrigerant as the working fluid in Agostini et al. [21], Bae et al. [36], and Mandel et al. [37] are relatively comparable. In these studies, each cooler required less than one thousandth of the power to drive the cooling fluid than heat removed by it. The manifold microcooler with HFE-7100 as the working fluid [35] less effectively used the available latent heat of vaporization, and therefore, required a substantially higher fluid flow rate with a comparable pressure drop to the refrigerant studies, resulting in a substantially decreased COP. The highest COPs are generated by Han et al. [34] and Palko et al. [38], both using water as the phase-change coolant, demonstrating the potency of water as a heat transfer fluid. The benefits and drawbacks of the fluids used for phase-change electronics cooling will be discussed in the following section.

Table 1.2: High heat flux chip-scale two-phase cooling approaches—embedded

Ref.	Cooling Approach	Fluid	Sub-cooling (°C)	Peak heat flux (W/cm^2)	Outlet quality	Saturation temperature (°C)	Super-heat (°C)	Superheat reference temperatures	Flow rate	Press-ure drop (kPa)	COP [4]
[12]	Si microgap with central inlet, flow expanding radially through pin-fin array	R1234ze	7	350 [1] 20 [2]	-	32 [3]	36	$T_{junction}$ - T_{in}	4.2 g/s	320	-
[21]	Parallel microchannels in Si, manifold with central inlet and two outlets at ends	R236fa	0	255	74%	25	27	T_{chip} - T_{sat}	827 kg/m^{2}s	90	1550
[33]	Microgap with Si hydrofoil pin-fins	R245fa	-	326	13%	10 [3]	130	T_{chip} - T_{in}	1610 kg/m^{2}s	-	-
[34]	Si pin-fin microgap, atm. pressure inlet, low vacuum outlet (~30 kPa), low temperature inlet (~10°C)	Water	50+	444	7%	65	60	T_{wall} - $T_{sat,out}$	1784 kg/m^{2}s	130	1600
[35]	Manifold microchannels in Si	HFE-7100	7	910	8%	66	33	T_{chip} - T_{in}	2900 kg/m^{2}s	162	160
[36]	Manifold bonded to microchannels in SiC	R245fa	5	1000	85%	30	95	T_{chip} - $T_{sat,av}$	6 g/s 1400 [4] kg/m^{2}s	200	1110
[37]	Manifold (press-fit) microchannels in Si	R245fa	5	1100	50%	30	81	T_{chip} - $T_{sat,av}$	12 g/s 1200 [4] kg/m^{2}s	87	1400
[38]	Porous copper wick on diamond fins	Water	-	1342	-	110	30	T_{chip} - $T_{sat,in}$	3.1 g/s	42	7200

[1] Heat flux at processor cores, [2] Background heat flux, [3] Inlet temperature, [4] Estimated

1.6 Comparison of Working Fluids

In comparing several common fluids used for two-phase electronics cooling, it can immediately be seen that water is an excellent heat transfer fluid. The latent heat of vaporization and thermal conductivity of water are an order of magnitude greater than those of electronics cooling fluids (FC-72 and HFE-7100) and refrigerants often researched for electronics cooling (R236fa, R245fa, and R134a). Furthermore, the specific heat of water is more than three times greater than those fluids. Not to mention that, high-purity water is orders of magnitude less expensive than any of the engineered fluids. Therefore, water is in many ways a natural choice for high heat flux cooling.

Water is not without drawbacks for embedded cooling, though. Firstly, unless deionized, water is an electrical conductor. Secondly, water is a solvent, and therefore should be carefully isolated from electronic devices. Third, water can be absorptive of RF signals, and therefore results in an insertion loss when put in close proximity with RF devices [11]. Furthermore, the atmospheric pressure saturation temperature of water is 100°C, meaning that for two-phase operation, at atmospheric pressure, junction temperatures will be quite high. The saturation temperature can be reduced by operating the system under vacuum, but this approach raises reliability concerns of air ingress over time: a concern which is less relevant in systems operating with positive pressure. Water also has a higher freezing temperature than most engineering fluids, which could result in catastrophic failure in low ambient temperature environments; ethylene glycol reduces freezing temperature, but is detrimental to thermal performance.

Engineered fluids can mitigate many of the concerns presented by water. These fluids are quite inert, dielectric, are available in a variety of saturation temperatures, and have a more favorable liquid-vapor density ratio. FC-72 has been considered the industry standard for single- and two-phase electronics cooling because of these favorable properties. HFE-7100, also manufactured by 3M, has a lower global warming potential and 27% greater latent heat, but tends to be more corrosive than FC-72. R134a is an industry standard refrigerant, and may soon be replaced by R1234ze in some applications. The relatively high saturation pressure of R134a at room temperature (6.7 atm) presents structural challenges in electronics cooling, so application of this refrigerant to embedded electronics cooling is relatively rare.

The lower pressure refrigerants are reported more often for embedded cooling, with R245fa being most common for its low pressure, high latent heat, and high thermal conductivity compared to R236fa. The room temperature saturation pressure of R245fa is about ½ that of R236fa, with 1.5 atm compared to 2.7 atm, respectively. This reduced pressure requirement reduces the structural strength required by the embedded cooling package, which may also be used to reduce package size. Another advantage is that the latent heat of vaporization of R245fa exceeds that of R236fa a by 31% (190 kJ/kg compared to 145 kg/kg) while the liquid thermal conductivity is also 17% higher (0.081 W/m-K compared to 0.069 W/m-K). Both of these higher fluid property values both improve effectiveness of two-phase heat removal.

Table 1.3: Comparison of common working fluids for embedded two-phase coolers. All properties at 25°C unless otherwise noted.

Fluid	Saturation Temperature at Atmospheric Pressure (°C)	Saturation Pressure (kPa)	Specific Heat (kJ/kg-K)	Latent Heat of Vaporization [1] (kJ/kg)	Liquid Thermal Conductivity (W/m-K)	Liquid Density (kg/m^3)	Vapor Density [1] (kg/m^3)
FC-72	56	-	1.1	88	0.057	1680	13
HFE-7100	60	-	1.18	112	0.069	1510	9.9
R236fa	-	272	1.24	145	0.069	1360	18
R245fa	-	148	1.32	190	0.081	1340	8.5
R134a	-	666	1.43	178	0.083	1210	32
Water	100	-	4.18	2250	0.59	1000	0.6

[1] At normal boiling point

1.7 Summary of Motivation for High Heat Flux Electronics Cooling

Stack chip architectures and heterogeneous integration are increasingly becoming necessary for continued increases in processing speed and electronic system performance**.** Concurrently, while the use of wide bandgap devices is becoming increasingly prevalent, many of these components are thermally limited, failing to achieve their inherent electronic performance due to inadequate thermal management. Devices generating much higher heat fluxes than traditional silicon devices and traditional packages increase the need for localized high heat flux cooling solutions while minimizing the SWAP-C of the cooling system.

Electronics coolers have progressed from passive air cooling to forced air cooling, then to forced liquid cooling and to passive two-phase cooling [39, 40]. This trend is likely to continue, with a growing need for actively pumped two-phase cooling, as suggested by the growing number of studies on the topic. Pumped two-

phase cooling is advantageous because it can remove more heat per pumping power than single-phase pumped cooling when configured correctly [21]. Putting the semiconductor device in direct contact with the cooling fluid—embedded cooling—leads to further gains in heat transfer per temperature rise without any pressure drop penalty.

In an increasing number of studies, manifold-microchannels have shown excellent performance, producing very high chip-scale HTC's with excellent COPs [41, 42]. The focus of this dissertation is to gain phenomenological insight into how two engineered fluids perform as diabatic phase-change coolants within manifold-microchannel geometries, so as to enable prediction of performance limits and system design. One fluid is a standard electronics cooling fluid, FC-72, and the other is a low pressure refrigerant used in a growing number of electronics coolers, R245fa. Aside from reporting heat transfer and pressure drop, no previous studies have qualitatively and quantitatively characterized the complex two-phase flow phenomena and the associated local heat transfer occurring in manifold-microchannels.

1.8 **Dissertation Summary**

Chapter 2 will review literature on two-phase flow phenomena and the resulting heat transfer, further establishing the necessity of the current research. Chapter 3 will describe the experimental methods and data analysis used to present the results. Chapter 4 will qualitatively describe the visible flow phenomena found by high-speed imaging, then quantitatively map the flow regime outcomes while comparing with flow regime transition predictors. Chapter 5 presents the thermal imaging data in terms of average wall temperature profiles, wall temperature mean absolute deviation

(MAD) profiles, and average wall temperature MAD profiles. The pressure drop and average wall superheat with heat flux are also outlined in Chapter 5. Chapter 6 presents further analysis of the thermal data, presenting wall superheat profiles, wall heat flux profiles, and wall HTC profiles. Average wall HTC's are then presented in Chapter 6, with discussion on their relation to local wall HTC values. Chapter 7 compares the outlet flow regime results with HTC predictors, and the relationship between the two. The dissertation outcomes are summarized and main conclusions stated in Chapter 8, which are then followed by recommendations for future work.

Chapter 2: Literature Review of Two-Phase Flow Phenomena in Manifolded Microgap Channels

Manifold-microchannel geometries consist of a matrix of parallel microgap channels, as illustrated in Figure 2.1. For embedded cooling, microgrooves are etched in the inactive side of the chip or substrate. A manifold is stacked on the microgrooved chip, creating channels. Manifold flow dividers separate the flow into alternating inlets and outlets to split the flow length in the channels into much shorter lengths, reducing the frictional pressure drop and also reducing the mass flux per channel, further reducing frictional pressure drop. For high heat transfer coefficients, the microgrooves are high aspect ratio, having a hydraulic diameter much smaller than the width of the channels. The width of channels is the depth of the grooves etched into the chip. The disassembled (left) and assembled (right) illustration of this cooling approach is shown in Figure 2.1.

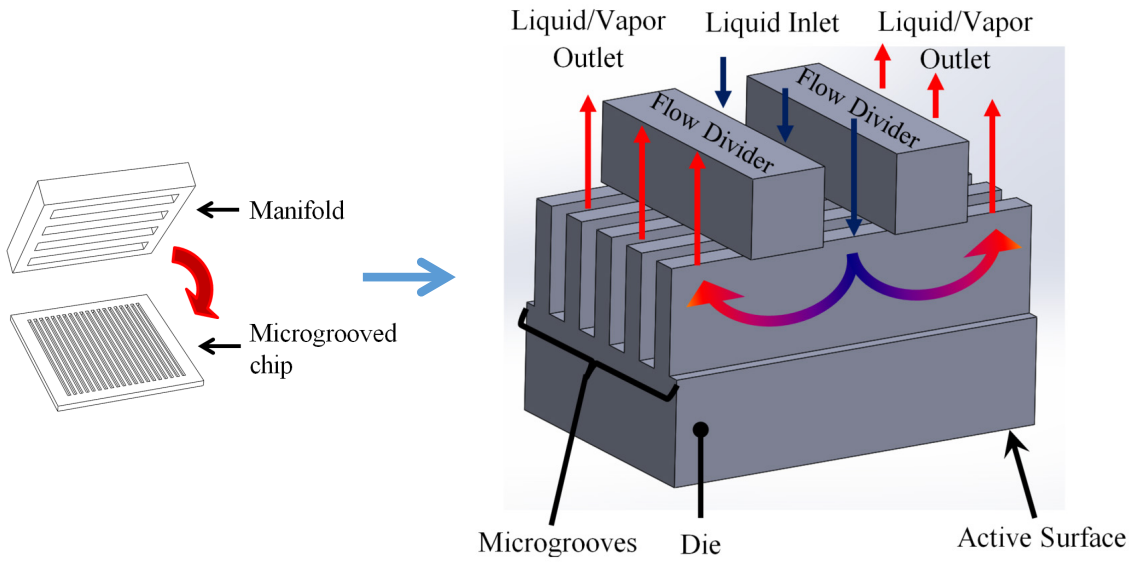

Figure 2.1: Illustration of a disassembled (left) and close-up assembled (right) illustration manifold-microchannel cooler

The resulting flow passages have several features that cause flow phenomena that can differ from the channels more commonly studied. First, the hydraulic diameter is microscale—on the order of tens to hundreds of microns. These small dimensions cause increased influence of surface tension and vapor shear, with decreased influence of gravity [43, 44]. Each of these changes in fluid forces may have ramifications for heat transfer. Second, as stated previously, the channel is high aspect ratio, having a hydraulic diameter significantly smaller than its width—a w_c/D_h ratio from about 3 to more than 10. Third, the length of the channel is a relatively small multiple of its hydraulic diameter—a L/D_h ratio from about 10 to 100. With an L/D_h ratio this small, single-phase flows are typically hydrodynamically developing, which can significantly increase the local heat transfer coefficient and axial pressure gradient. Similar trends may apply with two-phase flow in the channel, due to the "development length" required to stabilize a particular flow regime and compounded by the axial gradient in the vapor fraction and flow quality (vapor mass and volume) associated with diabatic flow. There is relatively little known about these developing two-phase flows, and it remains an area in need of further research [45].

Moreover, the cross-sectional area reduction incurred by the fluid at the entrance of the gap causes a sudden flow acceleration and pressure loss. Sufficient underpressure may exist to rapidly increase the vapor quality from the manifold to the entrance of the gap. This "flashing" is typically considered to be an adiabatic, isenthalpic process [46], although it does alter the liquid-vapor agglomeration at the entrance of the channel. And finally, because inlet and outlet of the microgap channels are located on the same side of the microgap, the flow follows a U-shaped

flow path. This tight flow path curvature causes enormous centripetal accelerations forces that can profoundly influence agglomeration of the liquid and vapor phases within the channel—and therefore, heat transfer. The flow passage features are illustrated in Figure 2.2.

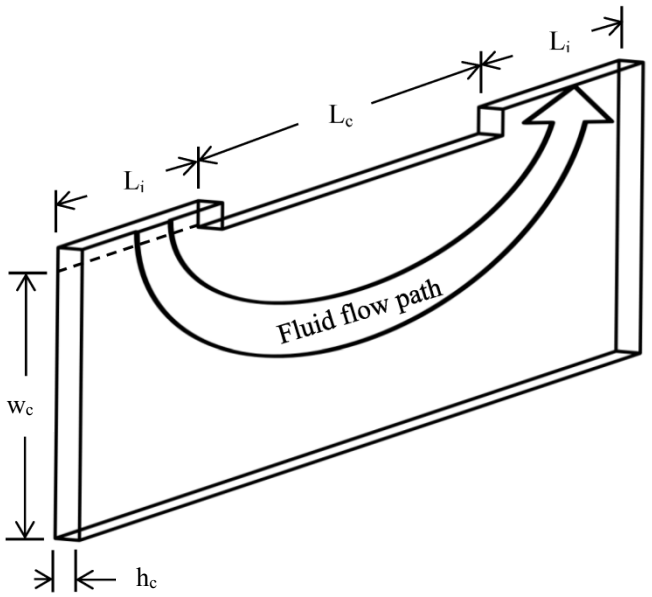

Figure 2.2: Illustration of a U-shaped microgap flow passage in a manifolded-microchannel cooler.

There are further differences and uninvestigated flow phenomena occurring in such embedded cooling structures, due to the interplay of manifolded channels. Perhaps the most investigated, but still in need of further research flow, are oscillations and the "cross-talk" occurring in manifolded microchannels flowing in parallel. These channels typically share only one inlet and outlet and it has been found that flow restrictions at the inlets of the channels can significantly reduce instabilities due to pressure oscillations between channels, improving thermal performance, but increasing pressure drop [47, 48].

The manifolded-microchannels of interest herein involve segmenting longer channels into shorter channels, so a divergence and confluence of fluid two-phase streams occur within a single microgroove channel at each inlet and outlet of the manifold. No studies to date have reported on the phenomena potentially resulting from combined confluence/divergence in this type of manifolding. The current study cannot address all potential two-phase flow phenomena occurring in manifolded-microchannels, instead focusing on a simpler configuration of—at most—two parallel U-shaped manifolded microgap channels simultaneously. It will, nevertheless, be shown that good insight can be gained into how the current geometry differs from more traditional two-phase geometries.

The heat transfer results obtained by several recent studies with manifolded-microchannel chip coolers show that there are some important differences when compared to traditional geometries. Notable studies include Bae et al. [36], Mandel [49], Cetegen [31], Ohadi et al. [42], and Drummond et al. [35]. There are some common trends in the HTC's exhibited between these studies, and the HTC's reported by Bae et al. [36] will be used as an example. Bae et al. [36] used R245fa as the working fluid to dissipate in excess of 1 kW from a 1 cm^2 SiC chip with embedded two-phase manifolded microchannels. The 10,000 parallel flow passages (manifolded microgaps) had heights of 10 μm and widths of 50 μm with lengths of 500 μm—forming a hydraulic diameter of 17 μm and L/D_h ratio of 30.

The wall HTC's from Bae et al. [36] were calculated as shown in Equation (3), in which the average wall heat flux is q''_w, the T_w is the average wall temperature, and T_{sat} is the fluid saturation temperature. The wall HTC results of Bae et al. [36] are

shown in Figure 2.3 (a). The mass fluxes of 700 kg/m^{2}s and 1,400 kg/m^{2}s correspond to a total R245fa flow rate of 3 g/s and 6 g/s to the chip. It can be seen that the HTC's increase approximately linearly with quality until about 40% and 30% quality for the 700 kg/m^{2}s and 1,400 kg/m^{2}s curves, respectively. After peaking at about 50,000 W/m^{2}k, the HTC's decline rapidly to plateaus at 17,000 W/m^{2}K and 27,000 W/m^{2}K, for the low and high mass fluxes, respectively.

$$HTC_w = \frac{q''_w}{T_w - T_{sat}} \tag{4}$$

The Chen [20] prediction has been adopted as a widely-applicable predictor of two-phase flow HTC's for decades, and will be discussed in more detail in the following sections of this chapter. But, for initial comparison, it can be seen that at the low qualities, the Chen prediction displays the same monotonic increase with quality observed in the empirical data. However, while for low qualities, the Chen relation underpredicts the experimental HTC's, as the empirical HTC's abruptly decline at qualities of 0.3 to 0.4, the Chen relation overpredicts the empirical values. The ratio of the Chen predicted HTC's to the experimental HTC's are shown in Figure 2.3 (b). A prediction ratio of one indicates that the Chen relation perfectly predicts the experimental HTC, while less than one is an underprediction and more than one is an overprediction.

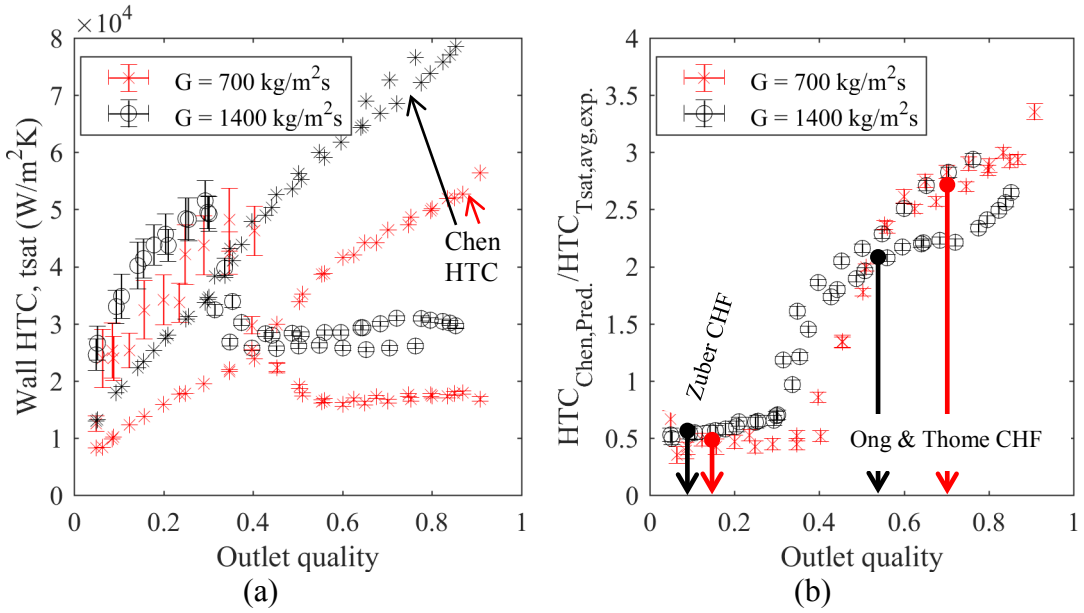

Figure 2.3: Wall HTC's in the study of Bae et al. [36] are shown in (a) at mass fluxes of 700 kg/m^{2}s and 1400 kg/m^{2}s. The Chen [20] HTC prediction (*) is shown at each data point. The Ong and Thome [50] predicted dryout/CHF quality are also shown. The ratio of the Chen correlation predicted HTC's to the experimental HTC's are shown in (b).

It can be seen that at the lower qualities, the experimental HTC's are underpredicted by about a factor of two, then after the inflection point, are over-predicted by a factor of two or more. An empirical departure from the Chen prediction is not unexpected, because two-phase flow cooling has documented limits.

One limit in two-phase cooling is caused when the vapor generation at the heated surface is so rapid that liquid cannot wet the surface, causing a rapid decline of HTC's. This phenomena is called by several names, including "departure from nucleate boiling (DNB)," "boiling crisis," and "film boiling," depending on the application and conditions under which it occurs. This prevention of wetting can occur in both pool boiling and convective boiling. The latter may result in "inverted annular" flow, in which a liquid core flows over a vapor film lining the channel wall.

A closely related thermal limit occurs at higher qualities when there is a deficiency of liquid available to wet the surface in the "normal" annular film, leading to dryout of the liquid film lining the channel wall. The closely related phenomena of DNB and dryout are often referred to under the blanket term of critical heat flux (CHF), and sometimes identified as low-quality CHF and high-quality dryout-type CHF. When either of these conditions occur, a rapid rise in wall temperature results in a rapid decline in wall HTC's.

An early and widely adopted CHF condition was developed by Forster and Zuber [51]. This Zuber CHF criteria was formulated analytically for pool boiling, and based on the bubble size and growth rate at the heated surface—the criteria will be discussed in more detail in the following sections. The Zuber CHF applied to the work of Bae et al. [36] is shown in Figure 2.3 (b), and it can be seen that the quality at which the HTC's inflect is underpredicted by a factor of about three. This is an expected result, because the Zuber CHF does not account for the suppression of bubble growth caused by the forced convection boundary layer [51], and therefore should underpredict the CHF for forced convection flows.

A recent forced convection CHF criteria empirically correlating mass flux, quality, and many more fluid properties than the Zuber CHF criteria was developed by Ong and Thome [50]. More specific details of the correlation will be discussed in the following sections, but it will be used to calibrate expectations here. It should be noted that this correlation was developed for 1-3 mm circular channels, so the 17 μm hydraulic diameters in Bae et al. [36] are outside the range of applicability of the correlation, but no strictly applicable correlations for two-phase manifold-

microchannels yet exist. The correlation predicts a dryout quality for which the HTC's should rapidly decline of 55% and 70% for the mass fluxes of 1,400 kg/m^{2}s and 700 kg/m^{2}s, respectively, for the work of Bae et al. [36]. These qualities are more consistent with expectations for the quality at which persistent dryout should occur, but over-predict the quality at which the HTC's decline in the work of Bae et al. [36] by a factor of about two.

This decline in HTC's at low qualities is reminiscent of those reported by Qu and Mudawar [52] with water in microchannels. The mechanistic cause was said to be a strong influence of droplet entrainment in vapor as the flow transitions to the annular regime at low quality. This entrainment of liquid may lead to an early deficiency in liquid, causing early dryout and declining HTC's.

The following sections will review literature relevant to the two-phase flow phenomena occurring in manifolded microgap channels. It will begin with discussion of two-phase flow regimes and their relationship to heat transfer. Literature on departures from long, straight, circular, macroscale—i.e. "traditional"—two-phase flows will be also be discussed.

2.1 **Overview of Two-Phase Flow Regimes**

In the high heat flux cooling solutions of interest, the phases constituting the two-phase flows are liquid and vapor. As vapor is generated by absorbing heat, the volume of vapor in the liquid flow continuously increases and causes the flow to evolve sequentially through flow regimes that can be identified by visual appearance. Each flow regime performs differently in terms of heat transfer and pressure drop,

and therefore understanding the flow regime evolution aids in understanding the fundamental fluid physics leading to that performance.

2.1.1 Traditional Two-Phase Flows

In macroscale flows, the four main flow regimes were identified and described by Taitel and Dukler [53]. These regimes were stratified, dispersed bubble (bubble), intermittent (slug), and annular. These flow regimes are shown in Figure 2.4. One of the identifying factors of macroscale flows is that gravity has a significant influence on the morphology of the flow, causing horizontal flow to be asymmetric about the pipe axis at low quality, with the heavier liquid tending to flow along the bottom and the lighter vapor along the top. For simplicity, stratified flow and wavy stratified flow will be identified here simply as stratified flow. In the dispersed bubble regime, the vapor phase consists of small bubbles mixed with the liquid phase; in this regime, the bubbles are driven axially at approximately the same speed as the liquid. The buoyancy of the bubbles may lead to a higher concentration of bubbles at the top of the tube.

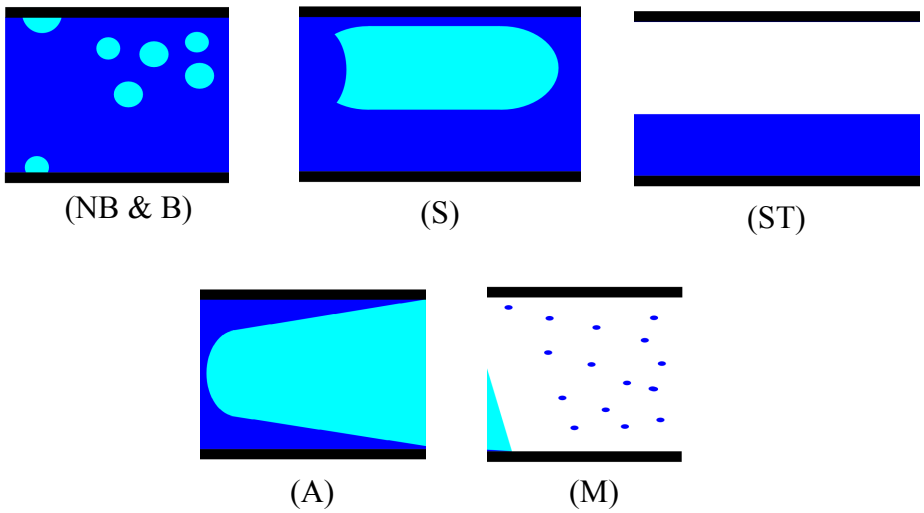

Figure 2.4: Illustration of flow regimes in macroscale channels. Nucleate boiling and bubble flow (NB & B) at low quality, slug flow at intermediate quality (S), stratified flow may alternatively occur at intermediate quality (ST), annular flow at higher quality (A), and finally, mist flow (M).

As quality increases, the intermittent (slug) regime occurs. In this regime, the smaller bubbles have coalesced into larger "slugs," that have cross-sectional area comparable to the pipe cross section but separated by liquid "plugs." In the stratified regime, the liquid and vapor phases are separated into layers, in which the buoyant gas phase flows along the upper part of the cross section while the heavier liquid phase travels along the lower part.

As the void fraction of the vapor increases, the high velocity vapor flow tends to drive the liquid phase into an annular ring lining the entire perimeter of the tube cross section with the vapor core flowing through the center. As more liquid is converted to vapor, the annular liquid film becomes depleted, leading to film rupture and local dryout.

Film depletion continues until the flow is single-phase vapor. Several flow phenomena may cause liquid droplets to become entrained with the vapor flow as the vapor flow interacts with the bulk liquid, including bubbles erupting through the liquid-vapor interface, turbulent fluctuations in the vapor, and vapor shear on the non-uniform liquid film. The entrained liquid is often broken into droplets by the turbulent vapor phase, generating the "mist" flow regime.

2.1.2 Two-Phase Flows with Microscale Hydraulic Diameters

Flow regime evolution occurs in microscale flows in a similar fashion in macroscale flows, but the forces imposed by gravity become less dominant while surface tension and viscous shear become much more influential, as can be shown though dimensionless groupings found in Appendix 9.1. The increasing role of surface tension relative to gravity is evidenced by the shrinking Bond number with decreasing hydraulic diameter. The increasing influence of surface tension over inertia is evidenced by the shrinking Weber number with decreasing hydraulic diameter, and similarly, the increasing influence of viscous shear over inertia is evidenced by the decreasing Reynold's number with decreasing hydraulic diameter [54]. The general flow phenomena occurring in microscale flows are illustrated in Figure 2.5.

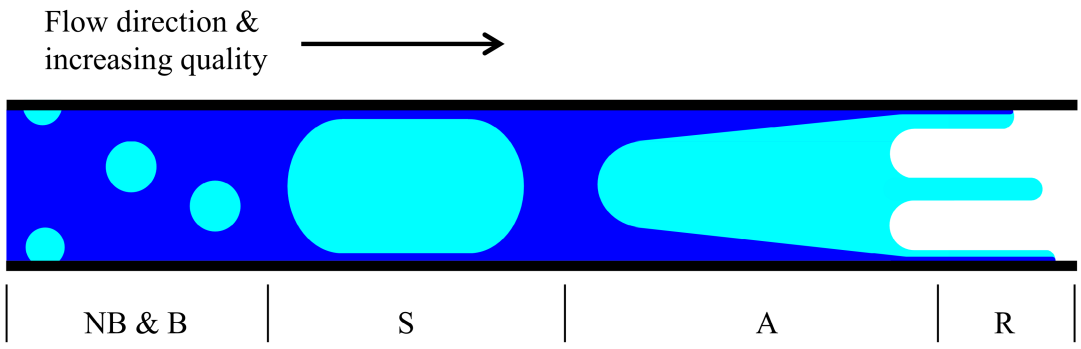

Figure 2.5: Illustration of flow regimes in microscale channels. Nucleate boiling and bubble flow (NB & B) at low quality, slug flow at intermediate quality (S), annular flow at higher quality (A), and finally, rivulet flow (R).

The increased influence of surface tension and shear causes microscale flows to become more axisymmetric; the stratified flow regime is typically not reported in microscale flows [55]. The symmetry of microscale flows is also manifested in the

more uniform film thickness around vapor slugs flowing in horizontal channels. The circumferential film thickness variation is measurable, and the uniformity has been used as an empirical criteria to predict the transition from micro to macroscale flow behavior. The Confinement number indicating the transition is shown in Equation (5), and it can be observed that this dimensionless group is simply the inverse square root of the more commonly used Bond number [44].

$$Co = \frac{1}{D_h}\sqrt{\frac{\sigma}{g(\rho_L - \rho_V)}} \tag{5}$$

In Equation (5), D_h is the hydraulic diameter, ρ is the liquid (subscript – L) and vapor (subscript – V) density, σ is surface tension, and g is the acceleration due to gravity. In the study, a Confinement number of 0.5-1 indicated that the transition from macroscale to microscale. In the current study, Co = 4.6 for FC-72 and Co = 6.2 for R245fa, both well within the region considered to be dominated by microscale phenomena. In another study, viscous shear was incorporated into the empirical criteria predicting a transition in flow behavior from microscale to macroscale with Reynolds number–Bond number product, referred to as a "convective Confinement number" [43]. This convective Confinement number incorporates effects from both viscous shear and flow velocity, and therefore, may be a more universal indicator for the flow conditions under which microscale or macroscale flow phenomena occur.

Within the annular regime, uniformity of the liquid film thickness around the perimeter of the channel is also increased in microscale flows compared to macroscale, because of the increased influence of surface tension and viscous shear. Furthermore, because of the increased influence of viscous shear, as well as the small

channel diameter, the vapor flow in the microscale annular regime is much less likely to be turbulent. Lack of turbulence combined with various wettability effects can give rise to "rivulet" flow in the high quality annular regime. This condition occurs when liquid ribbons form on the channel wall in the streamwise flow direction, driven in a meandering path by vapor shear [56].

Phenomena that can cause liquid to become entrained with the vapor can still occur in microscale two-phase flows. These phenomena include non-uniform liquid film thickness (waves, rivulets) and low liquid wettability (high contact angle) to the solid surface [56]. The absence of turbulence also decreases the breakup of liquid films into smaller droplets, and facilitates an increased probability of "filament" flow. Filament flow occurs when thread-like liquid formations flow along the center of the channel with little contact with the walls.

2.2 **Overview of Two-Phase Flow Heat Transfer**

As mentioned previously, the two-phase flow regimes are intimately connected with heat transfer from the channel wall into the fluid. This section will focus primarily on microscale two-phase flows.

Following Forster and Zuber [51], it is generally believed that **w**ith sufficient wall superheat (wall temperature rise above the local fluid saturation temperature) bubbles begin to form at nucleation sites, which are often in the form of a small crevice. As liquid is converted into vapor in the bubble, the bubble grows. This is the essence of nucleate boiling. With forced convection, the stationary bubbles on the channel wall disrupt the liquid boundary layer, and may enhance single phase convection into the liquid. With sufficient size, the drag caused by the hydrodynamic

boundary layer causes the bubbles to become entrained in the liquid flow. Increasing volume of bubbles in the flow causes the flow to accelerate, thinning and possibly further disrupting the thermal boundary layer. A large concentration of bubbles in the liquid flow causes the bubbles to agglomerate into larger bubbles, and eventually slugs.

In slug flow, the single-phase heat transfer continues to occur within the liquid plugs between slugs. The dominant mechanism of thermal transport from liquid to vapor may be in one of two forms: convective boiling or nucleate boiling. In diabatic microchannel visualization studies, both have been observed in annular liquid films [45]. Convective boiling (thin film evaporation) occurs via heat conduction from the wall through the liquid film into the convecting vapor core, in the absence of bubbles nucleating on the channel wall. Contrarily, strong evidence of nucleate boiling has also been reported in annular films [26], though the likelihood of nucleate boiling decreases as the wall superheat falls. The channel cross-sectional shape, surface roughness, and other variables often differed between contradictory studies, and may be important factors in determining the primary heat transfer modality. Regardless of the heat transfer mechanism, fluid-solid properties including wettability, surface roughness, surface tension, slug velocity, liquid viscosity (Capillary number), heat flux, and other factors, may allow the liquid film surrounding vapor slugs to locally dryout, causing locally low HTC's [57].

At a sufficiently high vapor quality, the flow transitions into annular flow, in which the thermal transport may either be dominated by convective boiling, or, perhaps, small-scale nucleate boiling. Regardless, the liquid film eventually becomes

too thin, and susceptible to local rupture and dryout [26]. Dryout and rewetting is often cyclical, and results in large temperature fluctuations (40°C) in this region [50].

In the transition from annular flow to dryout, rivulet flow can occur. In addition to the adiabatic phenomena that cause rivulet flow, the temperature dependency of surface tension (Marangoni effects) and temperature-dependent wettability effects may also play a role. In this post-dryout regime, local and intermittent dryout occur. The liquid ribbons flowing along the wall continue to evaporate, while a significant portion of the wall may be exposed to vapor, causing HTC's to decline in this flow regime.

Filament flow may also occur in diabatic microscale two-phase flows. In addition to the causes of liquid entrainment in the vapor described in the previous section, Marangoni effects and temperature-dependent wettability effects may also play a role. The filament regime is post-dryout, because the vapor is consistently in contact with the walls. Evaporation of the liquid entrained with the vapor only occurs when the vapor is sufficiently superheated. This post-annular flow produces HTC's much lower than the HTC's produced at qualities leading up to dryout. Filament flows expose large wall areas directly to the heated vapor, causing widespread—but not total dryout—and can enable dryout to occur at much lower mass fractions of vapor (quality) than 100%. At 100% quality, the flow becomes single-phase vapor, which produces relatively low HTC's, but continues to absorb heat through convective, sensible heating. The following sections discuss useful literature that quantifies the most relevant phenomena discussed up to this point.

2.3 Overview of Flow Regime Maps

Given the strong impact of phase aggregation on the thermal transport mechanism and limits, it can be expected that the heat transfer predictions should be mechanistically connected to flow regimes and that flow regime similitude would provide a strong basis for extrapolation from available data sets to new applications. The two primary mapping methods for characterizing prevailing flow regimes in two-phase systems use superficial velocities or mass flux and quality. Superficial velocity is the volume flow rate of each phase divided by the channel cross sectional area, therefore treating each phase as if it were flowing as a single phase absent of the other phase. Knowledge of the liquid and vapor density are necessary for calculating superficial velocities. Mass flux is the mass flow rate divided by the channel area. Quality is the mass fraction of vapor flowing as a fraction of the total mass flow rate, and can be determined from thermodynamics, assuming knowledge of the heat entering the flow. The relation between quality, mass flux, and superficial velocity are shown in Equations (6) – (7).

$$u_{SL} = \frac{G(1-x)}{\rho_L} \tag{6}$$

$$u_{SV} = \frac{Gx}{\rho_V} \tag{7}$$

where liquid superficial velocity is u_{SL} and gas/vapor superficial velocity is u_{SV}.

These relations can then be used to map the flow properties in the two common types of flow regime maps, as shown in Figure 2.6 and Figure 2.7. Superficial velocity plots have long been used for characterizing adiabatic flows, oftentimes for

air-water mixtures and similar classes of fluids with analytical or semi-empirical criteria [53]. The superficial velocity plot shown in Figure 2.6 shows the flow regime transitions of Ullmann and Brauner [58] limited to the velocity range of interest, and with regime boundaries modified by Rahim and Bar-Cohen [59] for a straight microgap with diabatic HFE-7100 and FC-87 flow. The flow regimes occurring in long and high aspect ratio straight channels, or microgaps, are similar to those occurring in circular channels [59, 60]. It can be seen that the flow regime transition from bubble to slug occurs at a constant void fraction (quality) based on the Ullmann and Brauner criteria [58], which is a diagonal line in Figure 2.6. The microgap slug-annular regime transition established by Rahim and Bar-Cohen [59] occurs at a constant vapor superficial velocity, which is a vertical line in Figure 2.6. A line of constant superficial vapor velocity indicates that the flow regime transition from slug to annular occurs at decreasing quality (x) with increasing mass flux (G).

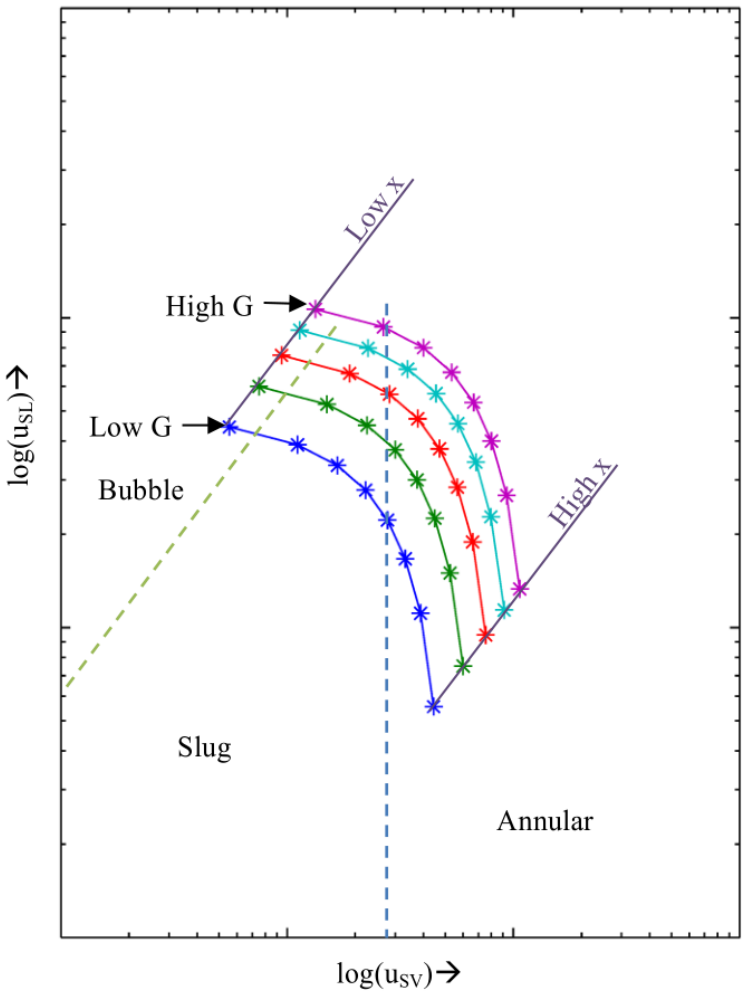

Figure 2.6: Qualitative flow regime map based on superficial velocities. Dashed lines (- -) indicate flow regime transitions and solid line with stars (-*) indicate contours of constant mass flux

The result of expressing superficial velocities in terms of mass flux and quality is shown in Figure 2.7. The highest superficial liquid velocity occurs at low quality, while the highest superficial vapor velocity occurs at high quality. Increasing mass flux increases both superficial velocities.

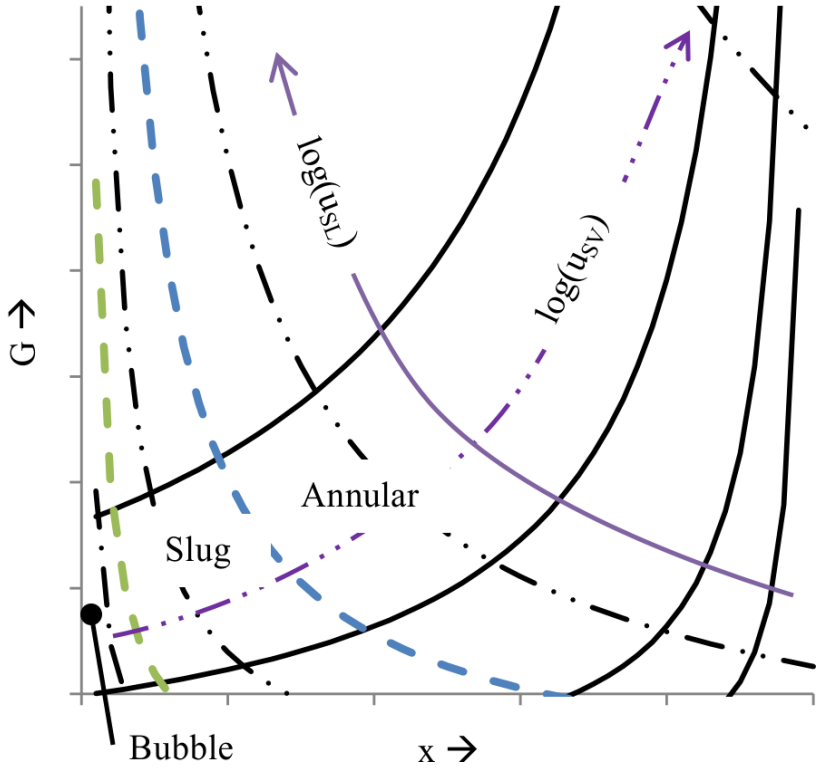

Figure 2.7: Qualitative flow regime transition map based on mass flux and quality. Dashed lines (- -) indicate flow regime transition, solid lines (-) indicate contours of constant liquid superficial velocity, and dash-double-dot-dash (-‥-) indicate contours of constant vapor superficial velocity.

Historically, flow regime transitions have been determined via a number of different methods. In general, it is preferable for flow regime transition predictions to be based on physical phenomena that can be universally calculated for any fluid, or gas-liquid mixture. Often, this is not possible due to the complexity of two-phase flows and the variety of conditions under which they occur in useful applications. If regime transitions are empirically determined, a large database with a variety of fluids and conditions is desirable. Ultimately, flow regime transitions may be affected by the fluid properties of both phases, including density and viscosity, as well as surface

tension, latent heat, heat flux, channel size, channel shape, surface roughness, and a variety of other factors.

The next three sections will review quantitative flow regime transitions that have been highly regarded in the literature, and that have been found useful for characterizing the flow regime transitions occurring in the current work. The flow regime transitions range from partially to entirely empirical. A flow regime transition boundary for bubble to slug, two flow regime transition boundaries from slug to annular, and one transition to dryout/CHF will be discussed.

2.4 Taitel and Dukler [53] Slug-Annular Flow Regime Transition

Taitel and Dukler [53] developed an adiabatic flow regime map for horizontal and near-horizontal macroscale channels. The flow regime maps have been widely adopted in part because the flow regime transitions incorporate minimal empiricisms. It was reported that a liquid hold-up—or void fraction—of ½ is a good criteria for the transition from the stratified or slug (intermittent) regime to annular flow [53, 61]. The analysis determines that this void fraction results in a Martinelli [62] parameter of 1.6 for horizontal flows [53]. From this, and assuming that the laminar exponents apply, the relationship can be simplified to Equation (8).

$$\frac{u_{SL}}{u_{SV}} = \frac{\mu_V}{\mu_L} X^2 \tag{8}$$

In Equation (8), u_S indicates superficial velocity for the liquid (subscript – L) and vapor (subscript – V), and μ is viscosity. From the superficial velocity ratio, the quality (x)—a constant, independent of mass flux for a given fluid—can be determined from Equation (9).

$$x = \frac{\rho_V}{\rho_L}\left(\frac{\mathrm{u_{SL}}}{\mathrm{u_{SV}}} + \frac{\rho_V}{\rho_L}\right)^{-1} \tag{9}$$

2.5 **Ong and Thome [44] Flow Regime Transitions**

In addition to suggesting a criteria for macroscale to microscale two-phase flows, Ong and Thome [44] also correlated the transitions from bubble to slug and slug to annular flow for flows within 1-3mm circular channels. Three working fluids were used to develop the correlation: R245fa, R236fa, and R134a. The room temperature vapor pressures of these refrigerants are 1.5, 2.7, 6.7 atm, respectively, spanning a range of vapor densities of about three times from most to least dense. The quality at which flow regime transitions occur between bubble-slug to slug ($x_{b/s}$) and slug to annular ($x_{s/a}$) predicted by the Ong and Thome model [44] are shown in Equation (10) and Equation (11), respectively.

$$x_{b/s} = 0.36\left(\frac{\mu_V}{\mu_L}\right)^{0.65}\left(\frac{\rho_V}{\rho_L}\right)^{0.9} Co^{0.2} Re_V^{0.75} BO^{0.25} We_L^{-0.91} \tag{10}$$

$$x_{s/a} = 0.047\left(\frac{\mu_V}{\mu_L}\right)^{0.7}\left(\frac{\rho_V}{\rho_L}\right)^{0.6} Co^{0.05} Re_V^{0.8} We_L^{-0.91} \tag{11}$$

The Boiling number (BO) is defined in Equation (12).

$$BO = \frac{q''}{Gh_{fg}} \tag{12}$$

In the Boiling number, the heat flux is q'', the mass flux (mass flow per channel cross-sectional area) is G, and the latent heat of vaporization is h_{fg}. Unlike the other flow regime transitions reported thus far, the BO makes this flow regime transition diabatic. The gravitational Confinement number is defined in Equation (5). The vapor Reynold's number $\mathrm{Re_V}$ is as follows:

$$Re_V = \frac{GD_h}{\mu_V} \tag{13}$$

The liquid Weber number is as follows:

$$We_L = \frac{G^2 D_h}{\sigma \rho_L} \tag{14}$$

In Equation (14), σ is the surface tension.

2.6 **Ong and Thome [50] Flow Critical Heat Flux**

Ong and Thome [50] developed a CHF correlation based on the same refrigerants used in the previous section. The CHF correlation was said to be applicable to all three refrigerants in 1-3 mm channels, as well as for square multichannels as small as 350 μm in heated equivalent diameter. The CHF can be estimated from Equation (15).

$$q''_{chf} = 0.12 G h_{fg} \left(\frac{\mu_L}{\mu_V}\right)^{0.183} \left(\frac{\rho_V}{\rho_L}\right)^{0.062} We_L^{-0.141} \left(\frac{L_{ev}}{D}\right)^{-0.7} \left(\frac{D}{D_{th}}\right)^{0.11} \tag{15}$$

The value of D_{th} is found with:

$$D_{th} = \frac{1}{Co} \sqrt{\frac{\sigma}{g(\rho_L - \rho_V)}} \tag{16}$$

In which $Co = 0.5$. The liquid Weber number is found with the length of the evaporator as the length scale:

$$We_L = \frac{G^2 L_{ev}}{\sigma \rho_L} \tag{17}$$

The total heat input into channel (Q_f) can be found by multiplying the CHF by the heated surface area. Then, subtracting the heat of subcooling (Q_{sub} – no subcooling effect was found on CHF for the current correlation), the quality at which

dryout/CHF occurs can be predicted with Equation (18). In Equation (18), $\dot{m}$ and h_{fg} are the mass flow rate in the channel and latent heat of vaporization, respectively.

$$x_{out} = \frac{Q_f - Q_{sub}}{\dot{m} h_{fg}} \tag{18}$$

The equivalent thermal diameter for square multichannels (with geometry labels shown in Figure 2.2) is:

$$D_{he} = \frac{4 w_c h_c}{h_c - 2 w_c} \tag{19}$$

It can be seen that this correlation incorporates the liquid and viscosity of both phases, as well as the length of the heated section, and the mass flux. Therefore, this correlation is more applicable to flow boiling, than pool-boiling based Zuber CHF. The experimental condition for CHF was reached when large temperature fluctuations were observed near the outlet of the evaporator, and the superheat reached 40°C. The correlation was compared with more than 650 CHF data points from varying studies, and achieved within ±30% accuracy for more than 90% of all the data. Now that useful flow regime boundaries have been identified, HTC predictions will be discussed.

2.7 **Chen [20] Heat Transfer Prediction**

The Chen [20] HTC prediction has been widely used for decades, because it is formulated with minimal empiricism, making it broadly applicable. Clarifications on the presentation of the Chen [20] prediction can be found in Chen and Fang [63]. The prediction is based on the combination of phase change HTC and the liquid convection HTC in the annular flow regime. A two-phase enhancement factor was

used to modify the Dittius-Boelter type of correlation, accounting for in increased velocity of two-phase flow and the enhanced thermal transport. The phase change HTC is based on nucleate boiling in the annular film, and modified by a bubble growth suppression factor to account for increased transport of bubbles from the channel wall in forced convection flow. The macroscale liquid convection HTC is found with Equation (20).

$$h_{mac} = 0.023 Re_L^{0.8} Pr_L^{0.4} \left(\frac{k_L}{D_h}\right) F \tag{20}$$

In which,

$$Re_L = \frac{G(1-x)D_h}{\mu_L} \tag{21}$$

and,

$$Pr_L = \frac{\mu_L c_{pL}}{k_L} \tag{22}$$

The macro enhancement factor, F, accounting for increased flow velocity if found with the following conditions:

$$F = 1 \qquad for\ X_{tt}^{-1} \leq 0.1 \tag{23}$$

and,

$$F = 2.35\left(0.213 + \frac{1}{X_{tt}}\right)^{0.736} \qquad for\ X_{tt}^{-1} > 0.1 \tag{24}$$

in which,

$$X_{tt} = \left(\frac{1-x}{x}\right)^{0.9} \left(\frac{\rho_V}{\rho_L}\right)^{0.5} \left(\frac{\mu_L}{\mu_V}\right)^{0.1} \tag{25}$$

The microscale HTC was developed by using the pool boiling relation of Forster and Zuber [51], and modifying it for forced convection boiling, as shown in Equation (26).

$$h_{mic} = 0.00122\left(\frac{k_L^{0.79} c_{pL}^{0.45} \rho_L^{0.49}}{\sigma^{0.5} \mu_L^{0.29} h_{fg}^{0.24} \rho_V^{0.24}}\right)(T_w - T_{sat})^{0.24}(P_{sat}(T_w) - P_{sat})^{0.75} S \quad (26)$$

The original suppression factor was shown graphically, based on empirical data. Later, Collier [64] introduced an analytical curve fit in the following form:

$$S = \frac{1}{1 + 2.53 \times 10^{-6} Re_{tp}^{1.17}} \quad (27)$$

In which the two-phase Reynolds number is:

$$Re_{tp} = Re_L F^{1.25} \quad (28)$$

The two-phase HTC is then found by combining the micro and macroscale HTC's:

$$h_{tp} = h_{mac} + h_{mic} \quad (29)$$

The following section will review the Chen [20] HTC relation, which was originally developed with 600 data points, producing average deviation of ±12%. The Chen HTC relation has been widely cited as a useful, and relatively universal HTC prediction, in the last five decades. The predictive accuracy of the Chen relation is also shown by recent studies with microgap channels, showing agreement with experimental results within 30% in the annular flow regime [59]. In this work, the Chen relation will be applied to manifolded microgap channels for comparison. The mass flux used for manifolded microgap channels is the average of the inlet, channel center, and outlet cross-sectional areas.

2.8 **Microgap Channels**

The previous discussion was based on lessons learned primarily from circular cross-section channels. It has been shown, though, that the flow regimes occurring in

high aspect ratio rectangular channels, or microgaps, tend to be qualitatively comparable to those occurring in circular channels [59, 60]. The difference in cross-sectional shape may result in shifts in flow regime transitions [65].

Yang and Fujita [66] produced an early study on microgap channels, with R-113 as the working fluid. The microgap gap heights ranged from 0.2 mm to 2 mm, with the gap width and length being 20 mm and 100 mm, respectively, for all tests. Heat transfer coefficients were reported for mass fluxes of 100 and 200 kg/m^{2}s. The study exhibited M-shaped HTC profiles with quality—with peaks occurring at low qualities of about 0% and high qualities of 60-80%.

Recent studies have found that large surface temperature fluctuations occur in microgap channels at higher qualities, at which annular flow begins to break down. Bar-Cohen, Sheehan, and Rahim [67] showed that, with a microgap channel possessing a 210 μm gap height, 10 mm width, 30 mm length, the highest HTC's and tend to occur at the inlet of the gap, and tend to monotonically decline along the length of the channel. With FC-72 as the working fluid, HTC's as high as 25,000 W/m^{2}k occurred at the inlet of the channel, with the best agreement with the Chen [20] prediction nearer to the outlet with HTC's of approximately 10,000 W/m^{2}k. Annular flow was found to be the dominant flow regime occurring throughout the quality range. Furthermore, it was observed that the largest temperature fluctuations occur as quality increases along the length of the channel, local dry patches develop, and the flow departs from the favorable, annular thin film evaporation.

Kabov et al. [68] identified adiabatic sub-regimes within shear-driven thin film flows for FC-72, including cells, structures, 2D waves, 3D waves, and film rupture. It

was found that water may exhibit smooth film flows for certain liquid flow and gas flow shear rates, while intensively evaporating FC-72 did not. Furthermore, CHF maps were developed for the shear-driven liquid film flows and it was found that the CHF could be up to 10 times higher than for gravity-driven film flows.

Bar-Cohen et al. [69] reported on the hydrodynamic waves that occur in high quality FC-72 flows in a microgap comparable to that of Bar-Cohen, Sheehan, and Rahim [67]. Good agreement was found between a linear stability analysis and the most probable experimental wavelengths. This model may be useful for better understanding and characterizing temperature fluctuations that occur in high quality annular flows.

2.9 **Effects of Flow Path Curvature on Two-Phase Flow Characteristics**

Previous research on the effects of centripetal acceleration on two-phase flows, discussed in the following sections, deals with macroscale flows. Other than two exceptions focusing on critical heat flux (CHF), the centripetal accelerations are orders of magnitude less than those occurring in the previously studied manifolded microchannel coolers by Bae et al. [36] and Mandel [37], and decrease with increasing hydraulic diameter. The flow phenomena, though, are expected to be qualitatively similar across the range of hydraulic diameters, with the exception of turbulence effects. The range of hydraulic diameter and centripetal acceleration occurring at the channel inlet of several studies are summarized in Figure 2.8.

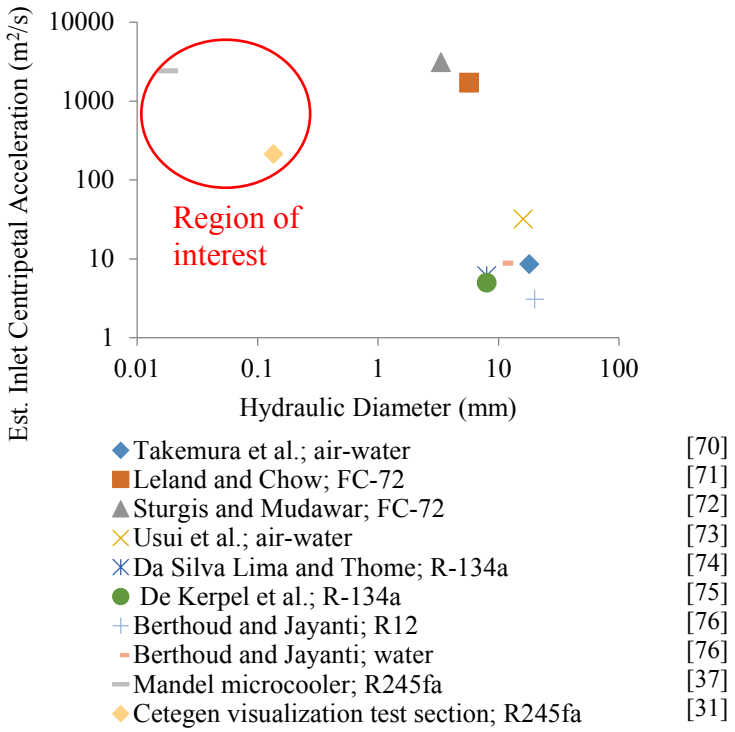

Figure 2.8: Estimated inlet centripetal acceleration in two-phase channels of various diameters

The vast majority of experimental studies on two-phase flow regimes have been with straight channels, with relatively few studies including the additional complexity of an induced centripetal acceleration field due to a curved flow path [74]. Curved channels have been shown to cause significant changes in flow morphology within the bend and therefore affect heat transfer performance. Most studies of two-phase flow in a curved tube have been with adiabatic macroscale channels of circular cross-section with fully developed flow entering the bend, making the following studies significantly different from those with a U-shaped microgap. Nevertheless, many of the same fluid physics principles do apply to the geometry of interest. For clarity, the terminology used in the proceeding sections is illustrated in Figure 2.9.

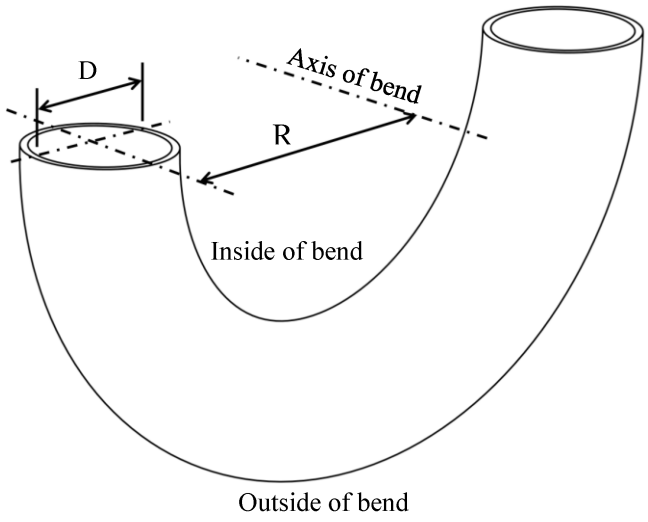

Figure 2.9: Illustration of terminology used to describe areas of the tube bend: diameter (D) and curvature radius (R)

2.9.1 Single-Phase Flow in Curved Tubes

It is well known that a force is required to cause an object to travel on a curved path—or to have a centripetal acceleration. The centripetal acceleration is proportional to the velocity squared, divided by the flow path radius of curvature. Since the cross-sectional velocity profile within laminar pipe flow is parabolic, the centripetal acceleration is greatest in the highest velocity fluid located in the center of the pipe. Fluids do not support shear, so the fluid in the center of the pipe tends to flow toward the outside of the bend, thus developing secondary flows in the pipe cross section, in addition to the primary (streamwise) flow along the length of the pipe, as first described by Dean [77]. The secondary flows are counter-rotating vortices in the channel cross section that also have a forward velocity; the two components of the flow combine to form counter-rotating helical flow paths. An illustration of this effect in the cross section of a curved channel is shown in Figure

2.10. The secondary flow in the channel cross section has the effect of shifting the peak velocity toward the outside of the channel (no longer generating a parabolic velocity profile), thus resulting in a steeper velocity gradient at the outer wall of the channel.

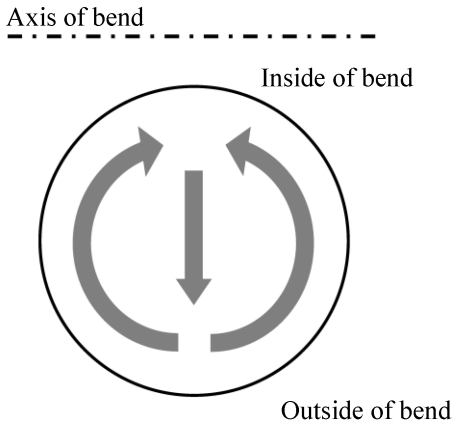

Figure 2.10: Illustration of secondary flows developed in cross section of curved channels

2.9.2 Bubbly Flow in a U-Bend

Bubbly flow regimes consist of a continuous liquid phase with smaller bubbles flowing within. This regime may be generated by gas-liquid flows, adiabatic liquid-vapor flows, or heated liquid-vapor flows. In addition to the secondary flows in the liquid phase, there also exists a buoyancy effect due to the centripetal acceleration induced by the U-bend. Since the velocity of small bubbles and the liquid flow are comparable, the centripetal acceleration on each phase is also comparable. Buoyancy for a given bubble is proportional to the acceleration field experienced by each of the fluids, so as centripetal acceleration increases, the buoyant force on the bubble

increases. Therefore, bubble transport toward the center of the bend also increases. In the case of boiling flow, the circumferential secondary flow (flowing toward axis of bend) of the liquid may also tend to drive bubbles from the outer wall toward the inner wall where they are more likely to coalesce into larger bubbles.

Takemura et al. [70] performed a study in the interest of characterizing the conditions in which bubbles contact the interior or exterior wall with varying flow rates in an inverted, or concave (∩), and "normal," or convex (∪), U-bend. The working fluid was an air-water mixture that flowed through an 18 mm inside diameter (ID) U-bend with 116 mm and 435 mm radii of curvature. It was found that with moderate superficial velocities (on the order of 0.1 to 1 m/s), the large radius of curvature could induce centripetal accelerations comparable to gravity. In the convex U-bend, it was found that since gravitational buoyancy and centripetal buoyancy work in the same direction, the bubbles always migrated toward the interior wall of the bend. In the concave U-bend configuration, it was found that the bubbles may either flow along the interior or exterior of the bend, depending on the flow rate and associated dominant force—centripetal buoyancy or gravitational buoyancy. Similar observations were made by Usui et al. [73].

2.9.3 Wavy Stratified Flow in a U-Bend

Stratified flow occurs when a continuous layer of liquid flows beneath a continuous layer of gas or vapor, and therefore only exists in large horizontal (or near horizontal) tubes where gravity dominates over surface tension and shear forces. Because the flow is composed of a significant volume of each phase, each phase has a large effect on flow morphology. Stratified flow occurs in the inlet and outlet tubes of

the U-bend with the axis of the bend oriented horizontally or vertically and the inlet and outlet tubes oriented horizontally. The stratified regime can also occur with the fluids flowing upward or downward though the bend (when the bend axis is horizontal), as shown with an air-water system by Usui et al. [78] and Usui et al. [79].

Da Silva Lima and Thome [74] studied adiabatic refrigerant flow in both orientations (bend axis horizontal and vertical) with both flow directions (flow upward and downward with horizontal bend axis). The refrigerant used was R-134a at 5°C with tube ID's of 13, 11 and 8 mm and bend diameters of 67, 38, 55, 32, 25 mm. In the stratified regime, the flow phenomena for all orientations were qualitatively similar. Due to the helical action imposed by turning the stratified flow, the wetted perimeter in the U-bend increased with stratified flow at the inlet. As long as stratified flow entered the bend, the phenomena intensified with increasing quality (up to about x = 0.36) and increasing mass flux (up to G = 500 kg/m^{2}s). Stratified flow redeveloped downstream of the bend at a distance sensitive to test conditions, but on the order of 2-5 tube diameters.

2.9.4 Slug Flow in a U-Bend

Da Silva Lima and Thome [74] also observed that at relatively low mass flux and low quality, when a high-amplitude wave of liquid (or plug) entered the bend, the entire perimeter of the channel could be wetted, thus generating localized, temporal annular flow. After exiting the bend, the slug would redevelop downstream, again at a distance sensitive to flow test conditions. Using quantitative image analysis, De Kerpel et al. [75] also showed that with R-134a and a similar geometry, slug flow was

the regime most morphologically disrupted by the U-bend immediately downstream of the bend, which agrees with the observations of Da Silva Lima and Thome [74].

2.9.5 Annular Flow in Curved Channels

Sufficiently high flow of the gas or vapor phase causes the liquid to annularly line the entire perimeter of the channel while the gas or vapor core flows through the center. In curved tubes, secondary flows develop in the vapor core in the same way secondary flows develop in single-phase liquid. The vapor circulating in the spanwise direction couples with the liquid and drives the liquid film toward the interior wall of the bend, thus thickening the liquid film on the inner wall [80]. At lower qualities, the liquid inertia exceeds the vapor inertia, causing film thickening on the outer wall of the bend, thus counteracting the film thinning on the outer wall caused by secondary flows.

Another mechanism that tends to thicken the film in the outer wall is liquid drops detaching from interfacial waves on the interior wall, then traveling in the direction of the shearing streamwise vapor flow and causing secondary flows to deposit on the outer wall of the bend. Da Silva Lima and Thome [74] observed a thicker liquid film on the outer wall of the bend for most of the annular flow regime with R-134a at 5°C due to the interplay of these phenomena. Sharper bends and higher mass fluxes (the same parameters reported in the previous section “Wavy Stratified Flow in a U-Bend”) were observed to intensify the phenomena [74] in these macroscale U-bends, which is an important consideration for microscale U-shaped channels that have considerably smaller bend radii of curvature.

2.9.6 Film Inversion Flow in Curved Channels

At high qualities, the vapor inertia exceeds the liquid inertia because the vapor flows relatively freely through the "core" of the channel formed by the liquid annulus while the liquid is subjected to a "no-slip" boundary condition at the channel wall. Thus, the role of centripetal buoyancy is reversed—the liquid phase is now pushed toward the center of the bend by vapor inertia. The effect of the secondary flows remains the same and so the forces become complementary, causing a thicker film to exist on the interior of the bend [81]. Although drops may still be transported to the exterior of the bend, thickening the film on the exterior wall, the film tends to be thicker at the interior of the bend at dryout inception qualities due to vapor inertia and secondary flows [74].

2.9.7 Dryout in Helical Coils

Berthoud and Jayanti [76] evaluated experimental data from previous researchers studying dryout in helical coils with macroscale tube diameters ranging from 11 mm to 20 mm and coil diameters one to two orders of magnitude larger than the tube diameter. The working fluids for all studies were either R-12 or water and the experiments were necessarily diabatic in order to study dryout. At dryout inception qualities, the flow was annular, and it was found that dryout occurs over a significant streamwise distance. Therefore, the conditions in which dryout begins to occur is referred to as the first dryout quality and the conditions in which the quality reaches unity is referred to as total dryout; others have referred to these effects as "local" or initial and "global" dryout.

The mechanisms influencing film thickness in this study are in agreement with other studies reported in the literature, including quality, secondary flows, and redeposition of liquid drops. Chong et al. [82] also found that drop deposition is a critical consideration in 15 cm diameter tubing for serpentine channels (alternating U-bends) in fired reboilers.

Berthoud and Jayanti [76] classified dryout in helical coils into a map consisting of the gravity-affected zone, the zone of entrainment, and the zone of redeposition. The gravity-affected zone corresponded to significant gravitational effects and a low mass flux and thus has the lowest dryout quality in part because the liquid film thickness is concentrated on the bottom of the channel (due to gravity), allowing the film at the top of the channel to deplete at a lower quality. The zone of entrainment generally has a higher mass flux and may facilitate more entrainment of liquid drops with less redeposition, and thus has an intermediate first dryout quality. The zone of redeposition is characterized by a smaller bend radius that generates a stronger driving force for redeposition, and the highest first dryout quality. Because gravity has less effect on microscale flows, the intermediate dryout qualities occurring in the entrainment and redeposition zones may be more prevalent. Increased mass flux and smaller bend radii were also reported to increase drop entrainment and redeposition by Da Silva Lima and Thome [74].

2.9.8 Pressure Drop

De Kerpel et al. [75] discussed in detail the pressure drop correlations available for two-phase flows in a U-bend for the entire quality range. . Little agreement has

been found among the available correlations for two-phase flow pressure drop in a U-bend, with predictions varying by up to a factor of four for identical conditions. A trend agreed upon by all correlations is that pressure drop generally increases with quality. It is reported, though, by De Kerpel et al. [75], that pressure drop should decrease monotonically from a peak value, which occurs just prior to dryout inception. The physical expectation for this trend was reported to be that the friction factor between the two phases decreases when as local dryout occurs, exposing the channel wall to the vapor flow. The most recent pressure drop correlations reported by De Kerpel et al. [75] for pressure drop in a two-phase U-bend show a peak pressure drop at a quality less than unity. Pressure drop is also increased in the straight channel more than 100 diameters downstream of the U-bend due to the flow perturbation imposed by the U-bend. All these factors indicate that further research is needed to understand and characterize the complex flow phenomena occurring in two-phase U-bends.

2.9.9 Introduction to Critical Heat Flux

The critical heat flux (CHF) occurs when vapor is generated at a rate rapid enough to inhibit liquid wetting of the heated surface, causing a rapid reduction in cooling and a sharp climb in wall temperature. In the absence of forced convection, when operating in pool boiling, it is generally agreed that CHF can be predicted with Equation (30) [83].

$$q''_m = Ch_{fg}\rho_V\left[\frac{\sigma g(\rho_L - \rho_V)}{\rho_V^2}\right]^{1/4} \tag{30}$$

When the value of the leading constant, C, in Equation (30) is 0.13, the relation is referred to by the author's name, Zuber [84], and has been shown to predict CHF for pool boiling on horizontal surfaces heating the fluid from below [83]. These upward-facing horizontal surfaces will be referred to as 0° oriented. Other C values may predict CHF more accurately for certain datasets [85] of 0° surfaces. Regardless, it can be seen that there is a ¼ power dependence of CHF on gravitational acceleration for 0° surfaces; an increased vapor bubble buoyancy due to gravity increases CHF for 0° surfaces.

Vertical (90° oriented) heated surfaces tend to exhibit a slightly lower CHF, ranging from about 70% to 100% that of 0° surfaces [86]. Howard and Mudawar [86] developed a model to predict CHF for vertical and near vertical heated surfaces. It was shown that with certain simplifications, such as neglecting shear stress or neglecting the momentum gradient, the model took on a form identical to Equation (30) for 90° surfaces, but with a different C value. Regardless of the leading coefficient, it can be seen that CHF also has a ¼ power dependence on gravity for 90° surfaces.

As the angle of the heated surface increases past 90°, the fluid becomes heated from above and the CHF decreases precipitously with increasing angle [86]. With a heated surface orientation of 180°, the CHF approaches 0 W/cm^2 because buoyancy no longer transports vapor away from the heated surface.

The Zuber [84] pool boiling correlation may predict CHF in forced convection boiling when the fluid flow velocities are sufficiently low in straight channels with 0° to 90° orientations [87]. As the flow velocity increases, though, the interplay of fluid

inertia and vapor buoyancy becomes more complex, and the CHF for all wall orientations changes. The CHF for the higher flow velocity with 0° to 90° (vertical upward flow) were increased by 0% to 30% due to forced flow, while the 180° orientation CHF increased from the pool boiling value of ~0 W/cm^2 to 70% that of the 0° pool boiling surface. The minimum CHF occurred in vertical downward flow, or an orientation of 270°, to less than 50% that of the 0° orientation. The decrease in CHF with vertical downward flow is due to the competing effects of buoyancy, which drives the bubbles upward, and drag (inertia) from the liquid, which drives the bubbles downward; thus the net transport of bubbles away from the heated surface is decreased.

The CHF occurring in U-bends encompasses all the effects described here, with centripetal acceleration having a similar effect as gravity, but a prerequisite for significant centripetal acceleration is a relatively high flow rate. Therefore, inertial effects will also have a significant effect on the transport of the vapor phase in two-phase U-bends, which will be discussed in the next section.

2.9.10 Critical Heat Flux in Rectangular Channels with U-Shaped Heated Outer Wall

Low quality CHF occurs in a bubbly regime and it has been shown that centripetal acceleration buoyancy can readily increase the CHF of concave heaters (outer wall of bend is heated) by 1.5 to 2 times that of a comparable straight channel [88]. The outer wall of the bend is in reference to the axis of the bend, as illustrated previously in Figure 2.9. The increased CHF is primarily attributed to the increased transport of bubbles away from the heated outer wall, and thus greater resistance to

the decreased heat flux associated with a continuous vapor blanket preventing liquid from wetting the wall.

Leland and Chow [71] studied the effect of concave heating on CHF for electronics cooling applications. The rectangular channel cross-sections consisted of heights (height direction is along the radius of the bend) of 3.18, 5.56, and 6.35 mm; channel widths of 27.0 mm; and radii of curvature of 28.6 and 56.4 mm. This channel geometry can be considered low aspect ratio because the channel is wider than it is tall with respect to the centripetal acceleration direction. The flow consisted of subcoolings of 5, 20, and 35°C, and velocities ranged between 1 and 7 m/s with FC-72 as the working fluid. Under these conditions, the flow was in the turbulent regime. Turbulent flow does not follow streamlines like laminar flow, secondary counter-rotating helical vortices in the bulk flow may develop with some similarity to that of laminar flows [71]. It was found that beneficial effects of channel curvature on increasing CHF were most pronounced at the smallest subcooling where vapor generation and the associated buoyant forces were greatest.

Sturgis and Mudawar [72] further characterized CHF in rectangular channels subject to concave heating. A channel 2.5 mm wide and 5 mm tall (aspect ratio of 2) was studied with a bend radius of curvature of 32 mm. Inlet velocities of the degassed FC-72 ranged from 0.5 to 10 m/s for a peak centripetal acceleration of 315 times the earth's gravitational acceleration. At the maximum inlet velocity of 10 m/s and subcooling of 3°C, the CHF of the straight channel was about 58 W/cm^2, while the comparable curved channel CHF exceeded 100 W/cm^2. If one substitutes the associated centripetal acceleration (315g) for gravity in the pool boiling correlation,

Equation (30) which has a ¼ power dependence on g, a CHF increase of about four times would be expected instead of the observed value of two. A first order estimate is established with the pool boiling correlation, though, and more sophisticated modeling can be used to account for other influential factors, such as secondary flows, inertial drag on bubbles, and liquid-vapor interface stability. Inward centripetal transport of bubbles was observed in the boiling flow, which again is a major driver of the enhanced CHF. The majority of the study was devoted to determining criteria for which the liquid-vapor interface (vapor separating heated surface from liquid) is neutrally stable, thus indicating the onset of CHF.

2.10 Summary of Two-Phase Flow Research Motivation

A single channel within a manifold-microchannel cooler is a unique geometry that differs from the more traditionally studied two-phase flow geometries. Key differences include microscale hydraulic diameter, high aspect ratio cross section, short length compared to hydraulic diameter ($L/D_h < 100$), and U-shaped flow path through the channel. Each of these differences—and their combined effects—have ramifications on flow phenomena and heat transfer that are not well-documented in the literature. This study seeks to research and characterize these effects in the pursuit of greater understanding of the parametric effects, greater predictability, and further performance enhancement in high-heat flux, embedded electronics coolers.

Chapter 3: Experimental Methods

The experimental methods used to study the thermo-fluid performance of the U-shaped manifolded microgap will be described in the following sections. First, the test section design will be shown, followed by the test loop design. Next, the data reduction methods and determination of fluid properties will be explained. Finally, the uncertainties associated with the measurements will be reviewed.

3.1 **Test Section**

An "exploded" assembly view of the test section is shown in Figure 3.1. This is an improved test section from that used in the visualization study of Cetegen [31]. A copper heat conductor was soldered into the test section base and a resistance heater was brazed to the heat conductor. The thickness of the brass test section base was reduced to 1 mm for a distance of 5 to 10 mm away from the heat conductor, to reduce heat loss by conduction away from the microgap, as was shown in the detail drawings in Cetegen [31]. An O-ring formed the seal between the test section base and the sapphire viewing lid. Polytetrafluoroethylene (PTFE) shims were used to both set the gap size and establish the flow path for the fluid (manifolding) to the gap. The PTFE shims were fabricated with micromachining. The top and bottom compression flanges were bolted together to seal the assembly, and were insulated from the test section base by polymer gaskets to reduce heat conduction losses from the test section to the surroundings.

Thermocouple probes measured the fluid temperature at the junction between the test section base and the outlet tubing. The inlet temperature was measured

upstream of the polymer insulation tubing, directly at the outlet of the preheater. The PTFE insulation tubing ensured that significant amounts of heat were not conducted from the preheater to the test section or vice versa.

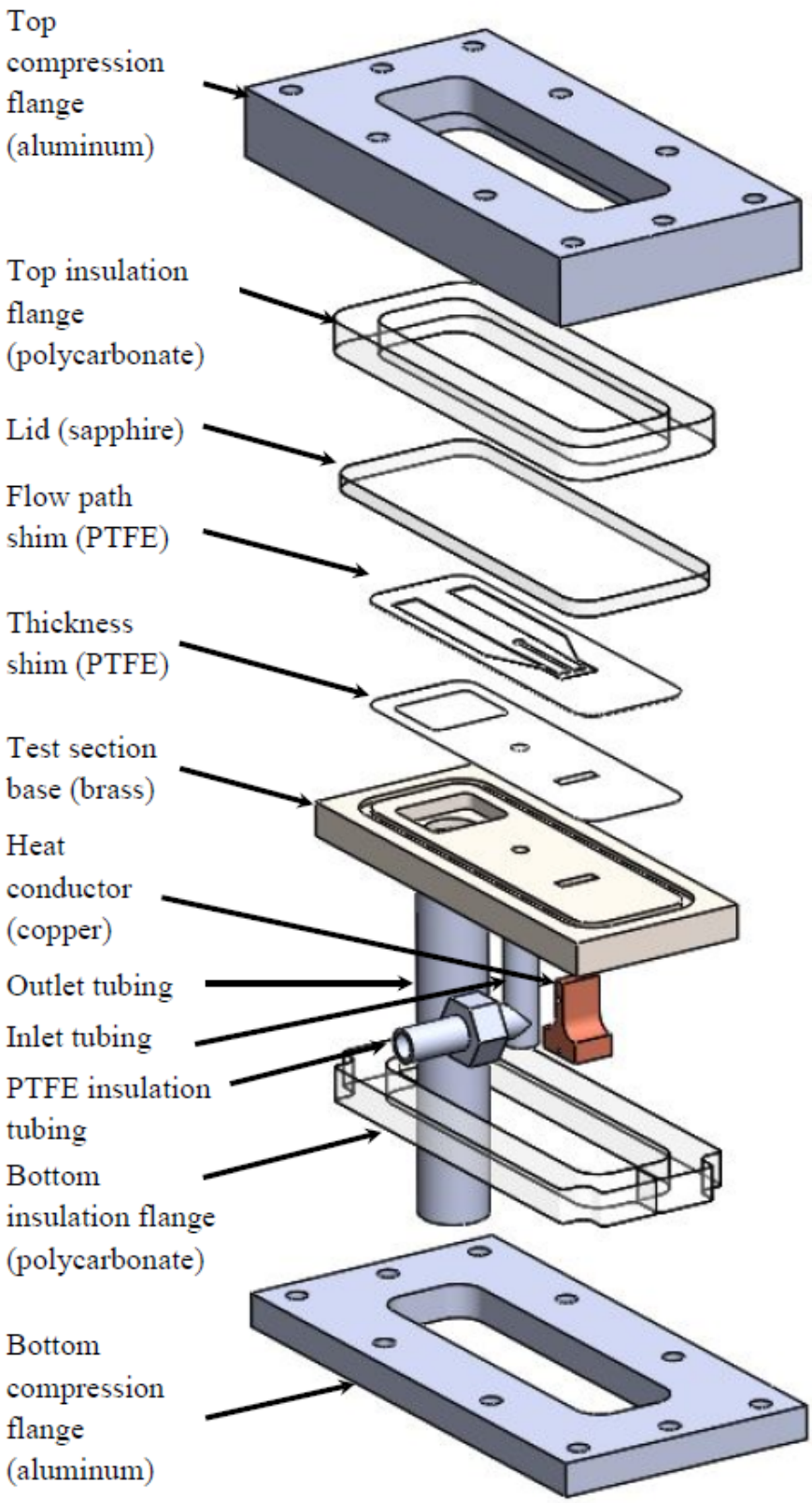

Figure 3.1: Test section assembly exploded view

The gap size was determined by precision grinding of the installed copper heat conductor and precision thickness PTFE shims. The copper heat conductor conducted heat from the 1 cm^2 heater to the inside of the test section. The rectangular end of the heat conductor (the right side of Figure 3.2), was the heated surface in the test section. Thermocouple probes measured the heater temperature and the local temperature near the center of the channel, as shown in Figure 3.2. The subsurface thermocouple probe shown on the right of Figure 3.2, measured the temperature of the copper block directly beneath the high emissivity coating. This thermocouple location will be referred to as T_{s1}. The temperature of the copper block is limited to 100°C due to the brazing and epoxy sealing.

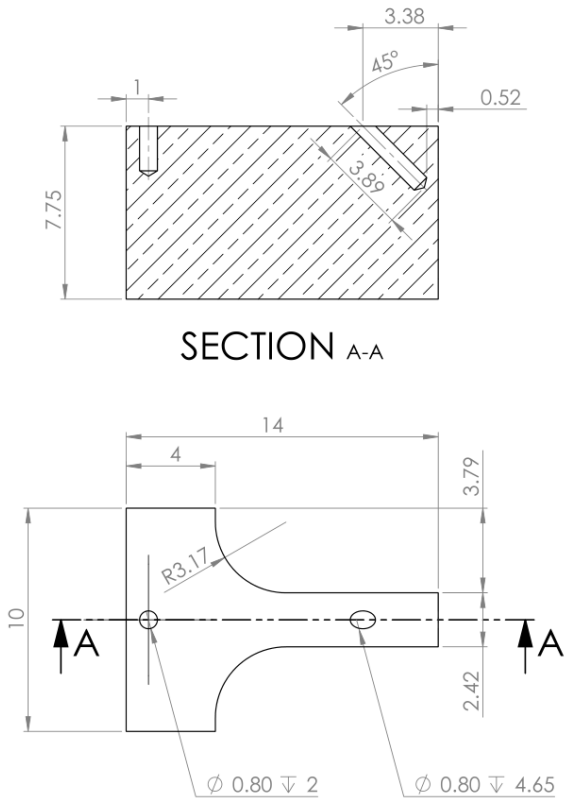

Figure 3.2: Cross-section view of copper heat conductor showing thermocouple locations

3.1.1 High Emissivity Coating

The assembled test section base and copper block were coated in Aeroglaze® Z306, a polyurethane-based, high emissivity material. The high emissivity generated a more intense infrared signal to be detected by the infrared camera. The applied coating was 25 μm thick ±4 μm, as confirmed via measurement. The RMS roughness of the surface was 5 μm. The coating thermal conductivity is 0.35 W/m-K, creating a known thermal resistance that can be used to determine both the superheat applied to the cooling fluid at the channel wall, as well as the heat flux into the fluid. The thermal diffusivity is estimated to be 0.2 mm^2/s. The coating was applied to both the heated surface of the copper block and to the test section base in order to maintain gap height when assembled, as shown in Figure 3.3.

Figure 3.3: Digital image of the high emissivity coating. The heat conductor is on the left.

3.1.2 Manifold Designs

One of the primary goals of this experimental campaign was to investigate the effect of manifold design on the flow phenomena and the associated heat transfer distributions occurring with varying manifold design. For all three manifold designs, the gap size was designed to be 80 μm, which was also verified with optical measurements after assembly.

The design of the test section allows for simple modification of the manifold geometry by changing the micro-machined shape of the PTFE flow divider shim, or manifold. The manifold design determines the flow path followed by the fluid, establishing the L/D_h ratio, the associated centripetal acceleration, and inlet jet velocity. By studying the flow behavior at the minimum, intermediate, and maximum practical manifold lengths, the effect of channel length and inlet size on heat transfer can be determined.

The first manifold design (Design 1) utilizes one inlet and two outlets, as shown in Figure 3.4. This manifold design produces an average flow path radius of curvature of 1.6 mm. The average radius of curvature is determined by averaging the local radius of curvature function for an elliptical flow path intersecting the center of the inlet, center of the outlet, and center of channel wall. This assumption of elliptical flow path has been previously shown to be a reasonable empirical approximation [54]. The inlet and outlet dimensions as tested are 1 mm and 1.1 mm, respectively.

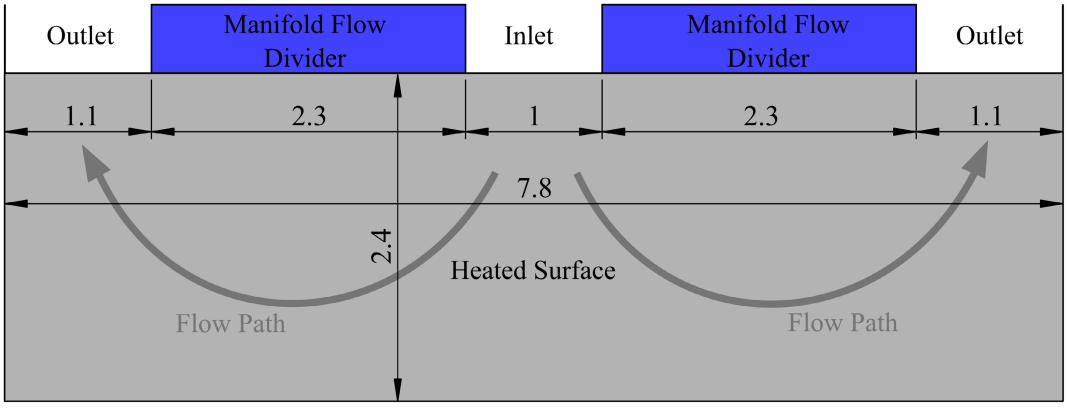

Figure 3.4: Manifolded-microgap with intermediate manifold length (Design 1). Dimensions in mm.

Design 2 increases the manifold length to the practical maximum for the test section heated surface, which represents a unit cell of a manifold-microchannel heat

exchanger. Design 2 has a single inlet and single outlet, as shown in Figure 3.5. The manifold length is 4.7 mm. A longer manifold imposes a larger radius of curvature on the average flow path, decreasing the average centripetal acceleration by a factor of three from the Design 1 to Design 2. The inlet dimension as tested is comparable to the Design 1 inlet dimension (within 10%), and the outlet size is comparable to that of the combined outlets of Design 1. Therefore, the inlet and outlet mass fluxes for the two designs is comparable for the same mass flow rates, but the mass flux at the channel center with Design 2 is double that of Design 1.

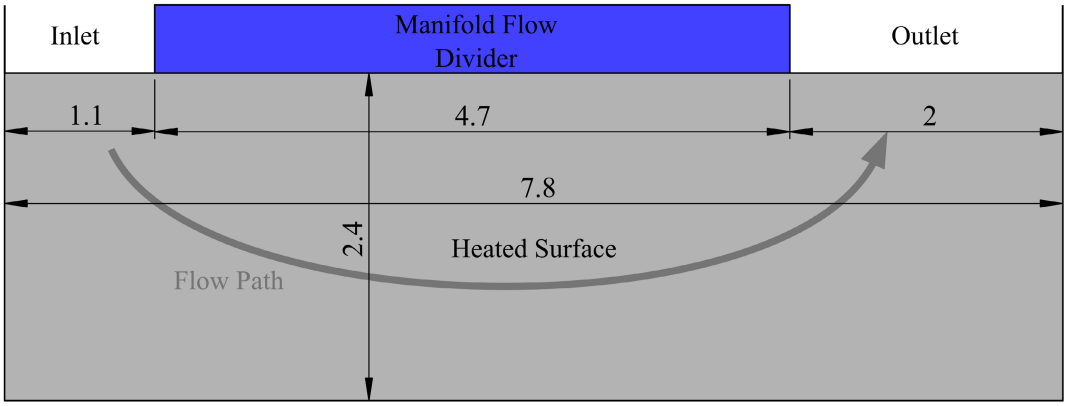

Figure 3.5: Manifolded-microgap with long manifold length (Design 2). Dimensions in mm.

The longer channel was expected to result in increased pressure drop, so shorter channels are expected to be preferred for functional microcoolers, within manufacturing limitations. The short channel length design (Design 3), possessing a single inlet and two outlets, is illustrated in Figure 3.6. The inlet and outlet sizes are all 2.4 mm, producing inlet and outlet mass fluxes less than half that of Design 1 and Design 2. The mass flux at the center of the channel is the same as that of Design 1.

The same mass flow rate was used for all designs for equivalent thermodynamic cooling capability for a given wall area.

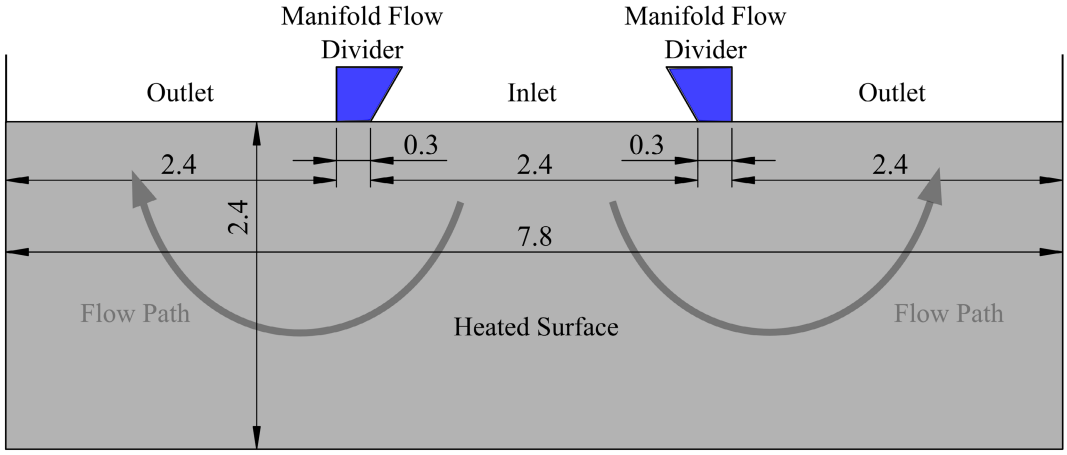

Figure 3.6: Manifolded-microgap with minimum practical manifold length (Design 3). Dimensions in mm.

Figure 3.7 illustrates the flow path generated by Design 1. It can be seen that the heated surface generates a step in the flow path. This step generates a flow restriction at the inlet, and therefore, a pressure drop that also decreases the local saturation temperature. The flow restriction also causes the flow to re-develop within the U-shaped microgap channel. Both of these effects produced in the test section are intended to mimic the same effects in operational manifolded microchannel coolers. The flat sapphire cap forms the nearest wall of the channel, allowing for visual and infrared imaging.

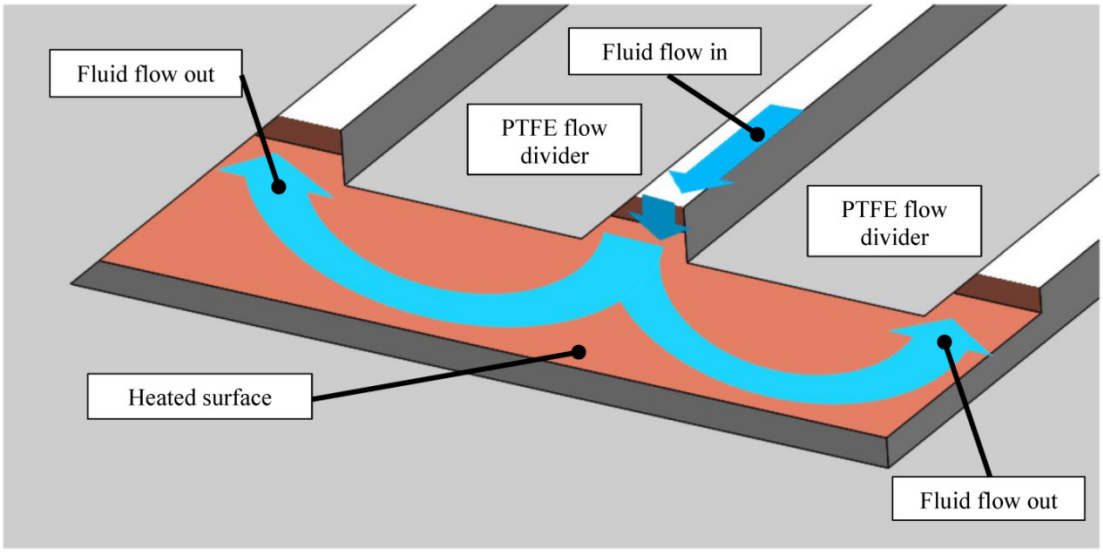

Figure 3.7: Illustration of visualization test section used to study two-phase flow regimes in a U-shaped manifolded microgap (gap size enlarged for illustration).

3.2 Test Loop and Metrology

A two-phase test loop was designed and constructed for these experiments, as shown in Figure 3.8. For the test section, Type-T thermocouples (two each) were used for the inlet and outlet temperatures, and are shown as T_i and T_o. The subsurface thermocouple probe (type-T) is shown as T_{s1}, and the heater voltage is V_h. The resistance of the test section resistor was tested and confirmed to be temperature independent. The test section heater supply voltage was recorded to determine the total heat produced by the heater. An Omega DP7002 on/off switch was used to cut power to the heater and prevent temperature excursions of the copper block past the set point temperature in the event of a loss of cooling.

The inlet pressure (P_i) was measured with a Setra 205 0-250 psia pressure transducer. The differential pressure (pressure drop) across the test section was measured with a Setra 230 0-50 psid transducer. The flow in the test section gap was

simultaneously imaged with a high speed camera (HSC) and an infrared camera (IRC).

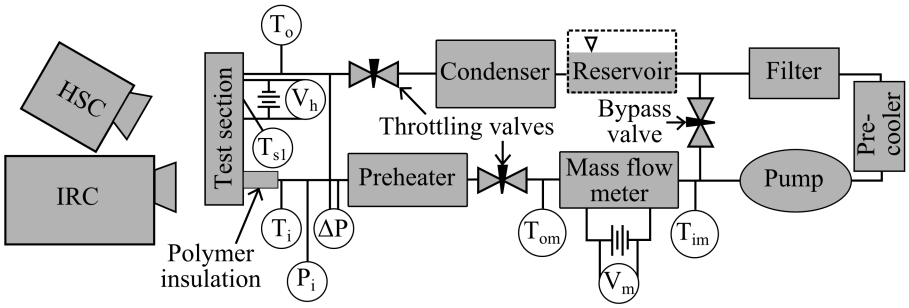

Figure 3.8: Test loop design and metrology. An atmospheric pressure reservoir was present for FC-72 tests. HSC – high speed camera, IRC – infrared camera.

The chiller temperature was used to set the system pressure with a type-T thermocouple probe when R245fa was the working fluid. When FC-72 was the working fluid, the test section outlet pressure was atmospheric pressure, set by an atmospheric pressure reservoir. The reservoir was kept near the saturation temperature to reduce gas solubility. The ambient temperature was also recorded with a type-T thermocouple for all tests. A preheater controlled the subcooling of fluid into the test section, while the inlet and outlet pressures were adjusted by throttling valves on the upstream and downstream sides of the test section. The throttling valves also provided sufficient pressure drop to stabilize system-wide flow oscillations, as also confirmed in the Appendix 9.3.1.

Mass flow rate to the test section is measured with a specific-heat based flow meter. A vacuum-insulated resistance heater heated the fluid in a stainless steel tube while temperature was measured before and after heating. The mass flow meter resistor was also verified to have a resistance that is independent of temperature. Care was taken to ensure the wall temperature of the mass flow heater did not exceed the

local saturation temperature, to prevent boiling. The thermocouple probes T_{im} and T_{om} consisted of three type-J thermocouples each, taken from the same thermocouple wire for maximum consistency. The voltage across the mass flow meter resistor was measured to determine heat input, and therefore determine the mass flow rate based on the local specific heat and temperature difference. The accuracy of the mass flow meter was confirmed by comparison with a Kobold DPM 1557N2L343 flow meter at a mass flow rate of about 5 times that of the mass flow rate needed during experiments.

A Micropump EG152-0036/REV pump was used to drive the flow. A pre-cooler was inserted before the pump to eliminate cavitation. The throttling valve in the bypass loop was partially opened in order to precisely control the flow rate to the test section.

The test section heater was powered by a Sorensen DLM 150-4 power supply and the mass flow heater powered by a Sorensen 35-10 power supply. Voltage dividers were implemented to reduce the power supply voltage signal to that of the allowable range of the data acquisition system. Data was acquired from all channels with a National Instruments NI cDAQ-9178 interfacing with LabVIEW for real time data monitoring. A Phantom Miro 4 high-speed camera sampling at 2000 frames per second (fps) with a Nikon macro zoom lens was used to visualize the flow. The test section was illuminated with an LED light source. A Cedip/FLIR DCOO2U-F SILVER infrared imager was used simultaneously with the HSC, and operated at 100 fps.

3.3 Experimental Procedure

Before assembly, all components of the test loop and test section were cleaned with ethanol as a solvent and particulate rinse. The components were then dried with pressurized nitrogen. Once fully assembled, the test loop was flushed with ethanol. Before filling with the working fluid, the test loop was vacuum sealed and pumped down to 300 mTorr or less. The FC-72 was degassed by vigorous boiling for 5 minutes, while the vapor was condensed and gravity drained back to the reservoir. Once the degassing procedure was complete, the FC-72 was immediately drawn from the reservoir into the test loop. The FC-72 was also degassed daily.

The heater voltage was adjusted to the desired heat input, then the pump voltage and bypass valve were adjusted to reach the appropriate mass flux. The voltages, temperatures, pressures, and mass flux were monitored in real time with LabVIEW. The criteria for steady-state operation of the test section was the stability of the subsurface thermocouple probe, displaying less than 0.2°C temperature change in 20 minutes. The non-optical sensor signals were captured at 100 Hz for 5s while the high-speed camera (HSC) and infrared camera (IRC) were simultaneously triggered to initiate recording for 1s. The HSC imaged at 2000 fps while the IRC imaged at 100 fps. The last test of the previous day was repeated on the subsequent testing day. Tests were performed with heat inputs both increasing and decreasing in subsequent tests—no thermal hysteresis was observed.

3.4 **Data Reduction**

3.4.1 Fluid Properties

Two different test fluids were used in the experimental campaign. The first was a low-pressure refrigerant, R245fa, which is increasingly reported for use in embedded two-phase cooling research. The second fluid was FC-72, a Fluorinert™ fluid manufactured by 3M, which has been used for many electronics cooling applications. A summary of the basic fluid properties is shown in Section 1.6, and it can be observed that the liquid thermal conductivity of R245fa is about 40% higher than FC-72, while the latent heat of vaporization of R245fa is about double that of FC-72. These properties tend to make R245fa a more effective heat transfer fluid, but the chemical stability of FC-72 is often preferred. FC-72 is a liquid at room temperature and R245fa has a vapor pressure of about 1.5 atm at room temperature.

3.4.1.1 R245fa

The properties of R245fa were established by MATLAB communication with Engineering Equation Solver (EES) [89]. For the relevant locations in the test loop, the local temperature, pressure, or quality was used to determine the fluid properties from the electronic database. The properties include saturation temperature and pressure, enthalpy, viscosity, surface tension, density, and specific heat.

3.4.1.2 FC-72

The fluid properties of FC-72 were determined by the functions provided in the 3M product data sheet [90]. Temperature, pressure, or quality varying properties not included in the product information datasheet were quadratically interpolated from the values published in the Encyclopedia of Thermal Packaging [91] or

REFPROP from the National Institute of Standards and Technology. The properties include saturation temperature and pressure, enthalpy, viscosity, surface tension, density, and specific heat.

3.4.2 Gap Inlet and Outlet Pressure

Knowledge of the pressure at the gap inlet is essential for determining values of the pressure-dependent fluid properties within the gap, including saturation temperature. The pressure transducer measures pressure at the test section inlet, so the pressure drop from the transducer to the gap inlet must be calculated. The pressure drop from in the large diameter tubing from the sensor to the test section is negligible, so the pressure drop only needs to be calculated within the test section. The flow path within the test section is shown in Figure 3.9, using Design 1 for illustration.

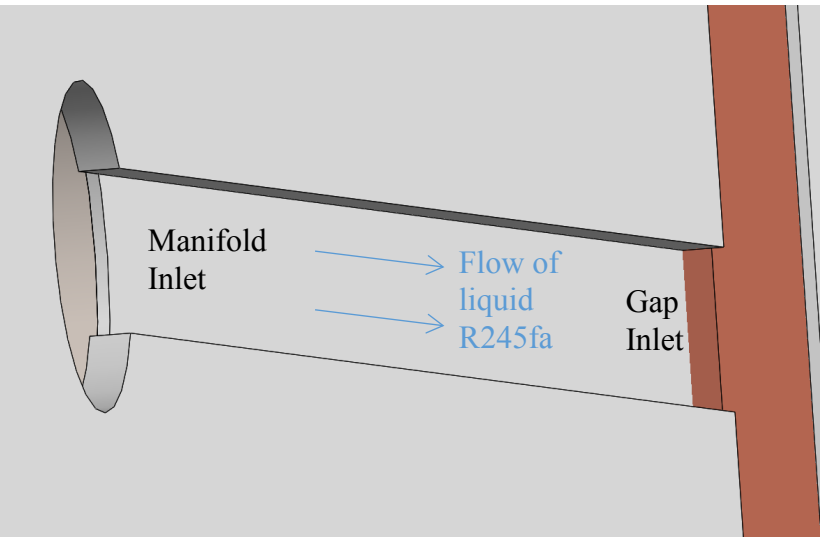

Figure 3.9: Illustration of the inlet flow path within the test section, with Design 1 used as an example

As the flow enters the test section, it turns a sharp 90° corner; simultaneously the cross-sectional area decreases by a factor of about two. The flow then travels 17 mm along the manifold (the flow path determined by the PTFE shim) to the

microchannel gap inlet. The majority of the pressure drop occurs at the gap inlet, where the flow cross sectional area decreases by a factor of three.

Three-dimensional computational fluid dynamics (CFD) simulations were performed in order to determine the pressure drop occurring from pressure transducer to the gap inlet. The software used was ANSYS Fluent [92] with laminar, adiabatic flow. The solutions were checked for continuity and grid independence For a microchannel flow rate of 1150 kg/m^2s, it was observed that the pressure drop from the manifold inlet to the end of the manifold is quite small (1 kPa) compared to the pressure drop caused by the gap inlet constriction (18 kPa)—indicating a significant potential for flashing across the flow restriction.

Since CFD simulations take significant amounts of time to compute and a separate computation must be performed for each flow rate, channel geometry, and temperature (liquid viscosity is temperature sensitive), a far simpler approach to estimating pressure drop is preferred. By accounting for the area constriction at the manifold inlet, the 90° bend at the inlet, the pipe flow along the length of the manifold, the constriction at the gap inlet, and the velocity change, the pressure drop can also be accurately calculated with laminar pipe flow correlations [93], as shown in Equations (43) – (50) in the Appendix 9.2. The pressure drop predicted by pipe flow correlations can then be compared with the CFD results, as shown in Figure 3.10.

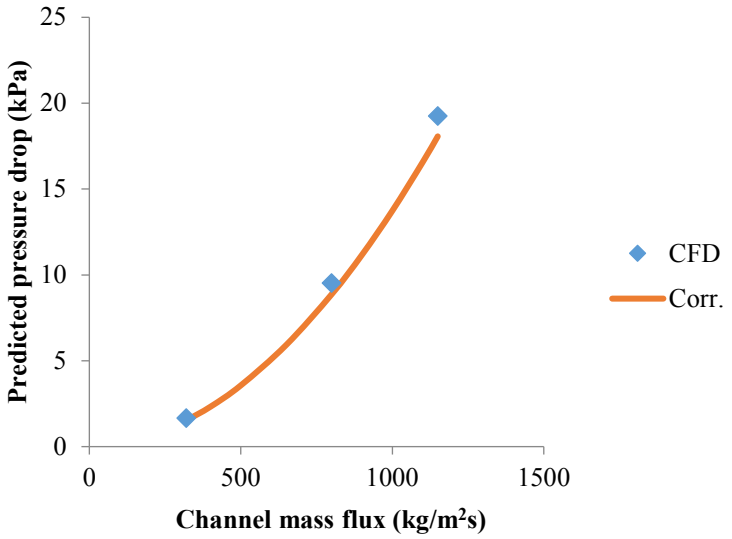

Figure 3.10 Pressure drop from transducer to gap inlet for the experimental range of microchannel mass fluxes, liquid R245fa at 25°C

It can be seen that the maximum discrepancy between CFD and the correlations occurs at the maximum microchannel mass flux and a minimum at the minimum mass flux. The discrepancy is about 1 kPa at the maximum and 0.1 kPa at the minimum. This small difference in absolute pressure at the inlet (about 0.5%) corresponds to discrepancy in saturation temperature well within the experimental uncertainty. The pressure drop from the transducer to the inlet of the gap decreases the absolute pressure of the R245fa by about 10% at a mass flux of 1,200 kg/m^{2}s.

It should be noted that some vapor generation may occur upstream of the inlet manifolding and flow into the gap. But, because the precise quality is unknown and two-phase pressure drop correlations have a high degree of uncertainty, the single-phase correlations are used to estimate the inlet pressure drop for R245fa. The two-phase multiplier from single to two-phase pressure drop for FC-72 at a quality below 50% is generally less than 1.5 [94]. So, for FC-72, which exhibits a higher pressure drop and higher saturation temperature dependence on pressure, a two-phase

multiplier of 1.25 with uncertainty of ±25% was applied. Regardless, the calculated pressure drop remains a relatively small deviation in the absolute pressure used to determine the fluid properties. The gap outlet pressure is determined by subtracting the pressure drop measured by the differential pressure transducer from the estimated gap inlet pressure.

3.4.3 Mass Flux

The mass flow rate to the test section is measured with the specific heat based mass flow meter, as shown in Equation (31), in which Q is the total heat into put into the vacuum-insulated tubing, c_p is the constant pressure specific heat of the fluid, and ΔT_{fm} is the measured temperature change in the flow meter.

$$\dot{m} = \frac{Q}{c_p \Delta T_{fm}} \tag{31}$$

The cross-sectional area of the microgap channel (either one or two channels, depending on manifold design) can then be used to find the microgap mass flux, as shown in Equation (32). The channel cross-sectional area is twice as large for Designs 1 and 3 compared to Design 2.

$$G = \frac{\dot{m}}{A_c} \tag{32}$$

3.4.4 Test Section Heat Input

The total heat generated by the test section heater can be found with Equation (33), in which V is the applied voltage and R is the temperature-independent electrical resistance.

$$Q_h = \frac{V^2}{R} \tag{33}$$

The heat losses to the ambient were then found by performing single-phase tests with FC-40 (properties taken from 3M datasheet) with the inlet and outlet temperatures set at the values produced with R245fa and FC-72. The heat loss was the difference between the total heat produced by the heater and the heat transferred to the fluid. Tests were performed at individual levels of heat input at steady state. The heat flux was incremented with increasing and decreasing heat flux between test runs to assure no thermal hysteresis existed. The mass flow rate was increased with increasing surface temperature to maintain constant inlet and outlet temperatures. The heat loss is expressed in terms of the ambient temperature and the subsurface thermocouple probe as shown in Equation (34).

$$\Delta T_{amb} = T_{s1} - T_{amb} \tag{34}$$

The best-fit relationship between the temperature difference to the ambient and the heat loss to the ambient can then be found, as shown in Figure 3.11.

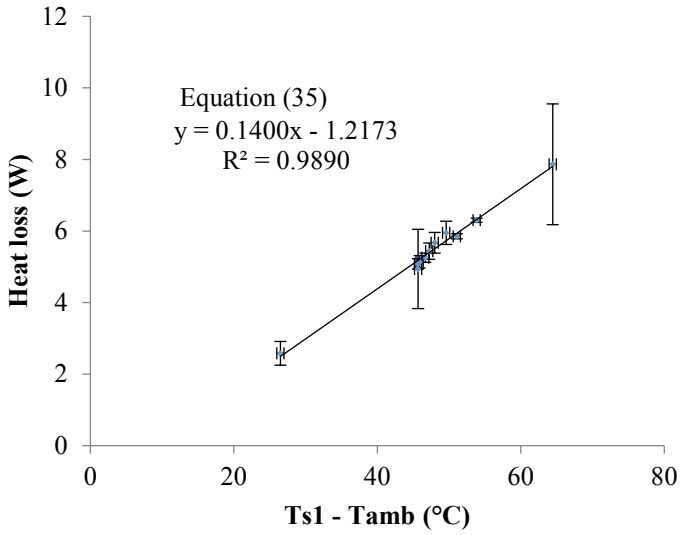

Figure 3.11: Heat loss to ambient from test section as a function of copper heat conductor temperatures and ambient temperature

The best fit ($R^2 = 0.989$) Equation for the heat loss as a function of temperatures is shown in Equation (35).

$$Q_{loss} = 0.1400\Delta T_{amb} - 1.2173 \tag{35}$$

Finally, the total heat transferred into the fluid within the test section can be found with Equation (36).

$$Q_f = Q_h - Q_{loss} \tag{36}$$

3.4.5 Subcooling

The fluid subcooling was determined using the test section outlet pressure ($T_{sat,o}$) and the test section inlet temperature (T_i). The fluid subcooling was found with Equation (37).

$$\Delta T_{sub} = T_{sat,o} - T_i \tag{37}$$

The sensible heat transferred to the fluid was then found with Equation (38).

$$Q_{sub} = \dot{m} c_p \Delta T_{sub} \tag{38}$$

3.4.6 Outlet Quality

The thermodynamic outlet quality was determined after accounting for the heat of subcooling as shown in Equation (39).

$$x_{out} = \frac{Q_f - Q_{sub}}{\dot{m} h_{fg}} \tag{39}$$

3.4.7 Wall Temperature

3.4.7.1 Infrared Camera Calibration

The temperature of the channel wall was measured by infrared thermography and the digital images were processed in MATLAB. The infrared camera was calibrated to the emissive surface (channel wall), intermediate media (fluid, sapphire window, and air), and ambient *in situ*. The channel wall temperature was set—and maintained adiabatic—by matching the fluid temperature to the subsurface thermocouple probe temperature. The digital level generated by the imager was then correlated with the temperature of the emissive surface, an example of which is shown in Figure 3.12. Tests were performed to verify that there was no measureable difference in signal intensity with the liquid or vapor of each of the two working fluids within the gap, indicating that the thin layer of either phase of either fluid did not alter the infrared signal detected by the imager.

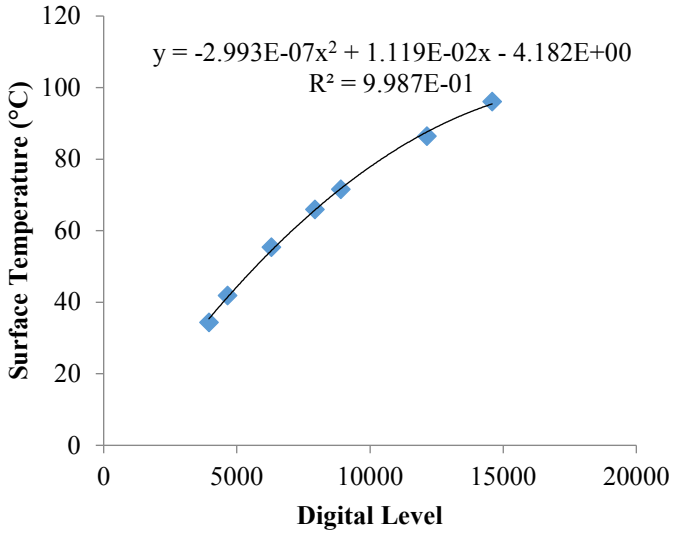

Figure 3.12: Example of digital level-temperature calibration

3.4.7.2 Infrared Image Smoothing

The infrared images of active two-phase flow were smoothed by eliminating the room temperature imager noise. The room temperature signal was recorded, and then subtracted from the individual images for a given dataset. The average of the room temperature digital signal was then added to the images, effectively smoothing the room temperature pixel noise from the images and improving thermal image clarity. This method was developed for the current study in order to compensate for limitations of the apparatus and improve experimental throughput.

3.4.7.3 Infrared Image Analysis

The infrared image sets were analyzed in several ways in order to compare flow and heat transfer properties under varying conditions and manifold designs. The first method was averaging pixel temperatures in time—or temporally averaging the wall temperature—which generates a spatial image of the time-averaged temperatures across the channel wall. The second method was to calculate the mean absolute deviation (MAD) of the individual pixel temperatures in time. The temporal MAD calculation evaluated the average deviation of an individual pixel temperature from its average temperature for the 1s imaging time period. Finally, the average wall temperature MAD was calculated by first averaging the channel wall temperature at each time step, then calculating the MAD of the average temperature of the 1s imaging period.

Temporal average temperature is an indicator of a typical moment in time. The temporal MAD measures how much the wall temperature varies at a given location on the channel wall, indicating how consistent the cooling—or lack

thereof—is along the channel wall. The average wall temperature MAD indicates the severity of the "global" dryout events across the entire channel wall.

For the manifold designs with two outlets (Design 1 and 3), the analyzed infrared images were "folded" in half—or, alternatively, the average values equidistant from the center of the image were averaged and presented in one image. This method collapses the two channels into a more compact format, and removes small discrepancies due to geometric tolerances. This approach is further justified in Appendix 9.3.2 by comparing average wall temperatures of the left and right channels, which were found to vary less than the measurement uncertainty.

3.4.8 Local Wall Heat Flux

The local wall heat flux was calculated by 3D computational conduction heat transfer in Ansys Mechanical R16.2. The boundary condition on the channel wall was taken directly from the local average wall temperatures. The pixel temperatures were aligned with nodes of the simulation mesh, with interpolated nodes in between each of the node temperatures defined by the pixel temperature boundary condition. The other thermal boundary condition was the time-averaged subsurface thermocouple probe temperature over the given time period, which was located beneath 520 μm of copper. From these boundary conditions, the local heat flux into the fluid was computed. An example of simulation of local heat fluxes is shown in Figure 3.13. For further data reduction, the local wall heat fluxes can be averaged and presented as a single value.

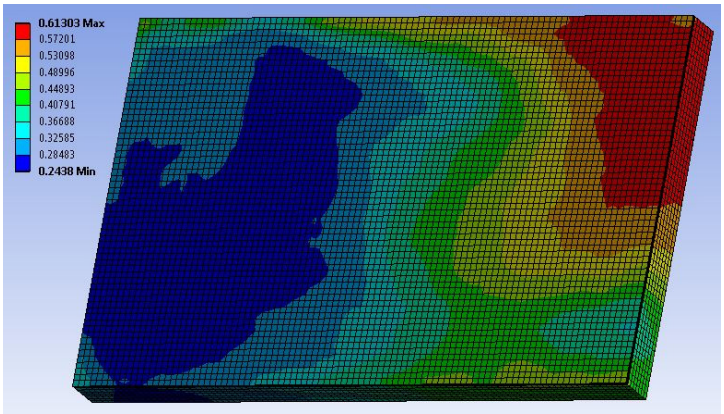

Figure 3.13: Example of local heat flux calculated with infrared and subsurface temperature boundary conditions simulated in Ansys. Units in W/mm^2

With this approach, the heat transfer into the fluid in the gap is calculated independently of the total heat transfer to the fluid from the test section. As expected, the heat transfer occurring within the gap accounts for the majority of the heat transfer into the fluid, as shown in Appendix 9.3.3.

3.4.9 Local Wall Superheat

The local wall superheat was found by taking the local average wall temperature and subtracting the estimated local saturation temperature based on the calculated pressure at the inlet of the gap and an assumed linear pressure drop from the inlet of the gap to the outlet. Equation (40) is applied to each pixel of the infrared boundary condition, with estimated local values of saturation temperature at each pixel.

$$\Delta T_{sup} = T_w - T_{sat} \tag{40}$$

This local saturation temperature estimation does not account for spanwise pressure gradients due to flow curvature, but the majority of the pressure variation occurs in the streamwise direction in single phase flow of this geometry [31], and the same concept is assumed to apply to two-phase flow in the same geometrical

configuration. Plots of calculated saturation temperature difference from inlet to outlet are shown in the Appendix 9.3.4. The saturation temperature variation from inlet to outlet is generally less than 1°C with R245fa, while it may exceed 10°C with FC-72 due to the high pressure drop. For further data reduction, the local wall superheat values can be averaged and presented as a single value, as will be shown in presentation of the experimental results.

3.4.10 Local Wall Heat Transfer Coefficients

The local wall HTC's were found by dividing the local heat flux profiles by the local superheat profiles. Equation (41) is applied to each pixel of the superheat profile and each pixel of the local heat flux profile.

$$h = \frac{q''}{\Delta T_{sup}} \tag{41}$$

The average wall HTC's are then found by averaging all the local values of the profile. This localized approach to determining average HTC's is in contrast to a more traditional method for determining HTC's, which would typically consist of first averaging wall temperature, averaging wall heat flux, and average saturation temperature, then applying these values to Equation (41). Because the HTC's are determined before averaging in the local HTC approach, the compound effect of high heat fluxes occurring at low superheat areas and low heat fluxes occurring at high superheat areas can shift the value of average HTC. As can be seen in Appendix 9.3.4, the difference in the two approaches is moderate, generally shifting the "locally averaged" HTC's to values about 20% larger than the HTC's based on average wall superheat and average wall heat flux.

3.4.11 Identification of Flow Regimes

Distinct regions in the channel become important as the flow regimes evolve. These areas are labeled in Figure 3.14. The area labels are determined based on the flow curvature direction. Thus, the interior of the bend is at the flow divider while the exterior of the bend is at the bottom wall. The exterior corner is similarly at the exterior of the bend. The divergence zone is the point at which the flow splits into two streams from the single inlet stream. The terminology for the single inlet, single outlet design is the same, but with only the right half of Figure 3.14.

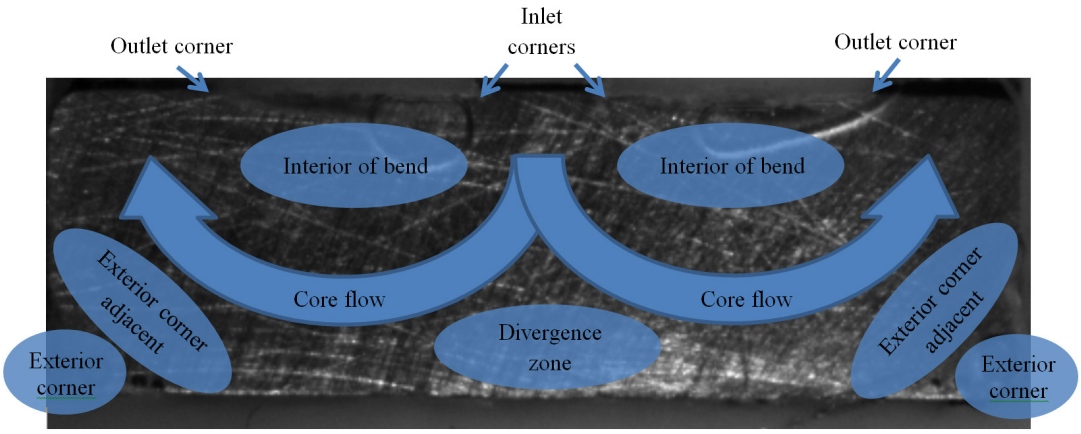

Figure 3.14: Areas of interest in the manifolded-microgap

Four main flow regimes will be identified in this visualization study. The first regime (at lowest quality) is "bubbly," in which the bubble diameter does not exceed the size of the gap. The second flow regime (increasing quality) is "slug" in which the bubbles have grown to exceed the size of the gap, with dimensions sometimes approaching the height of the channel. The "annular" flow regime occurs when divisions between bubbles are no longer apparent, and a liquid film lines the channel walls. "Rivulet" flow occurs when liquid film visibly ruptured and dry patches appear

on the wall, while liquid threads pass through the channel. These liquid threads are more prevalent on the adiabatic upper wall of the channel. The criteria for rivulet flow is when less than half of the channel cross section is wetted and liquid is largely bypassing the heated surface. The flow regimes observed here are quite comparable to those observed in other work, particularly with Ong and Thome [44] and Taitel and Dukler [53], as shown in Table 3.1.

Table 3.1: Comparison of flow regime characterizations

Current study	Taitel and Dukler [53]	Ong and Thome [44]
Bubble	Dispersed bubble	Isolated bubble
Slug	Intermittent	Coalescing bubble
Annular	Annular	Annular

Although the flow regimes can be labeled in similar ways, some significant differences occur in the U-shaped manifolded-microgap that do not occur in straight circular channels. For example, oftentimes two flow regimes occur simultaneously in the same region of the channel. In particular, the bubble and slug regimes may occur at the same time when, locally, a large slug and small bubbles flow in parallel; large slugs are often generated by stagnant zones in the flow while small bubbles are generated by nucleate boiling in the core of the flow. Furthermore, the slug and annular regimes may also coexist when slugs are exiting at the interior corner of the outlet while a smooth annular film occurs at the exterior of the outlet.

Sometimes, two flow regimes may also alternate periodically. For example, small bubbles may appear due to nucleate boiling in the liquid threads (similar to

liquid plug flow in straight circular channels) that separate large vapor slugs. The slug and annular regime may also occur when the flow appears annular for an extended period of time, and then is disrupted by a passing liquid thread, making the flow appear slug-like. Annular and rivulet flow alternated in time under the conditions tested here. Flow regimes were categorized as having two simultaneous flow regimes if the secondary regime occurred more than 30% of the time in a typical image sequence of 20 images.

3.5 **Measurement Uncertainties**

The uncertainty in measured quantities causes uncertainties in calculated quantities, which must be accounted for. The uncertainty in the inlet pressure measurement is ±0.073% full scale [95], and the pressure drop uncertainty is 0.25% full scale [96], each of which amount to about 1 kPa uncertainty. The uncertainty of the calculated pressure drop from the transducer to the gap inlet is taken to be ±25%, based on the two-phase pressure drop multiplier used to determine the gap inlet pressure [94]. Each of these pressure uncertainties is taken into account in the uncertainty of the saturation temperature and quantities calculated therefrom. The uncertainty in the temperature difference measured by the type-J thermocouples in the sensible heat mass flow meter is ±0.1°C, which is double the maximum measured discrepancy between the thermocouples from the same wire. This temperature uncertainty amounts to ±3% uncertainty in the mass flow rate. The uncertainty in the channel gap size is ±5 μm. The wall temperature uncertainty taken by infrared thermography was found to be ±1°C by comparing the maximum disparity between adiabatic calibration conditions and accounting for the uncertainty in the

thermocouple measurement used in calibration. The high emissivity coating thickness uncertainty is ±4 μm and the thermal conductivity uncertainty is ±15%, resulting in a thermal resistance uncertainty of ±21%. The measurement uncertainty for the type-T thermocouples are ±0.5°C [97]. The sources of measurement uncertainty are summarized in Table 3.2.

Table 3.2: Summary of experimental uncertainties

Source	**Uncertainty**
Inlet pressure	0.073% FS
Pressure drop	0.25% FS
Calculated single-phase pressure drop into gap	±25%
Mass flow rate	±3%
Gap height	±5 μm
Wall temperature	±1°C
High-ε coating thickness	±4 μm
High-ε coating thermal conductivity	±15%
Thermocouples	±0.5°C

The uncertainty of parameters calculated as a direct function of these uncertainties were based on the local slope of the dependent function. The uncertainty propagation for a function of several uncertain variables with can be determined with Equation (42) [98]. All calculated quantities discussed in this section have associated uncertainties found with Equation (42).

$$U_Y = \sqrt{\sum_i \left(\frac{\partial Y}{\partial X_i} U_{Xi}\right)^2} \tag{42}$$

Chapter 4: Results and Discussion: Flow Regime Characterization

4.1 **Flow Observations**

The majority of tests described in this section were performed before the high emissivity coating was applied because the reflective copper surface generated improved lighting and visibility of flow features and have been previously described and discussed by the author in [99]. Using the mass flux of 530 kg/m^{2}s with R245fa as an example, the flow phenomena occurring at increasing qualities (increasing average heat fluxes) will be discussed.

At a heat flux just large enough to generate sufficient superheat for nucleate boiling (Q_f = 2.1 W, x_{out} = -3%), bubbles begin to nucleate at the center of the inlet due to the flow constriction caused by the step due to the protrusion of the copper block (out of the page), as shown in Figure 4.1. Note that the step in the copper block is intended to mimic the step generated by fins in the operational manifold-microchannel geometry. Bubbles nucleate at the center of the inlet, then travel toward the divergence zone and typically rest in the divergence zone momentarily, growing to a peak size, then eventually becoming entrained with the core flow and flowing to the outlet.

Bubbles also nucleate at the divergence zone, the interior of the bend, and exterior corner. Bubbles nucleating at the interior of the bend grow and flow approximately vertically (but partially toward the outlet), coalescing into the interior slug. The interior slug grows to a peak size, then migrates toward the outlet, pinching

off in a series of smaller slugs. The interior slug then begins growing again and the process repeats. The bubbles at the exterior corner similarly grow to a peak size, become entrained in the core flow, and then flow to the outlet. The outlet flow regime under these conditions is bubble-slug.

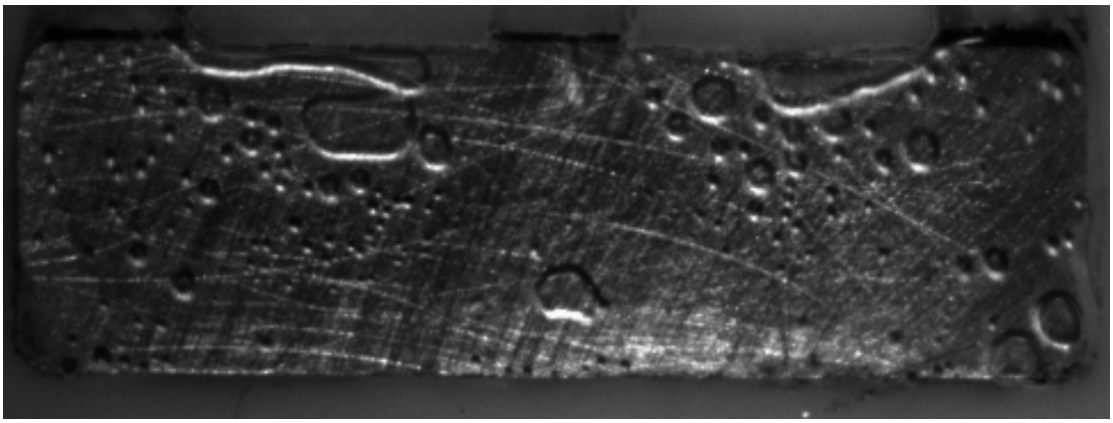

Figure 4.1: Flow phenomena occurring with R245fa Design 1 at Q_f = 2.1 W, x_{out} = -3%, and G = 530 kg/m^{2}s

Increased heat flux (Q_f = 3.6 W, x_{out} = 4%) causes the bubbles nucleating at the inlet to grow rapidly, and generally no longer become stagnant in the divergence zone, instead alternating left and right core streams toward the outlet, as shown in Figure 4.2. Bubbles still nucleate and grow to a peak size in the divergence zone, then become entrained with the core flow and are swept toward the outlet.

The interior slugs continue to grow, pinch off, and repeat. The peak size of the interior slugs constitutes a considerable fraction of the channel area. Sufficient heat flux exists to cause the large slugs to intermittently dryout and rewet the interior of the bend. Dryout also occurs intermittently in the large slugs forming in the divergence zone. Similarly, there is intermittent dryout and rewetting of the large slugs growing and departing from the exterior corner. The outlet flow regime under these conditions is slug.

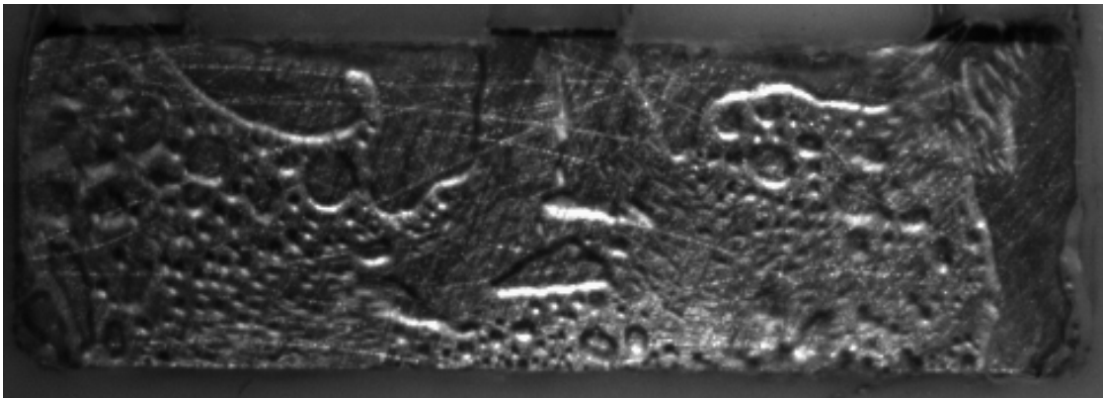

Figure 4.2: Flow phenomena occurring with R245fa Design 1 at Q_f = 3.6 W, x_{out} = 4%, and G = 530 kg/m^{2}s

With increased heat flux (Q_f = 4.5 W, x_{out} = 5%,), the flow becomes more chaotic due to the large size of the slugs occupying the majority of the channel and their interaction with each other and the walls, as shown in Figure 4.3. The magnitude of size fluctuation and peak size of the interior slugs begins to decrease as the portion of the slugs near the outlet continuously coalesces with outgoing slugs. Nucleate boiling is still evident at the center of the core flow. Large slugs grow from the divergence zone, sometimes spreading to merge with bubbles at the exterior corners. Intermittent dryout and rewetting occurs at three points: the interior of the bend, the divergence zone, and the exterior corners. The outlet flow regime is slug-annular.

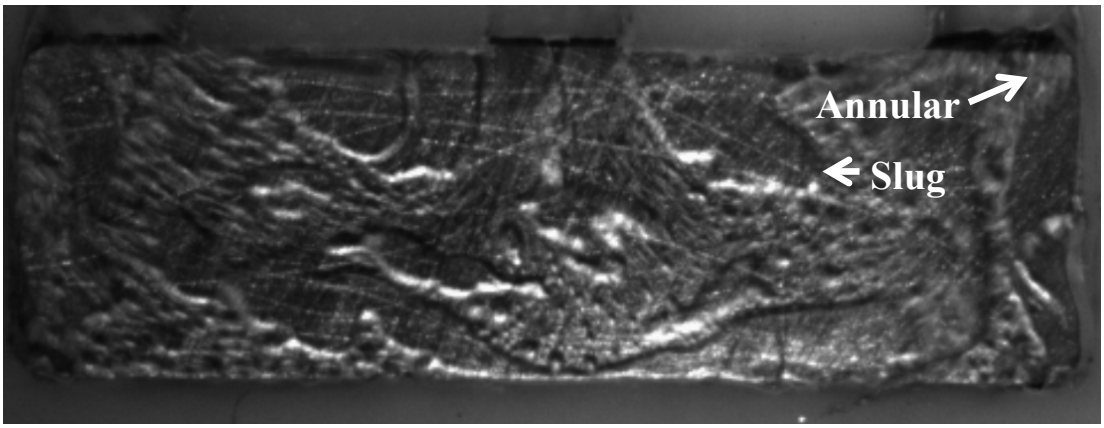

Figure 4.3: Flow phenomena occurring with R245fa Design 1 at Q_f = 4.5 W, x_{out} = 5%, and G = 530 kg/m^{2}s

Significantly increased heat flux (Q_f = 8.2 W, x_{out} = 14%) causes further increases in slug size, as shown in Figure 4.4. Perhaps the most interesting characteristic caused by the increased heat flux is the diminishing prevalence of slugs at the interior of the bend. The boundary of the interior slug near the inlet is occasionally marked by liquid threads, while the boundary of the interior slug near the outlet no longer exists consistently. Due to the changed morphology of the flow at the interior of the bend, dryout is much less prevalent at the interior of the bend. The regime occurring at the outlet is primarily annular, but transport of liquid threads (plugs) to the outlet makes the outlet regime sometimes slug-like. Small bubbles sometimes appear in the liquid threads.

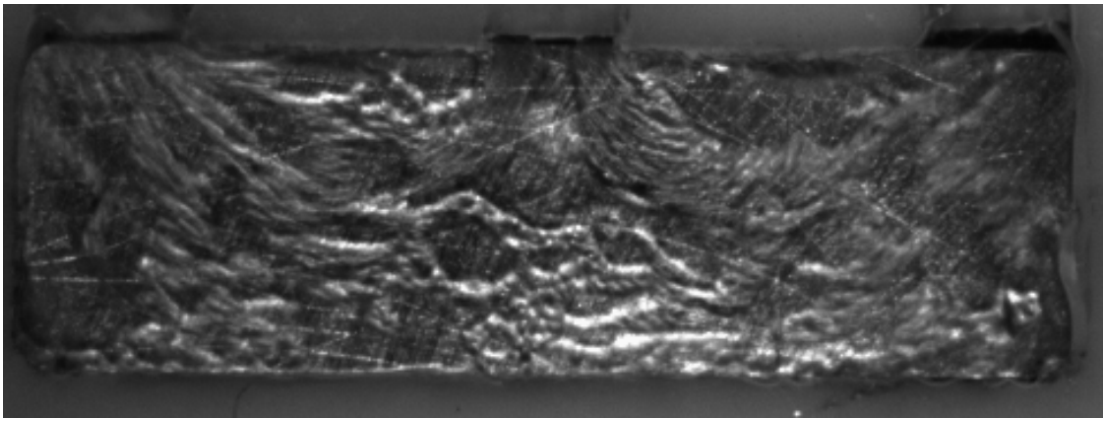

Figure 4.4: Flow phenomena occurring with R245fa at Q_f = 8.2 W, x_{out} = 14%, and G = 530 kg/m^{2}s

A further increase in heat flux (Q_f = 11 W, x_{out} = 22%) expands the area of annular flow and shrinks the area of slug flow, as shown in Figure 4.5. The divergence zone is now primarily annular and dryout is no longer apparent in the

divergence zone. Dryout does intermittently appear adjacent to the exterior of the bend, with liquid buildup occurring in the exterior corners.

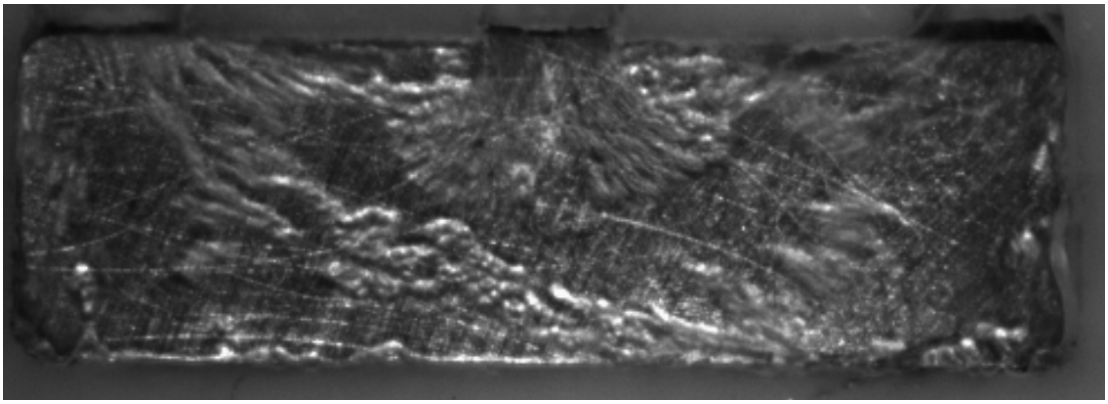

Figure 4.5: Flow phenomena occurring with R245fa Design 1 at Q_f = 11 W, x_{out} = 22%, and G = 530 kg/m^{2}s

A further increase in heat flux (Q_f = 17 W, x_{out} = 36%) causes the flow to appear entirely annular, with nucleation of the annular flow essentially occurring inlet of the gap (nucleated by pressure drop caused by protrusion of copper block). At these particular conditions, dryout is not apparent anywhere in the channel, as shown in Figure 4.6.

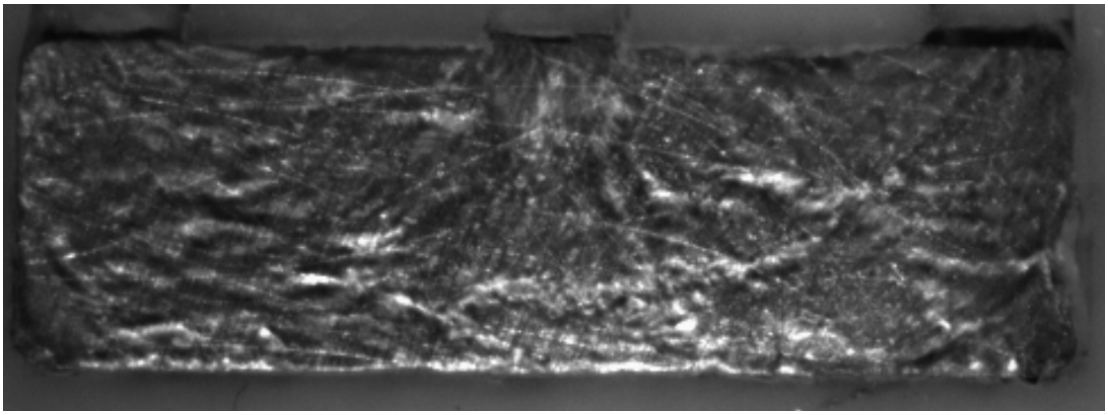

Figure 4.6: Flow phenomena occurring with R245fa Design 1 at Q_f = 17 W, x_{out} = 36%, and G = 530 kg/m^{2}s

Although it was not observed in the preliminary data set before the high emissivity coating was applied, it was found that a further increase in heat input and outlet quality resulted in the transient occurrence of annular and rivulet flow, as shown in Figure 4.7.

It is to be noted that visible light images from the data set that incorporated simultaneous high speed and infrared imaging appear compressed in the vertical direction because the high speed camera was located above the infrared camera, viewing from an angle, so that the infrared camera view field could be aligned parallel to the heated surface. Regardless, the occurrence of rivulet flow is evident, in which the liquid is only consistently contacting the heated surface beyond the inlet region, and primarily flowing on the adiabatic upper wall.

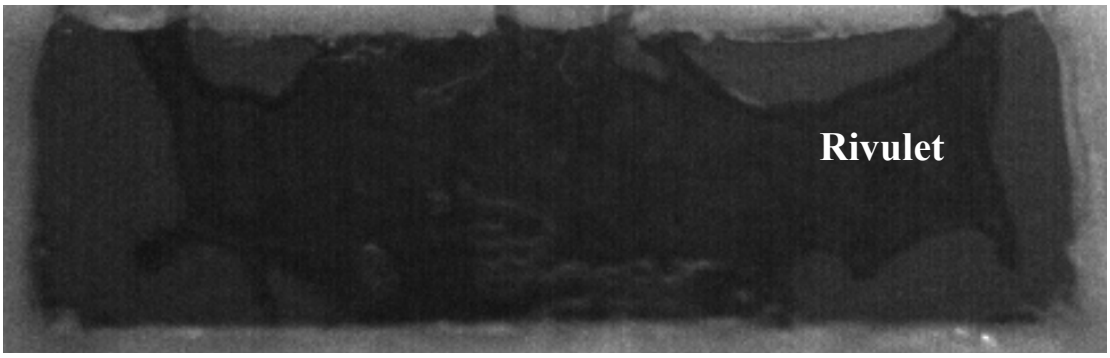

Figure 4.7: Flow phenomena occurring with R245fa at q''_{av} = 38 W/cm^2, x_{out} = 39%, and G = 500 kg/m^{2}s

4.1.1 Parametric Effects on Flow Observations

The types of flow phenomena occurring with FC-72 were generally consistent with those of R245fa, although the conditions under which they occur tend to differ. One phenomena that was consistently evident in FC-72, but not R245fa, was wavy

liquid films during annular flow, as is shown in Figure 4.8. These 2D and 3D waves occurred in annular flow under many conditions, with both Design 1 and Design 2.

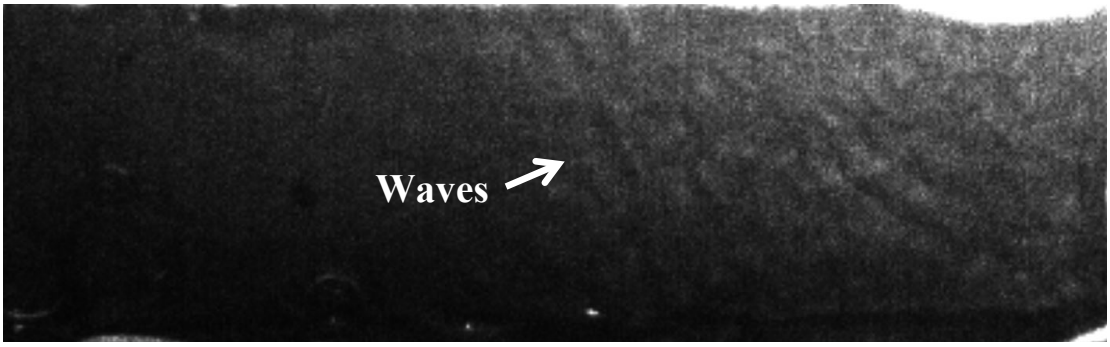

Figure 4.8: Flow phenomena occurring with FC-72 Design 2 at q''_{av} = 18 W/cm^2, x_{out} = 37%, and G = 600 kg/m^{2}s

The phenomena occurring at intermediate mass fluxes of 500-600 kg/m^{2}s are generally representative of those occurring between 300 and 800 kg/m^{2}s with both fluids and all three manifold designs. Higher and lower mass fluxes change the frequency and severity at which the phenomena occur, while manifold design can cause shifts in flow regime transitions and heat transfer performance. Lower mass fluxes of 150 kg/m^{2}s caused increased frequency and magnitude of global dryout events, causing the flow to be increasingly consistent with churn flow, although the observed phenomena could usually be categorized within the flow regime definition criteria detailed previously. In the remainder of this chapter, the outlet flow regimes occurring with varying mass flux and heat input will be reported and compared with existing flow regime transition criteria.

4.2 **Flow Regime Characterization**

Five sets of data were obtained in the current experimental campaign. Manifold Design 1 and Design 2 were used with R245fa and FC-72. Manifold Design 3 was

used only with FC-72. In addition to manifold design, the primary independent variables within each data set were heat flux and mass flux. These parameters control outlet quality, and the associated flow and heat transfer phenomena. For the manifold designs with a single channel, the same mass flow rate was used as the dual outlet designs, generating the same potential cooling capacity, but doubling the channel mass flux and channel length. The experimental procedure detailed previously was used for the following data sets. A summary of the experimental campaign used for this chapter and the remaining chapters is shown in Table 4.1.

Table 4.1: Summary of experimental campaign

	R245fa Design 1	R245fa Design 2	FC-72 Design 1	FC-72 Design 2	FC-72 Design 3
Channel Mass Flux (kg/m^2s)	150, 300, 600, 800	300, 600, 1000, 1600	300, 600, 800	600, 1000, 1600	300, 600, 800
Peak Avg. Heat Flux (W/cm^2)	44	38	35	30	32
Subcooling (°C)	6 ± 1.5	6 ± 1.5	6 ± 1.5	6 ± 1.5	6 ± 1.5
Max. Avg. Superheat (°C)	32	34	14	17	21
Max. Pressure Drop (kPa)	12	13	48	49	40
Peak Outlet Quality	0.68	0.61	0.51	0.43	0.54

The subcooling was maintained at approximately 6°C, with 1.5°C variation between tests. Because the heat capacity of the liquid, resulting from subcooling, is generally small compared to the latent heat, the effect of small variations in subcooling is minimal. The heat of subcooling as a fraction of total heat input into the fluid is shown in Appendix 9.3.6**.** It can be observed that the fraction of cooling due

to subcooling begins 5% quality is about one, but quickly falls to less than 0.2 by outlet quality of 20%.

The peak heat fluxes obtained with R245fa with manifold Design 1 and 2 were about 25% higher than those with FC-72 with the same manifolds, as shown in Table 4.1. The peak superheats with R245fa were about double that of FC-72 because of the lower saturation temperature and upper temperature limit of the test section. The pressure drop exhibited with R245fa was about ¼ that of FC-72, even as vapor qualities nearly 20% higher (in absolute vapor quality) were achieved. These results are not unexpected, as R245fa is clearly a more potent heat transfer fluid.

The goal of the remainder of this chapter is to characterize the differences in flow regime and dryout phenomena resulting from the differing properties of these two fluids. In the following sections, each data point represents an individual test at steady state. The flow regime occurring at the channel outlet is then reported, subject to the criteria established in the experimental methods chapter. For all five data sets, the regime observations will be presented with outlet quality and mass flux coordinates, as well as vapor superficial velocity and liquid superficial velocity coordinates for comparison to the two flow regime mappings protocols.

Because of the uniqueness of manifolded-microgap geometries, there is lack of universal correlations for predicting flow regimes or dryout/CHF that are strictly applicable. Therefore, the closest widely accepted criteria will be applied. The data sets will also be compared with flow regime transition predictions from Ong and Thome [44], flow regime transition predictions from Taitel and Dukler [53], and dryout/CHF predictions from Ong and Thome [50]. As discussed previously, two

flow regimes often occur simultaneously at the channel outlet due to the nature of the manifolded-microgap channel. And so, the bubble to slug and slug to annular transition criteria from the literature will be applied to the bubble-slug to slug and slug-annular to annular flow regime transitions identified empirically.

4.2.1 R245fa Manifold Design 1 (Figure 3.4)

Comparing the geometry and dimensionless numbers recommended for applicability—and underpinning the correlation—of the Ong and Thome [44] flow regime transition, it was found that the Confinement number (Co) of the R245fa Design 1 experiments was about a factor of four larger than the maximum Co recommended. This is because the hydraulic diameter is also smaller than recommended. The vapor Reynolds number is smaller than the recommended range for the tests with mass fluxes less than 600 kg/m^{2}s, while the liquid Weber number is within the recommended range for all cases. For the dryout/CHF predictions of Ong and Thome [50], the hydraulic diameter was again a factor of two smaller than recommended and the vapor-liquid density ratio is below the recommended range. The liquid Weber number, liquid-vapor viscosity ratio, and L/D_h ratio are within the recommended ranges, though. So, the Ong and Thome empirical transitions are not strictly applicable based on the recommended parameter ranges, and also noting that they were developed with straight, circular channels, without inlet restrictions. As has been discussed previously, flow characterizations strictly applicable to manifolded microgap channels have not yet been identified and validated. Therefore, the empirical flow regimes are compared with the Ong and Thome transition criteria, as shown in Figure 4.9.

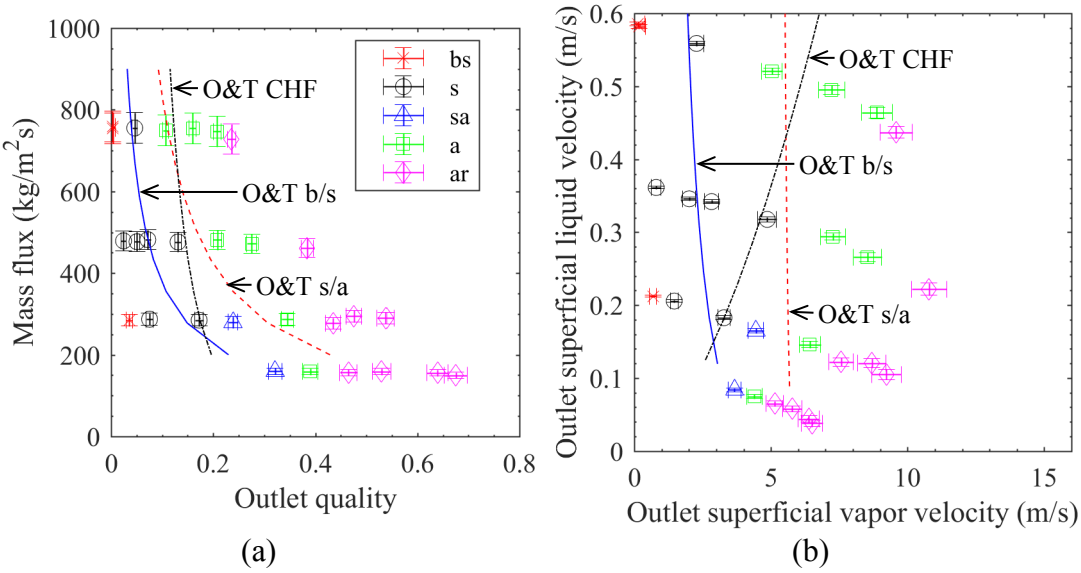

Figure 4.9: R245fa Design 1 outlet flow regimes in terms of (a) outlet vapor quality and mass flux, and (b) superficial velocities. Outlet flow regimes at each point are: bs – bubble-slug, s – slug, sa – slug-annular, a – annular, ar – annular-rivulet. Predicted transitions: Ong and Thome [44] bubble to slug transition (O&T b/s: —), Ong and Thome [44] slug to annular transition (O&T s/a: - - -), Ong and Thome [50] dryout/CHF prediction (O&T CHF: -·-).

Using the mass flux of 500 kg/m^{2}s as an example, it can be seen that the empirical transition to slug flow occurs at less than 2% quality. The slug-annular to annular transition occurs at about 17% quality, and the annular to annular-rivulet transition occurs at about 30% quality. Comparing with the Ong and Thome [44] bubble to slug transition, it can be seen that the prediction lies within the empirical slug region—providing at least a reasonable estimate of the prevailing flow regime. The Ong and Thome [44] slug to annular transition predicts the transition to annular flow quite well under these conditions. Finally, the Ong and Thome [50] dryout/CHF prediction tends to significantly underpredict the quality at which dryout occurs. Comparing with Figure 4.9 (b), it can be observed that both the bubble to slug and

slug to annular flow regime transitions occur at relatively constant vapor superficial velocities.

4.2.2 R245fa Manifold Design 2 (Figure 3.5)

The Co for R245fa Design 2 is unchanged from R245fa Design 1, meaning that it is still approximately a factor of four larger than recommended for applicability of the Ong and Thome [44] flow regime transitions. The vapor Reynolds number is, again, smaller than the recommended range with mass fluxes less than 600 kg/m^{2}s. The liquid Weber number is within the recommended range for tests with mass flux less than 1500 kg/m^{2}s. For the dryout/CHF predictions of Ong and Thome [50], the hydraulic diameter was again a factor of two smaller than the recommended range of applicability of the correlation, and the vapor-liquid density ratio remains below the recommended range. The liquid Weber number, liquid-vapor viscosity ratio, and L/D_h ratio are again within the recommended ranges. So, the Ong and Thome empirical transitions are again not strictly applicable based on the recommended parameter ranges or geometry. Nevertheless, and in the absence of validated criteria for manifold-microchannel configurations, the empirical flow regimes, compared with the Ong and Thome transition criteria are shown in Figure 4.10.

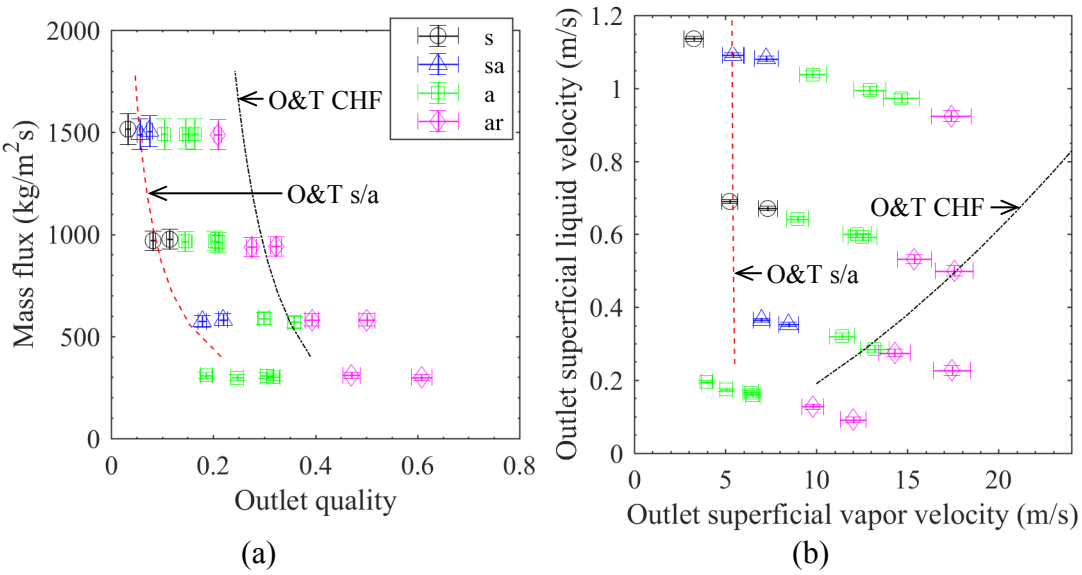

Figure 4.10: R245fa Design 2 outlet flow regimes in terms of (a) outlet vapor quality and mass flux, and (b) superficial velocities. Outlet flow regimes at each point are: s – slug, sa – slug-annular, a – annular, ar – annular-rivulet. Predicted transitions: Ong and Thome [44] slug to annular transition (O&T s/a: - - -), Ong and Thome [50] dryout/CHF prediction (O&T CHF: -·-).

Using the mass flux of 1,000 kg/m^{2}s as an example, it can be seen that bubble-slug flow was not observed within this data set. The slug-annular to annular transition occurs at about 12% quality, and the annular to annular-rivulet transition occurs at about 25% quality. The Ong and Thome [44] slug to annular transition tends to underpredict the transition to fully annular flow, although intermittent annular flow is occurring at the transition for the 600 kg/m^{2}s and 1,600 kg/m^{2}s tests. The Ong and Thome [50] dryout/CHF prediction aligns with the empirical transition to annular-rivulet flow quite well at lower mass fluxes, but with increasing deviation with increasing mass flux.

Comparing with Figure 4.10 (b), in terms of vapor superficial velocity, the discrepancy between the empirical data and the dryout/CHF prediction is quite large.

It can be observed that the slug to annular flow regime transition prediction occurs at approximately the same vapor superficial velocity as with R245fa Design 1, which now tends to underpredict the vapor superficial velocity at which the empirical flow transitions to annular.

4.2.3 FC-72 Manifold Design 1 (Figure 3.4)

The slug to annular flow regime transition criteria developed by Taitel and Dukler [53] was developed for macroscale, circular, adiabatic flows, so it is not strictly applicable to the manifolded-microgap. The transition was, though, developed with minimal empiricism, meaning that it should be more universally applicable. For the dryout/CHF predictions of Ong and Thome [50], the hydraulic diameter was again a factor of two smaller than recommended and the vapor-liquid density ratio is below the recommended range. The liquid Weber number, liquid-vapor viscosity ratio, and L/D_h ratio are within the recommended ranges, though. So, the Ong and Thome empirical transitions are not strictly applicable based on the recommended parameter ranges, and also noting geometrical differences. The empirical flow regimes are compared with the Taitel and Dukler [53] and Ong and Thome [50] transition criteria and are shown in Figure 4.11.

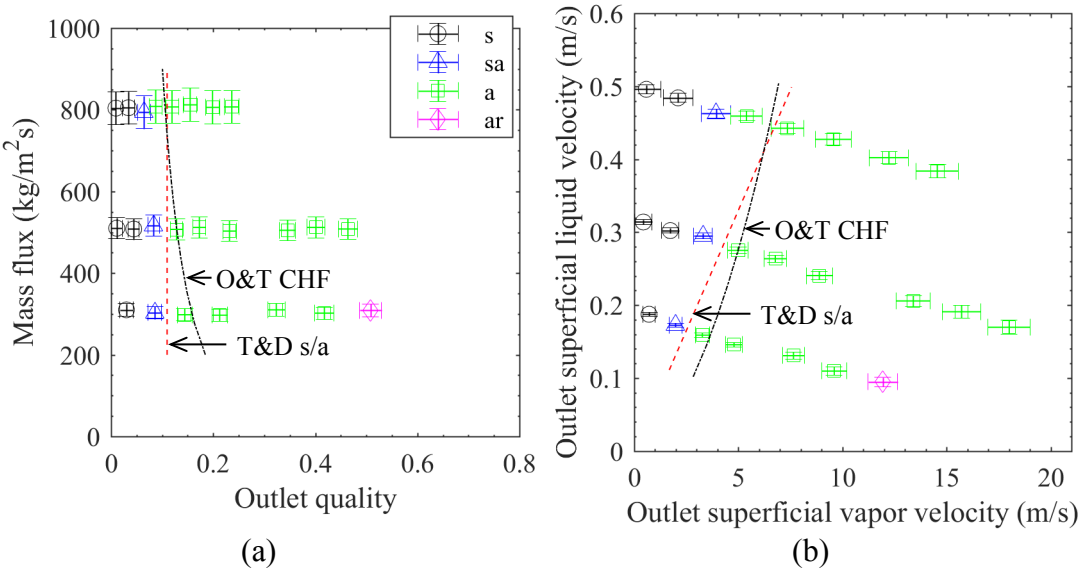

Figure 4.11: FC-72 Design 1 outlet flow regimes in terms of (a) outlet vapor quality and mass flux, and (b) superficial velocities. Outlet flow regimes at each point are: s – slug, sa – slug-annular, a – annular. Taitel and Dukler [53] slug to annular transition (T&D s/a: - - -), Ong and Thome [50] dryout/CHF prediction (O&T CHF: -·-).

In Figure 4.11 can be seen that the Taitel and Dukler [53] prediction aligns quite well with the empirical transition from slug to annular flow, although it may slightly overpredict the transition at 800 kg/m^{2}s. The transition to annular flow occurs at a constant quality, in contrast to R245fa, which transitions at conditions more consistent with constant vapor superficial velocity.

Furthermore, FC-72 Design 1 exhibits decreased occurrence of annular-rivulet flow compared to R245fa Design 1 at the same qualities. The surface tension of FC-72 in the conditions tested is about 30% lower than that of R245fa, while, as discussed previously, the liquid viscosity is higher and the vapor density is lower, all of which play a role in the flow regime transitions. The Ong and Thome [50]

dryout/CHF prediction tends to significantly underpredict the quality at which dryout occurs.

4.2.4 FC-72 Manifold Design 2 (Figure 3.5)

For the dryout/CHF predictions of Ong and Thome [50], the hydraulic diameter was again a factor of two smaller than recommended and the vapor-liquid density ratio is below the recommended range, consistent with the previous tests. The liquid Weber number, liquid-vapor viscosity ratio, and L/D_h ratio are within the recommended ranges, though. So, again, the Ong and Thome empirical transitions are not strictly applicable based on the recommended parameter ranges, and also noting geometrical differences. The empirical flow regimes are compared with the Taitel and Dukler [53] and Ong and Thome [50] transition criteria and are shown in Figure 4.12.

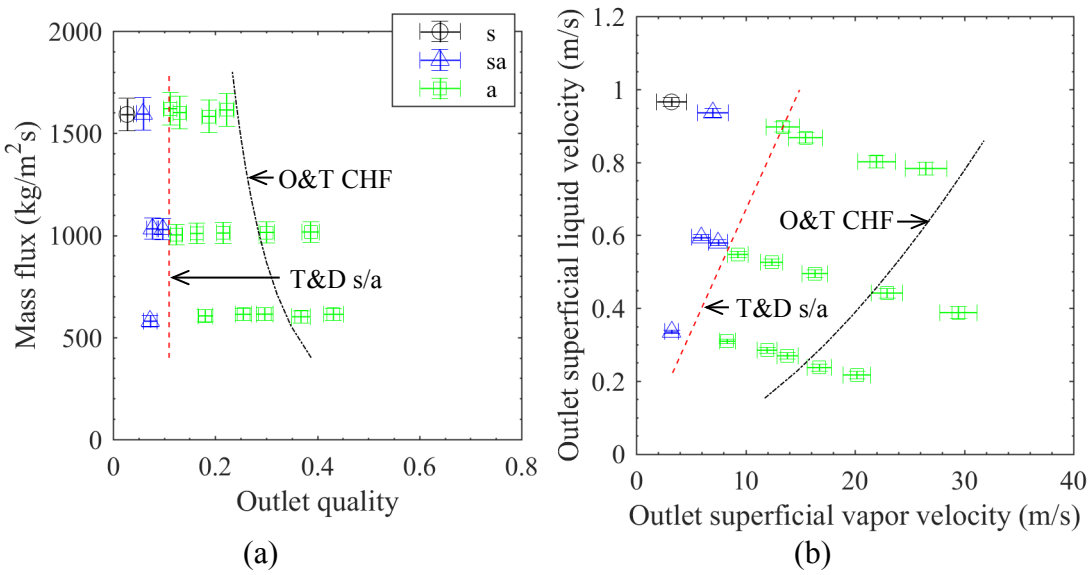

Figure 4.12: FC-72 Design 2 outlet flow regimes in terms of (a) outlet vapor quality and mass flux, and (b) superficial velocities. Outlet flow regimes at each point are: s – slug, sa – slug-annular, a – annular. Predicted transitions: Taitel and Dukler [53] slug to annular transition (T&D s/a: - - -), Ong and Thome [50] dryout/CHF prediction (O&T CHF: -·-).

Examining Figure 4.12, it can be seen that the Taitel and Dukler [53] prediction aligns quite well with the empirical transition from slug to annular flow, again. The transition to annular flow with FC-72 Design 2 is, again, at a constant quality with increasing mass flux. Indeed, the flow regime transition criteria is independent of mass flux, and is well aligned with the transition of FC-72 with Design 1 and Design 2.

FC-72 Design 2 exhibited no occurrence of annular-rivulet flow under the conditions tested. The Ong and Thome [50] dryout/CHF prediction predicts that dryout will begin to occur at 15 m/s and 20 m/s for 600 kg/m^{2}s and 1,000 kg/m^{2}s, respectively. These velocities are in good agreement with the conditions at which the average wall HTC's decline due to intermittent dryout and rewetting with FC-72 Design 2, although the flow regime does not meet the criteria for annular-rivulet flow. This will be discussed in more detail in the next chapter.

4.2.5 FC-72 Manifold Design 3 (Figure 3.6)

The comparison of geometries and dimensionless numbers for the range of applicability of the Ong and Thome [50] dryout/CHF prediction from Design 1 to Design 3 is unchanged. Therefore, the flow regime predictions are not strictly applicable based on these parameters. The primary difference between Design 1 and Design 3 is the decreased manifold length, causing significantly decreased average flow path radius curvature, as well as decreased inlet and outlet velocity. The empirical flow regimes are compared with the Taitel and Dukler [53] and Ong and Thome [50] transition criteria and are shown in Figure 4.13.

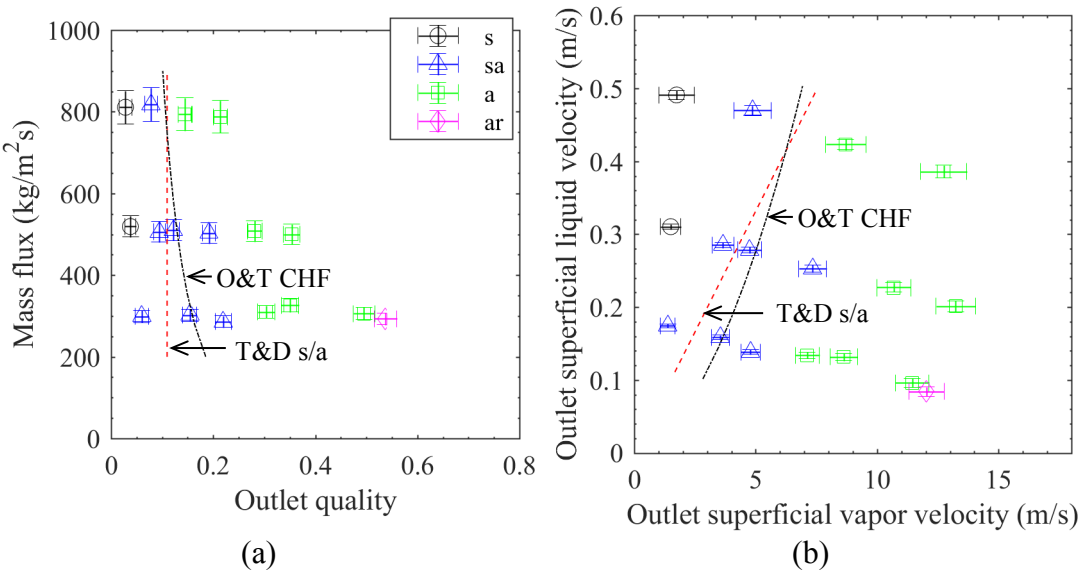

Figure 4.13: FC-72 Design 3 outlet flow regimes in terms of (a) outlet vapor quality and mass flux, and (b) superficial velocities. Outlet flow regimes at each point are: s – slug, sa – slug-annular, a – annular. Taitel and Dukler [53] slug to annular transition (- - -), Ong and Thome [50] dryout/CHF prediction (-·-).

It can be seen that with Design 3 the Taitel and Dukler [53] prediction no longer aligns with the empirical flow regime transition for the 300 kg/m^{2}s or the 500 kg/m^{2}s mass fluxes. The increased prevalence of slug flow with annular flow stems from the bypass effect of the short manifold design, in which the flow can travel from inlet to outlet with decreased evaporation efficacy.

FC-72 Design 3 continues to exhibit decreased occurrence of annular-rivulet flow compared to R245fa Design 1 at the same qualities. The Ong and Thome [50] dryout/CHF prediction tends to significantly underpredict the quality at which dryout occurs, which is consistent with both fluids and Design 1.

4.3 Summary of Flow Regime Characterization

With both manifold designs 1 and 2, R245fa tended to exhibit flow regime transitions more consistent with constant vapor superficial velocity, in which the transition occurs at decreasing quality with increasing mass flux. In contrast FC-72 exhibited a flow regime transition from slug-annular to annular at a constant quality. The quality at which the flow regime transitions occurred were hardly shifted between the two manifold designs with both fluids, indicating that channel mass flux only a weak driver of flow regime transitions under the present conditions.

This is further evidenced by the fact that the Taitel and Dukler [53] flow regime transition consistently predicted the flow regime transition for FC-72 with both manifold designs. In contrast, the Ong and Thome [44] slug to annular prediction aligned well with the empirical transition for R245fa Design 1, but underpredicted the transition with Design 2. Furthermore, the Ong and Thome [50] dryout/CHF prediction aligned reasonably well with both fluids with Design 2, but quite poorly with Design 1 and Design 3. This again indicates that channel mass flux is a weaker driver of flow regime transitions with the current geometry than might be otherwise expected, and inlet mass flux is, perhaps, a more influential driver of flow phenomena.

Chapter 5: Results – Wall Temperature

In this chapter, the channel wall temperatures data will be presented. The temperatures will be expressed in three ways in order to provide direct insight into the thermal video data. First, the "local temperatures" will be shown. Local temperatures are the time-averaged wall temperature at each location across the surface. Then, the local temperature mean absolute deviation (MAD) will be shown. The local temperature MAD indicates the average magnitude of wall temperature fluctuation in time, at each location on the wall. Finally, the global temperature MAD will be shown. The global temperature MAD is the MAD of the average temperature of the channel wall at each video frame.

A selection of data points, within evenly spaced vapor superficial velocity intervals, will be used to show the wall temperature profiles occurring with varying mass fluxes and vapor superficial velocities—noting that vapor superficial velocity is approximately proportional to heat flux. The wall temperature profiles show the temperature at each location along the channel wall, like that shown in Figure 5.1.

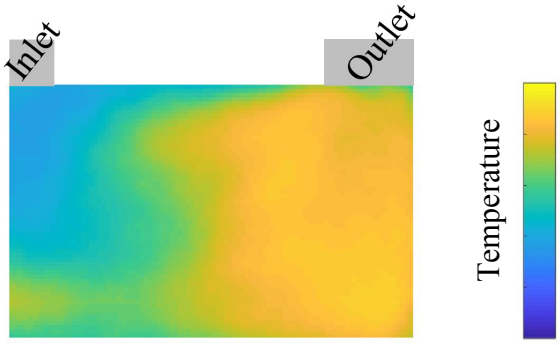

Figure 5.1: Example wall temperature profile, illustrating the location of the inlet and outlet relative to the local superheat profile

In all cases, the inlet is on the upper left and the outlet is on the upper right. As stated previously, this "folded" image is an average of the local values occurring in each of the two channels for manifold Designs 1 and 3, generating a compact composite image. For manifold Design 2, the long manifold design with a single inlet and outlet, the images were scaled in the horizontal direction to be the same size as those for Designs 1 and 3, for compact presentation and direct comparison. The flow regime occurring at each condition will be indicated as those in the previous chapter, with vapor superficial velocity on the horizontal axis and mass flux on the vertical axis. The outlet flow regimes at each condition will be indicated by the symbols used in the previous chapter.

5.1 **R245fa Manifold Design 1 (Figure 3.4)**

5.1.1 Local Temperatures

The local temperature profiles occurring with R245fa Design 1 are plotted in Figure 5.2 in terms of outlet vapor superficial velocity on the horizontal axis and mass flux on the vertical axis. Using the mass flux of 500 kg/m^{2}s as an example, it can be seen that the wall temperature increases relatively slowly from the lowest velocity up to 9 m/s. But, above 9 m/s, the wall temperature in the exterior corner region increases substantially—from a temperature of less than 55°C at 9 m/s to about 80°C at 11 m/s. The wall temperature at the inlet region increases from 41°C to 56°C from 3 m/s to 11 m/s, consistently remaining much cooler than the exterior corner, and exhibiting less change in temperature throughout the velocity range than the exterior corner.

This trend is consistent in all four mass fluxes, although the vapor superficial velocity at which the exterior corner temperature jump occurs, increases with increasing mass flux. The rise in wall temperature occurs quite suddenly as vapor superficial velocity increases, and is caused by a sudden deficiency of liquid wetting the surface—or persistent dryout occurring within the post-annular regime of annular-rivulet flow. Dryout first occurs in the exterior corner region because that location is furthest from the inlet, and also likely because of film inversion phenomena caused by the centripetal acceleration of the vapor driving the liquid film toward the interior of the bend.

It can be seen that when dryout is occurring consistently in the exterior corner, the temperature at the divergence zone remains low at the lower wall—or divergence zone. This is caused by large liquid drops impinging on the wall opposite of the inlet, and in the highest mass flux case, traveling along the exterior of the bend, keeping the temperatures low. This trend is consistent with droplet entrainment and deposition on the exterior of the bend in smooth U-shaped channels. But, the orthogonality of the channel walls generates a relatively stagnant region in the flow at the divergence zone, which causes the deposited liquid drops to sometimes remain stationary while evaporating. The fluctuation in local wall temperature will next be discussed.

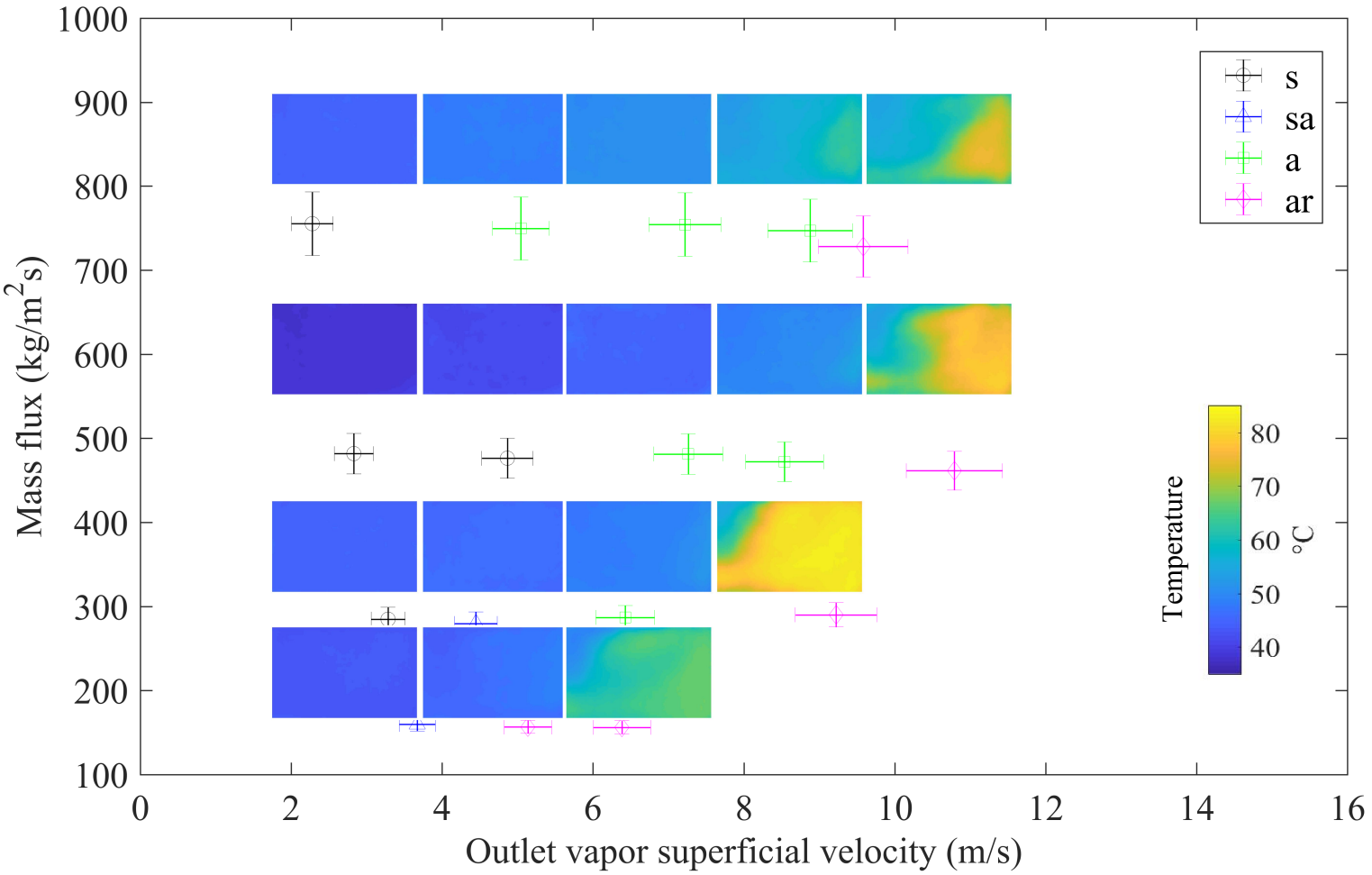

Figure 5.2: R245fa Design 1 local temperature profiles at intervals of outlet vapor superficial velocity and mass flux. Outlet flow regimes at each point are: s – slug, sa – slug-annular, a – annular, ar – annular-rivulet.

5.1.2 Local Temperature MAD

The local mean absolute deviation (MAD) of the wall temperature is shown in Figure 5.3. Using the tests at 500 kg/m^{2}s as an example, it can be seen that the temperature variation is quite low, near 0°C, at vapor superficial velocities from 1 m/s to 7 m/s. Then, at 9 m/s, the exterior corner MAD increases to more than 3°C, indicating intermittent dryout and rewetting. The lowest fluctuation (about 0°C) consistently occurs at in the inlet region, indicating consistent wetting under all conditions tested. At 500 kg/m^{2}s, and 11 m/s dryout is consistently occurring. This is evidenced by 10°C of temperature MAD at the boundary between the wetted and dryout regions, indicating that the wetting front oscillates in time. The transient nature of dryout and rewetting by liquid drop deposition is evident in the divergence zone, as shown by the elevated local temperature MAD of 8°C. The trends occurring at a mass flux of 500 kg/m^{2}s are fairly consistent for all mass fluxes, except for 150 kg/m^{2}s, in which the MAD is more consistently elevated, evidencing the more churn-like nature of the low mass flux flow.

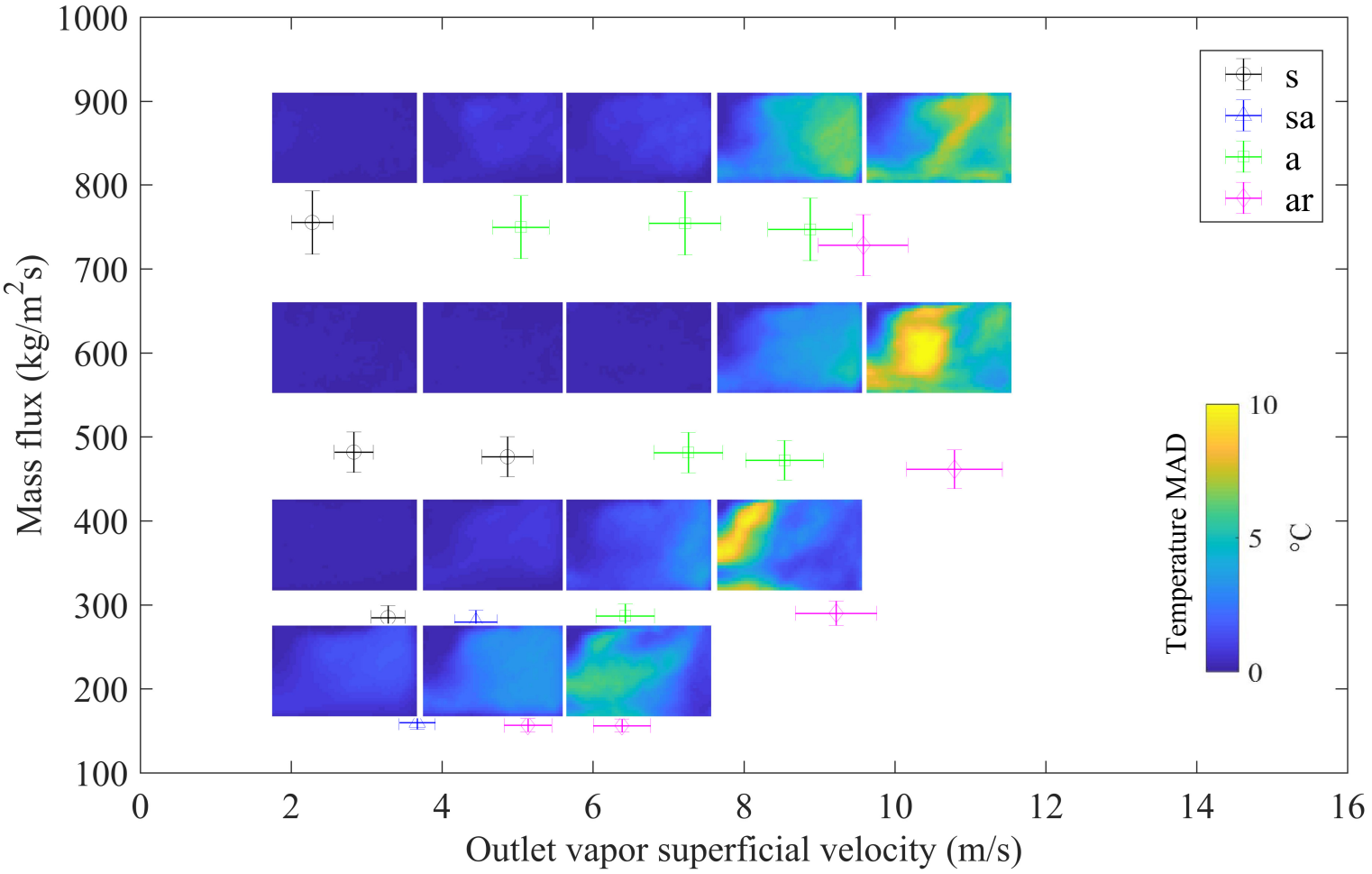

Figure 5.3: R245fa Design 1 local temperature MAD profiles at intervals of outlet vapor superficial velocity and mass flux. Flow regimes at each point are: s – slug, sa – slug-annular, a – annular, ar – annular-rivulet.

5.1.3 Global Temperature MAD

Another measure of wall temperature variation is the global temperature MAD—the MAD of the average wall temperature of each frame (taken at 100 fps), which is shown in Figure 5.4. High global temperature MAD is an indicator of the frequency and intensity of global dryout events. It can be observed that the global temperature MAD corresponds with increases in the local temperature MAD (rising sharply above 7 m/s at 500 kg/m^{2}s) and is similarly an indicator of impending, sustained local dryout in the exterior corner region. Sustained global dryout is exhibited by the decrease in the global temperature MAD, along with an increase in the average wall temperature, with increasing vapor superficial velocity. The global temperature MAD peaks at 6 m/s and 9 m/s with mass flux of 150 kg/m^{2}s and 300 kg/m^{2}s, respectively, after which the decline indicates a consistently dry surface.

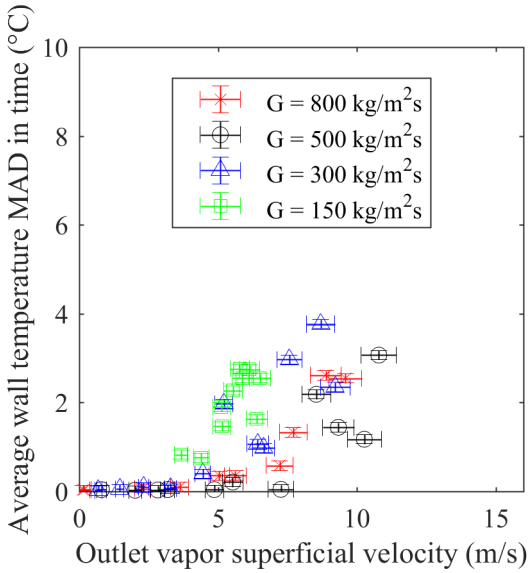

Figure 5.4: R245fa Design 1 average wall temperature MAD outlet with vapor superficial velocity at four mass fluxes

5.2 **R245fa Manifold Design 2 (Figure 3.5)**

5.2.1 Local Temperatures

The results of the local temperature occurring on the channel wall, of Manifold Design 2 for the flow of R245fa, will now be presented. As stated previously, the thermal property profiles presented in the following sections with R245fa Manifold Design 2 are scaled in the horizontal direction to maintain size proportion for comparison with Manifold Design 1 and compactness for presentation.

The local temperature profiles are plotted in Figure 5.5. Using the mass flux of 1,000 kg/m^{2}s as an example, it can be seen that the wall temperature increases slowly from 45°C at 5 m/s to about 55°C at 12 m/s. But, from 12 m/s to 15 m/s, the wall temperature in the exterior corner region increases from 60°C to 75°C. By 17 m/s, the exterior corner temperature has increased to 85°C. The wall temperature at the inlet area remains comparatively low, between 45°C to 60°C for all tests.

This trend is consistent in all four mass fluxes, although the vapor superficial velocity at which the temperature jump occurs, increases with increasing mass flux, consistent with the trends observed with R245fa Manifold Design 1. The vapor superficial velocity at which persistent dryout becomes evident for equivalent mass flow rates (channel mass fluxes are doubled from Design 1 Design 2) does not increase by a factor of two from R245fa Design 1 and Design 2, and it will become clear in the following sections that the quality at which the HTC's decline increases from R245fa Design 1 to R245fa Design 2.

When dryout begins to occur consistently in the exterior corner (15 m/s for 500 kg/m^{2}s), the temperature at the divergence zone remains lower, at about 60°C to

70°C. This is again caused by liquid drops impinging on that relatively stagnant flow location, then evaporating while remaining relatively stationary. The outlet flow regime is again, annular-rivulet when persistent dryout is occurring. The wall temperature fluctuation will next be discussed.

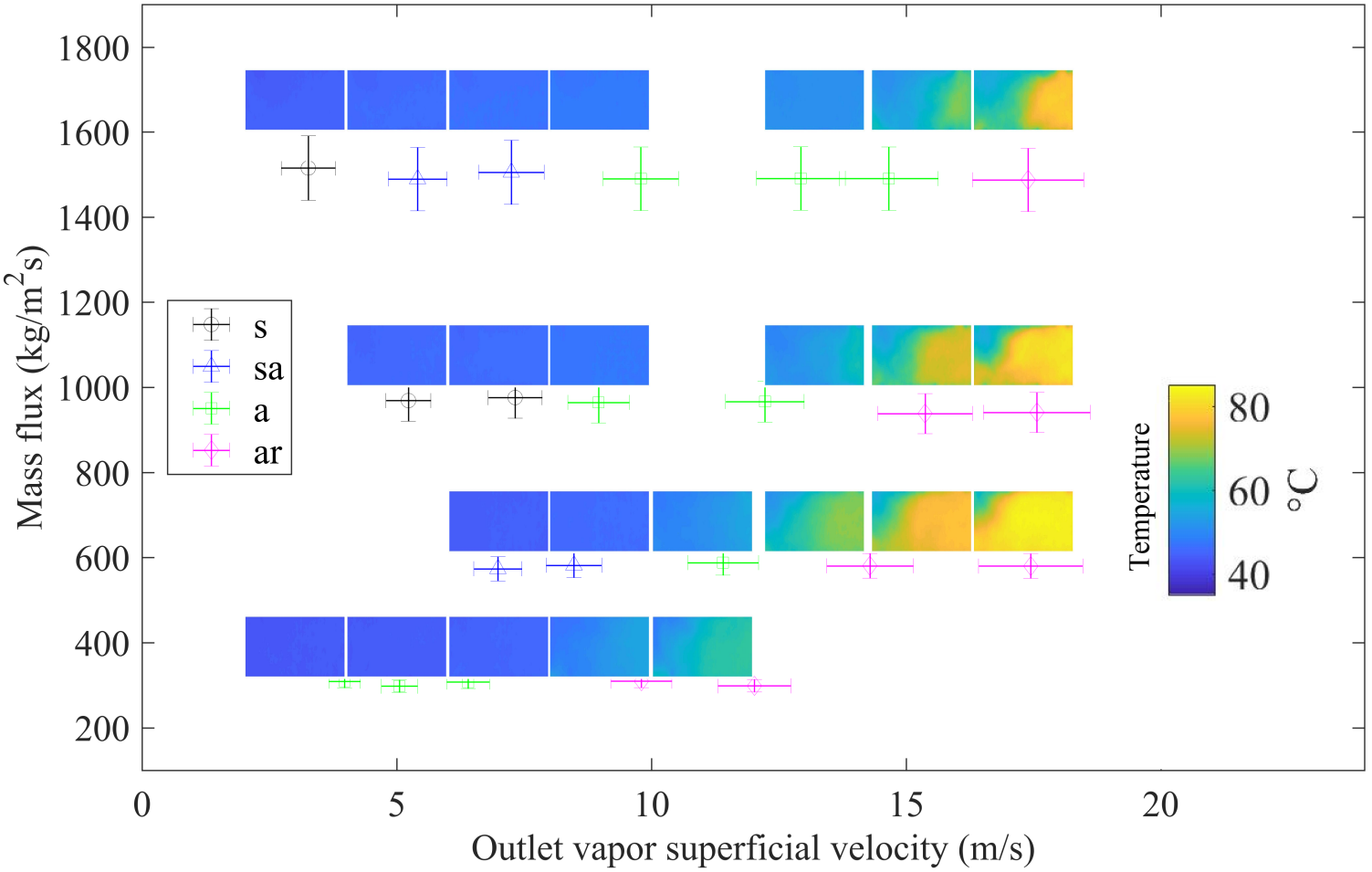

Figure 5.5: R245fa Design 2 local temperature profiles at intervals of outlet vapor superficial velocity and mass flux. Outlet flow regimes at each point are: s – slug, sa – slug-annular, a – annular, ar – annular-rivulet.

5.2.2 Local Temperature MAD

The local mean absolute deviation (MAD) of the wall temperature is shown in Figure 5.6. Using the tests at 1,000 kg/m^{2}s as an example, it can again be seen that the temperature variation is quite low, between 0°C to 1°C vapor superficial velocities below 10 m/s. Low temperature fluctuation consistently occurs at in the inlet region with increasing velocity, but exhibits higher fluctuations than Design 1 at high velocities—more than 6°C with 300 kg/m^{2}s and 600 kg/m^{2}s. At 15 m/s at 1,000 kg/m^{2}s, dryout is consistently occurring in the exterior corner, and the wetting front generates the highest temperature fluctuations of 8°C due to oscillation. Liquid drop deposition at the exterior of the bend, generating intermittent dryout and rewetting is again evidently occurring with the annular-rivulet regime.

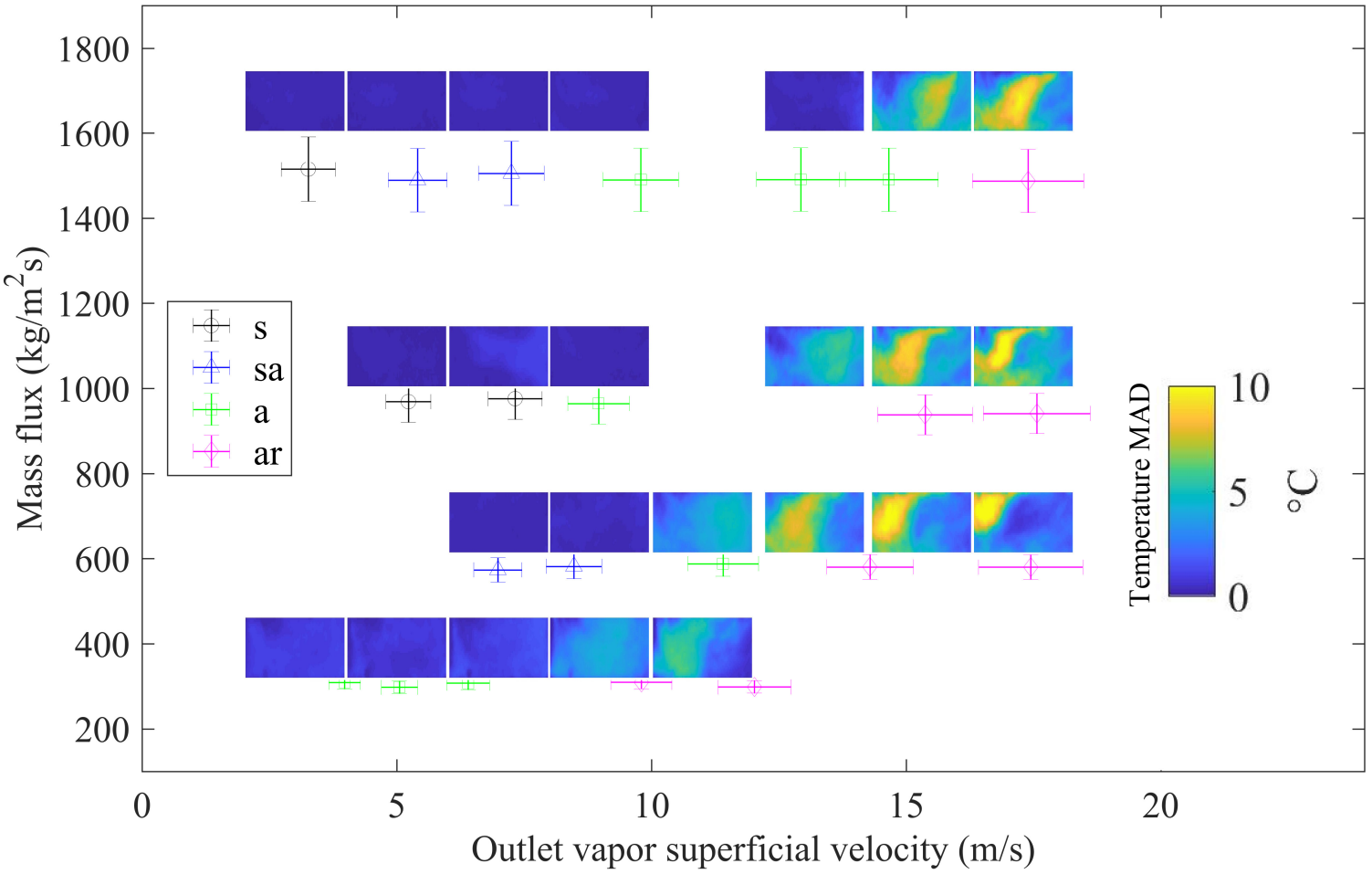

Figure 5.6: R245fa Design 2 Local temperature MAD profiles at intervals of outlet vapor superficial velocity and mass flux. Outlet flow regimes at each point are: s – slug, sa – slug-annular, a – annular, ar – annular-rivulet.

5.2.3 Global Temperature MAD

The global temperature MAD is shown in Figure 5.7. The R245fa Design 2 data show the trend of global temperature MAD decreasing after peaking more clearly than R245fa Design 1. This trend is evident with mass fluxes of 600, 1,000, and 1,600 kg/m^{2}s, which peak at 14 m/s, 15 m/s, and 16 m/s, respectively. The decrease in temporal temperature oscillation is due to the high consistency of dryout and lack of liquid penetration after the global temperature MAD peak. The global temperature MAD also exhibits values about 25% higher in R245fa Design 2 compared with Design 1. It can be observed that the global temperature MAD corresponds with increases in the local temperature MAD and is similarly an indicator of impending, sustained global dryout, which occurs at 10 m/s at 1,000 kg/m^{2}s.

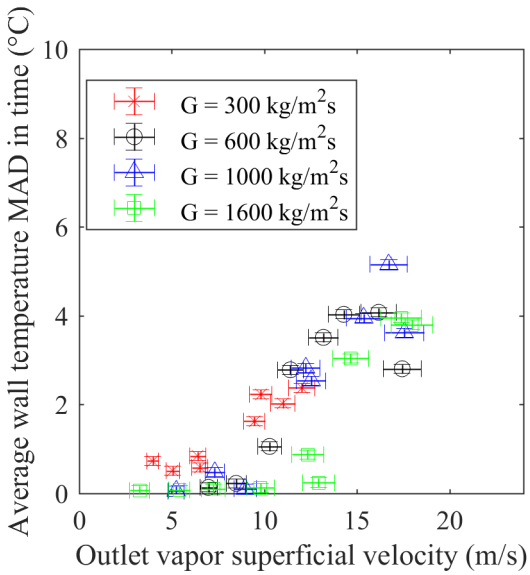

Figure 5.7: R245fa Design 2 average wall temperature MAD outlet with vapor superficial velocity at four mass fluxes

5.3 **FC-72 Manifold Design 1 (Figure 3.4)**

5.3.1 Local Temperatures

The results of the local temperatures occurring on the channel wall with FC-72 Design 1 will now be presented. The average temperatures profiles for Manifold Design 1 are determined with FC-72 in the same way as with R245fa. The local temperature profiles are plotted in Figure 5.5. As discussed previously, the range of outlet vapor qualities for FC-72 Design 1 and R245fa Design 1 are comparable for the same mass fluxes—but, also note that the vapor superficial velocities for FC-72 are higher because of the lower vapor density. The wall temperature range for FC-72 Design 1 is only 25°C to reach the same outlet qualities as R245fa, which spanned a 50°C range. The peak temperature (85°C) is the same, though, and the difference in the low temperature stems from higher saturation temperature of FC-72.

Using the mass flux of 500 kg/m^{2}s as an example, it can be seen that the wall temperature increases relatively slowly and consistently throughout the test range, from 62°C at 3 m/s to 67°C at 13 m/s. At 13 m/s, a slight temperature rise of 70°C begins to occur in the exterior corner, due to intermittent dryout. The exterior corner temperature increases to 77°C at 17 m/s and 500 kg/m^{2}s.

Annular-rivulet flow was only exhibited with FC-72 Design 1 data set at a mass flux of 300 kg/m^{2}s at 12 m/s, at which persistent dryout did occur within the exterior corner. When dryout was occurring consistently in the exterior corner, the temperature at the divergence zone remained lower, at 73°C comparted to 81°C in the exterior corner. This was again caused by liquid drops impinging on the exterior of the bend, consistent with the trend observed with R245fa Design 1, although with

significantly lower temperature gradients. The wall temperature fluctuation will next be discussed.

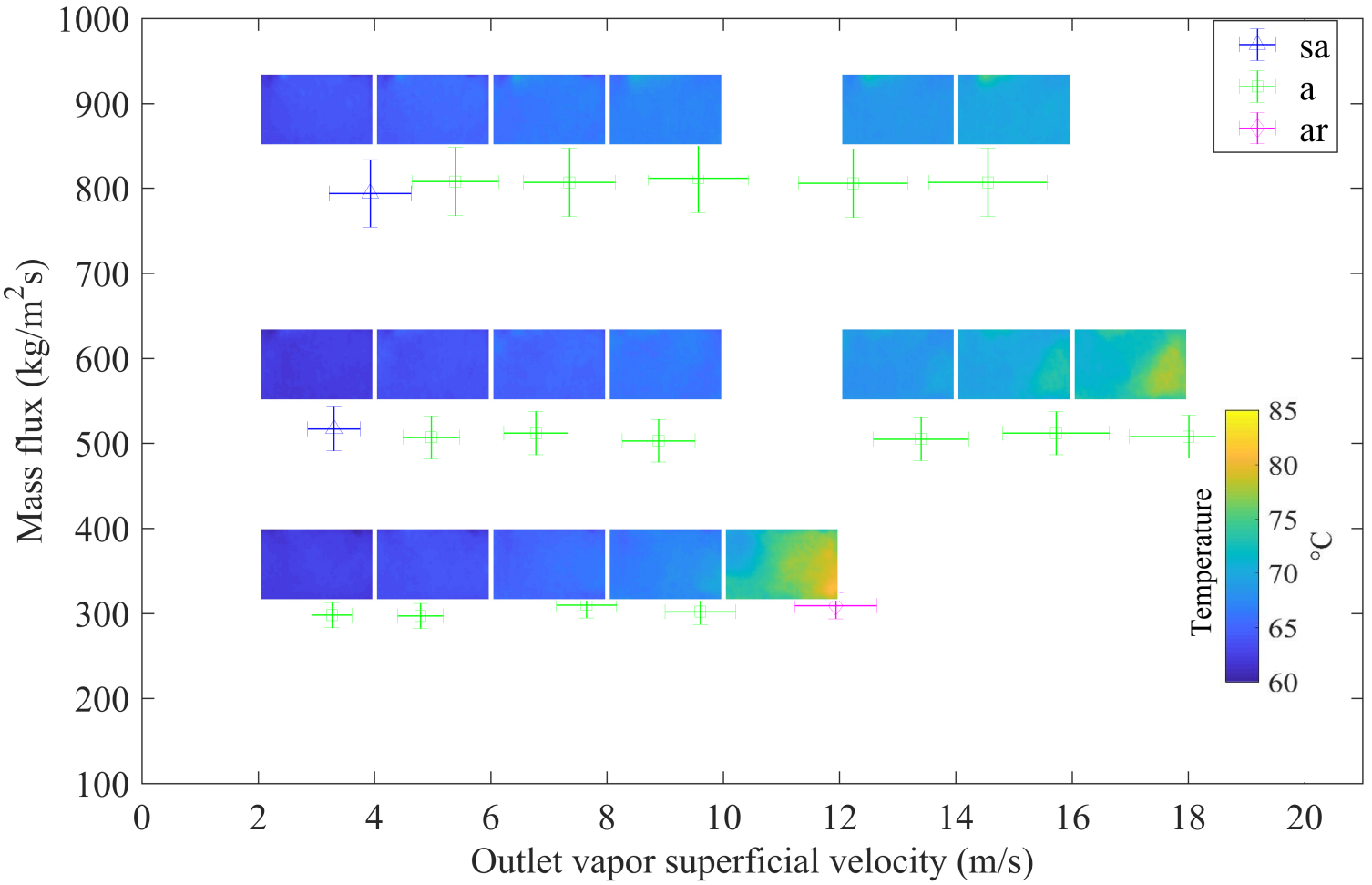

Figure 5.8: FC-72 Design 1 local temperature profiles at intervals of outlet vapor superficial velocity and mass flux. Outlet flow regimes at each point are: sa – slug-annular, a – annular, ar – annular-rivulet.

5.3.2 Local Temperature MAD

The local mean absolute deviation of the wall temperature exhibited by FC-72 Design 1 is shown in Figure 5.9. Comparing with R245fa Design 1, the temperature fluctuations are significantly lower, about 6°C for FC-72 in contrast to more than 10°C with R245fa. Using the mass flux of 500 kg/m^{2}s as an example, it can be seen that the wall temperature fluctuation remains quite low, near 0°C until 13 m/s, at which the intermittent dryout and rewetting begin to occur in the exterior corner. As the velocity increases, the area and magnitude of temperature fluctuations increase.

At the test that met the criteria for annular-rivulet flow, at a mass flux of 300 kg/m^{2}s at 12 m/s, the only instance of persistent dryout with FC-72 Design 1 occurs. Similarly with the R245fa tests, the highest MAD exists at the oscillating wetting front, with average temperature fluctuations in this region of 5°C. The inlet side of the wetting front is consistently wetted, exhibiting MAD of near 0°C. At the same time, the exterior corner region is persistently dry, exhibiting MAD of about 2.5°C at the previously discussed elevated temperature of 81°C.

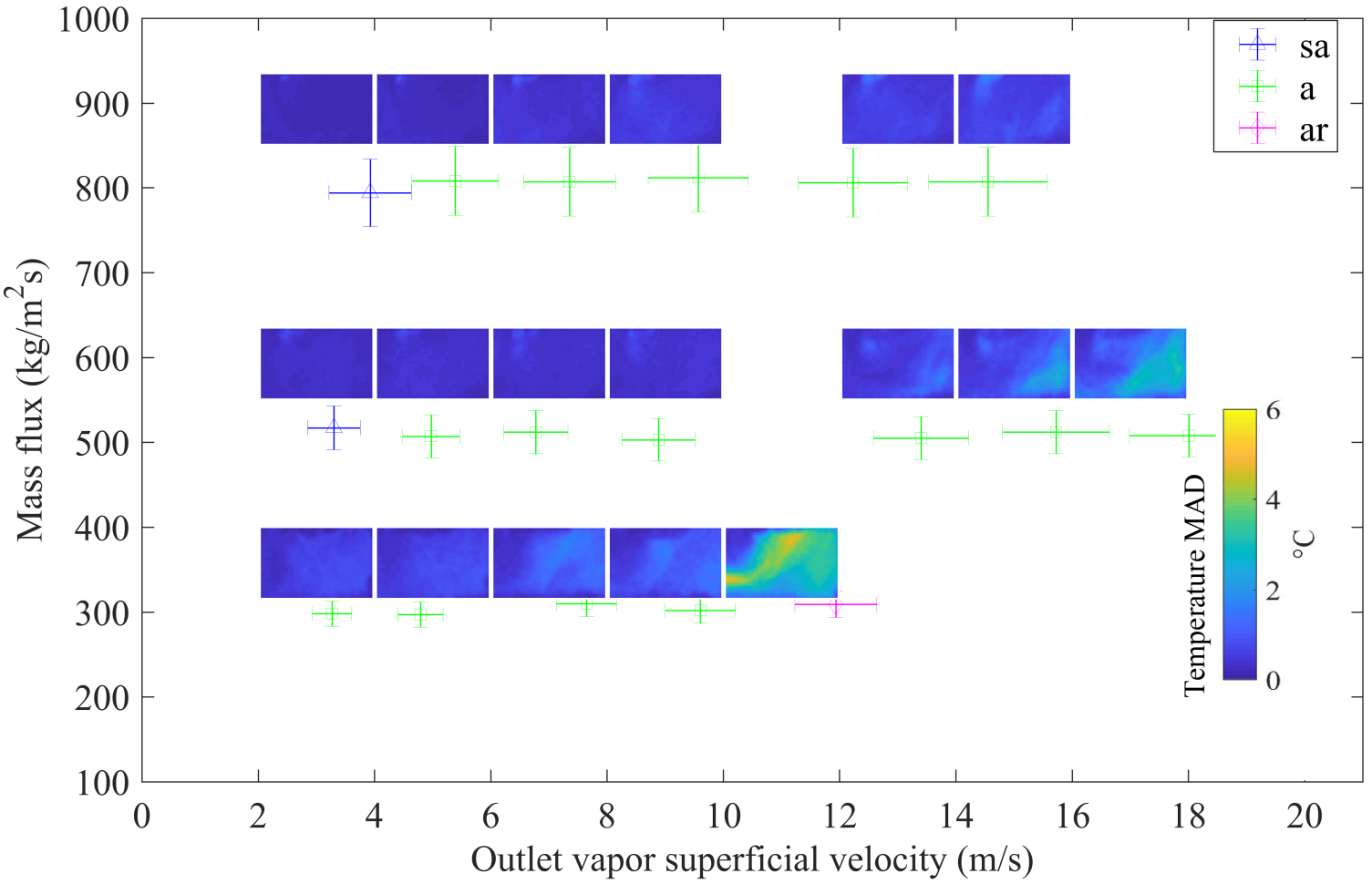

Figure 5.9: FC-72 Design 1 local temperature MAD profiles at intervals of outlet vapor superficial velocity and mass flux. Outlet flow regimes at each point are: s – slug, sa – slug-annular, a – annular, ar – annular-rivulet.

5.3.3 Global Temperature MAD

The MAD of the average wall temperature of each frame is shown in Figure 5.10. Compared with R245fa Design 1, the average wall temperature fluctuation tends to be significantly lower for the same outlet qualities. For the same mass flow rates, the increase in global temperature MAD also occurs less abruptly with FC-72. The highest global temperature MAD of 2°C occurs at 300 kg/m^{2}s at 12 m/s with FC-72, which corresponds with an outlet quality of about 50%. This global temperature MAD is half that of R245fa at 300 kg/m^{2}s and 50% outlet quality, indicating less thermal intensity in global dryout events.

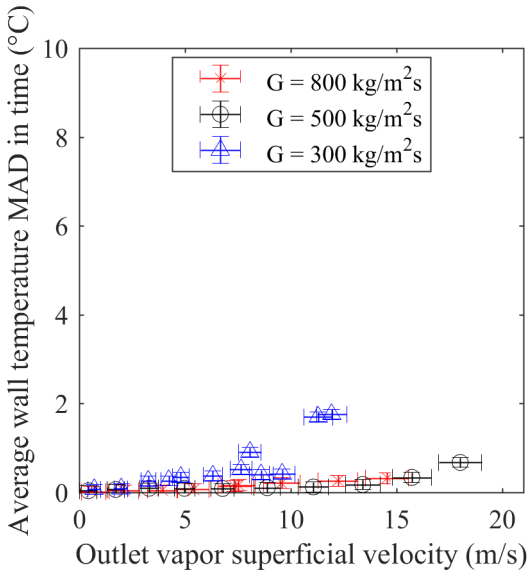

Figure 5.10: FC-72 Design 1 average wall temperature MAD outlet with vapor superficial velocity at three mass fluxes

5.4 **FC-72 Manifold Design 2 (Figure 3.5)**

5.4.1 Local Temperatures

The results of the local temperatures occurring on the channel wall with FC-72 Design 2 will now be presented. The average temperatures profiles for Manifold Design 2 are determined with FC-72 in the same way as with R245fa Design 2. The local temperature profiles are plotted in Figure 5.11. As discussed previously, the range of outlet vapor qualities for FC-72 Design 2 and R245fa Design 2 are comparable for the same mass fluxes, while the vapor superficial velocities for FC-72 are higher because of the lower vapor density. The wall temperature range for FC-72 Design 2 is, again, half that of R245fa with the same manifold.

Using the mass flux of 1,000 kg/m^{2}s as an example, it can be seen that the wall temperature increases relatively slowly from 62°C to 70°C from 5 m/s to 22 m/s. In this velocity range, the wall temperature also varies by at most 3°C across the wall in each test. At 27 m/s, the exterior corner temperature rises significantly, to 85°C while the inlet temperature remains 72°C. For the comparable peak quality, about 35%, at 1,000 kg/m^{2}s as R245fa with the same manifold design, the highest velocity test exhibits wavy annular with intermittent dryout, in contrast to persistent dryout with annular-rivulet flow.

When dryout was occurring consistently in the exterior corner, the temperature at the divergence zone, again, remained low, near 75°C. This was again caused by liquid drops impinging on the exterior of the bend, consistent with the trend observed

with R245fa Design 2, although with significantly lower temperature gradients. The wall temperature fluctuation will next be discussed.

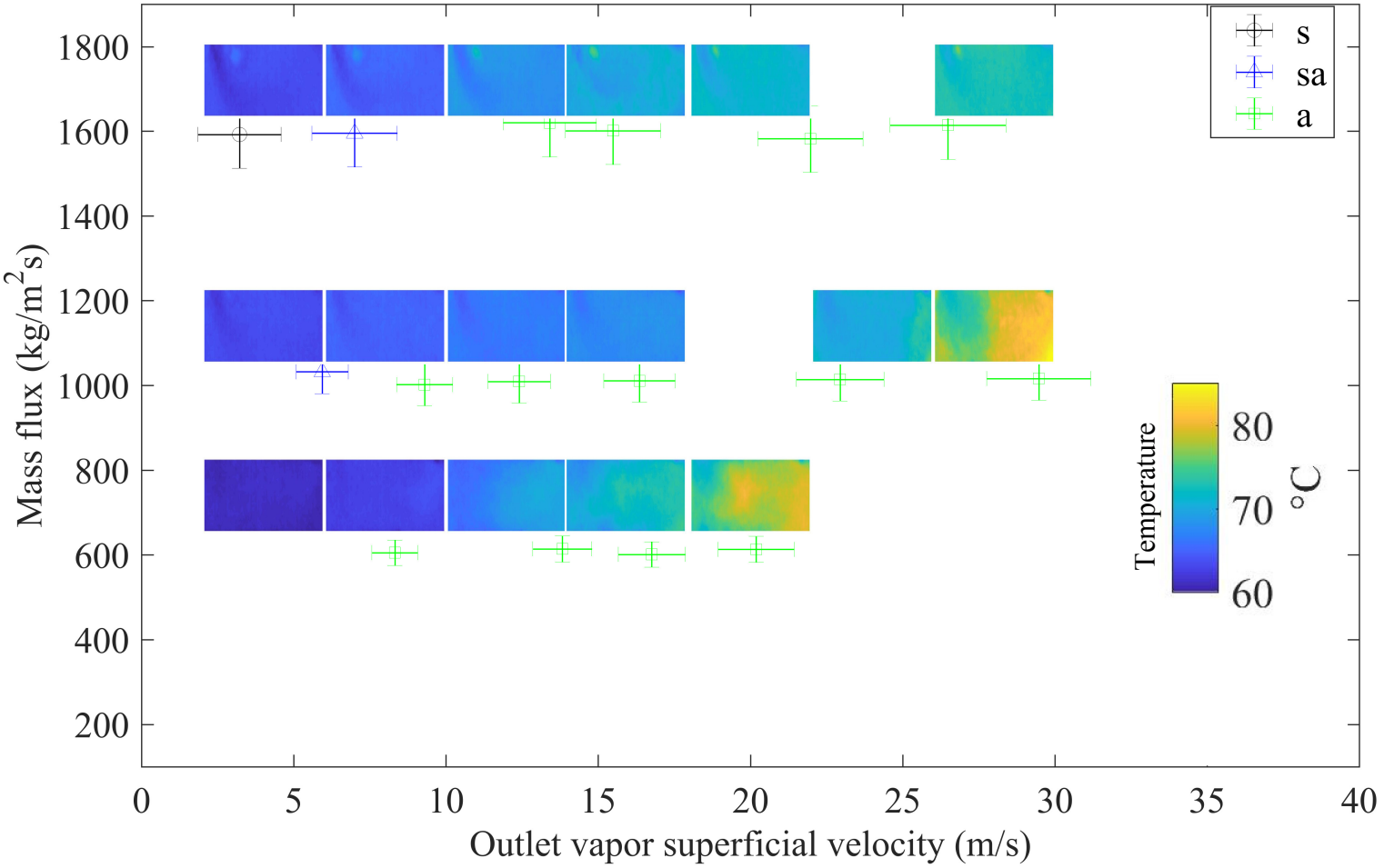

Figure 5.11: FC-72 Design 2 local temperature profiles at intervals of outlet vapor superficial velocity and mass flux. Outlet flow regimes at each point are: s – slug, sa – slug-annular, a – annular.

5.4.2 Local Temperature MAD

The local mean absolute deviation of the wall temperature exhibited by FC-72 Design 2 is shown in Figure 5.12. Comparing with the R245fa tests, the temperature fluctuations are, again, significantly lower. Using the mass flux of 1,000 kg/m^{2}s as an example, it can be seen that the wall temperature fluctuation remains below about 2°C until 27 m/s, at which the intermittent dryout and rewetting become apparent in the exterior corner. Similarly to the previous tests, the highest MAD (5°C or more) exists at the oscillating wetting front with similar character to that in R245fa Design 1. At the highest mass flux of 1,600 kg/m^{2}s, temperature fluctuations of 1.5°C occur at the interior of the bend, due to dryout and rewetting of the large, stagnant slug in that region. Temperature fluctuations of similar magnitude are also visible near the divergence zone due to the lateral oscillation in the inlet jet.

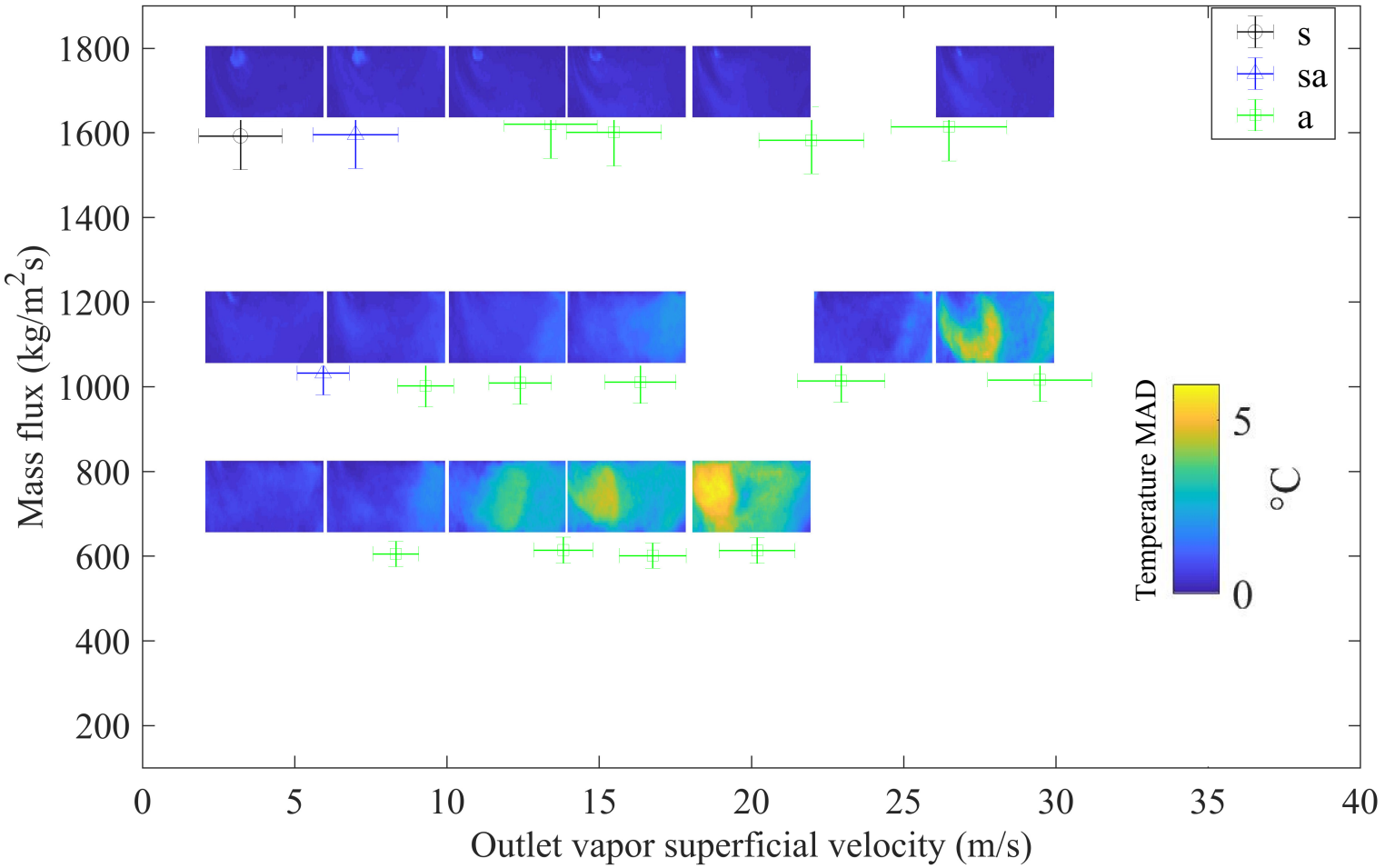

Figure 5.12: FC-72 Design 2 local temperature MAD profiles at intervals of outlet vapor superficial velocity and mass flux. Outlet flow regimes at each point are: s – slug, sa – slug-annular, a – annular.

5.4.3 Global Temperature MAD

The MAD of the average wall temperature of each frame is shown in Figure 5.13. Compared with FC-72 Design 1, the global temperature fluctuation is higher, but still lower than the values observed in both R245fa manifold designs. For the same mass flow rates, the increase in global temperature MAD continues to occur less abruptly with FC-72 for both manifold designs, compared with R245fa. The vapor superficial velocity at which the global temperature MAD begins to consistently increase is comparable to that of FC-72 Design 1, indicating that intermitted dryout is occurring at lower qualities with Design 2. The peak global temperature MAD at each mass flux is, again, about half that of R245fa Design 2 at comparable mass fluxes and outlet qualities, indicating less thermal intensity in global dryout events.

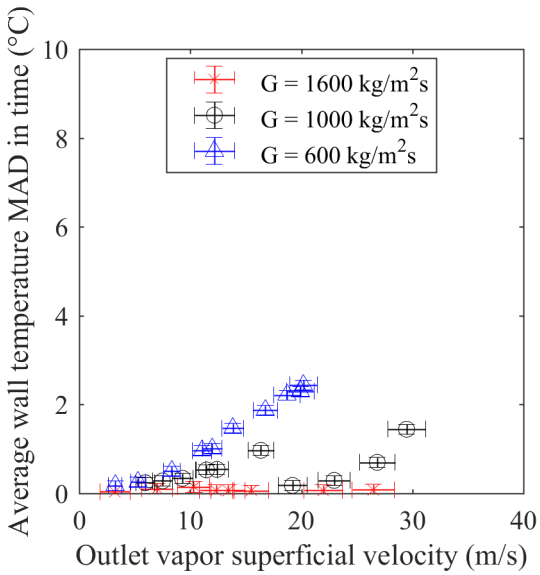

Figure 5.13: FC-72 Design 2 average wall temperature MAD outlet with vapor superficial velocity at three mass fluxes

5.5 **FC-72 Manifold Design 3 (Figure 3.6)**

5.5.1 Local Temperatures

The results of the local temperatures occurring on the channel wall with FC-72 Design 3 will now be presented. The average temperatures profiles for Manifold Design 3 are determined in the same way as Design 1. The local temperature profiles are plotted in Figure 5.14.

Using the mass flux of 500 kg/m^{2}s as an example, it can be seen that the exterior corner temperature begins to rise above the inlet temperature, from 66°C at 5 m/s to over 70°C at 7 m/s. The exterior corner temperature exceeds 80°C by 13 m/s. With the short manifold design, intermittent dryout begins at lower quality than either of the other manifold designs, with Design 3 exhibiting intermittent dryout at 15% quality in contrast to 25% and 35% quality for Design 2 and Design 1, respectively.

Because of the wide manifold, the inlet jet has significantly lower velocity, which causes the wetting front to form more horizontally than either of the longer manifold designs. The test at 300 kg/m^{2}s at 12 m/s exhibited annular-rivulet flow, along with a nearly horizontal wetting front. Much of the flow bypassed the heated area of the channel with this short manifold design, resulting in exterior corner temperatures in excess of 85°C.

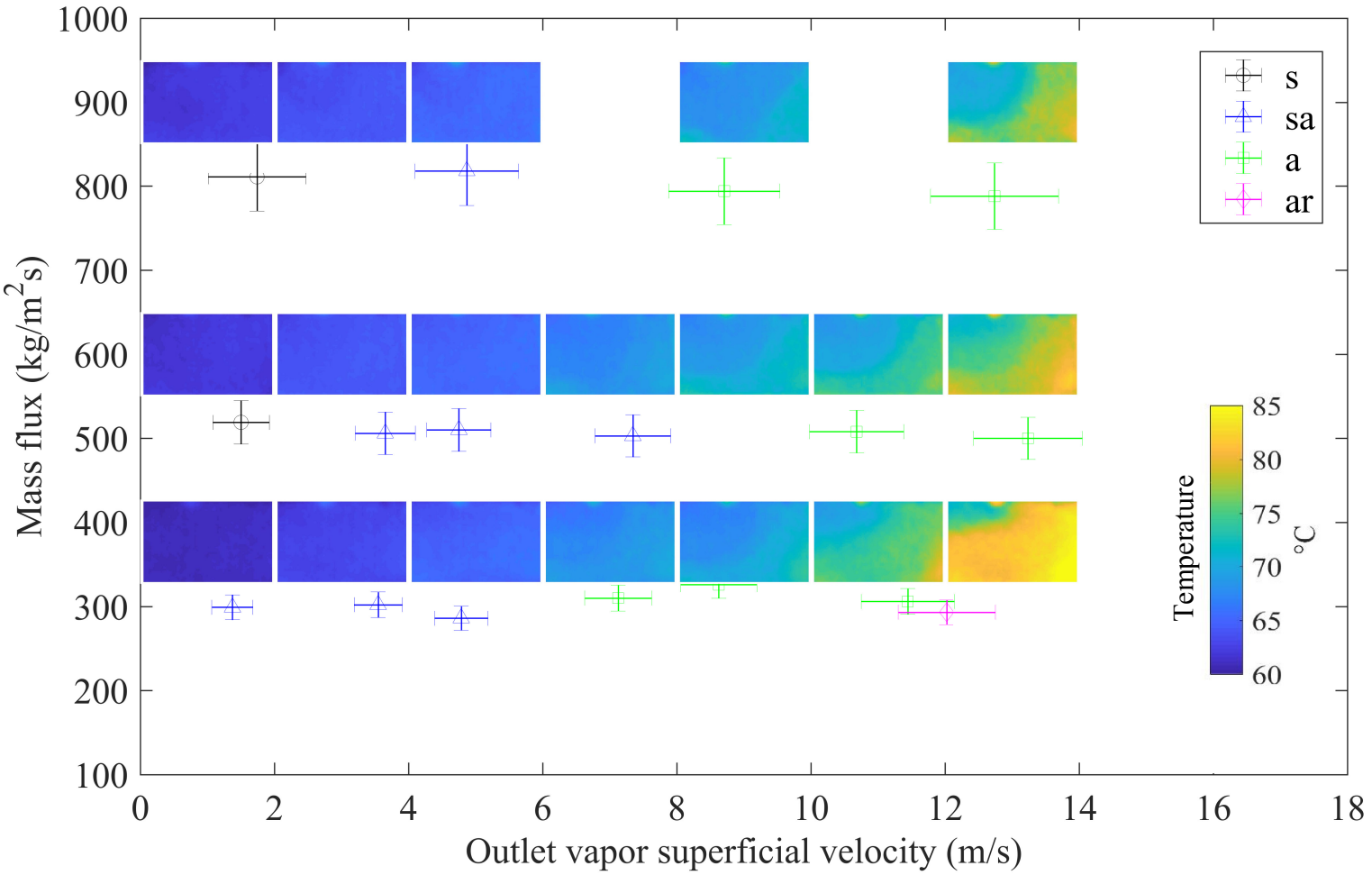

Figure 5.14: FC-72 Design 3 local temperature profiles at intervals of outlet vapor superficial velocity and mass flux. Outlet flow regimes at each point are: s – slug, sa – slug-annular, a – annular, ar – annular-rivulet

5.5.2 Local Temperature MAD

The local mean absolute deviation of the wall temperature is shown in Figure 5.15. The mass flux of 500 kg/m^{2}s used as an example, shows that FC-72 Design 3 takes on a higher MAD than FC-72 Design 1 across a larger portion of the channel wall, and especially in the exterior corner. At the peak vapor superficial velocity of 13 m/s, the exterior corner region is persistently dry, and the lack of inlet jet penetration is shown by the horizontality of the high MAD region demarcating the oscillating wetting front. The wetting front exhibits MAD of more than 5°C, while the inlet and exterior corner regions exhibit less than 2.5°C MAD. At the highest vapor superficial velocity (12 m/s) with the lowest mass flux (300 kg/m^{2}s), annular-rivulet flow occurred and resulted in the largest MAD across the largest fraction of the channel wall, which was 4°C or more across the majority of the wall area.

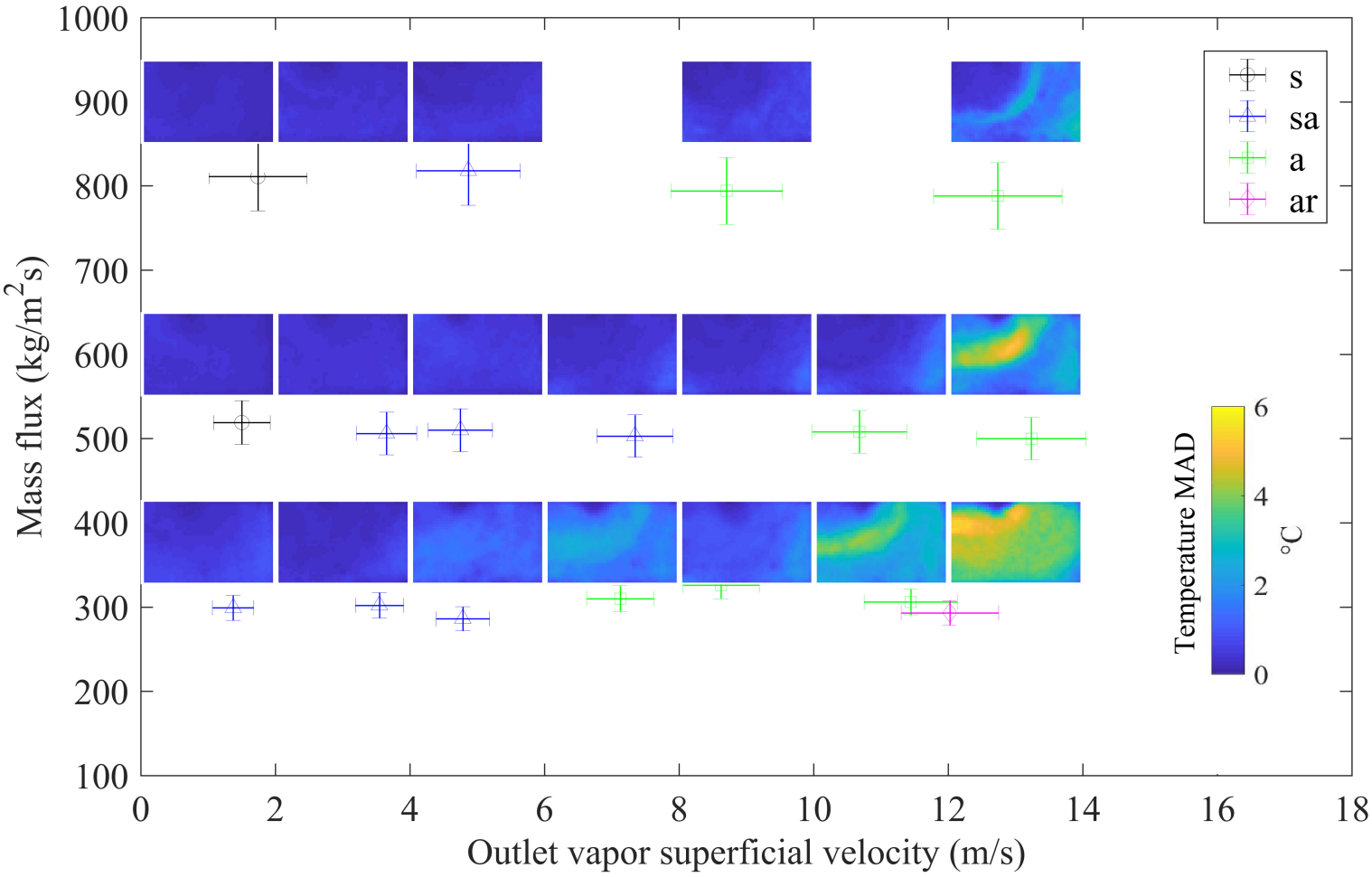

Figure 5.15: FC-72 Design 3 local temperature MAD profiles at intervals of outlet vapor superficial velocity and mass flux. Outlet flow regimes at each point are: s – slug, sa – slug-annular, a – annular, ar – annular-rivulet.

5.5.3 Global Temperature MAD

The MAD of the average wall temperature of each frame is shown in Figure 5.16. Compared with FC-72 Design 1, the average wall temperature fluctuation of FC-72 Design 2 tends to be significantly higher for the same outlet qualities, peaking at 2°C and 3°C in contrast to 1°C and 2°C with mass fluxes of 300 kg/m^{2}s and 500 kg/m^{2}s, respectively. The rapid rise in temperature fluctuations at about 12 m/s occurs more rapidly than exhibited with either of the other manifold designs with FC-72, indicating less stable thermal performance with the short manifold design.

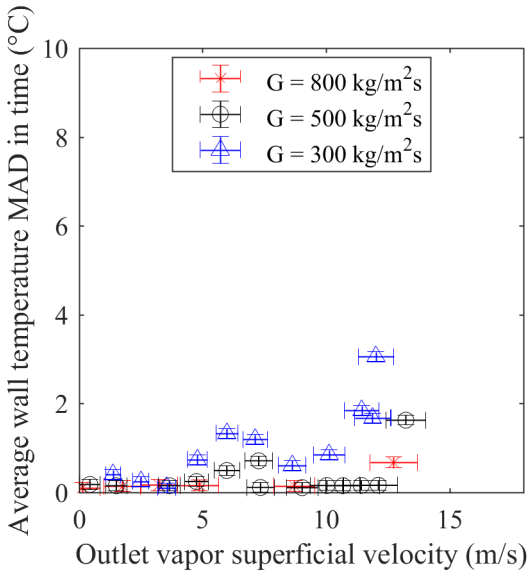

Figure 5.16: FC-72 Design 3 average wall temperature MAD outlet with vapor superficial velocity at four mass fluxes

5.6 **Summary of Wall Temperature Results**

The peak wall temperatures reached 85°C as dryout progressed in the exterior corner. Dryout first occurred in the exterior corner region because that location is furthest from the inlet, and also likely because of film inversion phenomena caused

by the centripetal acceleration of the vapor driving the liquid film toward the interior of the bend. In all cases, the wall temperature at the inlet remained low as dryout progressed. R245fa exhibited consistently higher mean absolute deviation in wall temperature during dryout (10°C) compared to FC-72 (6°C), as well as significantly higher intensity of global dryout events. For both fluids, Design 2 exhibited an earlier onset of—and higher temperature variations during—intermittent dryout and rewetting than with Design 1.

Chapter 6: Discussion – Wall Superheat, Heat Flux, and Heat Transfer Coefficients

In the following sections, heat transfer quantities calculated from the temperature and pressure data will be discussed. The quantities include pressure drop, average wall superheat, local wall superheat, average wall heat flux, and local wall heat flux. Additionally, local wall HTC's and average wall HTC's will be presented, discussed, and compared.

6.1 **Thermal Characteristics: R245fa Manifold Design 1 (Figure 3.4)**

6.1.1 Data Summary: Pressure Drop and Average Superheat with Average Heat Flux

The tests with the R245fa Manifold Design 1 are shown in Figure 6.1. It can be observed that the pressure drop trends are generally as would be expected. Firstly, the pressure drop increases monotonically with increasing quality. Secondly, the pressure drop increases proportionally with mass flux.

The wall heat flux variation with superheat also exhibit consistent trends at each mass flux. The wall heat flux increases relatively linearly, within a narrow locus across all mass fluxes, at lower heat fluxes. Then, at a certain point, for example, at 30 W/cm^2 with a mass flux of 300 kg/m^2s, the wall superheat rises drastically for a very small increase in heat flux. The sudden change in slope occurs at increasing heat flux (approximately proportional to vapor superficial velocity) with increasing mass flux.

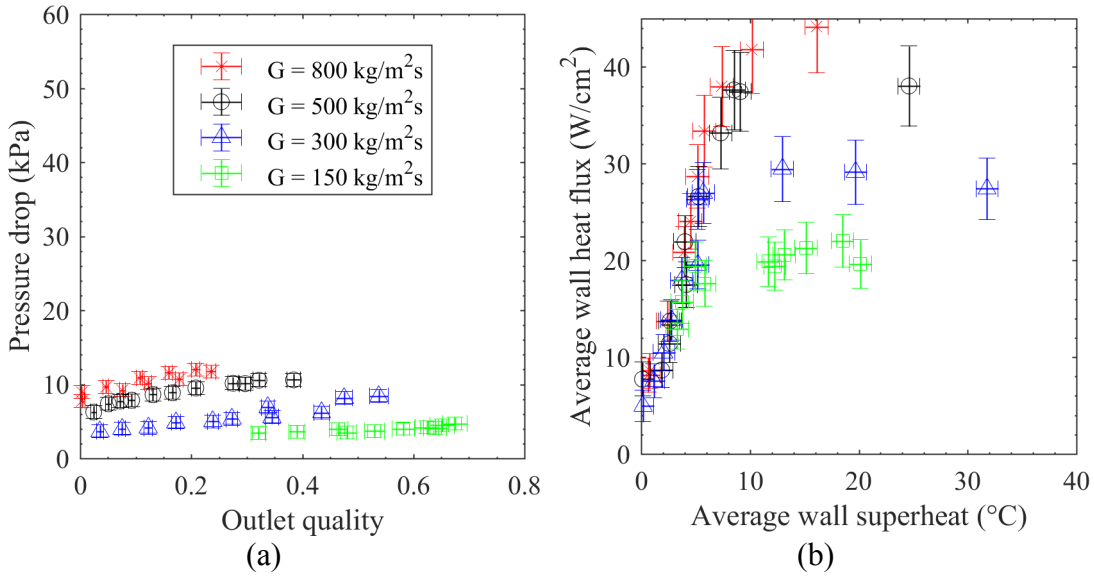

Figure 6.1: R245fa Manifold Design 1 (a) pressure drop with quality and (b) average heat flux with average superheat for four mass fluxes

6.1.2 Local Superheat

The results of the local superheat occurring on the channel wall—the data that was averaged to determine the average wall superheat in the previous section—will now be presented. The local superheat profiles are plotted in Figure 6.2, and handled in the same way as the local wall temperatures and local wall temperature MAD in the previous chapter. Because temperature and superheat are closely connected, nearly all of the discussion about local wall temperatures in the previous chapter remain true, although the local magnitudes have shifted.

As discussed in the previous section, increasing quality (vapor superficial velocity) and increasing mass flux both increase the pressure drop. Increased pressure drop corresponds with increased inlet pressure, and therefore, increased inlet saturation temperature. The increased reference temperature (saturation temperature)

causes the temperature rise at the channel inlet, observed in the previous chapter, to correspond to a far lower increase in wall superheat at the inlet with increasing velocity. The same consideration makes the liquid drop deposition on the exterior of the bend more evident.

In all cases, the local saturation temperature decreases from inlet to outlet. In cases in which persistent dryout is occurring, the wall temperature rises significantly from the inlet to outlet. The combined effect of the two temperatures changing in opposing magnitudes from inlet to outlet results in a much greater superheat change than absolute temperature change from inlet to outlet. For example, at 500 kg/m^2s and 11 m/s, the wall superheat varies from 7°C to 35°C from inlet to exterior corner, respectively.

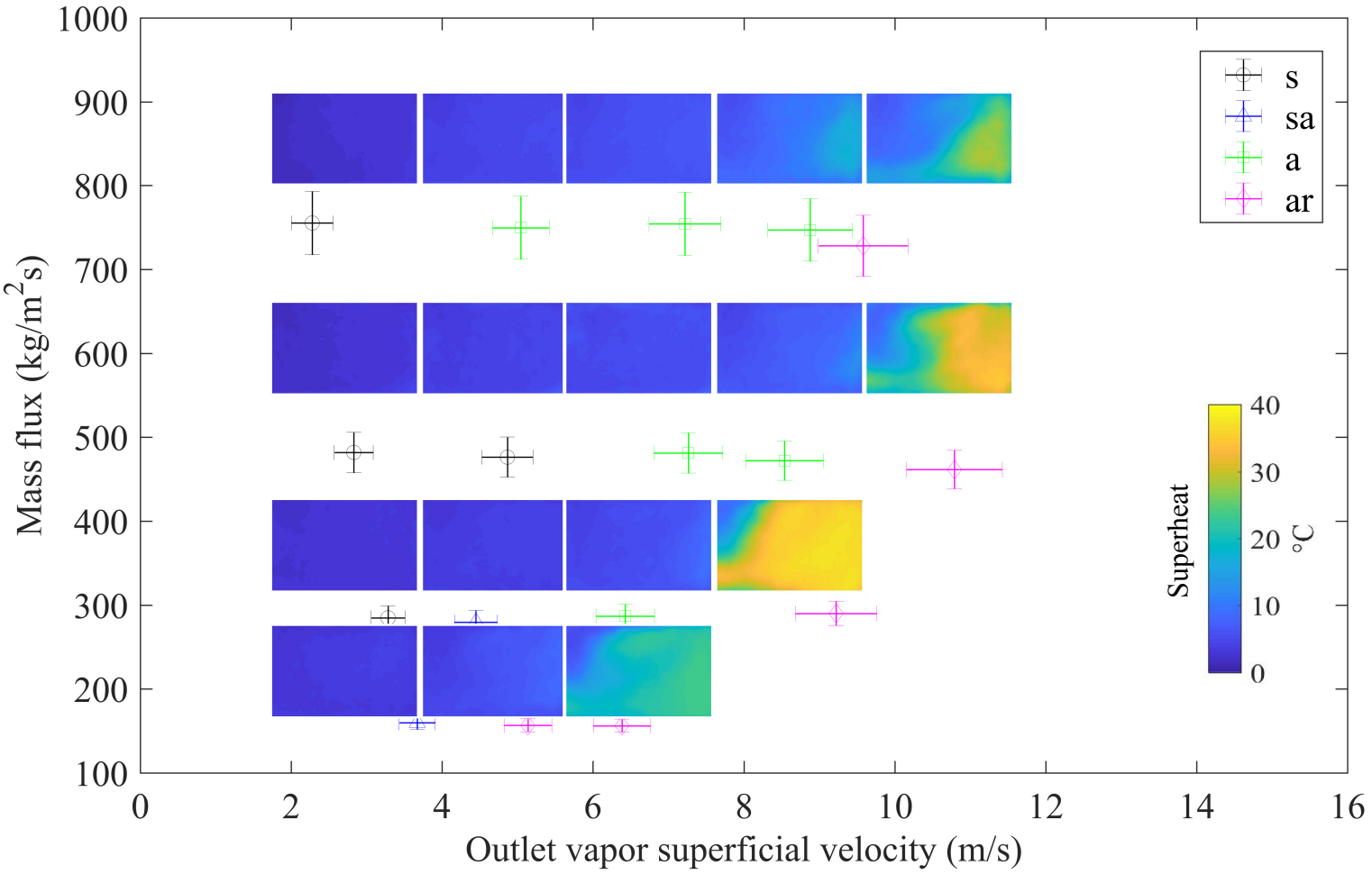

Figure 6.2: R245fa Design 1 local superheat profiles at intervals of outlet vapor superficial velocity and mass flux. Outlet flow regimes at each point are: s – slug, sa – slug-annular, a – annular, ar – annular-rivulet.

6.1.3 Local Heat Flux

The time-averaged local heat flux occurring on the channel wall will now be shown in the same way as the local superheat was in the previous section, in Figure 6.3. It can be seen that the local heat flux is in many ways converse to the local superheat—the locations of lower superheat correspond to the locations of higher heat flux.

By the definition of vapor superficial velocity, the total heat flow from the wall must increase in order to increase vapor superficial velocity. Using the mass flux of 500 kg/m^{2}s as an example, it can be observed that at the lower velocities, the heat flux increases uniformly across the channel wall with increasing vapor superficial velocity. But, as dryout begins to occur in the exterior corner, above 9 m/s, the heat flux in the exterior corner ceases to increase, while the heat flow becomes increasingly concentrated in the inlet region. The peak heat fluxes of 60 W/cm^2 occur at the inlet are approximately double that of the Zuber [51] CHF and 2.5 times that of the Ong and Thome [44] predicted CHF. The local heat transfer coefficients resulting from the local superheat profiles and local heat fluxes will next be discussed.

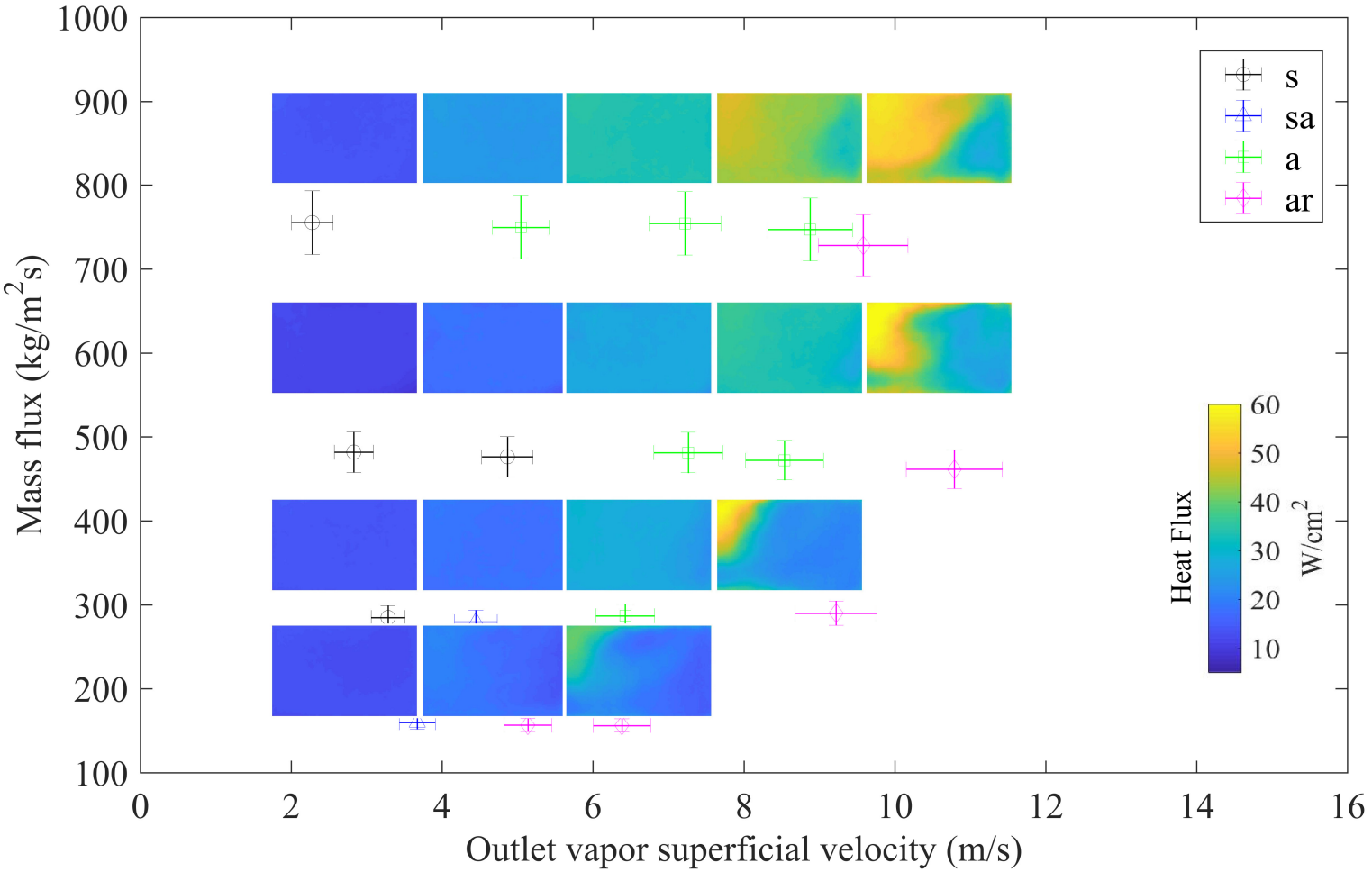

Figure 6.3: R245fa Design 1 local heat flux profiles at intervals of outlet vapor superficial velocity and mass flux. Outlet flow regimes at each point are: s – slug, sa – slug-annular, a – annular, ar – annular-rivulet.

6.1.4 Local and Average Heat Transfer Coefficients

The local HTC's resulting from the local wall superheat and wall flux are shown in Figure 6.4. It can be observed that the same trends occurring in the local superheat and heat flux occur in the HTC's, but the disparity between the wetted inlet region and the dried-out exterior corner region are significantly amplified.

Compared with either the superheat or the local heat flux, the local HTC's are far more indicative of intermittent dryout, showing the rapid decline of thermal transport efficiency beginning to occur in the exterior corner at a mass flux of 500 kg/m^2s and velocity of 9 m/s. At this condition, there is a factor of four difference between the inlet and exterior corner HTC's ranging from 90,000 W/m^2K to 30,000 W/m^2k, respectively, which is significantly greater than the differences indicated by the local superheat or heat flux alone.

Comparing the HTC profiles with the local temperature MAD of the same tests is, perhaps, the clearest indicator of the locations of consistent wetting, intermittent dryout, persistent dryout, and the oscillating wetting front in between. The highest local HTC's, near 100,000 W/m^2K, occur where there is consistent wetting. Moderate local HTC's, in the range of 50,000 W/m^2K, occur in regions of intermittent wetting, and the lowest HTC's, approaching 0 W/m^2K, occur where there is consistent dryout. The oscillating wetting front between consistently wetted and persistently dry regions produces intermediate HTC's. For vapor superficial velocities between 2 and 5 m/s, it can be seen that the cooling penetration of the inlet jet increases with increasing mass flux. As the persistently dry area on the wall increases, the average wall HTC's decline, as shown in Figure 6.5.

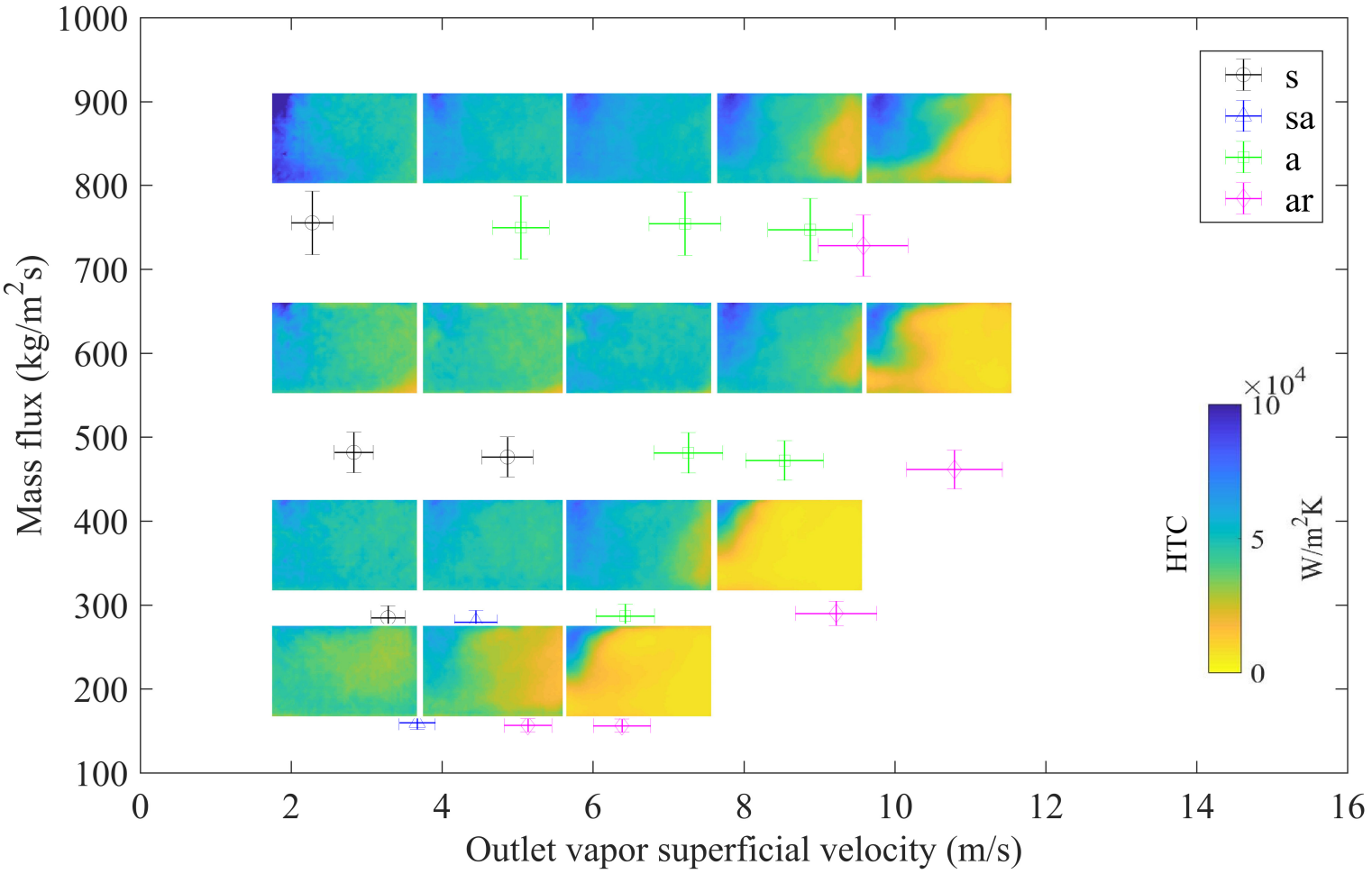

Figure 6.4: R245fa Design 1 local HTC profiles at intervals of outlet vapor superficial velocity and mass flux. Outlet flow regimes at each point are: s – slug, sa – slug-annular, a – annular, ar – annular-rivulet.

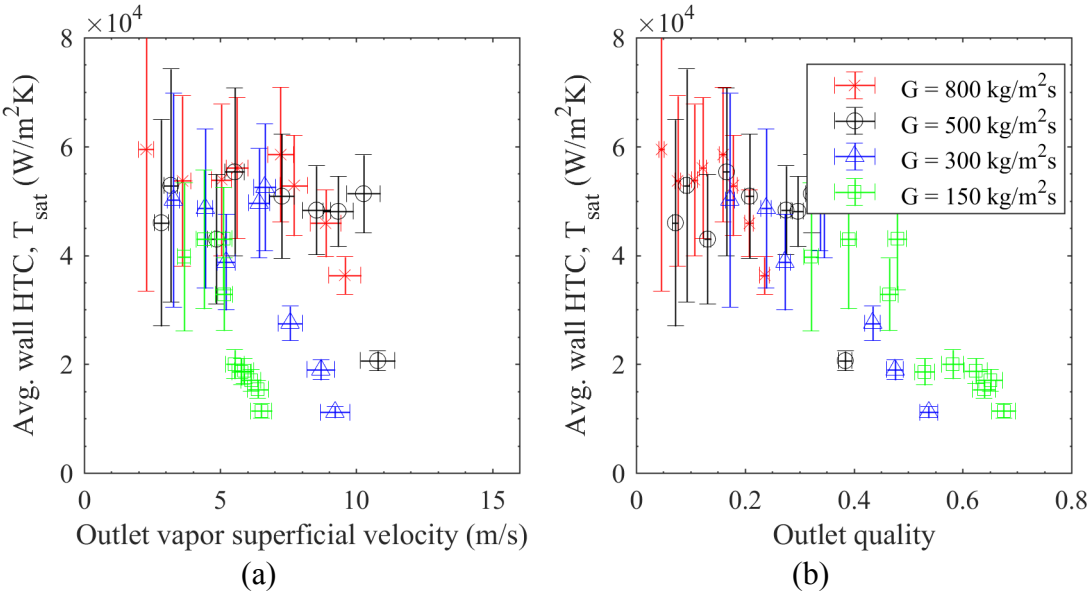

Figure 6.5: R245fa Design 1 (a) average HTC's with vapor superficial velocity and (b) average HTC's with outlet quality for four mass fluxes

The HTC uncertainty associated with low superheat is most apparent at low qualities, because of the low superheat at low quality. As shown in Figure 6.1 (b), the uncertainty of the temperature measurements can be significant compared with the magnitude of the superheat at low superheat values, thus generating a larger HTC uncertainty at lower superheats.

It can be seen from Figure 6.5 that at low velocities and qualities, the average wall HTC's remain approximately constant or slightly increasing. Then, the onset of any dryout on the channel wall decreases the average HTC, regardless of uncertainty. Comparing with Figure 6.4, it can be seen that the average HTC drops precipitously as the dryout area increases. Comparing the superficial velocities at which the peak average HTC's occur for each mass flux with the temperature MAD profiles and local HTC profiles, it can be observed that the intermittent dryout and rewetting in the

exterior corner is associated with the rapid decline in local HTC's, which decrease the average wall HTC's. As dryout spreads to become persistent locally in the exterior corner, the average HTC's continue to decline.

As shown in Figure 6.5 (b), somewhat counter intuitively, the quality at which the average wall HTC's begin to decline increases with decreasing mass flux, with an inflection point at 16% for 800 kg/m^{2}s but at 45% for 150 kg/m^{2}s. Thus, while at the low qualities, the HTC's for high mass flux are higher than for low G values, the opposite appears to be true for the higher qualities. This trend is consistent with the shift in quality at which transition from annular to annular-rivulet flow occurs**.** Furthermore, this trend is also is consistent with qualitative expectations from long, straight, circular, macroscale flow boiling literature [100].

6.2 **Thermal Characteristics: R245fa Manifold Design 2 (Figure 3.5)**

6.2.1 Data Summary: Pressure Drop and Average Superheat with Average Heat Flux

The tests for with R245fa Manifold Design 2 are shown in Figure 6.6. It can be observed that the pressure drop trends with the longer manifold design are consistent within the data set. As previously, the pressure drop increases monotonically with quality and the pressure drop increases proportionally with mass flux. Because the mass flux is doubled with Manifold Design 2, maintaining the same mass flow rate with manifold design 1, it might be expected that the pressure drop would significantly increase from Manifold Design 1 to Design 2. But, this is not the case. The pressure drop with the longer manifold is in close proximity to Design 1 at higher mass fluxes, but reaches values of 60% higher than comparable qualities and mass

flow rates in some cases—the difference between the pressure drops of Design 1 and Design 2 is largest at the lowest mass fluxes. The larger pressure drop induced by a tighter flow path radius of curvature may mitigate the pressure drop reduction generated by shorter channels from Design 1 to Design 2, resulting in more comparable pressure drop between the two designs.

The wall heat flux with superheat also exhibit a self-consistent trends, as well as consistency with Manifold Design 1. At lower heat fluxes, the wall heat flux increases relatively linearly, within a narrow locus across all mass fluxes. Then, at a certain point, the wall superheat rises drastically with a very small increase in heat flux. At a mass flux of 300 kg/m^2s, the inflection occurs at 17 W/cm^2. The sudden change in slope, again, occurs at increasing heat flux with increasing mass flux—but, at lower heat fluxes (about 25%) with Manifold Design 2 compared to Manifold Design 1. The peak average wall heat flux for each mass flux also decreased by 10-20% at comparable superheats from Design 1 to Design 2 with R245fa as the working fluid.

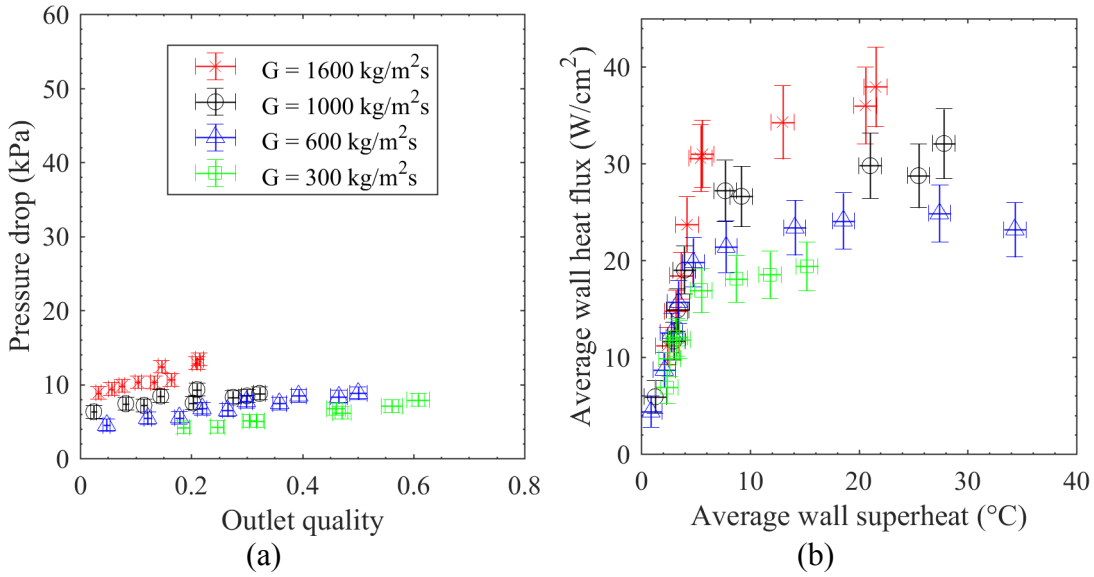

Figure 6.6: R245fa Design 2 (a) pressure drop with quality and (b) average heat flux with average superheat for four mass fluxes

6.2.2 Local Superheat

The results of the local superheat occurring on the channel will now be presented. The thermal property profiles presented in this section and in the following sections with R245fa Design 2 are scaled in the horizontal direction, as was discussed previously in the local wall temperature and temperature MAD profiles.

The local superheat profiles are plotted in Figure 6.7. At a mass flux of 1,000 kg/m^{2}s, the wall superheat increases from only 1°C to 10°C from 5 m/s to 12 m/s. Then, from 12 m/s to 15 m/s, the wall superheat in the exterior corner region increases from 15°C to 30°C, then to 40°C at 17 m/s. The wall superheat at the inlet area remains more comparable to the superheats occurring at the inlet at lower vapor superficial velocities, increasing from 1°C to 10°C from 5 to 17 m/s. Consistent with R245fa Design 1, expressing the wall superheat (in contrast to absolute temperature),

again, increases the clarity of liquid drop deposition and evaporation in the exterior of the bend.

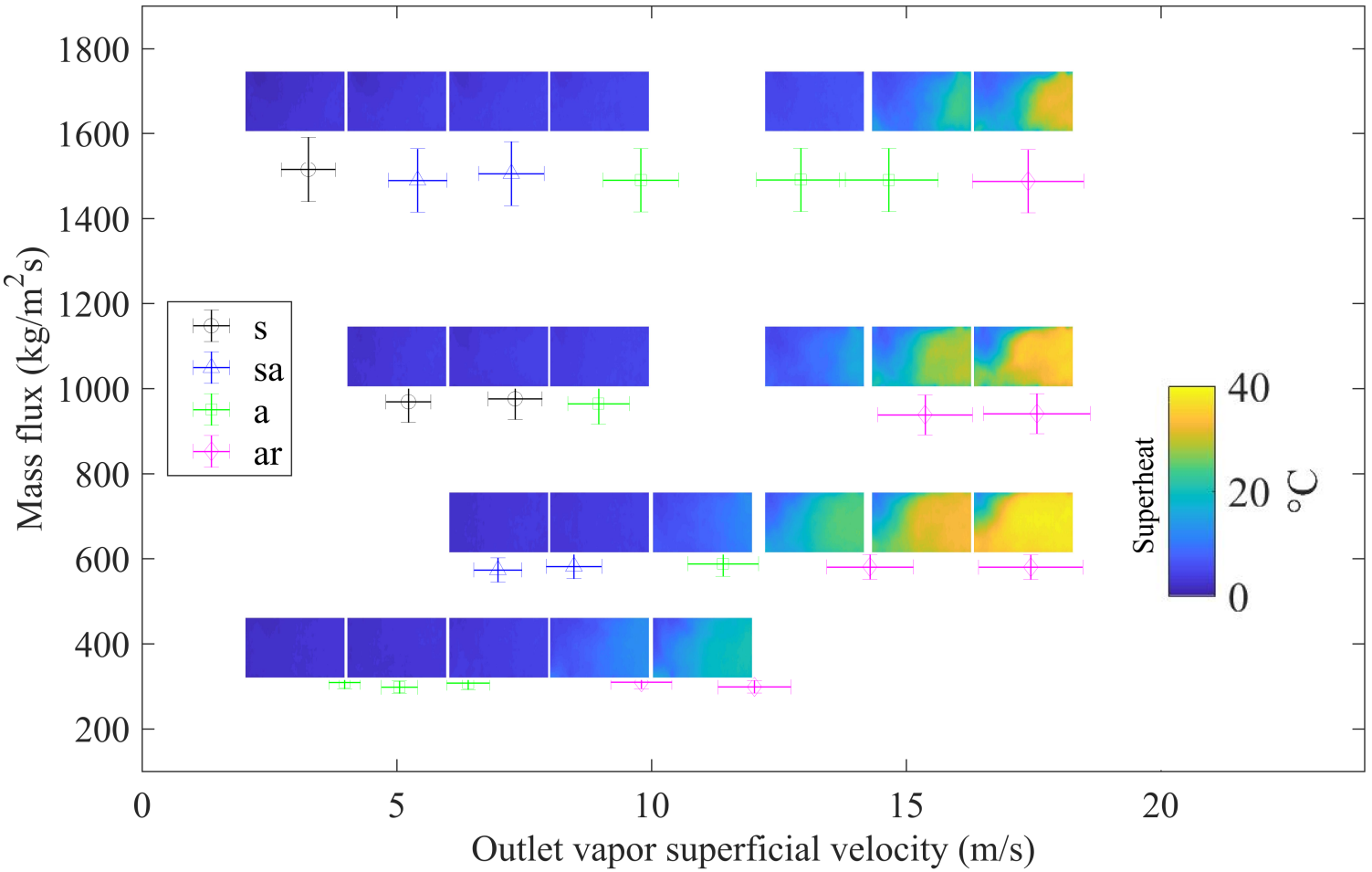

Figure 6.7: R245fa Design 2 local superheat profiles at intervals of outlet vapor superficial velocity and mass flux. Outlet flow regimes at each point are: s – slug, sa – slug-annular, a – annular, ar – annular-rivulet.

6.2.3 Local Heat Flux

The local heat flux occurring on the channel wall will now be shown in the same way as the local superheat was in the previous section, in Figure 6.8. The local heat flux results are consistent with those occurring in R245fa Design 1, in which the local heat flux profiles have nearly identical shape to the superheat profiles, but converse magnitudes. As dryout begins to occur in the exterior corner, the heat flux in the exterior corner ceases to increase, while the heat flow becomes increasingly concentrated in the inlet region. The peak heat fluxes occurring at the inlet are, again, approximately double that of the Zuber [51] CHF at 60 W/cm^2. At 1,000 kg/m^2s, the Ong and Thome [44] CHF prediction is aligned with the Zuber [51] CHF prediction of 30 W/cm^2. The local heat transfer coefficients resulting from the local superheat profiles and local heat fluxes will next be discussed.

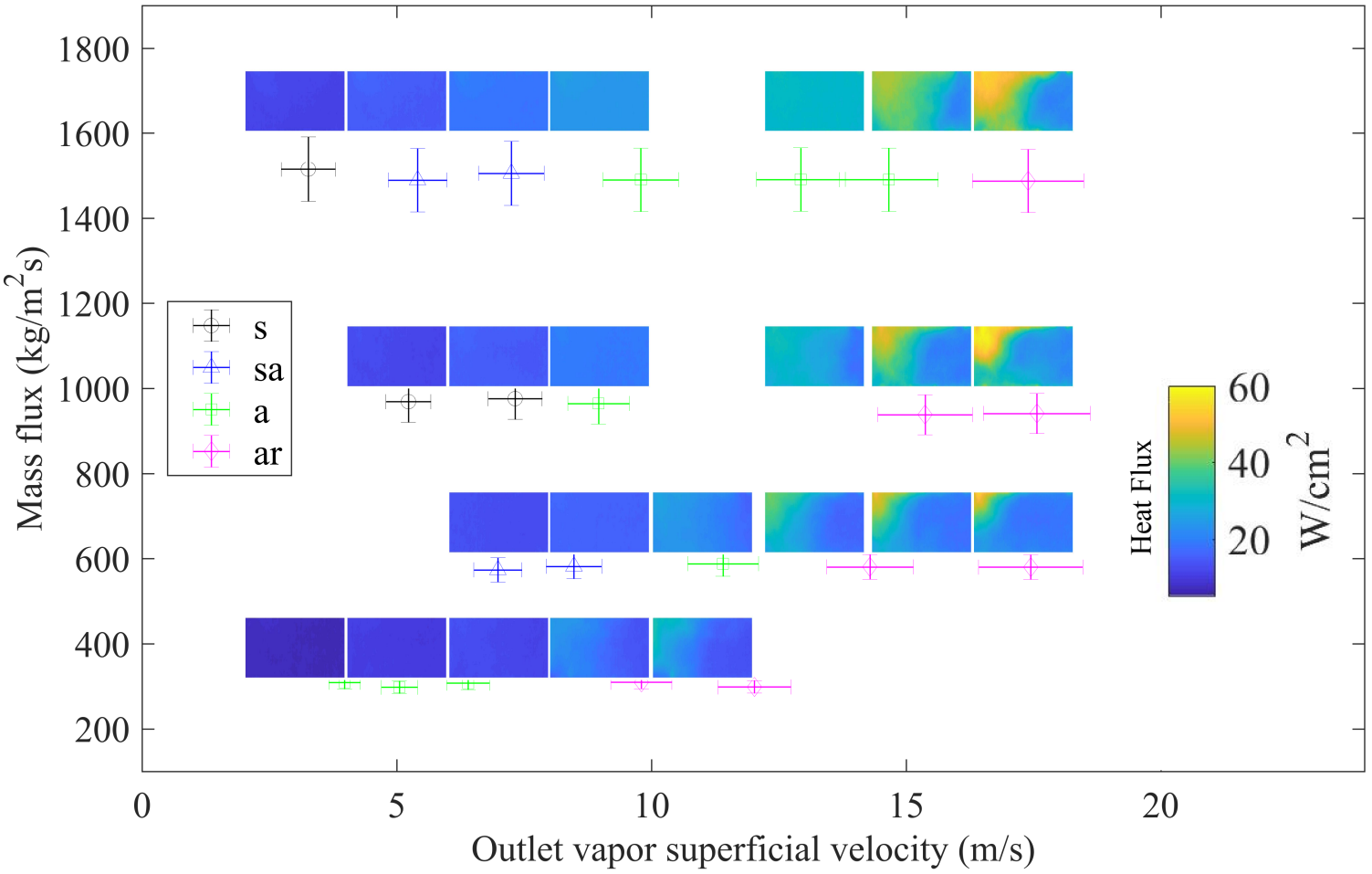

Figure 6.8: R245fa Design 2 local heat flux profiles at intervals of outlet vapor superficial velocity and mass flux. Outlet flow regimes at each point are: s – slug, sa – slug-annular, a – annular, ar – annular-rivulet.

6.2.4 Local and Average Heat Transfer Coefficients

The local HTC's resulting from the superheat and wall heat flux are shown in Figure 6.9. It can be observed that the same trends occurring in the superheat and heat flux occur in the HTC's, but the disparity between the wetted inlet region and the dried-out exterior corner region are, again, amplified. In all cases, along lines of constant vapor superficial velocity, the cooling jet penetration increases with mass flux. The high inlet HTC's, near 100,000 W/m^2K are maintained even as dryout occurs within the exterior corner region where the HTC's approach 0 W/m^2k. The highest velocities in R245fa Design 2 correspond with comparable outlet qualities to the highest velocities of R245fa Design 1, and the area of high HTC's near the inlet is decreased in Design 2. This generally indicates that average HTC's decline at slightly lower qualities than in Design 1. For example, the average wall HTC's decline at 25% with Design 2 compared with 35% with Design 1 at the same mass flow rate, which corresponds to 1,000 kg/m^2s and 500 kg/m^2s for the two designs, respectively. The average HTC trends are shown in further detail in Figure 6.10.

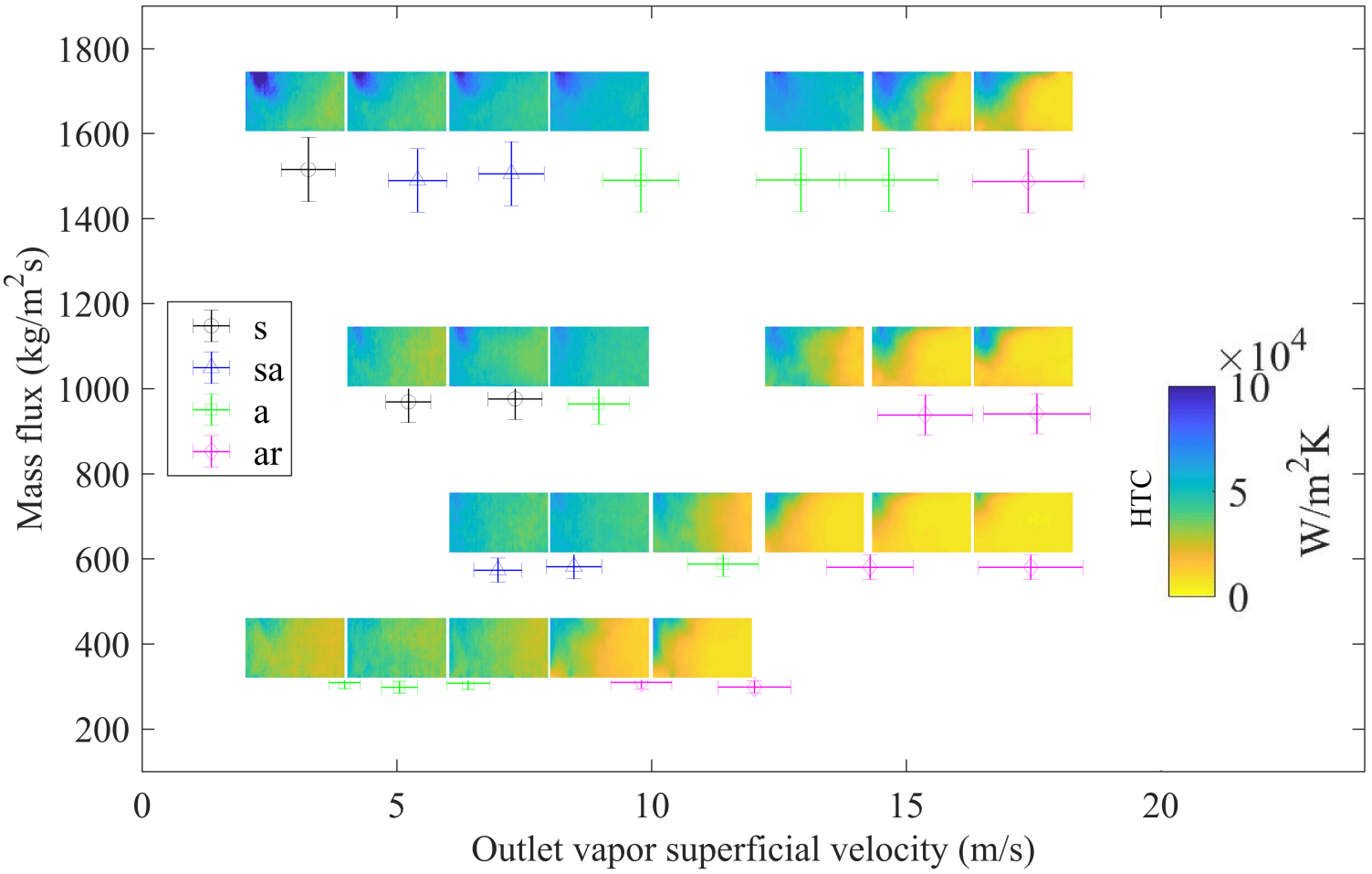

Figure 6.9: R245fa Design 2 local HTC profiles at intervals of outlet vapor superficial velocity and mass flux. Outlet flow regimes at each point are: s – slug, sa – slug-annular, a – annular, ar – annular-rivulet.

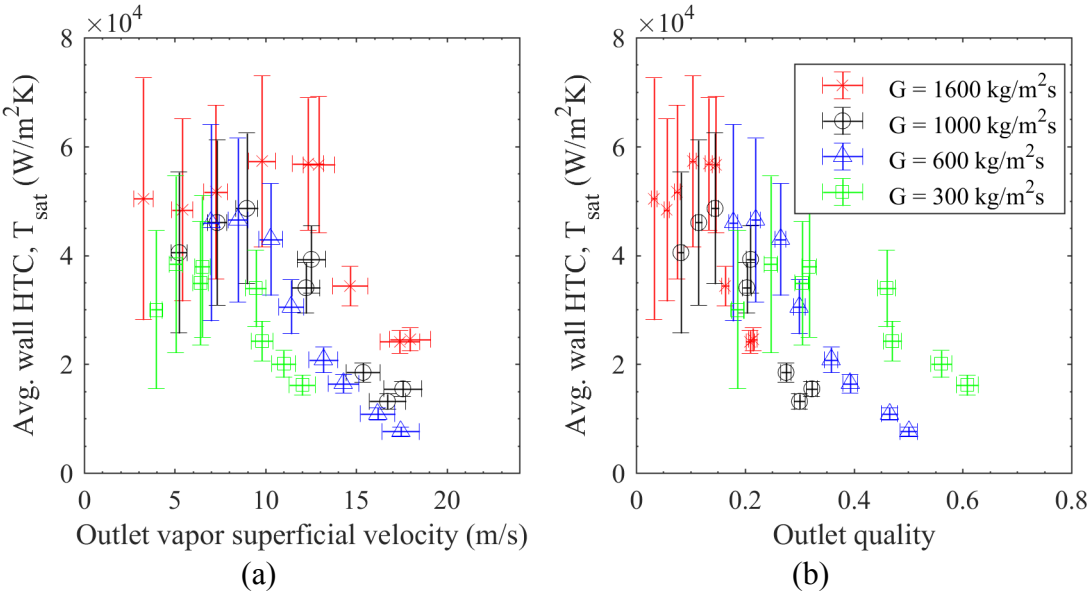

Figure 6.10: R245fa Design 2 (a) average HTC's with vapor superficial velocity and (b) average HTC's with outlet quality for four mass fluxes

It can be seen from Figure 6.10 that, starting from low velocities and qualities, there is a subtle increasing trend in HTC's until peaking. With higher mass fluxes, the peak HTC's are slightly higher, with 1,600 kg/m^{2}s peaking at 56,000 W/m^{2}K, and 300 W/m^{2}K peaking at less than 38,000 W/m^{2}K. The average wall HTC peak occurs with decreasing quality with increasing mass flux, occurring at 13% and 35-45% with 1,600 kg/m^{2}s and 300 kg/m^{2}s, respectively. This trend data set is most consistent with the HTC trends reported by Bae et al. [36], as shown in Figure 2.3 (a), with a chip-scale manifold-microchannel cooler dissipating 1 kW/cm^2.

Comparing the superficial velocities at which the peak average HTC's occur for each mass flux (7 m/s at 500 kg/m^{2}s) with the temperature MAD profiles (Figure 5.6) and local HTC profiles (Figure 6.4), it can be observed that the intermittent dryout and rewetting in the exterior corner is associated with the initial rapid decline in local

HTC's that begin the decline in global HTC's. This trend is comparable to R245fa Design 1.

The HTC inflection point is more pronounced with the longer manifold of Design 2. As dryout spreads to become persistent locally in the exterior corner, the average HTC's continue to decline. The trend of increasing quality at which peak HTC's occur is consistent with the trend in the transition from annular to annular-rivulet flow, which is also consistent with the trends of Design 1.

6.3 **Thermal Characteristics FC-72 Manifold Design 1 (Figure 3.4)**

6.3.1 Data Summary: Pressure Drop and Average Superheat with Average Heat Flux

The tests for with FC-72 Design 1 are shown in Figure 6.11. The data trends are again self-consistent: the pressure drop increases monotonically with quality proportionally with mass flux. The peak qualities at equivalent mass fluxes are comparable to those of R245fa Design 1. The pressure drop of 39 kPa at 500 kg/m^2 with FC-72 is, though, three to four times higher than R245fa Design 1. The consistently increased pressure drop is largely explained by the differences in fluid properties: the FC-72 outlet vapor density is 15% lower, the vapor viscosity is 10% higher, and the liquid viscosity is 42% higher.

The wall heat flux variation with superheat, again, exhibit self-consistent trends. The wall heat flux increases relatively linearly, within a narrow locus across all mass fluxes, at the lower heat fluxes. Then—for example—at 22 W/cm^2, the locus of 300 kg/m^{2}s tests, exhibits a drastic increase in the wall superheat with a small increase in heat flux. The sudden change in slope, again, occurs at increasing heat

flux with increasing mass flux. Compared with the R245fa tests, the slope of the superheat-heat flux curve is lower, indicating poorer performance. But, in contrast, the change in slope is less pronounced at comparable qualities, indicating more stable thermal performance.

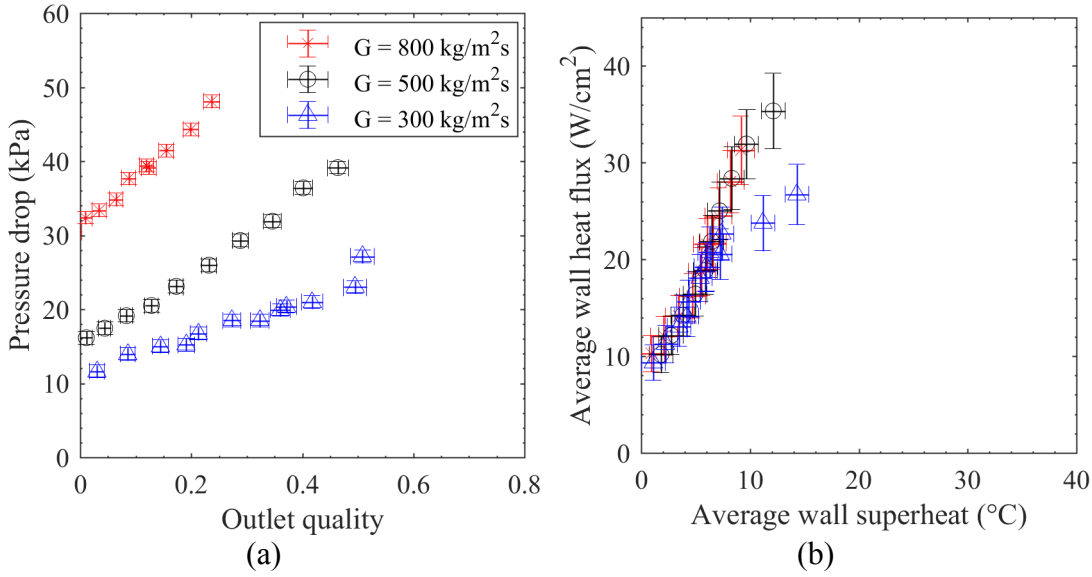

Figure 6.11: FC-72 Manifold Design 1 (a) pressure drop with quality and (b) average heat flux with average superheat for four mass fluxes

6.3.2 Local Superheat

The results of the local superheat occurring on the channel wall with FC-72 Design 1 are shown in Figure 6.11. Referring to back to the local absolute temperature profiles which exhibited uniform wall temperatures until dryout occurred, it can be seen that the superheat profiles exhibit significant variation from the inlet to the outlet under all conditions. For example, at 800 kg/m^{2}s and 4 m/s, the superheat varies by nearly 10°C from inlet to outlet, in contrast to R245fa Design 1, which exhibited less than 1°C variation.

The higher pressure drop of FC-72 is the cause of the higher variation in the saturation temperature from inlet to outlet, which is the primary driver of the significantly varying superheat from inlet to outlet for all tests with vapor superficial velocity of less than 10 m/s. The variation in saturation temperature from inlet to outlet is shown in more detail in Appendix 9.3.4. The variation in saturation temperature also amplifies the evidence of dryout occurrence above 10 m/s for mass fluxes of 300 kg/m^{2}s and 500 kg/m^{2}s, which vary by more than 15°C from inlet to outlet. The peak superheat and superheat variation occurs at 300 kg/m^{2}s and 12 m/s, while the outlet flow regime is annular-rivulet.

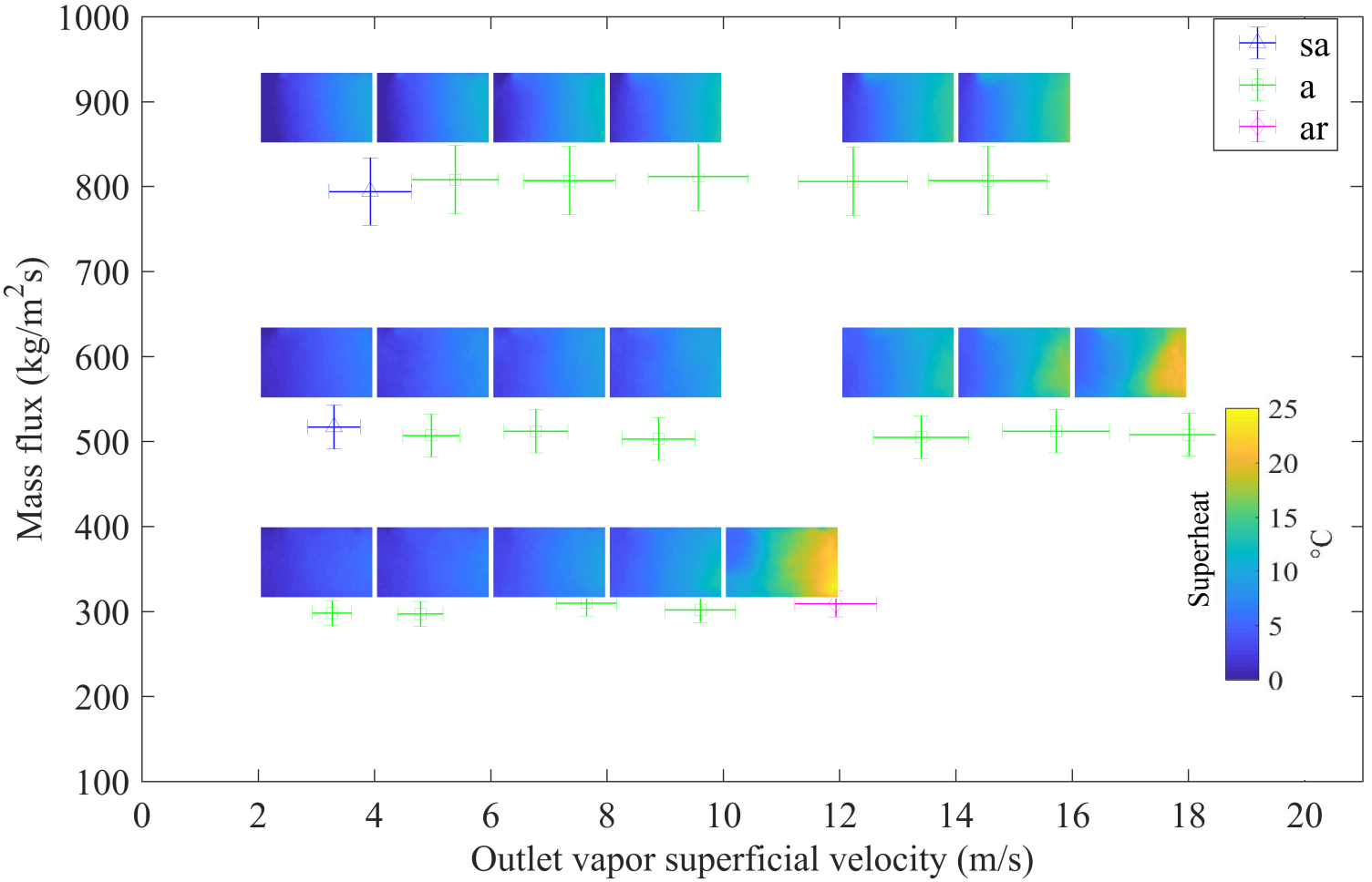

Figure 6.12: FC-72 Design 1 local superheat profiles at intervals of outlet vapor superficial velocity and mass flux. Outlet flow regimes at each point are: sa – slug-annular, a – annular, ar – annular-rivulet.

6.3.3 Local Heat Flux

The local channel wall heat flux is shown in Figure 6.13 in the same way the thermal maps have been presented previously. The trend in the local heat flux results are consistent with those occurring in the previous tests, in which the local heat flux profiles have nearly identical shape to the temperature profiles, but converse magnitudes. The peak heat fluxes produced with FC-72 are about 40% lower than those produced with R245fa.

The peak heat fluxes of 35 W/cm^2 occurring at the inlet remain approximately double that of the Zuber [51] CHF for FC-72 (about half that of R245fa), as well as double that of the Ong and Thome [44] CHF prediction. As dryout begins to occur in the exterior corner, the heat flux in the exterior corner ceases to increase, while the heat flow becomes increasingly concentrated in the inlet region. The local heat transfer coefficients resulting from the local superheat profiles and local heat fluxes will next be discussed.

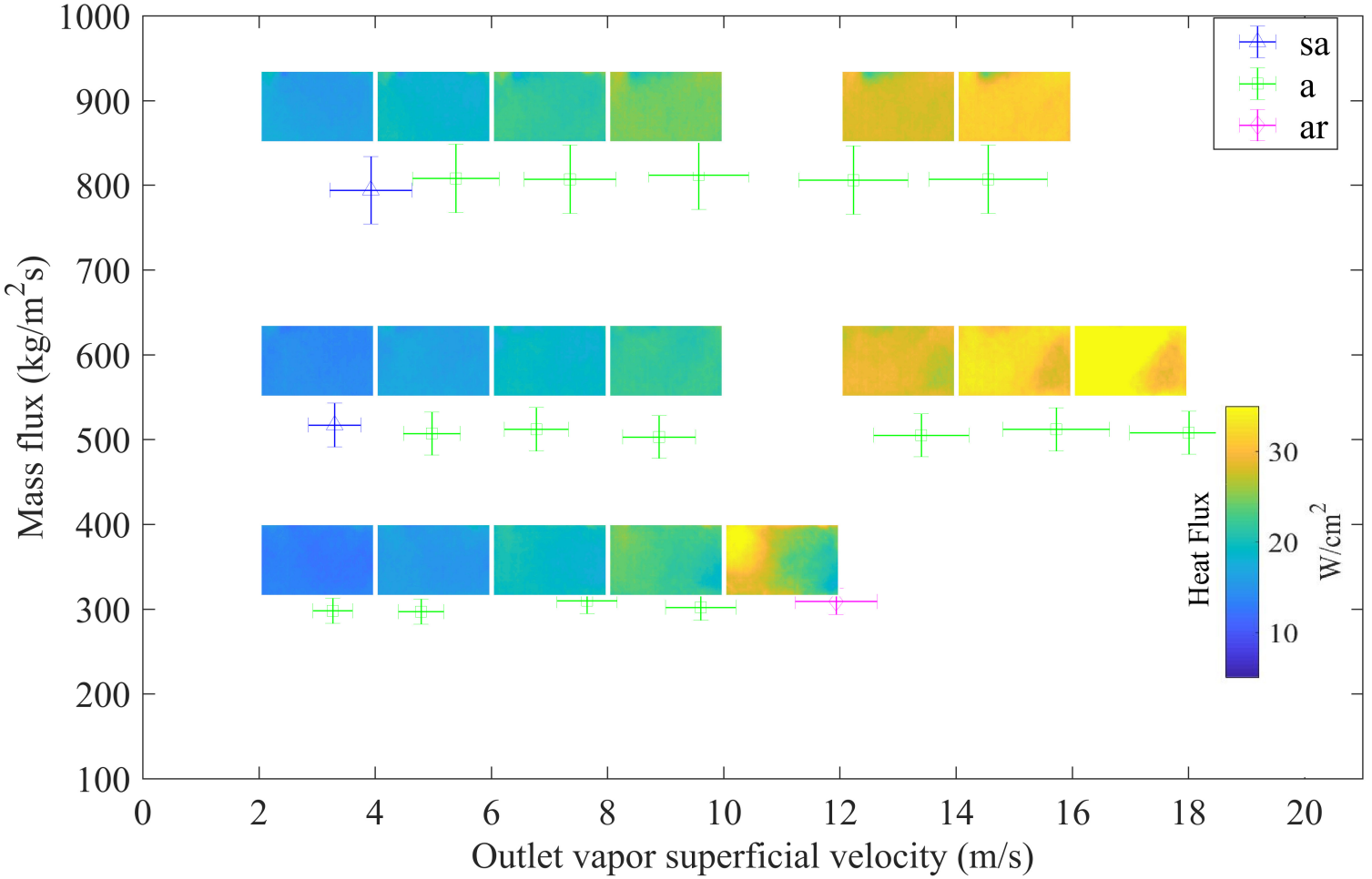

Figure 6.13: FC-72 Design 1 local heat flux profiles at intervals of outlet vapor superficial velocity and mass flux. Outlet flow regimes at each point are: sa – slug-annular, a – annular, ar – annular-rivulet.

6.3.4 Local and Average Heat Transfer Coefficients

The local HTC's resulting from the superheat and wall heat flux are shown in Figure 6.14. It can be observed that the same trends occurring in the superheat and heat flux occur in the HTC's, but the disparity between the wetted inlet region and the exterior corner region are, again, amplified. In all cases, along lines of constant vapor superficial velocity, the cooling jet penetration increases with mass flux.

Using the mass flux of 500 kg/m^{2}s as an example, it can be seen that at the lowest velocity of 3 m/s, the HTC's in the inlet region are "saturated," exceeding the maxima of the color scale in either direction, less than 0 W/m^{2}K and greater than 100,000 W/m^{2}K . As discussed in the local superheat section, the superheat at the inlet is quite low, while the calculations from the local heat flux section show that there is appreciable heat flux in that region. This generates very high HTC's. But, the temperature measurement uncertainties used to calculate both the local superheat and the heat flux result in very high HTC uncertainty in the inlet region, as shown in Appendix 9.3.7. In the same Appendix section, it can be seen that at the mass flux of 800 kg/m^{2}s, the very high HTC uncertainty at the inlet persists in all tests though the vapor superficial velocity range. It is difficult to draw conclusions about the inlet HTC's for any test in which the magnitude of local uncertainty exceeds the magnitude of the local HTC. But, referring to the R245fa results, which exhibit lower uncertainty in the inlet HTC's and extrapolating from the lower uncertainty regions in the FC-72 Design 1 HTC profiles, it can be reasonably assumed that the HTC's at the inlet are relatively high for tests in which the uncertainty is too high to strictly draw a conclusion.

Returning to 500 kg/m^{2}s as an example, it can be seen that at 5 m/s, the HTC's are not completely saturated at the inlet, and the uncertainty has also decreased. From this test, a key difference between R245fa and FC-72 can be observed—the HTC's vary significantly from the inlet to the outlet even at low qualities, from nearly 100,000 W/m^{2}K to less than 10,000 W/m^{2}K. This trend is in part due to the early transition to annular flow exhibited by FC-72 at lower mass fluxes, as well as the significantly higher variation in vapor density from inlet to outlet than that exhibited by R245fa.

The strong variation in HTC's from inlet to outlet make the transition to intermittent and persistent dryout less evident, in contrast to the R245fa tests. Comparing with the local temperature MAD, the areas of intermittent and persistent dryout are apparent, but the decline in HTC's in this area is far more subtle with FC-72 because the values were lower before dryout began. From this, the data suggest that the higher pressure drop exhibited by FC-72 causes the inlet region to be the primary driver of high HTC's and the total thermal transport efficiency of the channel wall. The averaged HTC's on the channel wall are shown in Figure 6.15.

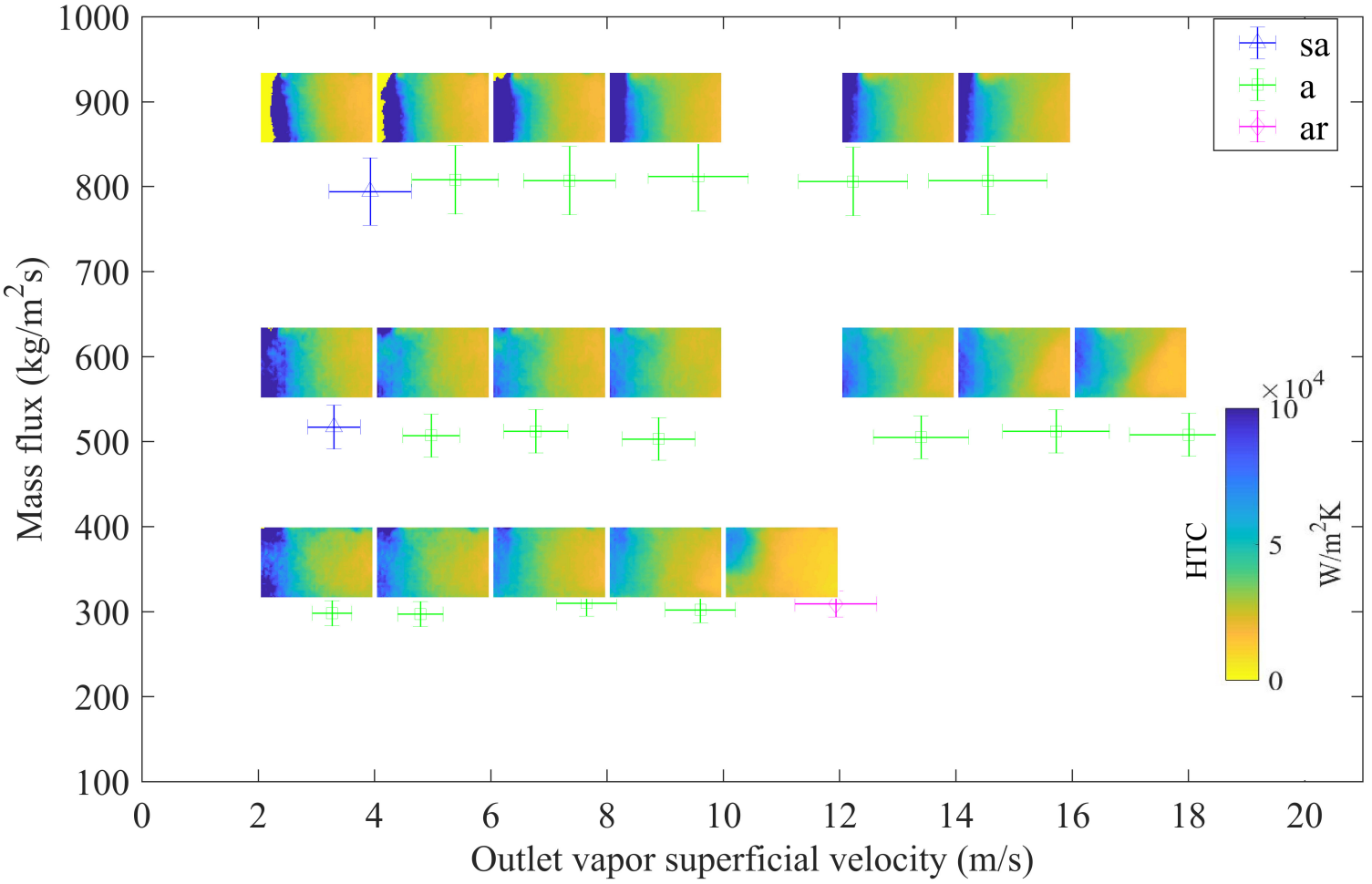

Figure 6.14: FC-72 Design 1 local HTC profiles at intervals of outlet vapor superficial velocity and mass flux. Outlet flow regimes at each point are: sa – slug-annular, a – annular, ar – annular-rivulet.

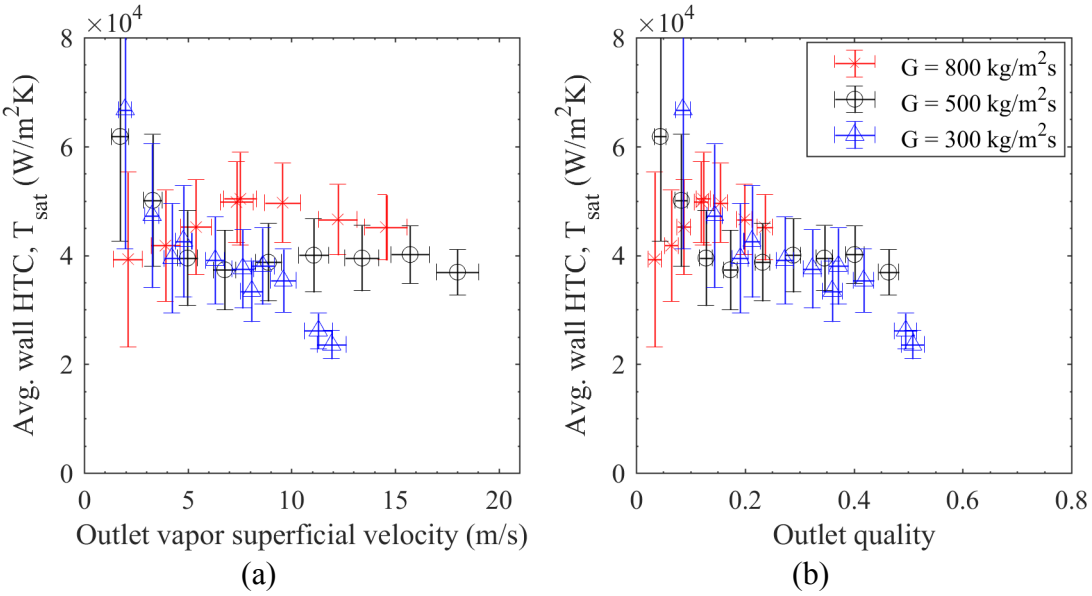

Figure 6.15: FC-72 Manifold Design 1 (a) average HTC's with vapor superficial velocity and (b) average HTC's with outlet quality for four mass fluxes

The average HTC's with FC-72 Design 1 tend to be much flatter than R245fa Design 1 and Design 2 for the same outlet quality range and mass fluxes, with typical values of 40,000 W/m^{2}K. Thus, from the discussion of local HTC profiles, it can be seen that the inlet HTC's are the primary driver of the HTC values, because low wall HTC's exist on the exterior corner region for the entire quality range. A drop in HTC's only becomes apparent with a mass flux of 300 kg/m^{2}s above a vapor superficial velocity of 10 m/s. Under this condition, the area of high HTC's near the inlet begins to decrease as the flow transitions to the annular-rivulet regime. The average wall HTC's tend to be 10-20% less than those exhibited by R245fa Design 1 at lower qualities, but then remain substantially higher than the R245fa Design 1 HTC's which rapidly decline at the onset of dryout.

6.4 **Thermal Characteristics FC-72 Manifold Design 2 (Figure 3.5)**

6.4.1 Data Summary: Pressure Drop and Average Superheat with Average Heat Flux

The tests for with FC-72 Design 2 are shown in Figure 6.16. The data trends are again self-consistent: the pressure drop increases monotonically with quality proportionally with mass flux. This trend is apparent by comparing the pressure drop at 20% quality with mass fluxes of 600 kg/m^{2}s, 1,000 kg/m^{2}s, and 1,600 kg/m^{2}s, respectively, which increase from 12 kPa to 30 kPa to 45 kPa at. The peak qualities at equivalent mass fluxes are fairly comparable to those of R245fa Design 2, although the 1,000 kg/m^{2}s data set extends to slightly higher quality (38% quality) while the 600 kg/m^{2}s reach slightly lower peak quality, at only 43%. The pressure drop generated with FC-72 Design 2 is the highest of all the data sets, consistently generating pressure drops 2-4 times higher than that of R245fa with the same manifold design, with a peak pressure drop of 49 kPa.

The average wall heat flux with superheat, exhibit self-consistent trends and trends that are consistent with the previous data sets. The wall heat flux increases relatively linearly, within a narrow locus across all mass fluxes, at the lower heat fluxes. Then, at a certain point, the wall temperature (superheat) rises drastically with a very small increase in heat flux. The sudden change in slope, again, occurs at increasing heat flux with increasing mass flux. FC-72 Design 2 exhibits a more pronounced inflection point than Design 1, which is consistent with the changes in superheat-heat flux profiles with R245fa between Design 1 and Design 2. But, in contrast, the lower slope (poorer performance) at low superheats results in a less

drastic change in slope indicating less change in thermal performance after the inflection point. The peak heat fluxes exhibited with FC-72 Design 2 are 15-20% lower than that of Design 1.

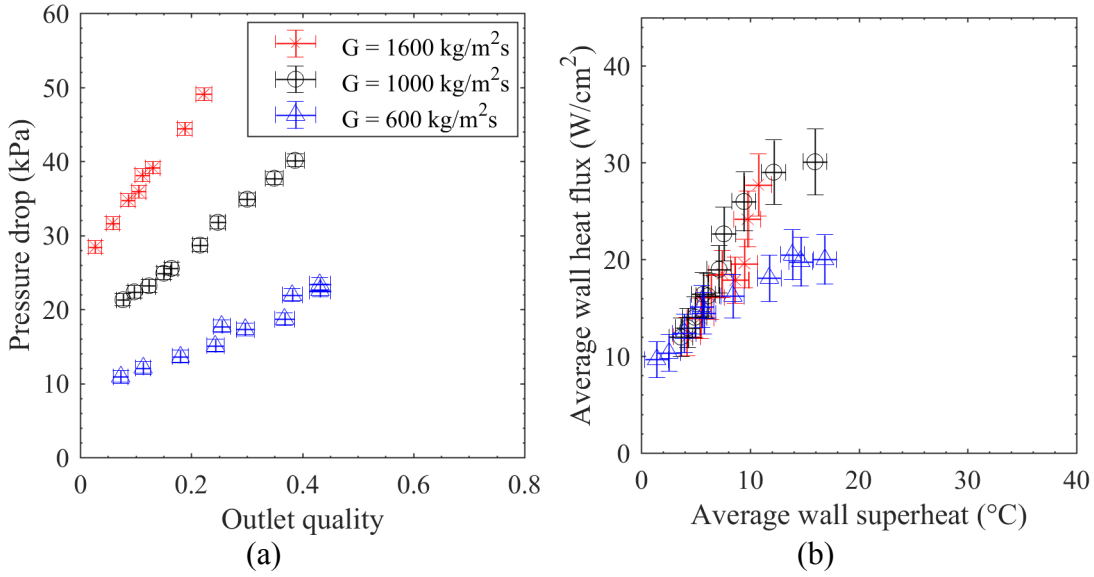

Figure 6.16: FC-72 Manifold Design 2 (a) pressure drop with quality and (b) average heat flux with average superheat for four mass fluxes

6.4.2 Local Superheat

The results of the local superheat occurring on the channel wall with FC-72 Design 2 are shown in Figure 6.17. Referring to back to the local absolute temperature profiles which exhibited uniform wall temperatures at each condition until dryout occurred, it can be seen that the superheat profiles exhibit significant variation from the inlet to the outlet under all conditions—a trend consistent with FC-72 Design 1, which is again, due to the higher pressure drop of FC-72. At 500 kg/m^{2}s, the superheat varies by 5°C at 5 m/s and 15°C at 15 m/s, before persistent dryout occurs. The variation in saturation temperature also amplifies the evidence of dryout

occurrence above 22 m/s with at temperature variation of nearly 25°C at a mass flux of 500 kg/m^{2}s. Under the conditions tested, the flow regime does not transition to the annular-rivulet regime.

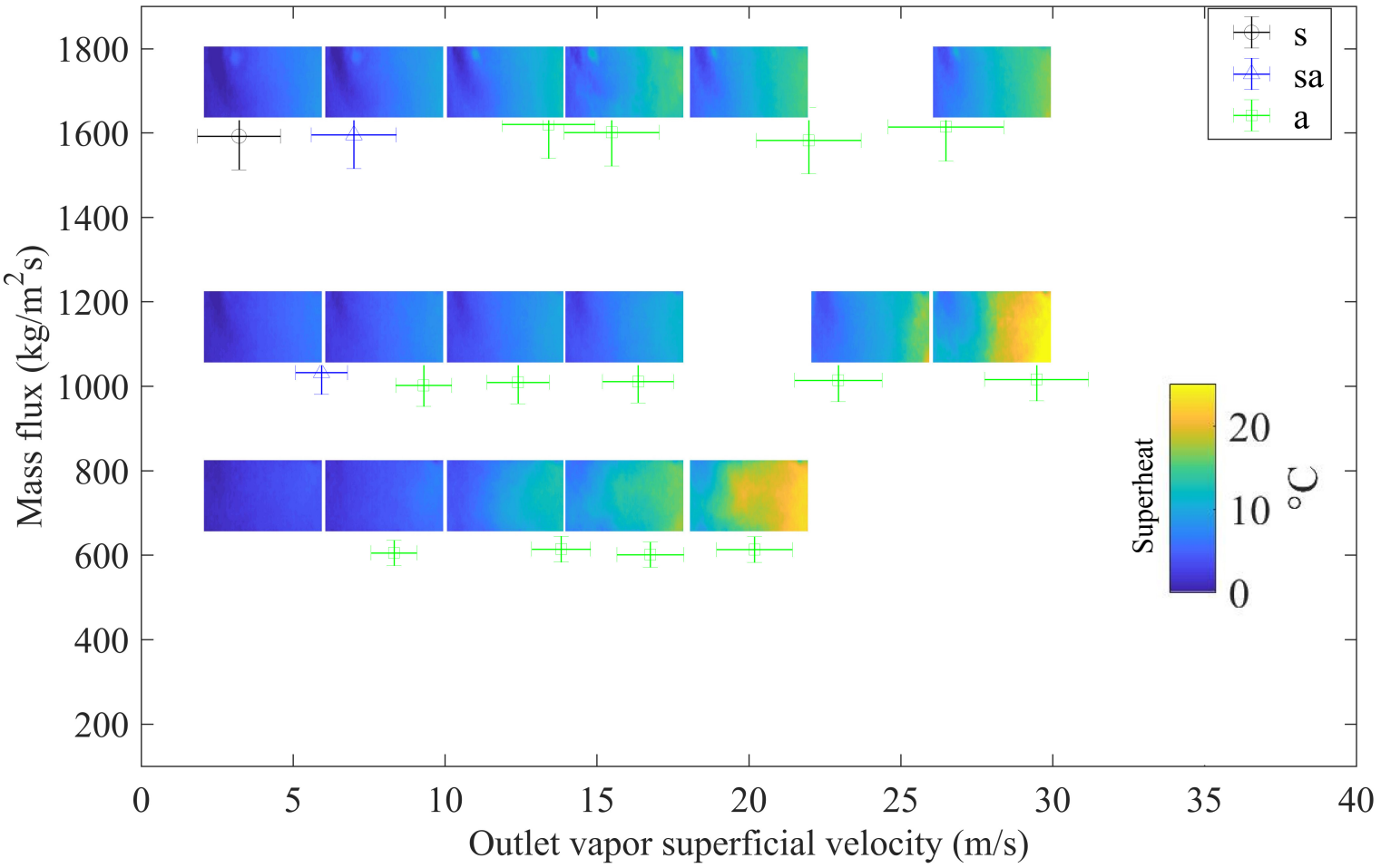

Figure 6.17: FC-72 Design 2 local superheat profiles at intervals of outlet vapor superficial velocity and mass flux. Outlet flow regimes at each point are: s – slug, sa – slug-annular, a – annular.

6.4.3 Local Heat Flux

The local channel wall heat flux is shown in Figure 6.18. The trend in the local heat flux results are consistent with those occurring in the previous tests, in which the local heat flux profiles have nearly identical shape to the temperature profiles, but converse magnitudes. The peak heat fluxes produced with FC-72 Design 2 are about 40% lower than those produced with R245fa. As dryout begins to occur in the exterior corner, the heat flux in the exterior corner ceases to increase, while the heat flow becomes increasingly concentrated in the inlet region. The peak heat fluxes occurring at the inlet remain approximately double that of the Zuber CHF for FC-72 (about half that of R245fa) at 35 W/cm^2. Under these conditions, the peak heat flux at the inlet at 500 kg/m^2s exceeds the Ong and Thome [44] CHF prediction by 34%.

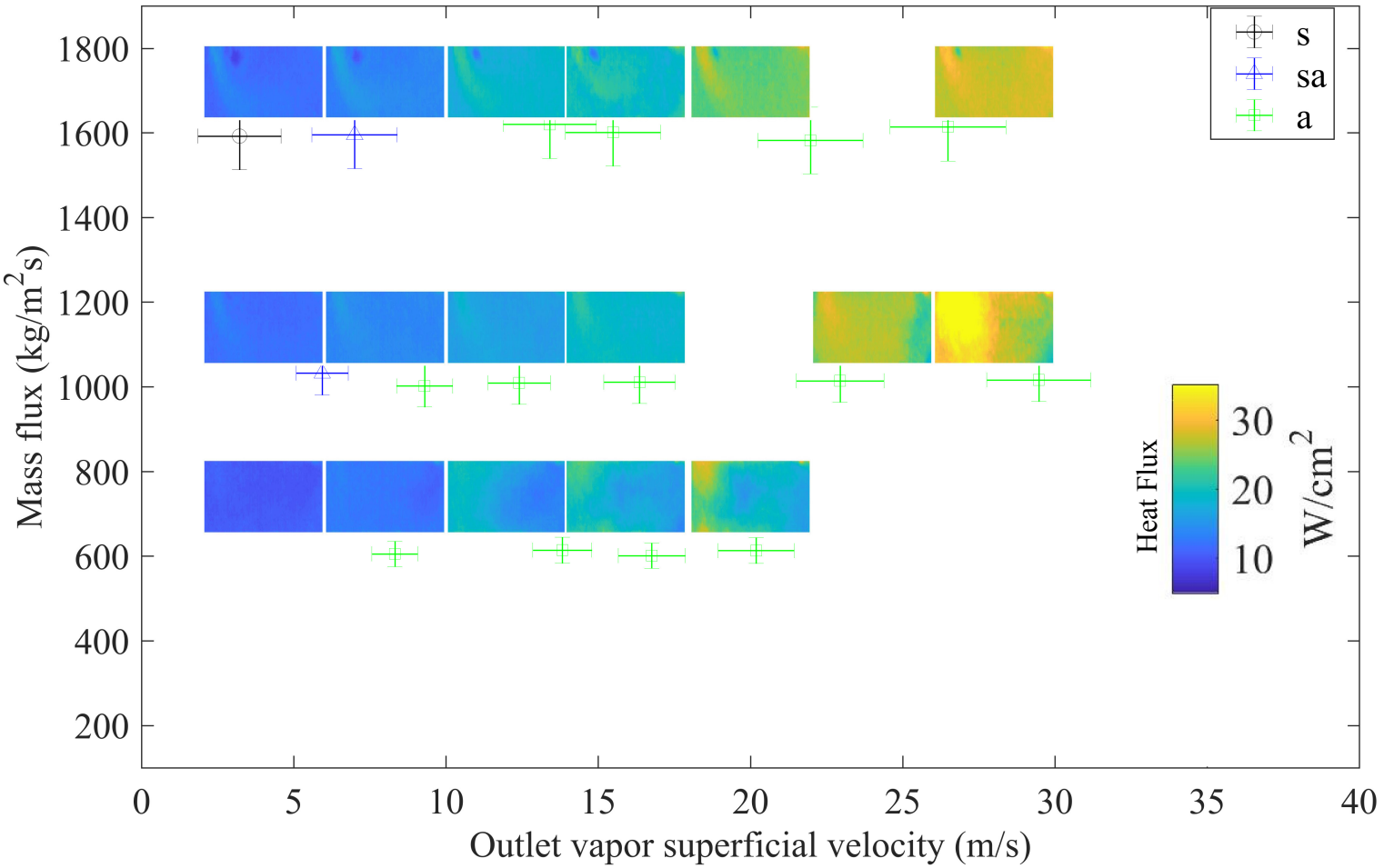

Figure 6.18: FC-72 Design 2 local heat flux profiles at intervals of outlet vapor superficial velocity and mass flux. Outlet flow regimes at each point are: s – slug, sa – slug-annular, a – annular.

6.4.4 Local and Average Heat Transfer Coefficients

The local HTC's resulting from the superheat and wall heat flux are shown in Figure 6.19. It can be observed that the same trends occurring in the superheat and heat flux occur in the HTC's. In all cases, along lines of constant vapor superficial velocity, the cooling jet penetration increases with mass flux. The "saturated" inlet HTC's again correspond with high local HTC uncertainty, consistent with FC-72 Design 1, and shown in further detail in Appendix 9.3.7.

At a mass flux of 1,000 kg/m^{2}s as an example, it can be seen that at 9 m/s, the inlet HTC's are not completely saturated, and the uncertainty has also decreased. The key difference between R245fa and FC-72 is again observed, in which the HTC's vary significantly from the inlet to the outlet even at low qualities from nearly 100,000 W/m^{2}K to 10,000 W/m^{2}K, which is in part due to the early transition to annular flow exhibited by FC-72 at lower mass fluxes, and the larger decrease in vapor density from inlet to outlet. The strong variation in HTC's from inlet to outlet, again, make the transition to intermittent dryout less evident, in contrast to the R245fa tests.

Comparing with the local temperature MAD, in which the areas of intermittent dryout are more apparent, the decline in HTC's in the exterior corner area is far more subtle with FC-72 because the values were lower before dryout began. From this, the data again suggests that the higher pressure drop exhibited by FC-72 causes the inlet region to be the primary driver of high HTC's and the total thermal transport efficiency of the channel wall. The averaged HTC's on the channel wall are shown in Figure 6.20.

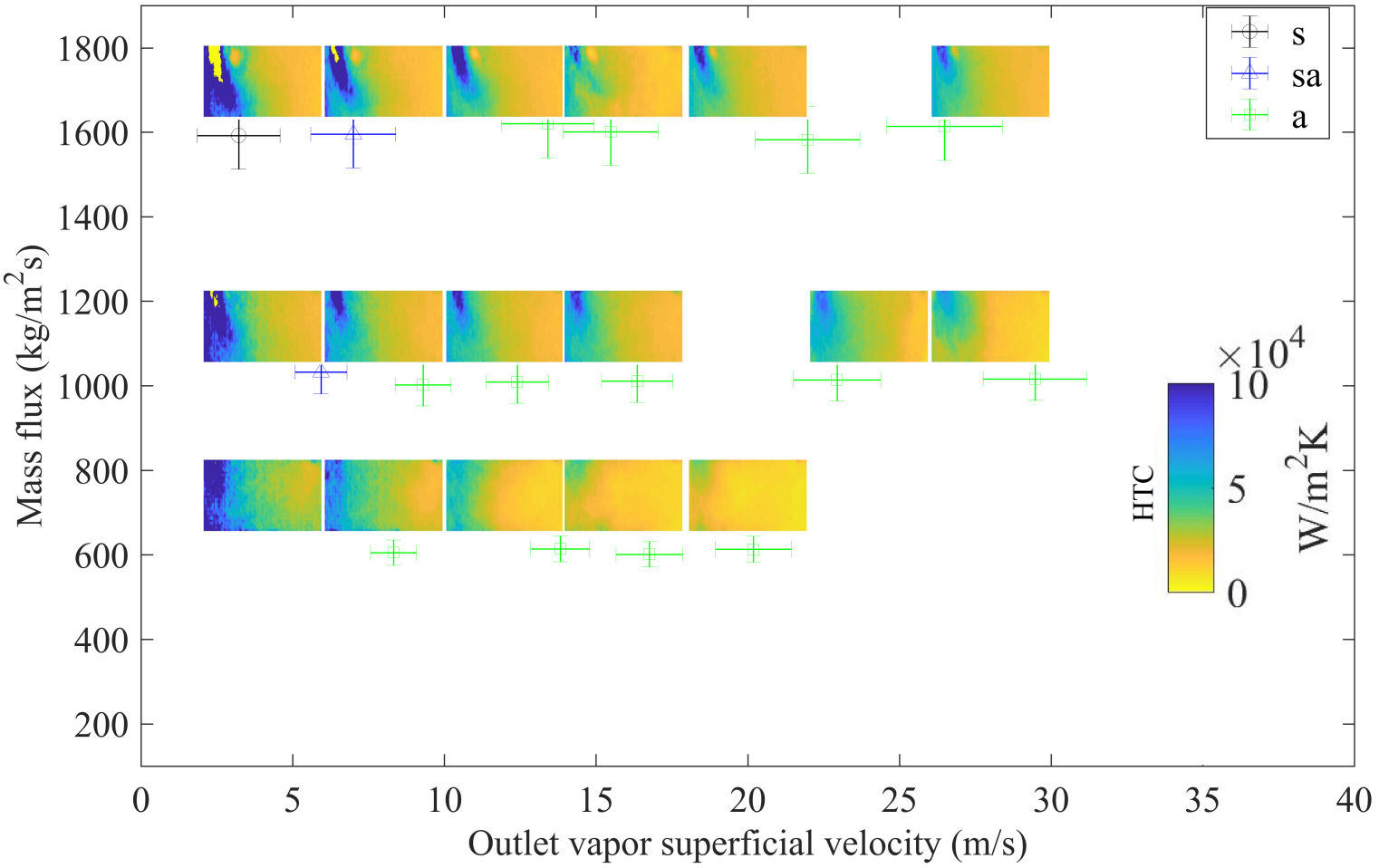

Figure 6.19: FC-72 Design 2 local HTC profiles at intervals of outlet vapor superficial velocity and mass flux. Outlet flow regimes at each point are: s – slug, sa – slug-annular, a – annular.

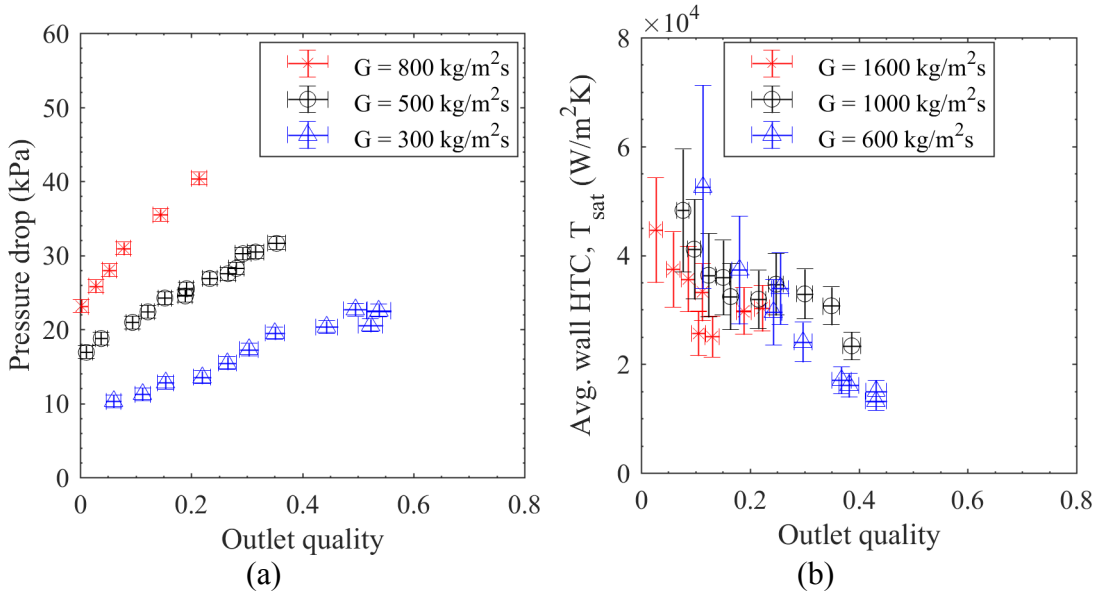

Figure 6.20: FC-72 Manifold Design 1 (a) average HTC's with vapor superficial velocity and (b) average HTC's with outlet quality for four mass fluxes

The average HTC's with FC-72 Design 2 tend to more steadily decline than FC-72 Design 1, or R245fa Design 2 and Design 2 for the same outlet quality range and mass flow rates. Again with FC-72 Design 2, it can be seen that the inlet HTC's are the primary driver of the HTC values, because low wall HTC's exist on the exterior corner region for the entire quality range. For mass fluxes of 1,000 kg/m^{2}s and 1,600 kg/m^{2}s, the HTC's become approximately level at a velocity of 15 m/s with HTC values of 35,000 W/m^{2}K. The mass flux of 1,000 kg/m^{2}s begins declining again due to dryout at 20 m/s. The average wall HTC's, again, tend to be 10-20% less than those exhibited by R245fa with the same manifold design at lower qualities, but then become higher with increasing quality as the R245fa HTC's rapidly decline at the earlier onset of dryout.

6.5 **Thermal Characteristics FC-72 Manifold Design 3 (Figure 3.6)**

6.5.1 Data Summary: Pressure Drop and Average Superheat with Average Heat Flux

The tests for with FC-72 Design 3 are shown in Figure 6.21. The data trends are again self-consistent: the pressure drop increases monotonically with quality and proportionally with mass flux. The peak qualities at equivalent mass fluxes are comparable to those of FC-72 Design 1, although the 500 kg/m^{2}s data set extends to a lower peak quality of less than 40%. The pressure drop generated with FC-72 Design 3 is comparable to FC-72 Design 1, except the 800 kg/m^{2}s consistently exhibited a pressure drop about 25% less than Design 1.

The average wall heat flux with superheat, exhibit self-consistent trends and trends that are consistent with the previous data sets. The wall heat flux increases relatively linearly, within a narrow locus across all mass fluxes, at the lower heat fluxes. Then, at a certain point, the wall superheat rises drastically with a very small increase in heat flux. The sudden change in slope, again, occurs at increasing heat flux with increasing mass flux. The inflection occurs at a narrower range of heat fluxes with Design 3, at 25 W/cm^2 with a mass flux of 300 kg/m^{2}s and 30 W/cm^2 with mass flux of 500 kg/m^{2}s, in contrast to 22 W/cm^2 and 32 W/cm^2 with Design 1 at the same mass fluxes.

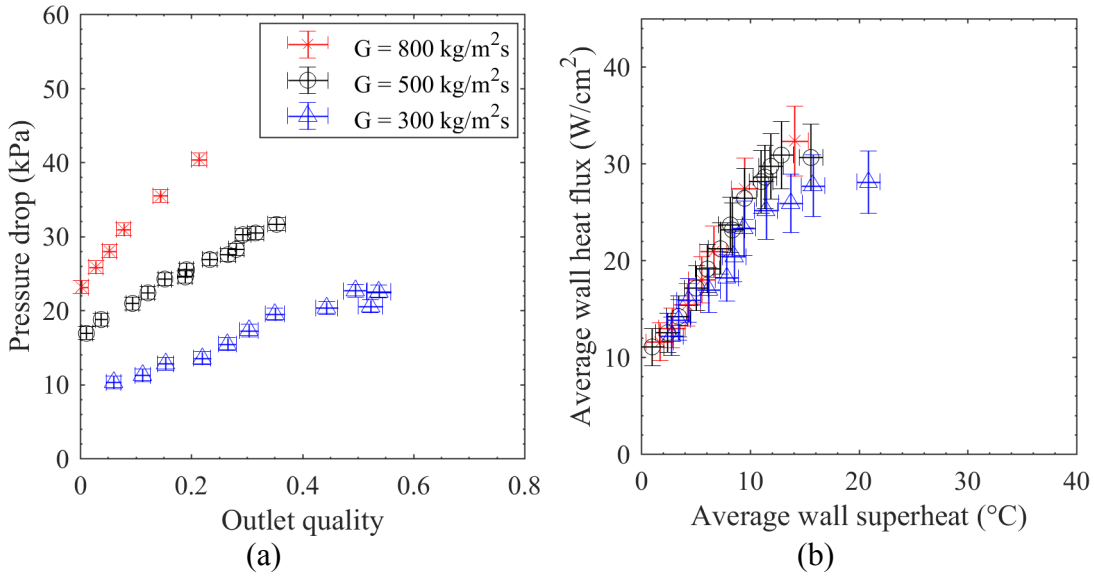

Figure 6.21: FC-72 Manifold Design 1 (a) pressure drop with quality and (b) average heat flux with average superheat for four mass fluxes

6.5.2 Local Superheat

The results of the local superheat occurring on the channel wall with FC-72 Design 1 are shown in Figure 6.22. For the third time with FC-72, it can be seen that the superheat profiles exhibit significant variation from the inlet to the outlet under all conditions, in contrast to the absolute temperature profiles, which tended to be constant until dryout began. The superheat profile makes the early onset of dryout even more evident with Design 3.The peak superheat and superheat variation occurs at 300 kg/m^{2}s and 12 m/s, while the outlet flow regime is annular-rivulet. This is consistent with FC-72 Design 1, but the dry area is significantly increased due to the lack of penetration of the inlet jet.

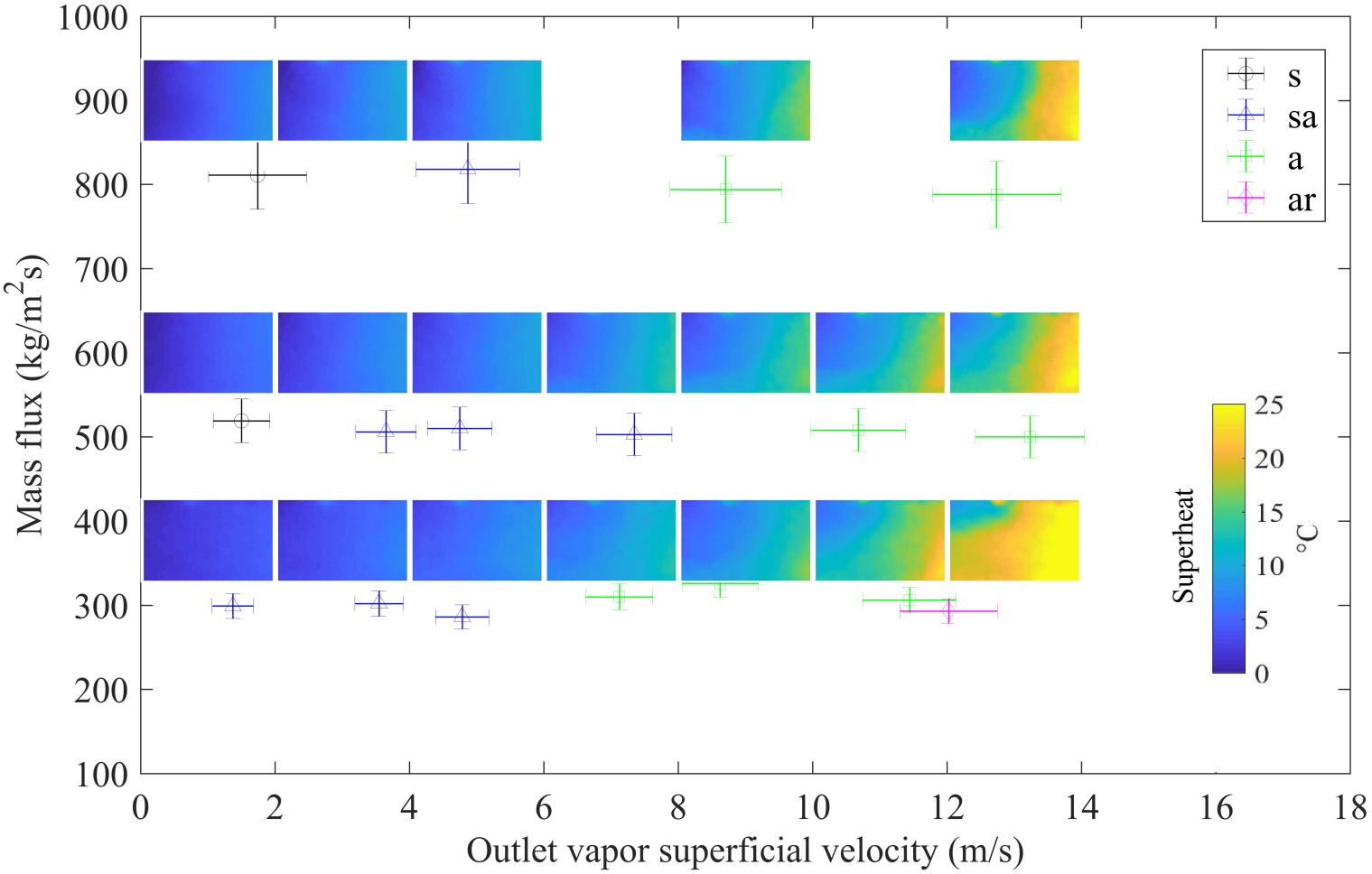

Figure 6.22: FC-72 Design 3 local superheat profiles at intervals of outlet vapor superficial velocity and mass flux. Outlet flow regimes at each point are: s – slug, sa – slug-annular, a – annular, ar – annular-rivulet.

6.5.3 Local Heat Flux

The local channel wall heat flux is shown in Figure 6.22 in the same way the thermal maps have been presented previously. The trends in the local heat flux results are, again, consistent with those occurring in the previous tests, in which the local heat flux profiles have nearly identical shape to the temperature profiles, but converse magnitudes. The peak heat fluxes of 35 W/cm^2 occurring at the inlet remain approximately double that of the Zuber [51] CHF for FC-72 (about half that of R245fa), as well as double that of the Ong and Thome [44] CHF prediction, consistent with FC-72 Design 1. The Ong and Thome [44] CHF prediction is in closer proximity to the peak inlet heat fluxes at 800 kg/m^{2}s, predicting CHF of 24 W/cm^2. As dryout begins to occur in the exterior corner, the heat flux in the exterior corner ceases to increase, while the heat flow becomes increasingly concentrated in the inlet region. The local heat transfer coefficients resulting from the local superheat profiles and local heat fluxes will next be discussed.

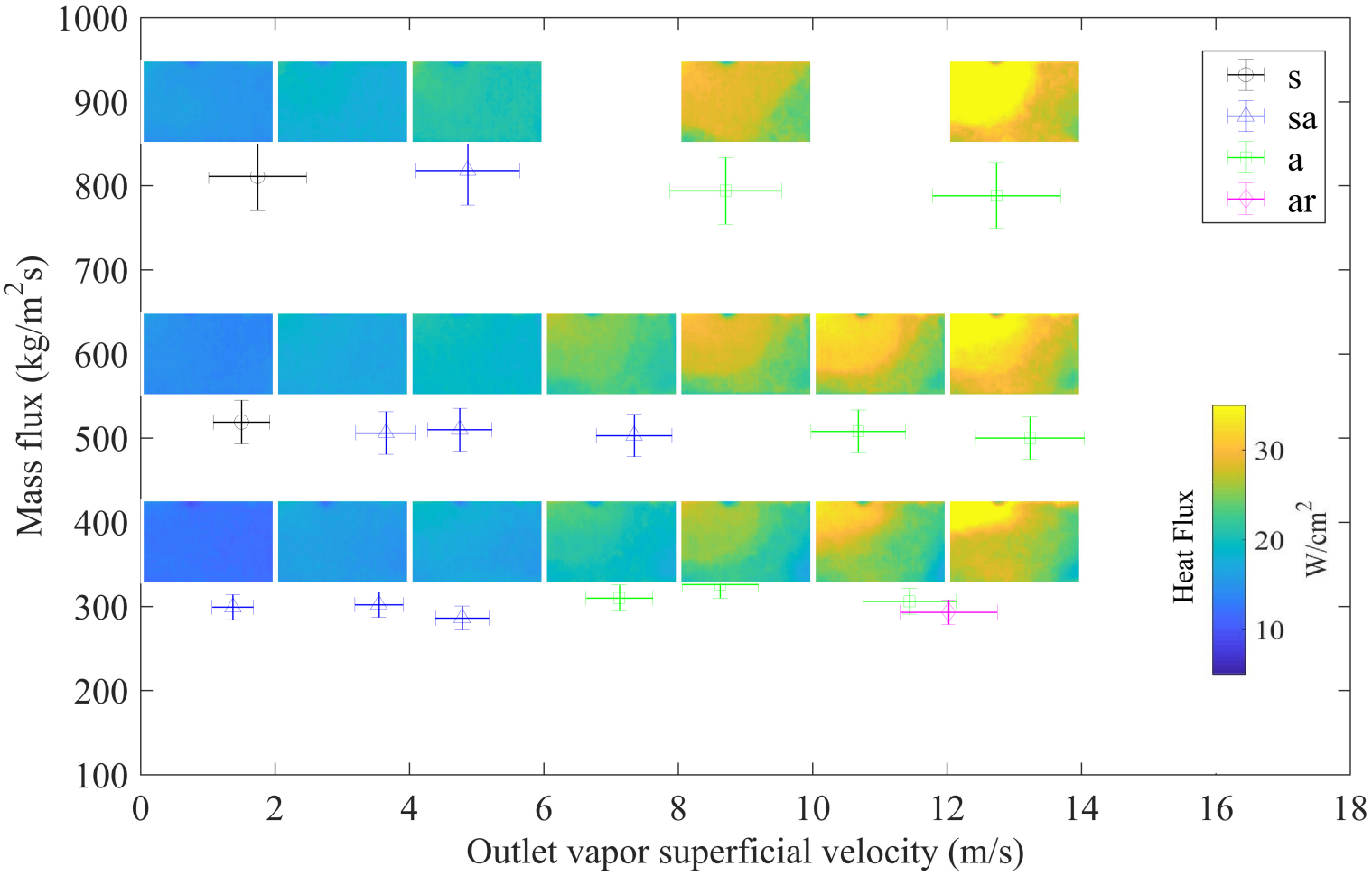

Figure 6.23: FC-72 Design 3 local heat flux profiles at intervals of outlet vapor superficial velocity and mass flux. Outlet flow regimes at each point are: s – slug, sa – slug-annular, a – annular, ar – annular-rivulet.

6.5.4 Local and Average Heat Transfer Coefficients

The local HTC's resulting from the superheat and wall heat flux are shown in Figure 6.24. The trends in HTC are very comparable to that of FC-72 Design 1. The "saturated" inlet HTC's again correspond with high local HTC uncertainty, shown in further detail in Appendix 9.3.7.

Again, along lines of constant vapor superficial velocity, the cooling jet penetration increases with mass flux. But, in Design 3, the penetration of the cooling jet is decreased from Design 1, resulting in more rapid decline in the HTC's occurring at the exterior of the bend. Aside from that difference from Designs 1 and 2, the HTC's evolve in a similar manner to the other manifolds, with the inlet region being the primary driver of HTC's. Evidence of intermittent and persistent dryout can be seen in the temperature MAD section (Figure 5.15), in significant levels of dryout occur above about 10 m/s for mass fluxes of 300 kg/m^{2}s and 500 kg/m^{2}s. The averaged HTC's on the channel wall are shown in Figure 6.25.

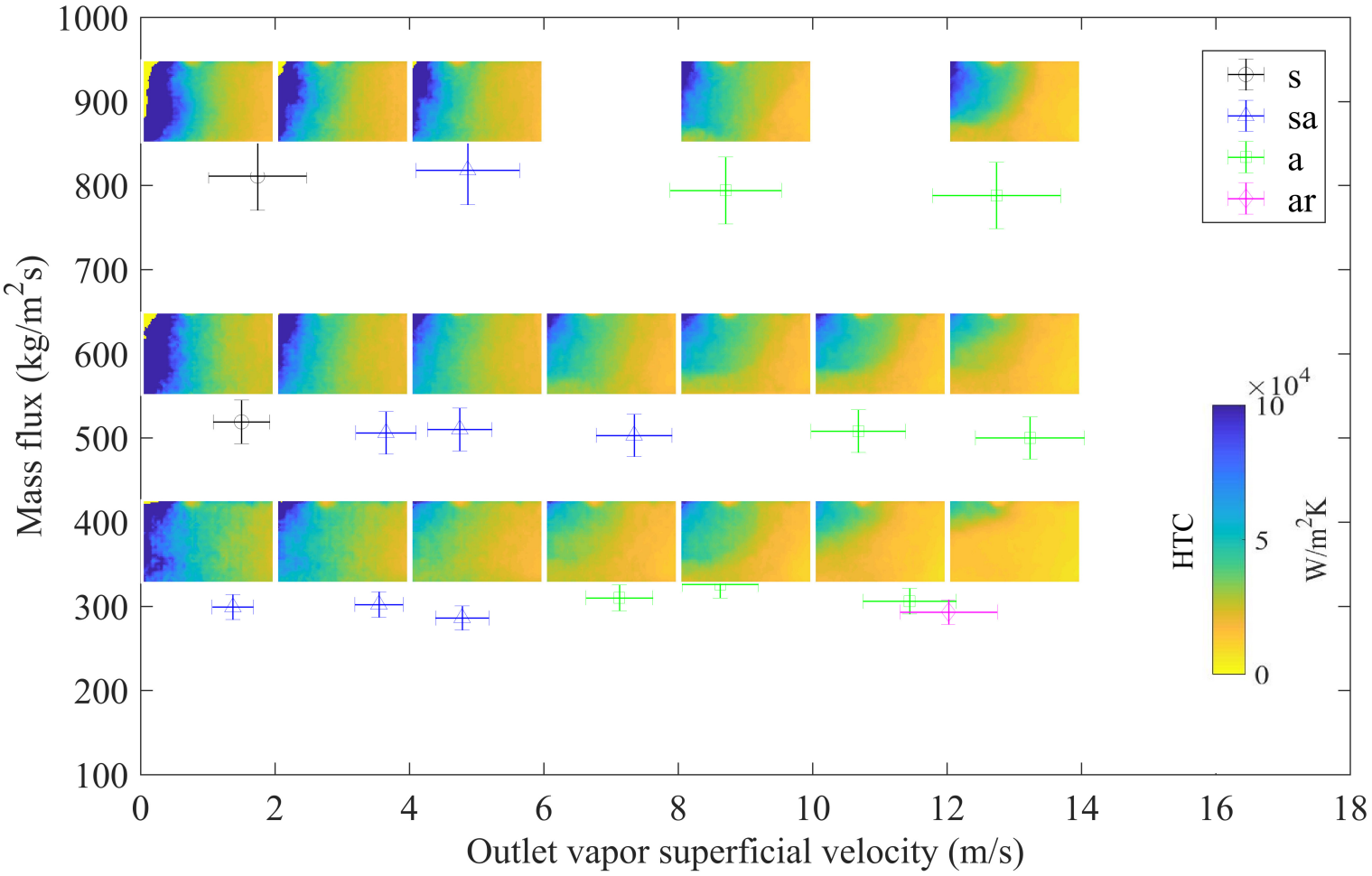

Figure 6.24: FC-72 Design 3 local HTC profiles at intervals of outlet vapor superficial velocity and mass flux. Outlet flow regimes at each point are: s – slug, sa – slug-annular, a – annular, ar – annular-rivulet.

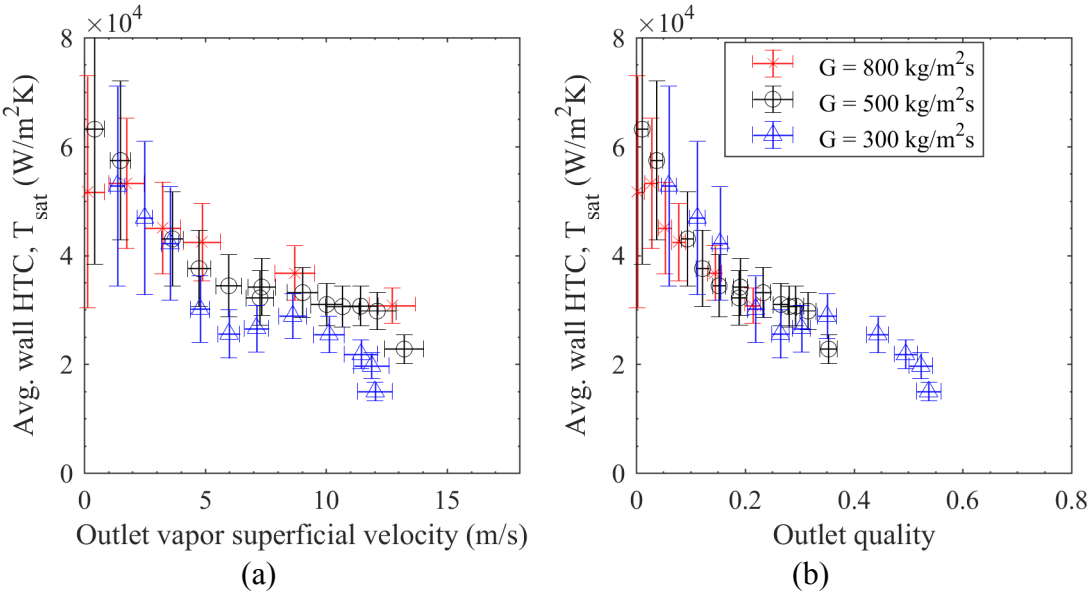

Figure 6.25: FC-72 Manifold Design 3 (a) average HTC's with vapor superficial velocity and (b) average HTC's with outlet quality for four mass fluxes

The average HTC's with FC-72 Design 3 exhibit the most consistent declining trend of all the tests. At low velocities, the decline is due to decreasing penetration of the inlet jet with increasing quality. Then, for mass fluxes of 300 kg/m^{2}s and 500 kg/m^{2}s above 10 m/s the HTC's decline more rapidly with the increased presence of dryout. The HTC's produced with Design 3 are the generally the lowest of all tests, except for at very low qualities where the uncertainty is also very high.

6.6 Summary of Wall Superheat, Heat Flux, and HTC Results and Discussion

With R245fa Design 1, the peak average wall heat flux reached 44 W/cm^2 at a mass flux of 800 kg/m^{2}s with a pressure drop of only 12 kPa. R245fa Design 2, exhibited a peak average wall heat flux of 38 W/cm^2 at a mass flux of 1,600 kg/m^{2}s with a pressure drop of 13 kPa. FC-72 with Design 1 generated a peak average wall heat flux of 35 W/cm^2 at 800 kg/m^{2}s with a pressure drop of 48 kPa. With FC-72

Design 2, the peak average wall heat flux was 30 W/cm^2 at a mass flux of 1,600 kg/m^{2}s with a pressure drop of 49 kPa. And finally, FC-72 Design 3 exhibited a peak average wall heat flux of 32 W/cm^2 at 800 kg/m^{2}s with a pressure drop of 40 kPa. In all cases, the peak local heat fluxes occurring at the channel inlet were double that of the Zuber CHF prediction, at 35 W/cm^2 and 60 W/cm^2 for FC-72 and R245fa, respectively.

The peak average HTC's with R245fa Design 1 reached more than 50,000 W/m^{2}K before rapidly declining, and the peak average HTC's for R245fa Design 2 reached more than 55,000 W/m^{2}K before rapidly declining. These results are consistent with HTC profiles developed in chip-scale manifold-microchannel coolers with R245fa as the working fluid. In contrast, FC-72 exhibited significantly flatter HTC profiles with outlet quality and vapor superficial velocity. FC-72 Design 1 produced HTC's in the range of 40,000 W/m^{2}K and FC-72 Design 2 produced HTC's in the range of 35,000 W/m^{2}K. FC-72 Design 3 produced the worst HTC's which were less than 30,000 W/m^{2}K for all tests with more than 15% outlet quality.

Design 2 exhibited an earlier onset of—and higher temperature variations during—intermittent dryout and rewetting, generating a sharper decline in HTC's from the pre-dryout conditions, compared Design 1 with R245fa. The onset of dryout occurred at 25% outlet quality with Design 2 compared to 35% with Design 1 for the same mass flow rate with R245fa. Design 3 exhibited low penetration of inlet jet and flow bypass around the heated surface in the short channel length. The short manifold design also exhibited early onset dryout, generating low HTC's and high temperature fluctuations with only a small pressure drop benefit.

Chapter 7: Comparison with Heat Transfer Predictions and Flow Regimes

In this chapter, the Chen [20] prediction will be applied to each data set. The results will be presented as a ratio of the predicted HTC's to the empirical HTC's, consistent with the application of the Chen [20] prediction to Bae et al. [36] in Chapter 2. Also consistent with the application of the Chen [20] prediction to Bae et al. [36] in Chapter 2, the mass flux was based on an average of the inlet area, channel area, and outlet area. The flow regimes characterized in Chapter 4 will be compared with the HTC performance and predictive accuracy. It should again be noted that the Chen [20] prediction was developed for HTC's generated in the annular regime, and with minimal empiricism. The predictive accuracy of the Chen relation has been shown by recent studies with microgap channels, showing agreement with experimental results within 30% in the annular flow regime [59], with HFE-7100 and FC-72 as the working fluids.

7.1 **R245fa Manifold Design 1 (Figure 3.4)**

The empirical flow regimes and the Ong and Thome [44, 50] transition predictions for R245fa Design 1 and the HTC prediction ratio of the Chen [20] relation to the empirical HTC's are shown Figure 7.1 (a) and (b), respectively. Using the mass flux of 500 kg/m^{2}s as an example, it can be seen that the inflection in the prediction ratio occurs at about 30% quality. The quality of the inflection in the prediction ratio is consistent with the quality at which the empirical HTC's rapidly decline. Comparing with the outlet flow regime, it can be seen that the HTC

prediction inflection point occurs at a comparable quality to that at which the flow transitions to annular-rivulet. This quality corresponds to a vapor superficial velocity of 9 m/s, at which the wall local and global wall temperature MAD increases significantly, indicating intermittent dryout, and the wall HTC's in the exterior corner begin to rapidly decline. This trend is generally consistent with all four mass fluxes.

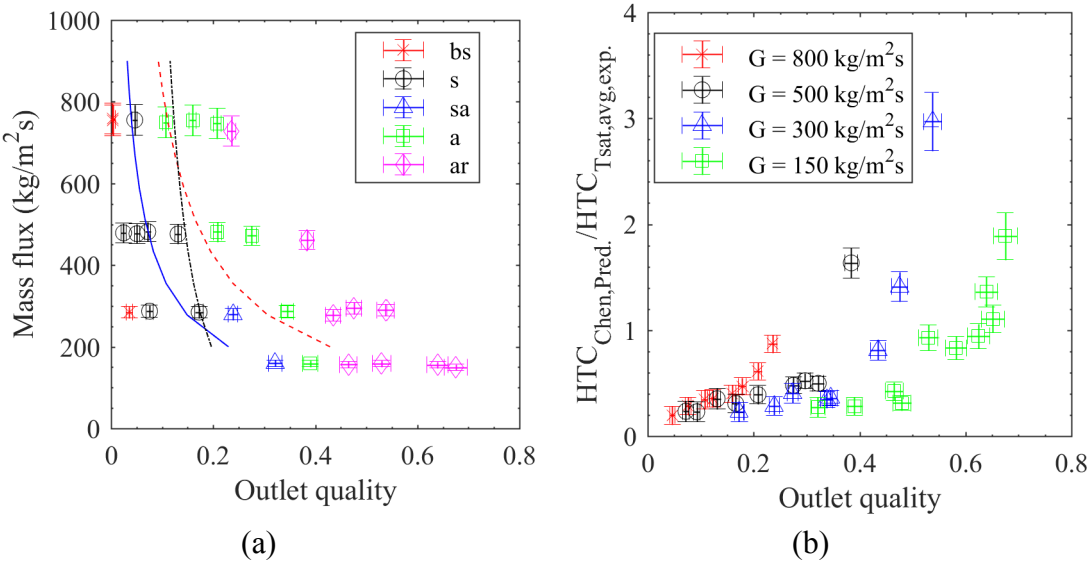

Figure 7.1: (a) R245fa Design 1 outlet flow regimes in terms of outlet vapor quality and mass flux. Outlet flow regimes at each point are: bs – bubble-slug, s – slug, sa – slug-annular, a – annular, ar – annular-rivulet. Predicted transitions: Ong and Thome [44] bubble-slug transition (—), Ong and Thome [44] slug-annular transition (- - -), Ong and Thome [50] dryout/CHF prediction (-·-). (b) R245fa Design 1 HTC prediction ratio of the Chen [20] relation.

The value of the prediction ratio is less than 0.5 at each mass flux leading up to the inflection point, indicating that the empirical HTC's are underpredicted by the Chen [20] relation, which is consistent with the result of applying the Chen [20] relation to the work of Bae et al. [36]. After the inflection point, the prediction ratio increases rapidly to a factor of two or more, which is a trend that is consistent with application of the Chen [20] relation to the work of Bae et al. [36].

7.2 **R245fa Manifold Design 2 (Figure 3.5)**

The empirical flow regimes and the Ong and Thome [44, 50] transition predictions for R245fa Design 2 and the HTC prediction ratio of the Chen [20] relation to the empirical HTC's are shown Figure 7.2 (a) and (b), respectively. Using the mass flux of 1,000 kg/m^{2}s as an example, it can be seen that the inflection in the prediction ratio occurs at about 20% quality, which is a downward shift from the inflection point exhibited by R245fa Design 1. The slight downward shift of inflection point quality is a consistent trend when compared with Design 1 for all mass flow rates—or doubled mass fluxes. The sharpness of inflection is also increased in R245fa Design 2, consistent with the sharper decline in empirical HTC's exhibited by Design 2.

The Chen [20] relation offers a slightly better prediction of the empirical HTC's at the lowest quality of each mass flux with Design 2, because of the higher mass fluxes used in the predictive relation, which increase the predicted HTC's. After the inflection point, the prediction ratio increases rapidly to a factor of two or more, which is again consistent with application of the Chen [20] relation to the work of Bae et al. [36].

The value of the prediction ratio is, again, less than 0.5 for each mass flux leading up to the inflection point, indicating that the empirical HTC's are underpredicted by the Chen [20] relation, which is, again, consistent with the result of applying the Chen [20] relation to the work of Bae et al. [36]. The precise cause of the factor of 2 or more discrepancy between the lower quality empirical HTC's and the Chen [20] prediction with R245fa is difficult to determine directly. The Chen

relation, though, has shown agreement with experimental HTC results within 30% in the annular flow regime [59], with HFE-7100 and FC-72 as the working fluids in microgap channels with L/D_h greater than 100. So, under those conditions, it does not appear that the high aspect ratio of the microgap channel cross-section alters the heat transfer performance significantly from the mechanisms predicted via the Chen relation. In contrast, the manifolded-microgap channels operating with R245fa have several features that differ from Rahim and Bar-Cohen [59], including an inlet restriction that leads to flashing to higher quality, a U-shaped flow path from inlet to outlet, and L/D_h significantly lower than 100—with Design 1 having $L/D_h = 25$, Design 2 having $L/D_h = 50$, and Bae et al. [36] having $L/D_h = 30$. These short length ratios are associated with hydrodynamically and thermally developing single-phase flows, which generate higher HTC's than developed single-phase flows. As discussed previously, the Chen [20] prediction incorporates heat transfer by single phase film convection, but does not incorporate considerations for developing flow.

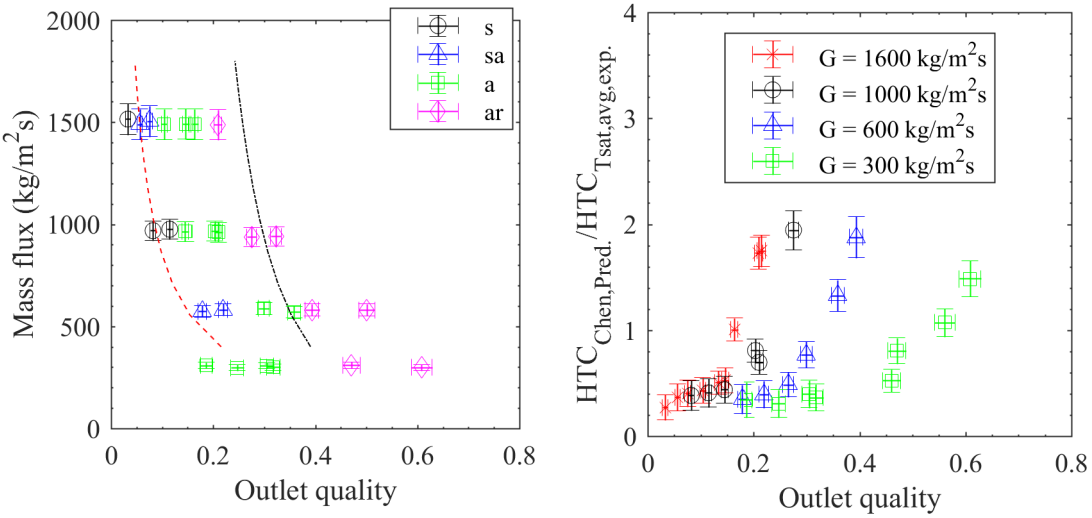

(a) (b)

Figure 7.2: (a) R245fa Design 2 outlet flow regimes in terms of outlet vapor quality and mass flux. Outlet flow regimes at each point are: s – slug, sa – slug-annular, a – annular, ar – annular-rivulet. Predicted transitions: Ong and Thome [44] slug-annular transition (- - -), Ong and Thome [50] dryout/CHF prediction (-·-). (b) R245fa Design 2 HTC prediction ratio of the Chen [20] relation.

Comparing with the outlet flow regime from Design 2 to Design 1, the qualities are quite comparable at which annular-rivulet flow begins to occur. But, the HTC inflection point occurs at lower qualities for each mass flux in Design 2. Referring back to the local and global temperature MAD, it can be seen that the intermittent dryout is more influential in the rapid inflection of HTC's in the longer channel of Design 2. The HTC's continue to decline as dryout becomes increasingly persistent. The Ong and Thome [50] dryout/CHF correlation predicts the HTC inflection quality well for the mass fluxes of 300 kg/m^{2}s and 600 kg/m^{2}s.

7.3 **FC-72 Manifold Design 1 (Figure 3.4)**

The empirical flow regimes, the Taitel and Dukler [53] slug to annular transition prediction, and the Ong and Thome [50] dryout/CHF correlation for FC-72 Design 1 are shown in Figure 7.3 (a). The HTC prediction ratio of the Chen [20] relation to the empirical HTC's are shown Figure 7.3 (b). The relative flatness of the FC-72 Design 1 HTC's is exhibited by the linear increase in accuracy of the prediction ratio with increasing quality for all three mass fluxes. The prediction ratio closest to one occurs after the inflection in prediction ratio at mass flux of 300 kg/m^{2}s in annular-rivulet flow. But, the empirical HTC at this condition is still underpredicted by 35%.

The prediction ratio trend is quite consistent with that of Bar-Cohen, Sheehan, and Rahim [67], but under slightly differing circumstances. In Bar-Cohen, Sheehan,

and Rahim [67], the HTC's were reported along the channel wall from inlet to outlet and compared to the Chen [20] prediction at each point along the flow centerline. The current HTC's differ slightly in nature because they are the averages across the wall of individual tests with increasing outlet quality. Nevertheless, the trend is reasonably consistent, at which FC-72 in a microgap channel produces HTC's higher than predicted by the Chen [20] relation at the inlet region at low qualities. As quality increases and dryout becomes more prevalent, the Chen [20] relation becomes increasingly accurate, which is expected because the prediction was developed for annular flows.

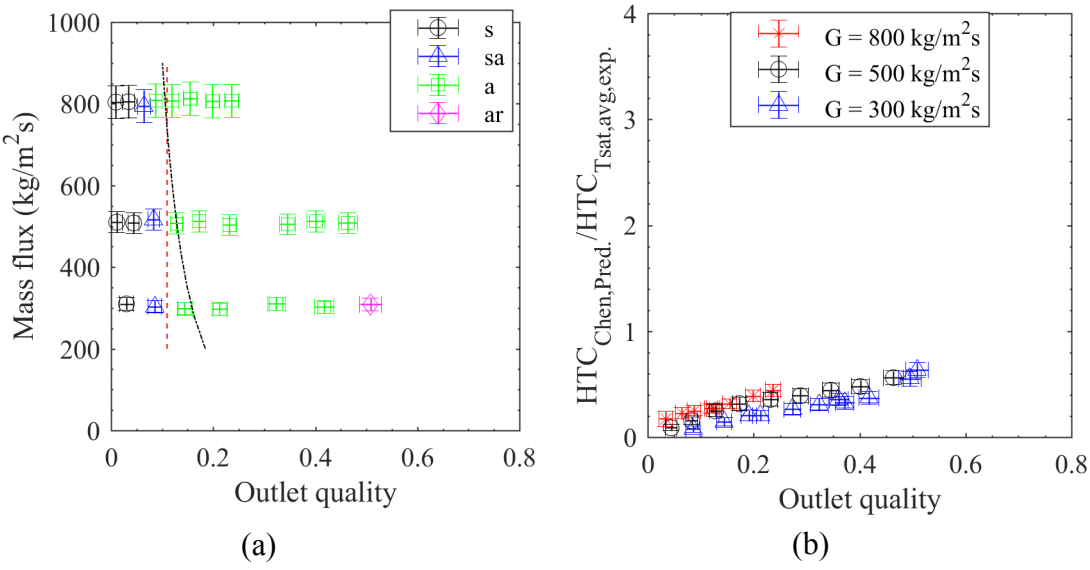

Figure 7.3: (a) FC-72 Design 1 outlet flow regimes in terms of outlet vapor quality and mass flux. Outlet flow regimes at each point are: s – slug, sa – slug-annular, a – annular, ar – annular-rivulet. Predicted transitions: Taitel and Dukler [53] slug-annular transition (- - -), Ong and Thome [50] dryout/CHF prediction (-·-). (b) FC-72 Design 1 HTC prediction ratio of the Chen [20] relation.

7.4 **FC-72 Manifold Design 2 (Figure 3.5)**

The empirical flow regimes, the Taitel and Dukler [53] slug to annular transition prediction, and the Ong and Thome [50] dryout/CHF correlation for FC-72 Design 2 are shown in Figure 7.4 (a). The HTC prediction ratio of the Chen [20] relation to the empirical HTC's are shown Figure 7.4 (b). The steady decline of the FC-72 Design 2 HTC's is exhibited by the monotonic increase in accuracy of the prediction ratio with increasing quality for all three mass fluxes. Generally, the predictive accuracy of the Chen correlation is better with Design 2, because of the higher mass fluxes used in the predictive relation, which increase the predicted HTC's. Furthermore, the longer L/D_h ratio of 50 may bring the flow conditions closer to thermally and hydraulically developed flow, which would be expected to yield better agreement with the Chen relation. The prediction ratio crosses one as the empirical HTC's inflect, when intermittent dryout becomes increasingly prevalent in mass fluxes of 600 kg/m^{2}s and 1,000 kg/m^{2}s. This inflection point, due to increasing prevalence of intermittent dryout, is well predicted by the Ong and Thome [50] dryout/CHF correlation, as shown in Figure 7.4 (b).

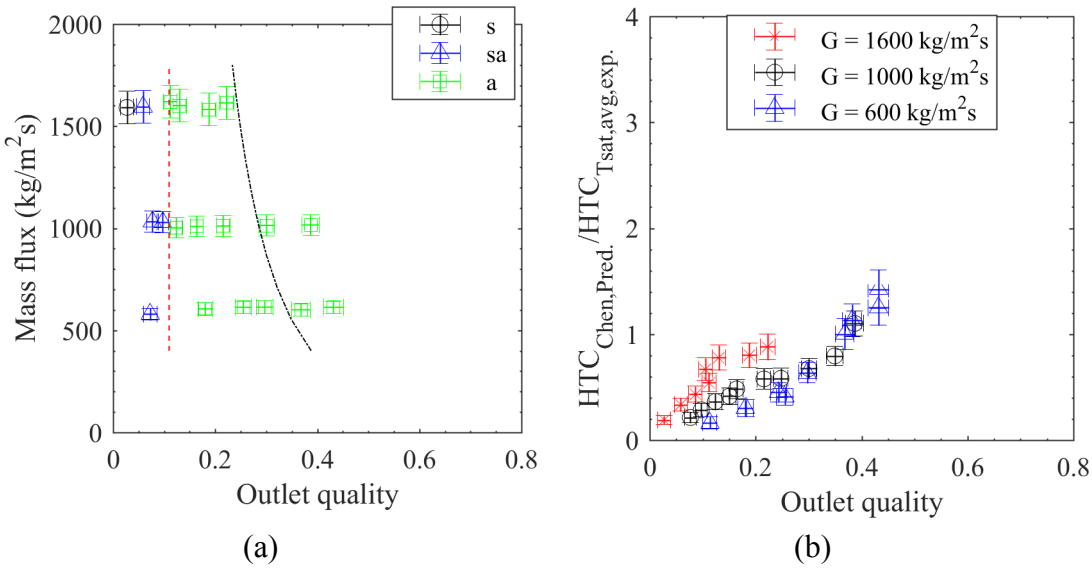

Figure 7.4: (a) FC-72 Design 2 outlet flow regimes in terms of outlet vapor quality and mass flux. Outlet flow regimes at each point are: s – slug, sa – slug-annular, a – annular. Predicted transitions: Taitel and Dukler [53] slug-annular transition (- - -), Ong and Thome [50] dryout/CHF prediction (-·-). (b) FC-72 Design 2 HTC prediction ratio of the Chen [20] relation.

7.5 FC-72 Manifold Design 3 (Figure 3.6)

The empirical flow regimes, the Taitel and Dukler [53] slug to annular transition prediction, and the Ong and Thome [50] dryout/CHF correlation for FC-72 Design 3 are shown in Figure 7.5 (a). The HTC prediction ratio of the Chen [20] relation to the empirical HTC's are shown Figure 7.5 (b). The steady decline of the FC-72 Design 3 HTC's is exhibited by the monotonic increase in the prediction ratio with increasing quality for all three mass fluxes. The Chen [20] relation exhibits the worst predictive accuracy with the short manifold of FC-72 Design 3. This result of poor predictive accuracy of the Chen correlation is due to the low inlet and outlet mass fluxes, which reduce the mass fluxes used in the predictive relation, which decrease the predicted HTC's. This result suggest that for very short channels with

developing flow and tight curvature yielding delayed development of annular flow—and the other geometrical considerations here—that the Chen prediction, based on the physics of annular flow, places too strong a dependence of the two-phase heat transfer coefficient on the mass flux.

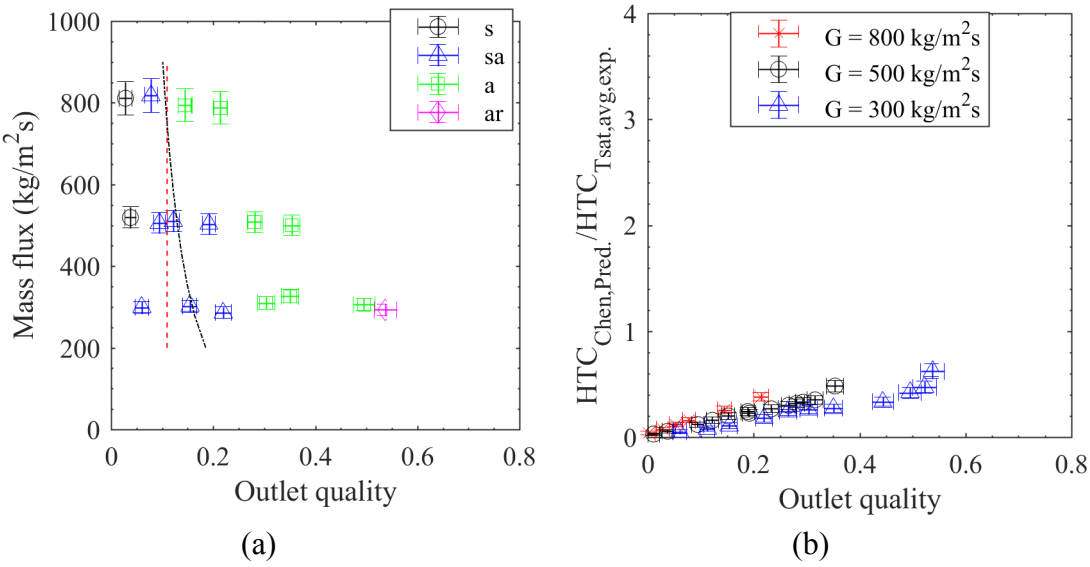

Figure 7.5: (a) FC-72 Design 3 outlet flow regimes in terms of outlet vapor quality and mass flux. Outlet flow regimes at each point are: s – slug, sa – slug-annular, a – annular, ar – annular-rivulet. Predicted transitions: Taitel and Dukler [53] slug-annular transition (- - -), Ong and Thome [50] dryout/CHF prediction (-·-). (b) FC-72 Design 3 HTC prediction ratio of the Chen [20] relation.

7.6 **Summary of Comparison with Predictive Relations**

The quality at which flow regime transitions and dryout occurred was approximately constant for a given fluid with Design 1 and Design 2. This suggests that the channel mass flux was only a weak driver of the prevailing flow regime under the conditions tested. As a result, the relation with no dependence on mass flux (Taitel and Dukler) consistently predicted the slug-annular to annular transition for FC-72, while the correlation dependent on mass flux (Ong and Thome) was only

accurate with one manifold design or the other with R245fa as the working fluid. Similarly, the predictive accuracy of the HTC relation was better with the long manifold design, which produced higher mass fluxes for the same mass flow rate, even though the empirical HTC's only varied slightly from one manifold design to the other for both fluids. Finally, with the predictive accuracy of the HTC relation was worst with the short manifold design, which had the lowest inlet and outlet mass fluxes and least prevalence of annular flow.

Chapter 8: Conclusions and Future Work

Stacked chip architectures and heterogeneous integration are increasingly becoming necessary for continued increases in processing speed and innovation of device capabilities. Concurrently, wide bandgap devices are becoming increasingly prolific, some of which have become thermally limited, sacrificing electronic performance due to inadequate thermal management. Devices generating much higher heat fluxes than those occurring in traditional silicon devices and in traditional packages increase the need for localized high heat flux cooling solutions while minimizing the SWAP-C of the cooling system. Putting the semiconductor device in direct contact with the cooling fluid—embedded cooling—leads to increasingly necessary gains in cooling performance.

In an increasing number of studies, manifold-microchannels have shown excellent performance for high heat flux cooler, producing very high chip-scale HTC's with low pressure drops. The focus of this dissertation was to gain phenomenological insight into diabatic phase-change cooling within manifold-microchannel geometries. The performance of two engineered fluids were compared. One fluid is a standard electronics cooling fluid, FC-72, and the other is a low pressure refrigerant used in a growing number of electronics coolers, R245fa. Aside from reporting heat transfer and pressure drop, no previous studies have qualitatively and quantitatively characterized the complex two-phase flow phenomena and the associated local heat transfer occurring in manifold-microchannels.

A single channel within a manifold-microchannel cooler is a unique geometry that differs from the more traditionally studied two-phase flow geometries. Key

differences include microscale hydraulic diameter, high aspect ratio rectangular cross section, short length compared to hydraulic diameter ($L/D_h < 100$), a step-like inlet restriction, and U-shaped flow path through the channel. Each of these differences—and their combined effects—have ramifications on flow phenomena and heat transfer that are not well-documented in the literature. This research sought to study and characterize these effects in the pursuit of further performance enhancement in high-heat flux, embedded electronics coolers. Following a review of the pertinent literature, a series of experiments were performed to elucidate the flow phenomena and its effects on heat transfer.

The experimental campaign used simultaneous high-speed imaging and infrared imaging to visualize the flow optically and thermally. This approach also allowed a direct connection between the prevailing visible flow regimes and wall heat transfer. A medium manifold length (Design 1), a long manifold length (Design 2), and a short manifold length (Design 3) were used to compare the effects of channel length on prevailing flow regimes and heat transfer. Experiments were carried out with a range of mass fluxes and heat fluxes, producing peak outlet qualities of nearly 70%. The infrared video was used to produce maps of thermal properties on the channel wall from the from inlet to outlet, including average wall temperatures, magnitudes of temporal temperature variation, wall superheat, wall heat flux, and wall heat transfer coefficients.

A microgap channel with a gap height of 80 μm and heated area of 7.8 mm by 2.4 mm was equipped with three manifold designs. The short manifold design (Design 3) was 0.3 mm long as tested, the medium manifold design (Design 1) was

2.3 mm long, and the long manifold design (Design 2) was 4.7 mm. The peak wall temperature was limited to about 85°C because of temperature limitations of the test section. All tests were performed with 6°C of subcooling, and mass fluxes ranged from 150 kg/m^{2}s to 1,600 kg/m^{2}s. Two test fluids, R245fa and FC-72, with varying fluid properties and heat transfer performance were used.

With R245fa Design 1, the peak average wall heat flux reached 44 W/cm^2 at a mass flux of 800 kg/m^{2}s with a pressure drop of only 12 kPa. R245fa Design 2, exhibited a peak average wall heat flux of 38 W/cm^2 at a mass flux of 1,600 kg/m^{2}s with a pressure drop of 13 kPa. FC-72 with Design 1 generated a peak average wall heat flux of 35 W/cm^2 at 800 kg/m^{2}s with a pressure drop of 48 kPa. With FC-72 Design 2, the peak average wall heat flux was 30 W/cm^2 at a mass flux of 1,600 kg/m^{2}s with a pressure drop of 49 kPa. And finally, FC-72 Design 3 exhibited a peak average wall heat flux of 32 W/cm^2 at 800 kg/m^{2}s with a pressure drop of 40 kPa. In all cases, the peak local heat fluxes occurring at the channel inlet were double that of the Zuber CHF prediction, at 35 W/cm^2 and 60 W/cm^2 for FC-72 and R245fa, respectively. Dryout first occurred in the exterior corner region because that location is furthest from the inlet, and also likely because of film inversion phenomena caused by the centripetal acceleration of the vapor driving the liquid film toward the interior of the bend of the flow path.

The peak average HTC's with R245fa Design 1 reached more than 50,000 W/m^{2}K before rapidly declining, and the peak average HTC's for R245fa Design 2 reached more than 55,000 W/m^{2}K before rapidly declining as dryout progressed. These results are consistent with HTC profiles developed in chip-scale manifold-

microchannel coolers with R245fa as the working fluid, providing new insight into the dryout progression in these types of channels. In contrast, FC-72 exhibited significantly flatter HTC profiles with outlet quality and vapor superficial velocity. FC-72 Design 1 produced HTC's in the range of 40,000 W/m^2K and FC-72 Design 2 produced HTC's in the range of 35,000 W/m^2K. FC-72 Design 3 produced the worst HTC's which were less than 30,000 W/m^2K for all tests with more than 15% outlet quality.

The high-speed images, synchronized with infrared images, were used to evaluate the visible flow phenomena and prevailing flow regimes. It was found that, because of curving flow path in the rectilinear channel, stagnant zones were generated in the flow, allowing a flow regime typically associated with lower mass fluxes to be generated simultaneously with the prevailing core of the flow regime. This resulted in simultaneous occurrence of two flow regimes in the channel outlet under a wide variety of conditions, which is not reported in traditional channels. Flow phenomena occurring at low mass fluxes (150 kg/m^2s to 300 kg/m^2s) generally could be categorized in the same flow regimes as higher mass fluxes. But, increasing global dryout events evidenced more churn-like behavior in low mass flux flows in these short microgap channels. These flow regime phenomena generally occurred with both fluids, although it was found that FC-72 more frequently produced wavy annular flow than R245fa. It was conclusively found that the transition from annular to annular-rivulet flow was characterized by persistent dryout associated with a steep decline in local, and therefore, average HTC's on the channel wall.

The long manifold design (Design 2) exhibited an earlier onset of—and higher temperature variations during—intermittent dryout and rewetting, generating a sharper decline in HTC's from the pre-dryout conditions, compared to the medium length manifold design (Design 1) with R245fa. More specifically, the onset of dryout occurred at 25% outlet quality with Design 2 compared to 35% with Design 1 for the same mass flow rate. The short manifold design (Design 3) exhibited low penetration of inlet jet and flow bypass around the heated surface in the short channel length. The short manifold design also exhibited early onset dryout, generating low HTC's and high temperature fluctuations with only a small pressure drop benefit.

In terms of thermal performance, it was no surprise that R245fa was a more potent heat transfer fluid, delivering higher peak HTC's (about 20% higher) and higher peak heat fluxes (about 25% higher). Furthermore, the pressure drop required for R245fa was 75% less than that of FC-72 under many conditions. This high pressure drop produces a large variation in saturation temperature (in excess of 10°C) and vapor density from inlet to outlet with FC-72. The result is high HTC's at the inlet (100,000 W/m^2k), and low HTC's near the outlet (10,000 W/m^2k) of the channel under most conditions. These consistently low HTC's near the outlet with FC-72 prevented the precipitous drop in HTC's associated with dryout, because the average wall HTC's are governed by the high inlet HTC's, regardless of the values occurring near the outlet. In contrast, the average wall HTC's exhibited by R245fa dropped precipitously in the presence of any dryout within the channel because uniform HTC's occur from inlet to outlet pre-dryout. R245fa also exhibited consistently higher mean absolute deviation in wall temperature (10°C) compared to FC-72 (6°C).

The lower temperature variation in time under nominally steady-state conditions, as well as the flatter HTC profiles with increasing quality or vapor superficial velocity indicate that FC-72 exhibits more thermal stability, but less potency, than R245fa for comparable mass fluxes and outlet qualities.

The outlet quality at which dryout occurred was approximately constant for a given fluid for either the medium (Design 1) or long manifold design (Design 2). This suggests that the channel mass flux was only a weak driver of the prevailing flow regime under the conditions tested. As a result, the relation with no dependence on mass flux (Taitel and Dukler) consistently predicted the slug-annular to annular transition for FC-72, while the correlation dependent on mass flux (Ong and Thome) was only accurate with one manifold design or the other with R245fa as the working fluid. Similarly, the predictive accuracy of the HTC relation was better with the long manifold design, which produced higher mass fluxes for the same mass flow rate, even though the empirical HTC's only varied slightly from one manifold design to the other for both fluids. Finally, with the predictive accuracy of the HTC relation was worst with the short manifold design, which had the lowest inlet and outlet mass fluxes. The lower average mass flux of the short manifold reduced the predicted HTC, which was also consistent with reduced prevalence of annular flow in the short manifold design.

8.1 **Recommendations for Future Work**

The experimental apparatus used in the current experiments has yielded excellent insights and quantification of the flow phenomena and resulting heat transfer occurring in manifolded-microgap channels. But, there is potential for

improvement in future work. One of the largest sources of uncertainty in the empirical data was the two-phase pressure drop from the transducer to the gap. Modern technology may enable *in situ* pressure measurement within the gap, such as with microelectromechanical (MEMS) pressure transducers. Measurement of the local pressures in the gap would greatly reduce the local saturation temperature uncertainty, as well as quantifying the pressure differential in the spanwise direction due to flow path curvature. MEMS sensors could also provide insight into transient pressure variations due to two-phase flow phenomena.

The current apparatus could also be improved by introducing heating on the transparent lid, generating heated walls on both sides of the channel, and improving the representation of flow conditions in functional manifold-microchannel coolers. Finally, the current apparatus could be used to study the effect of varying hydraulic diameter on thermal performance, as well as providing further data for the yet unestablished demarcation from microscale to macroscale flow phenomena, by changing the shim thickness.

Further development of the experimental apparatus and use of simultaneous infrared and high-speed visual imaging method developed here could provide profound insights into the unexplored flow phenomena occurring in channels with divergence and confluence of diabatic two-phase flow streams. A test section with multiple inlets and outlets could also provide insight into the flow phenomena and "cross-talk" occurring with multiple inlets and outlets along the length of a single, diabatic two-phase flow channel, which also occur in operational manifold-microchannel coolers.

There are also two-phase flow effects occurring in manifolded microchannels that require further systematic study. Specifically, the development of two-phase flow along the length of a channel from the inlet, is an area with increasing evidence of its importance, but little conclusive evidence of its effect on flow phenomena and heat transfer. This, combined with the inlet flashing effect in manifolded microchannels, may significantly influence performance.

Furthermore, the effect of high quality flow phenomena in microchannels/microgaps is an area meriting further investigation, in order to better utilize the latent heat of vaporization of the phase change fluid. Relatively little research focus has been devoted to the thermal and hydrodynamic characteristics in waves, rivulets, and film instabilities associated with post-annular flows. Thermocapillary effects, contact angle, and wettability all play an important role in flow regime development, and also merit further investigation.

The effects of fluid properties of each phase including density, viscosity, surface tension, and the temperature/pressure dependence of each on the flow regimes, and other hydrodynamic behavior leading to thermal performance remains to be thoroughly established. Further systematic investigation into the effects of fluid properties in engineered fluids, evolving from those shown here, will lead to increased heat flux dissipation and improved thermal performance. And so, from the current research and historical research it is grounded in, it is evident that two-phase heat transfer predictions must be mechanistically tied to the flow regimes, liquid films, and other structures with minimal empiricism for improved predictability in

pursuit of advantageous use of liquid-vapor phase change for high heat flux embedded electronics coolers and other two-phase flow applications.

Appendices

9.1 Dimensionless Groups for Two-Phase Flows

The two-phase nondimensional numbers used in the preceding analysis are shown in Table 9.1. Each dimensionless number is based on two forces occurring in the fluid, the combinations of which correspond to the horizontal and vertical directions of the table.

Table 9.1: Dimensionless parameters indicating force ratios in two-phase flows

	Inertia	**Shear**	**Surface tension**
Gravity or centripetal acceleration	Froude number*: $F = \sqrt{\frac{\rho_V}{\rho_L - \rho_V}} \frac{u_{SV}}{\sqrt{D_h g}}$	Dean number**: $De = \frac{\rho v D_h}{\mu} \left(\frac{D_h}{2R}\right)^{1/2}$	Bond number: $Bo_g = \frac{g(\rho_L - \rho_V) D_h^2}{\sigma}$
Inertia	-	Reynolds number: $Re = \frac{\rho v D_h}{\mu}$	Weber number: $We = \frac{\rho v^2 D_h}{\sigma}$
Shear	-	-	Capillary number: $Ca = \frac{\mu v}{\sigma}$

* Froude number modified by a density ratio
** Dean number is a balance between acceleration, inertia, and shear in single phase flows, so the comparison between acceleration and shear may be somewhat obfuscated

9.2 Pipe Flow Correlations for Pressure Drop from the Transducer to the Gap Inlet

Pressure drop at manifold inlet constriction

At the inlet, the area ratio is $A_2/ A_1 = 0.4$. From Munson et al. [93], the loss coefficient can then be found to be $K_L = 0.3$. The pressure drop due to manifold inlet constriction is shown in Equation (43).

$$\Delta P_{ic} = \frac{K_L v_m^2 \rho}{2} \tag{43}$$

The liquid velocity in the manifold is v_m, and the density of the liquid is ρ.

Pressure drop at manifold inlet 90° bend

From Munson et al. [93], the loss coefficient for a sharp 90° bend is $K_L = 1.1$ and the pressure drop can be determined with Equation (44).

$$\Delta P_{ib} = \frac{K_L v_m^2 \rho}{2} \tag{44}$$

Pressure drop at gap inlet constriction

Similarly with the manifold inlet constriction, the area ratio ($A_2/ A_1 = 0.2$) is used to find the loss coefficient, $K_L = 0.45$. The pressure drop due to gap inlet constriction can then be shown with Equation (45) [93].

$$\Delta P_{gc} = \frac{K_L v_g^2 \rho}{2} \tag{45}$$

The liquid velocity in the gap inlet is v_g.

Pressure drop due to laminar pipe flow in manifold

The friction factor for the rectangular duct flow with aspect ratio of 0.4 is as shown in Equation (46) [93].

$$f = \frac{67}{Re_h} \tag{46}$$

The hydraulic Reynold's number is as follows in Equation (47).

$$Re_h = \frac{\rho v D_h}{\mu} \tag{47}$$

The pressure drop due to laminar pipe flow in the manifold is then shown in Equation (48) [93].

$$\Delta P_p = f\frac{l}{D_h}\frac{v_m^2\rho}{2} \tag{48}$$

The length of the manifold is denoted with the letter l.

Pressure drop due to velocity change

Since the velocity at the manifold inlet is negligible, the velocity at only the inlet of the gap is needed. The pressure drop due to velocity change can then be found with Equation (49) [93].

$$\Delta P_v = \frac{v_g^2\rho}{2} \tag{49}$$

Total pressure drop from transducer to gap inlet

The total pressure drop to be subtracted from the transducer measurement to determine the pressure at the gap inlet can finally be found by summing the pressure drops due to each effect as shown in Equation (50).

$$\Delta P_t = \Delta P_{ic} + \Delta P_{ib} + \Delta P_{gc} + \Delta P_p + \Delta P_v \tag{50}$$

9.3 **Audits on Experiments and Calculation Assumptions**

9.3.1 Fast Fourier Transform on Inlet Pressure

A Fast Fourier Transform was performed on the inlet pressure to test for the existence of dominant frequencies in the channel pressure which might indicate pressure resonance within the test loop during two-phase testing, and a potentially erroneous influence on the flow behavior observed within the test section. A typical

result is shown in Figure 9.1, in which no dominant pressure frequency was detected, showing that system resonance was unlikely to be an influence on the empirical results.

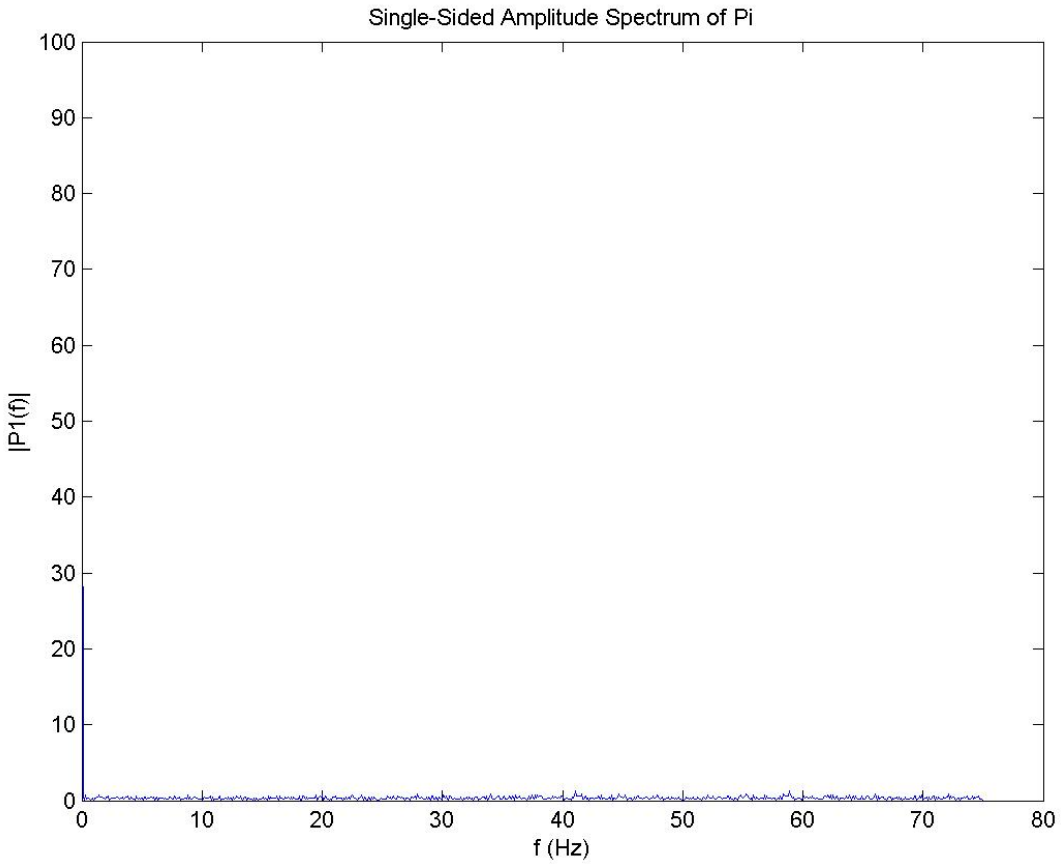

Figure 9.1: Example of FFT on inlet pressure

9.3.2 Left and Right Wall Temperature Comparison

This appendix section was developed to justify the data reduction assumption that the images can be "folded" to represent both channels in one compact thermal image. It can be observed from Figure 9.2 through Figure 9.4 that any bias in the average temperature from one half of the channel to the other is within the measurement uncertainty.

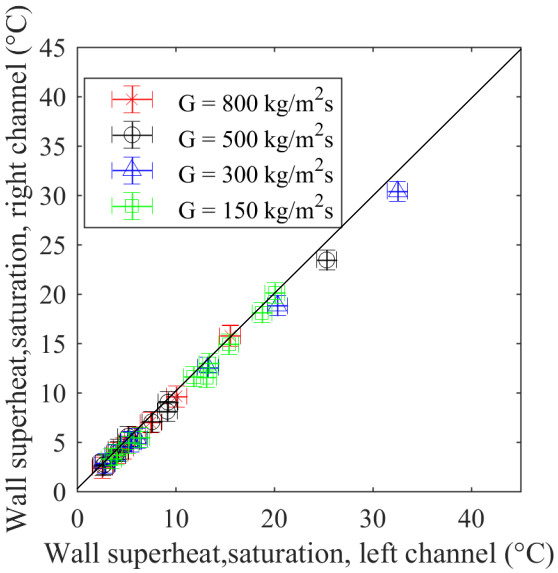

Figure 9.2: R245fa Manifold Design 1 left and right average wall temperature comparison

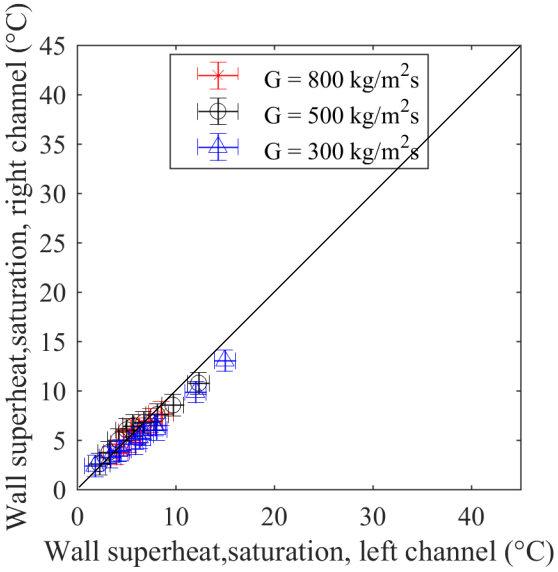

Figure 9.3: FC-72 Manifold Design 1 left and right average wall temperature comparison

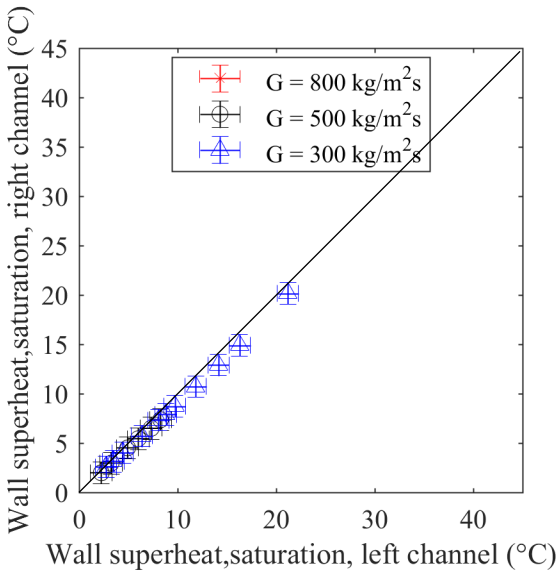

Figure 9.4: FC-72 Manifold Design 1 left and right average wall temperature comparison

9.3.3 Proportion of Heat Transfer in the Gap

The proportion of the heat transfer occurring within the gap compared to the total heat transfer to the fluid in the test section is shown in the Figure 9.5 through Figure 9.9. In most cases, the majority of the heat transfer is within the gap, where the heat source is supplied and the hydraulic diameter is smallest. The two heat transfer quantities are determined independently—the heat transfer in the gap is determined with by calculating the heat transfer through the high emissivity coating, and the heat transfer within the test section is calculated by accounting for the heater power and total heat loss. The profiles the curves follow similar trends to the gap HTC's. As the local HTC's in the gap decline, the proportion of heat transfer in the gap declines, suggesting increased spreading to the fluid upstream of the gap. At low superheat (low vapor superficial velocity), some FC-72 tests suggest that more heat transfer

occurs in the gap than total heat transfer to the fluid in the test section, but the uncertainty is quite high.

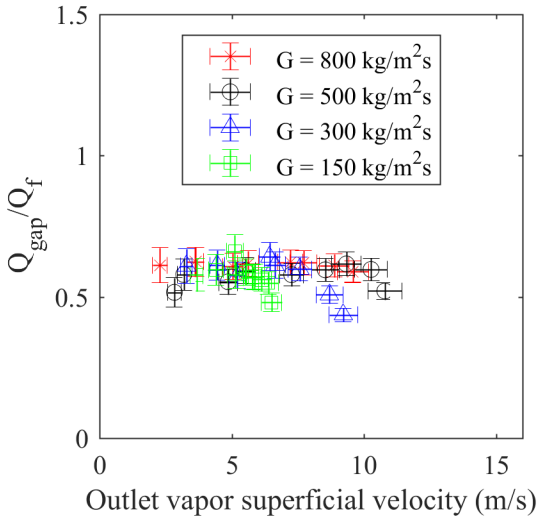

Figure 9.5: R245fa Manifold Design 1 proportion of the heat transfer occurring within the gap compared to the total heat transfer to the fluid

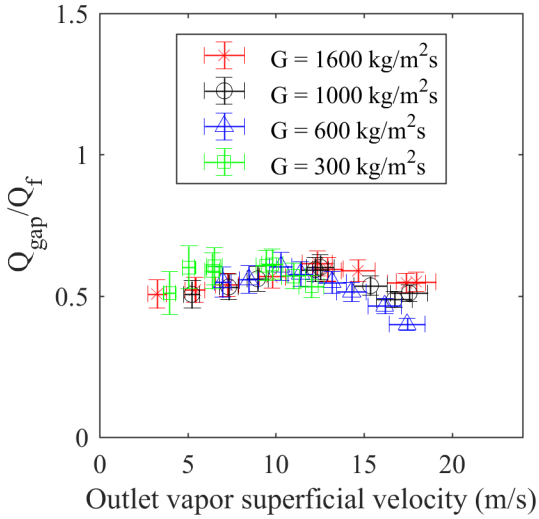

Figure 9.6: R245fa Manifold Design 2 proportion of the heat transfer occurring within the gap compared to the total heat transfer to the fluid

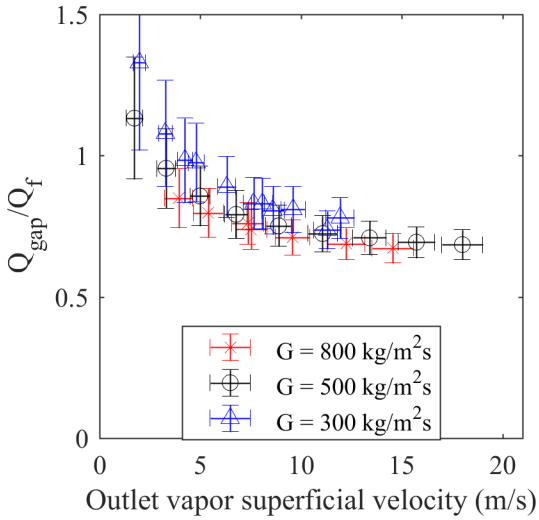

Figure 9.7: FC-72 Manifold Design 1 proportion of the heat transfer occurring within the gap compared to the total heat transfer to the fluid

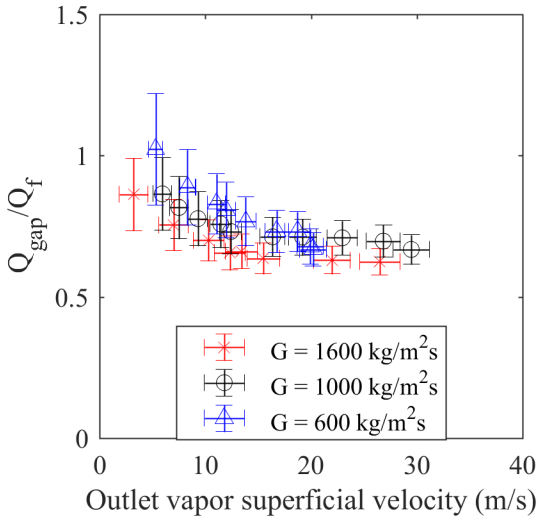

Figure 9.8: FC-72 Manifold Design 2 proportion of the heat transfer occurring within the gap compared to the total heat transfer to the fluid

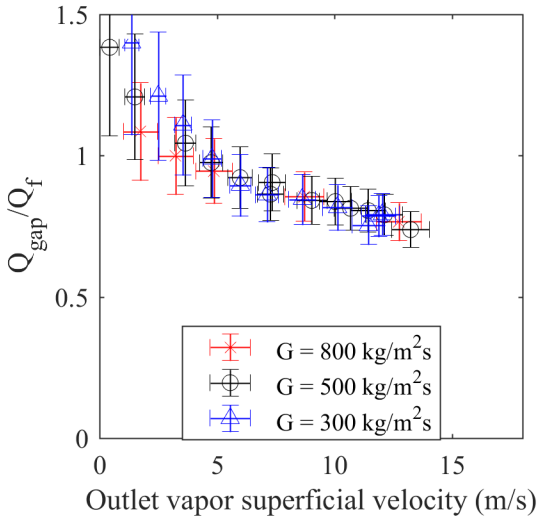

Figure 9.9: FC-72 Manifold Design 3 proportion of the heat transfer occurring within the gap compared to the total heat transfer to the fluid

9.3.4 Plots of Saturation Temperature Difference from Inlet to Outlet

The difference in saturation temperature from gap inlet to outlet are shown in Figure 9.10 through Figure 9.14. The saturation temperature difference is based on the estimated inlet pressure and pressure drop to the outlet. It can be seen that R245fa generally exhibits less than 1°C saturation temperature difference from inlet to outlet, in large part due to the lower pressure drop generated by the fluid. In contrast, FC-72 generates in excess of 10°C saturation temperature difference from inlet to outlet at the highest superheats and the associated outlet qualities. It can also be seen that the saturation temperature difference increases with increasing mass flux, and exhibits similar trends to that of the total pressure drop.

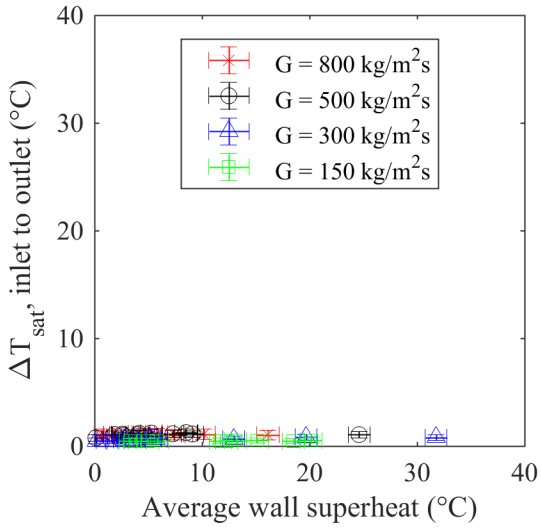

Figure 9.10: R245fa Manifold Design 1 saturation temperature difference from gap inlet to outlet

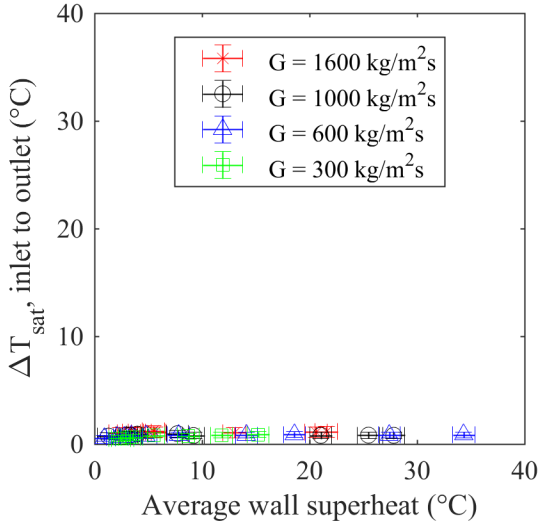

Figure 9.11: R245fa Manifold Design 2 saturation temperature difference from gap inlet to outlet

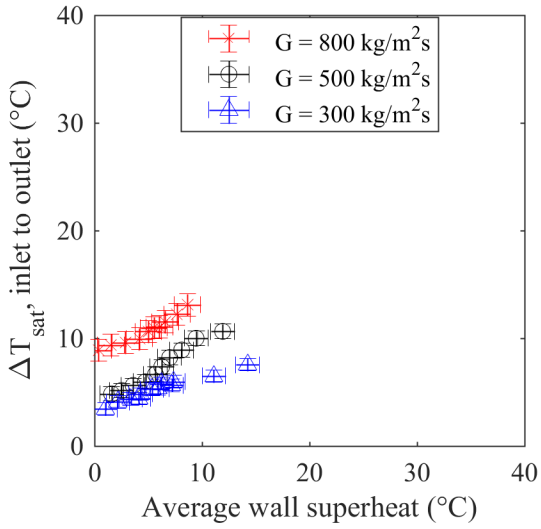

Figure 9.12: FC-72 Manifold Design 1 saturation temperature difference from gap inlet to outlet

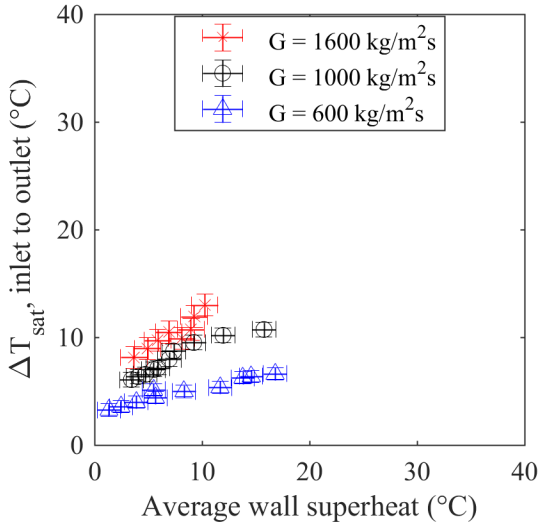

Figure 9.13: FC-72 Manifold Design 2 saturation temperature difference from gap inlet to outlet

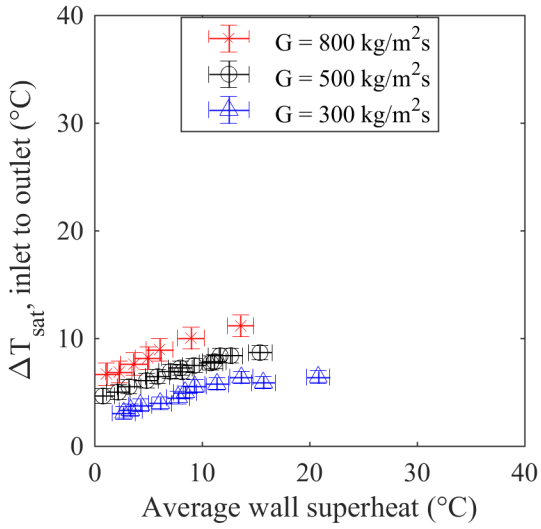

Figure 9.14: FC-72 Manifold Design 3 saturation temperature difference from gap inlet to outlet

9.3.5 HTC's: Average Wall Temperature, Average Wall Heat Flux, and Average Saturation Temperature

The HTC's calculated by first averaging wall temperature, saturation temperature, and wall heat flux, then calculating HTC are shown in Figure 9.15 through Figure 9.19. Comparing with the results presented in Chapter 6 based on locally averaged HTC's, it can be seen that averaging before calculating the HTC reduces the HTC's by about 20%. Therefore, the very high inlet HTC's generated with local temperatures and heat flux do have an effect on the average value, but not inordinately.

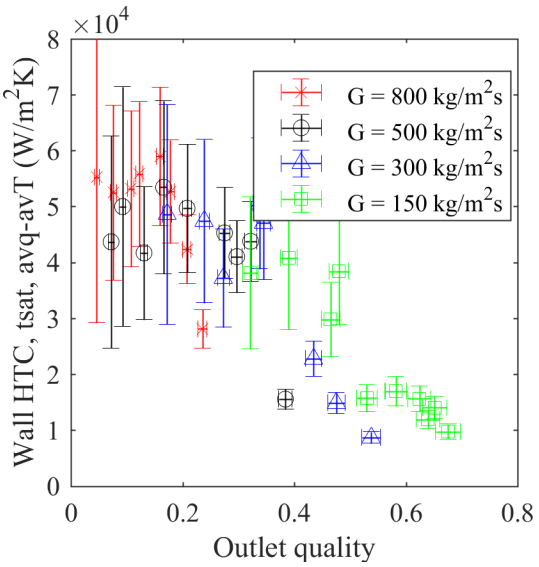

Figure 9.15: R245fa Manifold Design 1 wall HTC's calculated by first averaging wall temperature, saturation temperature, and wall heat flux, then calculating HTC

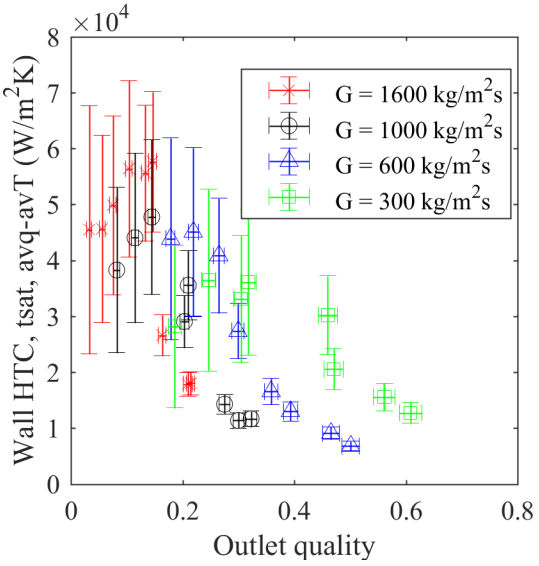

Figure 9.16: R245fa Manifold Design 2 wall HTC's calculated by first averaging wall temperature, saturation temperature, and wall heat flux, then calculating HTC

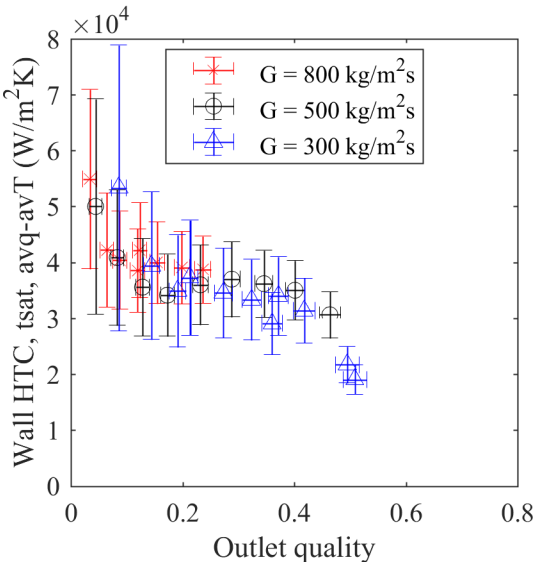

Figure 9.17: FC-72 Manifold Design 1 wall HTC's calculated by first averaging wall temperature, saturation temperature, and wall heat flux, then calculating HTC

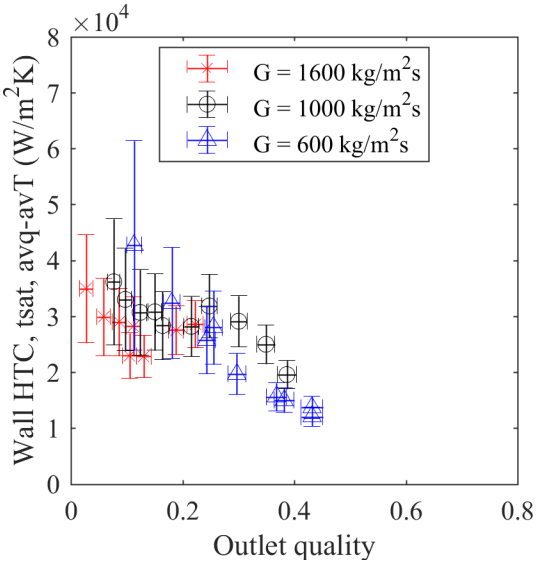

Figure 9.18: FC-72 Manifold Design 2 wall HTC's calculated by first averaging wall temperature, saturation temperature, and wall heat flux, then calculating HTC

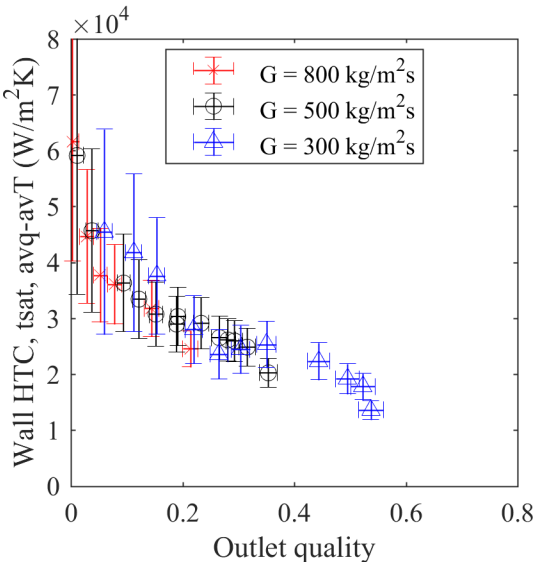

Figure 9.19: FC-72 Manifold Design 3 wall HTC's calculated by first averaging wall temperature, saturation temperature, and wall heat flux, then calculating HTC

9.3.6 Proportion of Heat of Subcooling to Total Heat to Fluid

The ratio of the heat absorbed by subcooling to the heat absorbed by latent heat is shown in Figure 9.20 through Figure 9.24. A value of 1 indicates that equivalent heat transfer occurs through sensible and latent heat. A diminishing value indicates that the heat absorbed by latent heat dominates over subcooling. From the narrow locus and value diminishing to less than 0.2 by 20% quality, it can be concluded that the effect of the small variation of ±1.5°C in subcooling is comparatively small, and an acceptable margin of variation.

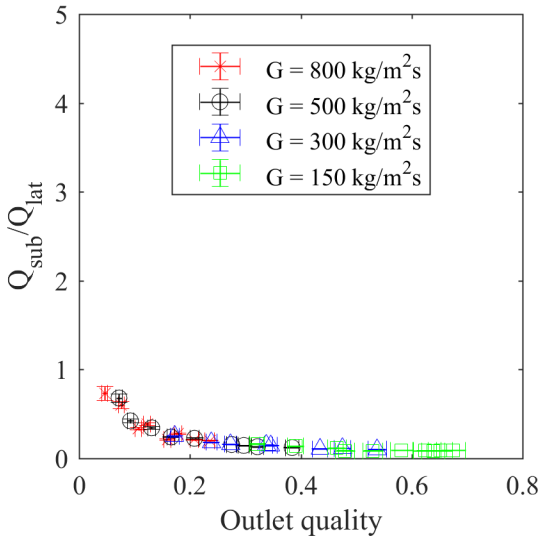

Figure 9.20: R245fa Manifold Design 1 heat of subcooling to latent heat ratio

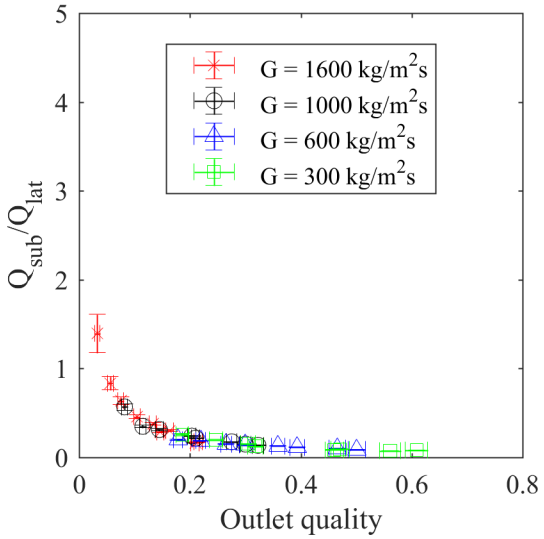

Figure 9.21: R245fa Manifold Design 2 heat of subcooling to latent heat ratio

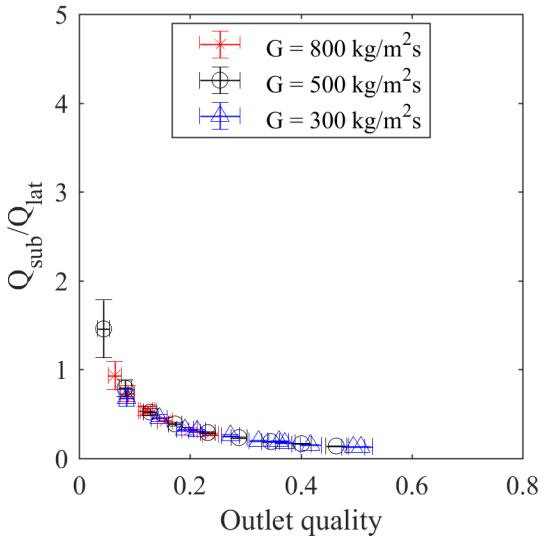

Figure 9.22: FC-72 Manifold Design 1 heat of subcooling to latent heat ratio

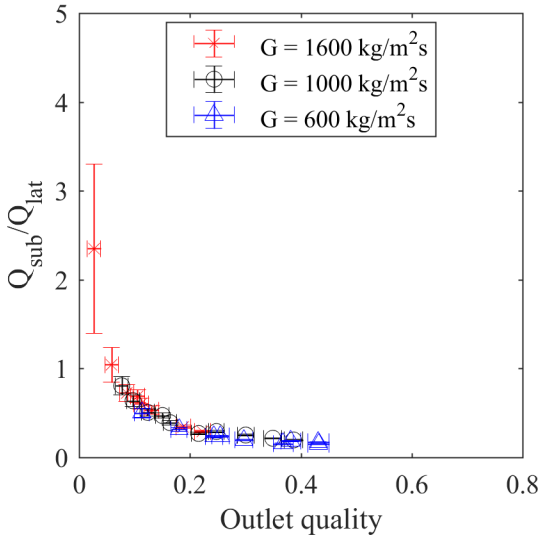

Figure 9.23: FC-72 Manifold Design 2 heat of subcooling to latent heat ratio

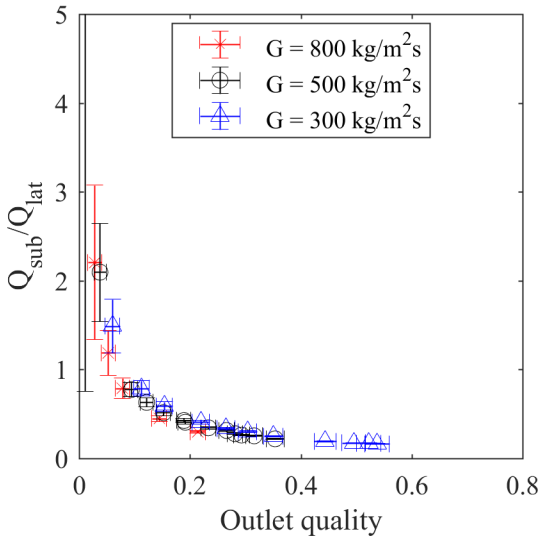

Figure 9.24: FC-72 Manifold Design 3 heat of subcooling to latent heat ratio

9.3.7 Local HTC Uncertainty

The local HTC uncertainty generated by the local saturation temperature uncertainty, local temperature uncertainty, and local heat flux uncertainty are shown in Figure 9.25 through Figure 9.29. It can be seen that for the majority of conditions, the uncertainty is less than about 10,000 W/m^{2}K across the channel wall. But, the inlet region with FC-72 at low velocities and high mass fluxes has a substantially greater uncertainty of more than 150,000 W/m^{2}K in some cases. This is because of the low superheat under in these areas under the tested conditions.

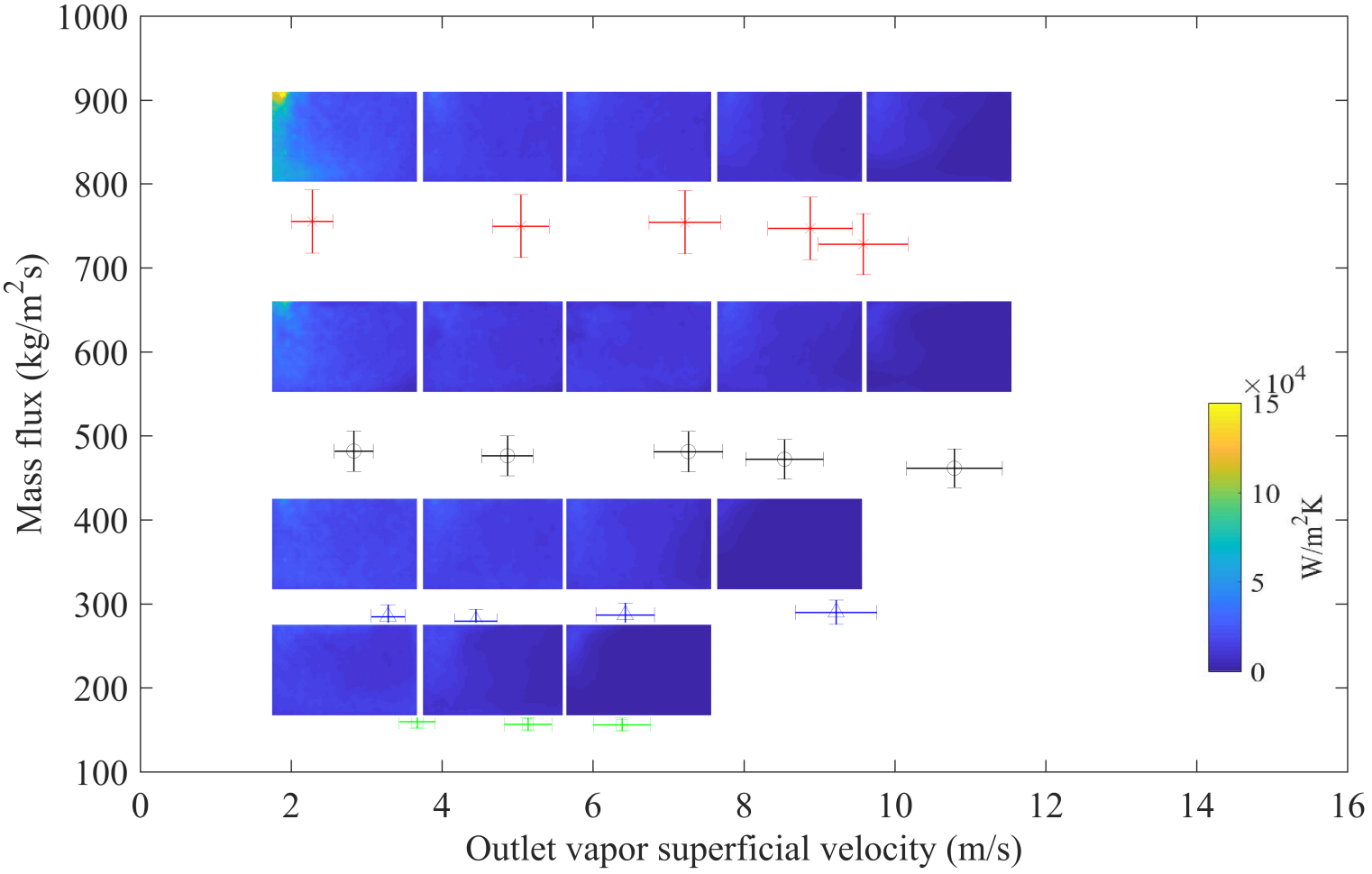

Figure 9.25: R245fa Design 1 Local HTC uncertainty profiles at intervals of outlet vapor superficial velocity and mass flux

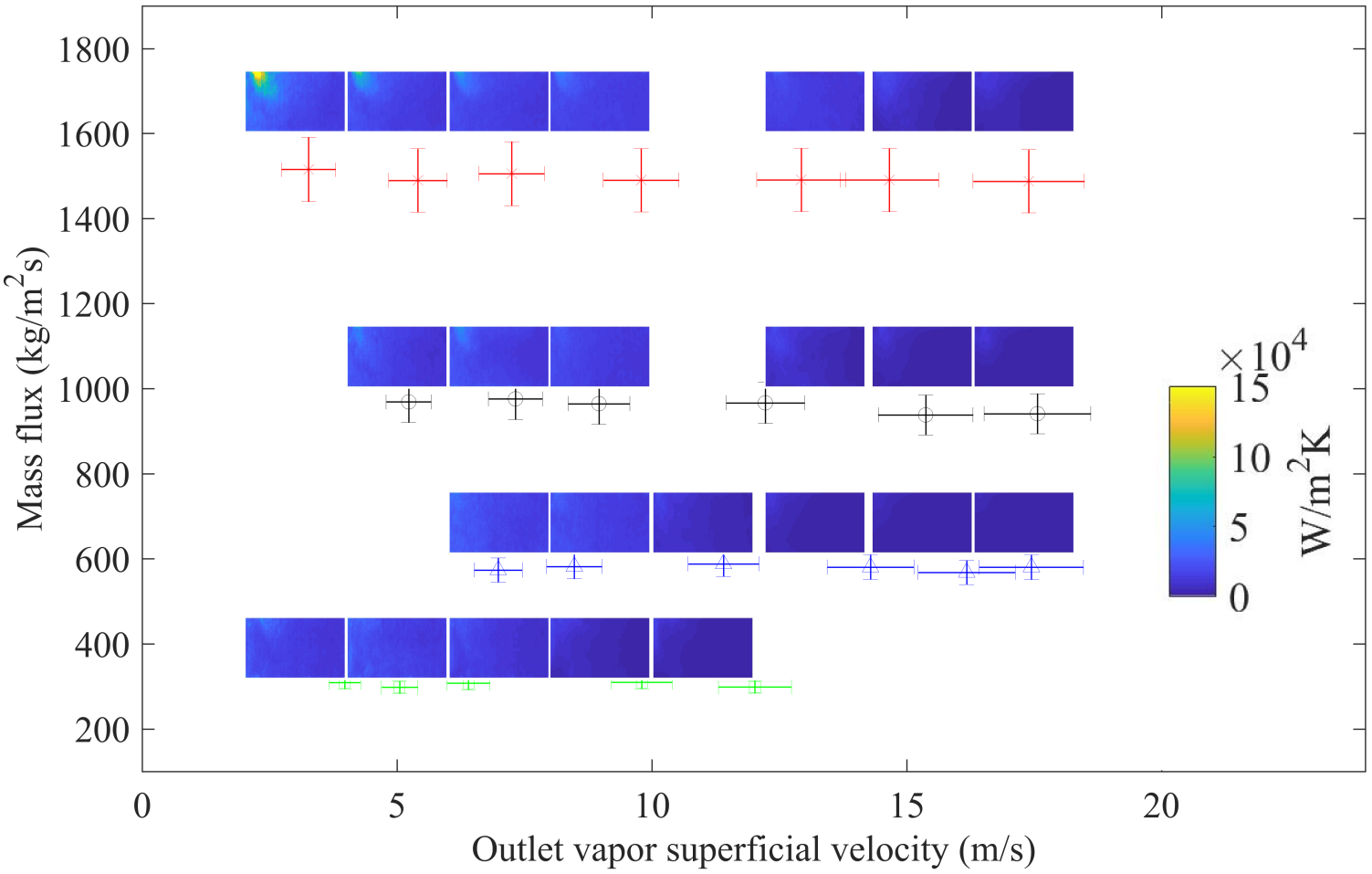

Figure 9.26: R245fa Design 2 Local HTC uncertainty profiles at intervals of outlet vapor superficial velocity and mass flux

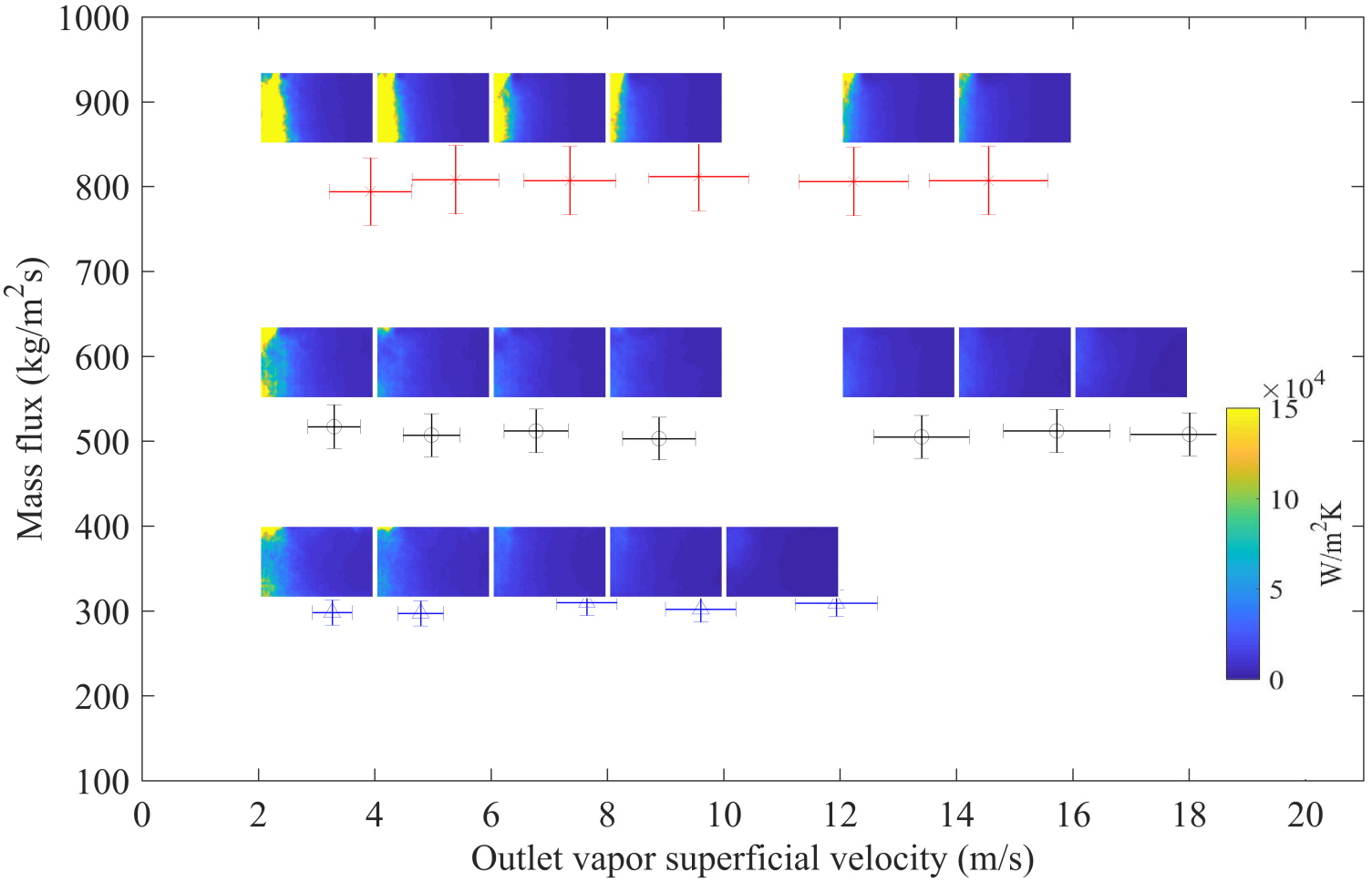

Figure 9.27: FC72 Design 1 Local HTC uncertainty profiles at intervals of outlet vapor superficial velocity and mass flux

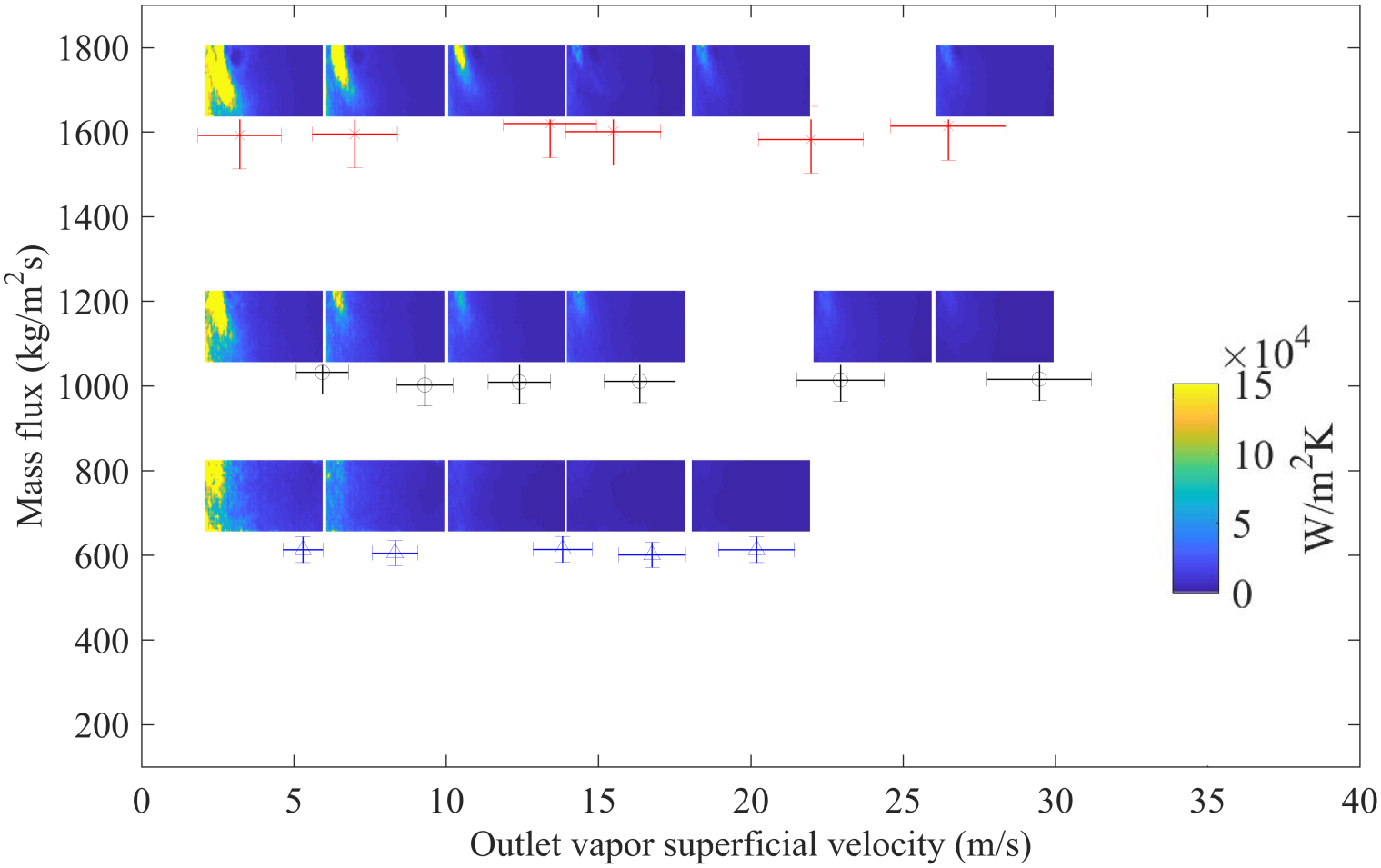

Figure 9.28: FC72 Design 2 Local HTC uncertainty profiles at intervals of outlet vapor superficial velocity and mass flux

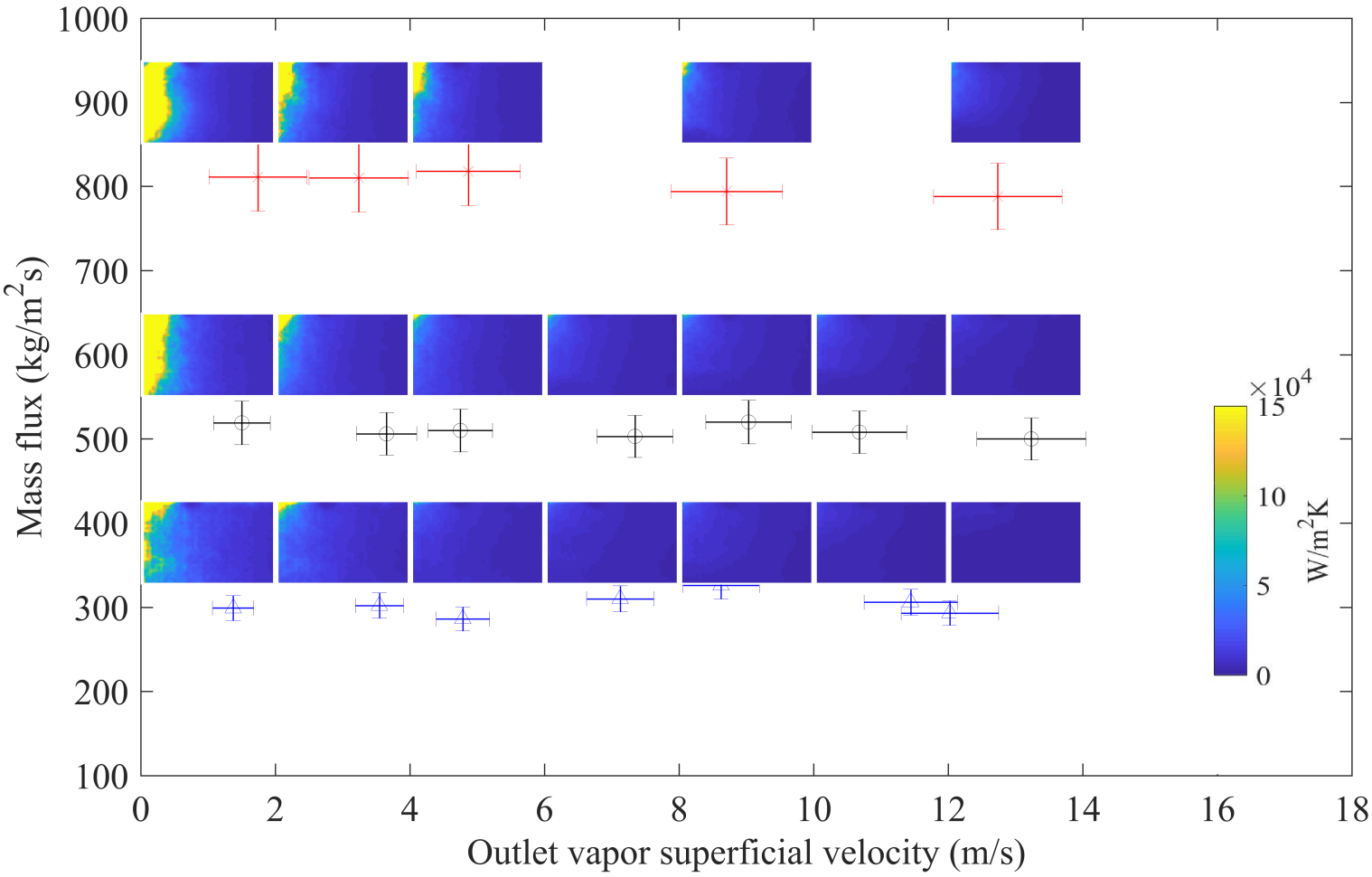

Figure 9.29: FC72 Design 3 Local HTC uncertainty profiles at intervals of outlet vapor superficial velocity and mass flux

Bibliography

[1] McCluskey, F. P., Grzybowski, R., and Podlesak, T., 1997, High temperature electronics, CRC Press, Boca Raton.
[2] Han, B., Jang, C., Bar-Cohen, A., and Song, B., 2010, "Coupled Thermal and Thermo-Mechanical Design Assessment of High Power Light Emitting Diode," IEEE Transactions on Components and Packaging Technologies, 33(4), pp. 688-697.
[3] Prasher, R., 2006, "Thermal interface materials: historical perspective, status, and future directions," Proc. of the IEEE, 94(8), pp. 1571-1586.
[4] Moore, A. L., and Shi, L., 2014, "Emerging challenges and materials for thermal management of electronics," Materials Today, 17(4), pp. 163-174.
[5] Ditri, J., Hahn, J., Cadotte, R., McNulty, M., Luppa, D., 2015, "Embedded cooling of high heat flux electronics utilizing distributed microfluidic impingement jets," *International Technical Conference and Exhibition on Packaging and Integration of Electronic and Photonic Microsystems*, ASME, p. V003T10A014.
[6] Bar-Cohen, A., Maurer, J. J., and Felbinger, J. G., 2013, "DARPA's intra/interchip enhanced cooling (ICECool) program," *Proc. CS MANTECH Conference*, New Orleans, pp. 171-174.
[7] Boteler, L. M., 2011, "Microfabrication and analysis of manifold microchannel coolers for power electronics," Ph.D. thesis, University of Maryland.
[8] Ditri, J., Cadotte, R., Fetterolf, D., and McNulty, M., 2016, "Impact of microfluidic cooling on high power amplifier RF performance," *Proc.15th IEEE Intersociety Conference on Thermal and Thermomechanical Phenomena in Electronic Systems (ITherm)*, IEEE, pp. 1501-1504.
[9] Tuckerman, D. B., and Pease, R. F. W., 1981, "High-performance heat sinking for VLSI," Electron Device Letters, 2(5), pp. 126-129.
[10] Kermani, E., Dessiatoun, S., Shooshtari, A., and Ohadi, M. M., 2009, "Experimental investigation of heat transfer performance of a manifold microchannel heat sink for cooling of concentrated solar cells," *Proc. Electronic Components and Technology Conference*, IEEE, pp. 453-459.
[11] Altman, D. H., Gupta, A., and Tyhach, M., 2015, "Development of a Diamond Microfluidics-Based Intra-Chip Cooling Technology for GaN," *International Technical Conference and Exhibition on Packaging and Integration of Electronic and Photonic Microsystems*, ASME, p. V003T004A006.
[12] Schultz, M., Yang, F. H., Colgan, E., Polastre, R., Dang, B., Tsang, C., Gaynes, M., Parida, P., Knickerbocker, J., Chainer, T., 2015, "Embedded two-phase cooling of large 3D compatible chips with radial channels," *International Technical Conference and Exhibition on Packaging and Integration of Electronic and Photonic Microsystems*, ASME, p. V003T10A007.
[13] Bar-Cohen, A., Maurer, J. J., and Sivananthan, A., 2016, "Near-junction microfluidic cooling for wide bandgap devices," MRS Advances, 1(2), pp. 181-195.
[14] Bar-Cohen, A., and Wang, P., 2012, "Thermal management of on-chip hot spot," J. of Heat Transfer-Trans. of the ASME, 134(5), p. 051017.

[15] Bar-Cohen, A., Maurer, J. J., and Sivananthan, A., 2015, "Near-junction microfluidic thermal management of RF power amplifiers," *Proc. Microwaves, Communications, Antennas and Electronic Systems (COMCAS)*, IEEE, pp. 1-8.
[16] Bergman, T. L., Lavine, A. S., Incropera, F. P., and DeWitt, D. P., 2011, Fundamentals of Heat and Mass Transfer, John Wiley & Sons, Hoboken, NJ.
[17] Charoensawan, P., Khandekar, S., Groll, M., and Terdtoon, P., 2003, "Closed loop pulsating heat pipes: Part A: parametric experimental investigations," Applied Thermal Engineering, 23(16), pp. 2009-2020.
[18] Adera, S., Antao, D., Raj, R., and Wang, E. N., 2016, "Design of micropillar wicks for thin-film evaporation," International Journal of Heat and Mass Transfer, 101, pp. 280-294.
[19] Chilton, T. H., and Colburn, A. P., 1934, "Mass transfer (absorption) coefficients prediction from data on heat transfer and fluid friction," Industrial & Engineering Chemistry, 26(11), pp. 1183-1187.
[20] Chen, J. C., 1966, "Correlation for boiling heat transfer to saturated fluids in convective flow," Industrial & Engineering Chemistry Process Design and Development, 5(3), pp. 322-329.
[21] Agostini, B., Thome, J. R., Fabbri, M., and Michel, B., 2008, "High heat flux two-phase cooling in silicon multimicrochannels," IEEE Transactions on Components and Packaging Technologies, 31(3), pp. 691-701.
[22] Garimella, S. V., and Sobhan, C. B., 2003, "Transport in microchannels-a critical review," Annual Review of Heat Transfer, 13, Begell House, Danbury, CT, Chap. 1.
[23] Thome, J. R., 2004, "Boiling in microchannels: a review of experiment and theory," International Journal of Heat and Fluid Flow, 25(2), pp. 128-139.
[24] Green, C., Kottke, P., Han, X., Woodrum, C., Sarvey, T., Asrar, P., Zhang, X., Joshi, Y., Fedorov, A., Sitaraman, S., and Bakir, M., 2015, "A Review of Two-Phase Forced Cooling in Three-Dimensional Stacked Electronics: Technology Integration," Journal of Electronic Packaging, 137(4), pp. 040802-040809.
[25] Szczukiewicz, S., Magnini, M., and Thome, J. R., 2014, "Proposed models, ongoing experiments, and latest numerical simulations of microchannel two-phase flow boiling," International Journal of Multiphase Flow, 59, pp. 84-101.
[26] Borhani, N., and Thome, J. R., 2014, "Intermittent dewetting and dryout of annular flows," International Journal of Multiphase Flow, 67, pp. 144-152.
[27] Rau, M. J., Garimella, S. V., Dede, E. M., and Joshi, S. N., 2015, "Boiling Heat Transfer From an Array of Round Jets With Hybrid Surface Enhancements," Journal of Heat Transfer-Transactions of the ASME, 137(7), p. 071501.
[28] Joshi, S. N., and Dede, E. M., 2017, "Two-phase jet impingement cooling for high heat flux wide band-gap devices using multi-scale porous surfaces," Applied Thermal Engineering, 110, pp. 10-17.
[29] Kalani, A., and Kandlikar, S. G., 2015, "Flow patterns and heat transfer mechanisms during flow boiling over open microchannels in tapered manifold (OMM)," International Journal of Heat and Mass Transfer, 89, pp. 494-504.
[30] Baummer, T., Cetegen, E., Ohadi, M., and Dessiatoun, S., 2008, "Force-fed evaporation and condensation utilizing advanced micro-structured surfaces and micro-channels," Microelectronics Journal, 39(7), pp. 975-980.

[31] Cetegen, E., 2010, "Force fed microchannel high heat flux cooling utilizing microgrooved surfaces," Ph.D. Thesis, University of Maryland, College Park, Md.
[32] DARPA, 2012, "Intrachip/Interchip Enhanced Cooling Fundamentals (ICECool Fundamentals), DARPA-BAA-12-50.
[33] Asrar, P., Zhang, X. C., Woodrum, C. D., Green, C. E., Kottke, P. A., Sarvey, T. E., Sitaraman, S., Fedorov, A., Bakir, M., Joshi, Y. K., 2016, "Flow Boiling of R245fa in a Microgap with Integrated Staggered Pin Fins," *Proc. 15th IEEE Intersociety Conference on Thermal and Thermomechanical Phenomena in Electronic Systems (ITherm)*, IEEE, pp. 1007-1012.
[34] Han, X. F., Fedorov, A., and Joshi, Y., 2016, "Flow Boiling in Microgaps for Thermal Management of High Heat Flux Microsystems," Journal of Electronic Packaging, 138(4), p. 040801.
[35] Drummond, K. P., Back, D., Sinanis, M. D., Janes, D. B., Peroulis, D., Weibel, J. A., and Garimella, S. V., 2018, "A hierarchical manifold microchannel heat sink array for high-heat-flux two-phase cooling of electronics," International Journal of Heat and Mass Transfer, 117, pp. 319-330.
[36] Bae, D. G., Mandel, R. K., Dessiatoun, S. V., Rajgopal, S., Roberts, S. P., Mehregany, M., and Ohadi, M. M., 2017, "Embedded two-phase cooling of high heat flux electronics on silicon carbide (SiC) using thin-film evaporation and an enhanced delivery system (FEEDS) manifold-microchannel cooler," *Proc. 16th IEEE Intersociety Conference on Thermal and Thermomechanical Phenomena in Electronic Systems (ITherm)*, IEEE, pp. 466-472.
[37] Mandel, R., Dessiatoun, S., McCluskey, P., and Ohadi, M., 2015, "Embedded Two-Phase Cooling of High Flux Electronics via Micro-Enabled Surfaces and Fluid Delivery Systems (FEEDS)," *Proc. ASME 2015 International Technical Conference and Exhibition on Packaging and Integration of Electronic and Photonic Microsystems*, ASME, p. V003T010A012.
[38] Palko, J. W., Lee, H., Agonafer, D. D., Zhang, C., Jung, K. W., Moss, J., Wilbur, J. D., Dusseault, T. J., Barako, M. T., Houshmand, F., Rong, G. G., Maitra, T., Gorle, C., Won, Y., Rockosi, D., Mykyta, I., Resler, D., Altman, D., Asheghi, M., Santiago, J. G., and Goodson, K. E., 2016, "High Heat Flux Two-Phase Cooling of Electronics with Integrated Diamond/Porous Copper Heat Sinks and Microfluidic Coolant Supply," *Proc. 15th IEEE Intersociety Conference on Thermal and Thermomechanical Phenomena in Electronic Systems (ITherm)*, IEEE, pp. 1511-1517.
[39] Soule, C. A., 2001, "Future trends in heat sink design," Electronics Cooling, 7(1), from https://www.electronics-cooling.com/2001/02/future-trends-in-heat-sink-design/.
[40] Wilson, J., 2005, "Cooling Solutions In The Past Decade," Electronics Cooling 11(4), from https://www.electronics-cooling.com/2005/11/cooling-solutions-in-the-past-decade/.
[41] Bar-Cohen, A., Robinson, F. L., and Deisenroth, D. C., 2018, "Challenges and opportunities in Gen3 embedded cooling with high-quality microgap flow," *Proc. Electronics Packaging and iMAPS All Asia Conference (ICEP-IAAC)*, IEEE, pp. K-1-K-12.

[42] Ohadi, M., Choo, K., Dessiatoun, S., and Cetegen, E., 2013, Next generation microchannel heat exchangers, Springer, New York.
[43] Harirchian, T., and Garimella, S. V., 2010, "A comprehensive flow regime map for microchannel flow boiling with quantitative transition criteria," International Journal of Heat and Mass Transfer, 53(13-14), pp. 2694-2702.
[44] Ong, C. L., and Thome, J., 2011, "Macro-to-microchannel transition in two-phase flow: Part 1–Two-phase flow patterns and film thickness measurements," Experimental Thermal and Fluid Science, 35(1), pp. 37-47.
[45] Karayiannis, T., and Mahmoud, M. M., 2018, "Flow Boiling in Micro-Passages: Developments in Fundamental aspects and Applications," *Proc. of the 16th Int. Heat Transfer Conference*, IHTC-16, Beijing, China, p. KN09.
[46] Çengel, Y. A., and Boles, M. A., 2011, Thermodynamics : an engineering approach, McGraw-Hill, New York, NY.
[47] Kosar, A., Kuo, C. J., and Peles, Y., 2006, "Suppression of boiling flow oscillations in parallel microchannels by inlet restrictors," Journal of Heat Transfer-Trans. of the ASME, 128(3), pp. 251-260.
[48] Kandlikar, S. G., Kuan, W. K., Willistein, D. A., and Borrelli, J., 2006, "Stabilization of flow boiling in microchannels using pressure drop elements and fabricated nucleation sites," Journal of Heat Transfer-Trans. of the ASME, 128(4), pp. 389-396.
[49] Mandel, R. K., 2016, "Embedded two-phase cooling of high flux electronics via micro-enabled surfaces and fluid delivery system (FEEDS)," Ph.D. thesis, University of Maryland.
[50] Ong, C. L., and Thome, J. R., 2011, "Macro-to-microchannel transition in two-phase flow: Part 2 – Flow boiling heat transfer and critical heat flux," Experimental Thermal and Fluid Science, 35(6), pp. 873-886.
[51] Forster, H. K., and Zuber, N., 1955, "Dynamics of vapor bubbles and boiling heat transfer," AIChE Journal, 1(4), pp. 531-535
[52] Qu, W., and Mudawar, I., 2003, "Flow boiling heat transfer in two-phase micro-channel heat sinks—I. Experimental investigation and assessment of correlation methods," International Journal of Heat and Mass Transfer, 46(15), pp. 2755-2771.
[53] Taitel, Y., and Dukler, A., 1976, "A model for predicting flow regime transitions in horizontal and near horizontal gas-liquid flow," AIChE Journal, 22(1), pp. 47-55.
[54] Deisenroth, D. C., Ohadi, M., and Bar-Cohen, A., 2017, "Two-phase flow regimes in a U-shaped diabatic manifolded-microgap channel," *Proc. Thermal and Thermomechanical Phenomena in Electronic Systems (ITherm)*, IEEE, pp. 208-219.
[55] Tibiriçá, C. B., and Ribatski, G., 2015, "Flow boiling phenomenological differences between micro-and macroscale channels," Heat Transfer Engineering, 36(11), pp. 937-942.
[56] Barajas, A. M., and Panton, R. L., 1993, "The effect of contact angle on two-phase flow in capillary tubes," International Journal of Multiphase Flow, 19(2), pp. 337-346.
[57] Wojtan, L., Ursenbacher, T., and Thome, J. R., 2005, "Investigation of flow boiling in horizontal tubes: Part II - Development of a new heat transfer model for stratified-wavy, dryout and mist flow regimes," International Journal of Heat and Mass Transfer, 48(14), pp. 2970-2985.

[58] Ullmann, A., and Brauner, N., 2007, "The prediction of flow pattern maps in minichannels," Multiphase Science and Technology, 19(1), pp. 49-73.
[59] Rahim, E., and Bar-Cohen, A., 2015, "Thermal Characteristics of a Chip-Scale Two-Phase Microgap Cooler," Heat Transfer Engineering, 36(5), pp. 511-520.
[60] Bar-Cohen, A., and Rahim, E., 2009, "Modeling and Prediction of Two-Phase Microgap Channel Heat Transfer Characteristics," Heat Transfer Engineering, 30(8), pp. 601-625.
[61] Taitel, Y., 1990, "Flow pattern transition in two-phase flow," *Proc. of the 9th International Heat Transfer Conference*, pp. 237-253.
[62] Lockhart, R., and Martinelli, R., 1949, "Proposed correlation of data for isothermal two-phase, two-component flow in pipes," Chemical Engineering Progress, 45(1), pp. 39-48.
[63] Chen, W. W., and Fang, X. D., 2014, "A note on the Chen correlation of saturated flow boiling heat transfer," International Journal of Refrigeration-Revue Internationale Du Froid, 48, pp. 100-104.
[64] Bergles, A. E., Collier, J., Delhaye, J. M., Hewitt, G., and Mayinger, F., 1981, Two-phase flow and heat transfer in the power and process industries, Hemisphere Publishing Corporation, New York.
[65] Qu, W., Yoon, S.-M., and Mudawar, I., 2003, "Two-phase flow and heat transfer in rectangular micro-channels," *Proc. ASME 2003 Heat Transfer Summer Conference*, ASME, pp. 397-410.
[66] Yang, Y., and Fujita, Y., 2004, "Flow boiling heat transfer and flow pattern in rectangular channel of mini-gap," *Proc. ASME 2004 2nd International Conference on Microchannels and Minichannels*, ASME, pp. 573-580.
[67] Bar-Cohen, A., Sheehan, J. R., and Rahim, E., 2012, "Two-phase thermal transport in microgap channels—theory, experimental results, and predictive relations," Microgravity Science and Technology, 24(1), pp. 1-15.
[68] Kabov, O. A., Zaitsev, D., Cheverda, V., and Bar-Cohen, A., 2011, "Evaporation and flow dynamics of thin, shear-driven liquid films in microgap channels," Experimental Thermal and Fluid Sci., 35(5), pp. 825-831.
[69] Bar-Cohen, A., and Holloway, C., "Waves, Instabilities, and Rivulets in High Quality Microgap Two-Phase Flow," *Proc. 7th European Thermal-Sciences Conference (Eurotherm),* Journal of Physics Conference Series, p. 022002.
[70] Takemura, T., Roko, K., Shiraha, M., and Midoriyama, S., 1986, "Dryout characteristics and flow behavior of gas water 2-phase flow through u-shaped and inverted u-shaped bends," Nuclear Engineering and Design, 95, pp. 365-373.
[71] Leland, J. E., and Chow, L. C., 1995, "Channel height and curvature effects on flow boiling from an electronic chip," Journal of Thermophysics and Heat Transfer, 9(2), pp. 292-301.
[72] Sturgis, J. C., and Mudawar, I., 1999, "Critical heat flux in a long, curved channel subjected to concave heating," International Journal of Heat and Mass Transfer, 42(20), pp. 3831-3848.
[73] Usui, K., Aoki, S., and Inoue, A., 1983, "Flow behavior and phase distribution in 2-phase flow around inverted u-bend," Journal of Nuclear Science and Technology, 20(11), pp. 915-928.

[74] Da Silva Lima, R. J., and Thome, J. R., 2012, "Two-phase flow patterns in U-bends and their contiguous straight tubes for different orientations, tube and bend diameters," International Journal of Refrigeration, 35(5), pp. 1439-1454.
[75] De Kerpel, K., Ameel, B., Huisseune, H., T'Joen, C., Caniere, H., and De Paepe, M., 2012, "Two-phase flow behaviour and pressure drop of R134a in a smooth hairpin," International Journal of Heat and Mass Transfer, 55(4), pp. 1179-1188.
[76] Berthoud, G., and Jayanti, S., 1990, "Characterization of dryout in helical-coils," International Journal of Heat and Mass Transfer, 33(7), pp. 1451-1463.
[77] Dean, W., and Hurst, J., 1959, "Note on the motion of fluid in a curved pipe," Mathematika, 6(01), pp. 77-85.
[78] Usui, K., Aoki, S., and Inoue, A., 1980, "Flow behavior and pressure drop of two-phase flow through C-shaped bend in vertical plane, (I) upward flow," Journal of Nuclear Science and Technology, 17(12), pp. 875-887.
[79] Usui, K., Aoki, S., and Inoue, A., 1981, "Flow behavior and pressure drop of two-phase flow through C-shaped bend in vertical plane, (II) downward flow," Journal of Nuclear Science and Technology, 18(3), pp. 179-190.
[80] Hazel, A. L., Heil, M., Waters, S. L., and Oliver, J. M., 2012, "On the liquid lining in fluid-conveying curved tubes," Journal of Fluid Mechanics, 705, pp. 213-233.
[81] Hewitt, G. F., and Jayanti, S., 1992, "Prediction of film inversion in 2-phase flow in coiled tubes," Journal of Fluid Mechanics, 236, pp. 497-511.
[82] Chong, L. Y., Azzopardi, B. J., and Bate, D. J., 2005, "Calculation of conditions at which dryout occurs in the serpentine channels of fired rebolilers," Chemical Engineering Research & Design, 83(A4), pp. 412-422.
[83] Brusstar, M. J., Merte, H., Keller, R. B., and Kirby, B. J., 1997, "Effects of heater surface orientation on the critical heat flux .1. An experimental evaluation of models for subcooled pool boiling," International Journal of Heat and Mass Transfer, 40(17), pp. 4007-4019.
[84] Zuber, N., 1958, "On the stability of boiling heat transfer," Trans. ASME., 80.
[85] Rohsenow, W. M., 1971, "Boiling," Annual Review of Fluid Mechanics, 3(1), pp. 211-236.
[86] Howard, A. H., and Mudawar, I., 1999, "Orientation effects on pool boiling critical heat flux (CHF) and modeling of CHF for near-vertical surfaces," International Journal of Heat and Mass Transfer, 42(9), pp. 1665-1688.
[87] Brusstar, M. J., and Merte, H., 1994, "Effects of buoyancy on the critical heat-flux in forced-convection," Journal of Thermophysics and Heat Transfer, 8(2), pp. 322-328.
[88] Hughes, T. G., 1974, "Critical heat fluxes for curved and straight surfaces during subcooled flow boiling," Ph.D. thesis, Pennsylvania State University.
[89] Klein, S., and Alvardo, F., 2015, "EES-Engineering equation solver: user's manual for Microsoft windows operating systems," F-Chart Software, Madison, WI, USA.
[90] 3M, 2000, "Fluorinert™ Electronic Liquid FC-72 Product Information," from https://www.3m.com/3M/en_US/company-us/all-3m-products/~/3M-Fluorinert-Electronic-Liquid-FC-72/?N=5002385+3290667393&rt=rud.

[91] Geisler, K., 2013, "Dielectric Liquid Cooling of Immersed Components," Encyclopedia of Thermal Packaging, A. Bar-Cohen, ed., World Scientific Publishing Co. Pte. Ltd., Hackensack, NJ.
[92] Ansys Inc., 2016, "Fluent Documentation."
[93] Munson, B. R., Young, D. F., Okiishi, T. H., and Huebsch, W. W., 2009, Fundamentals of Fluid Mechanics, John Wiley & Sons, Inc., USA.
[94] Choi, Y. S., Lim, T. W., You, S. S., and Kim, H. S., 2018, "Pressure drop characteristics for two-phase flow of FC-72 in microchannel," *Proc. of the Institution of Mechanical Engineers Part C-Journal of Mechanical Engineering Science*, The Institution of Mechanical Engineers, London, 232(6), pp. 987-997.
[95] Setra Systems, Inc., 2014, "Model 205 Gauge & Absolute Pressure Transducer."
[96] Setra Systems, Inc., 2017, "Model 230 True Wet-to-Wet Differential Pressure Transducer."
[97] Omega Engineering, Inc., 2018, "ANSI and IEC Color Codes for Thermocouples, Wire and Connectors."
[98] Holman, J. P., 2012, Experimental methods for engineers, McGraw-Hill, New York.
[99] Deisenroth, D. C., Bar-Cohen, A., and Ohadi, M., 2017, "Geometry Effects on Two-Phase Flow Regimes in a Diabatic Manifolded Microgap Channel," *Proc. ASME 2017 International Technical Conference and Exhibition on Packaging and Integration of Electronic and Photonic Microsystems*, ASME, pp. V001T002A025.
[100] Collier, J. G., and Thome, J. R., 1994, Convective boiling and condensation, Clarendon Press, New York.